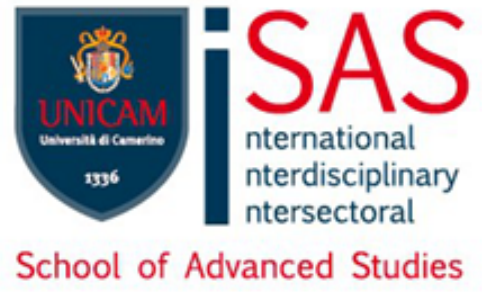

UNIVERSITÀ DEGLI STUDI DI CAMERINO

School of Advanced Studies

DOCTORAL COURSE IN

Materials Sciences

XXXVI cycle

Predictive Models in Espresso Coffee Percolation

Ph.D. Student:

Alessia Perticarini

Supervisor:

Prof. Pierluigi Maponi

Co-Supervisor:

Dr. Josephin Giacomini

Abstract

The trade of coffee market is comparable in size to that of oil and steel. This leads to a high level of competitiveness among the players operating in the sector, and the need to ensure the environmental sustainability of the sector. These aspects can be supported by the scientific research to improve the quality and the efficiency of the extraction process and to reduce the negative impact of coffee market on the environment. In this thesis we consider two different mathematical models for the espresso coffee extraction process to face the two main goals of coffee industry: the beverage customisation and the sustainability of the sector. The reduced model is used to predict the extraction efficiency. Two different numerical schemes are proposed: the finite difference approximation scheme and a radial basis functions (RBFs) approximation scheme; both the schemes are based on the Crank-Nicolson method for the integration with respect to time. The reliability of the model together with the proposed solving strategies is assessed experimentally, by comparing the efficiency of real and simulated extractions conducted under different physico-chemical conditions. Also a complete 3D model for the espresso coffee extraction is considered and a wide campaign of chemical laboratory analyses of espresso extracted samples is used for its calibration and validation. Finally, the equation governing the dynamics of the water during the espresso extraction to predict the flux behaviour is considered. The corresponding initial-boundary value problem is solved by using the Crank-Nicolson scheme with respect to the time, whereas the spatial derivatives are approximated via RBFs. The preliminary reliability of the proposed solving strategy is experimentally assessed by comparing the hydraulic head behaviour with different initial pressures of the incoming water.

Contents

Introduction

Brewing coffee is an art as well as a business, indeed, after natural gas, it represents the most exported raw material in the world. United States, with 400 million a day, are the main coffee consumer [1], while Europe has the highest per capita consumption, with about 5 kg of coffee per year [2].

Contrary to popular opinion, moderate consumption of coffee can bring health benefits due to the nutrients it contains, such as carbohydrates, proteins, lipids, riboflavin (vitamin B-2), niacin (vitamin B-3), and various phenolic acids, which have an antioxidant action. These nutrients, together with caffeine, seem to have a positive effect on the incidence of degenerative illnesses such as Parkinson's disease [3]. Some studies also show that coffee consumption can be associated with a lower risk of developing type 2 diabetes [4], while other studies show that coffee consumption can have beneficial effects on the risk of developing certain types of cancer, such as liver cancer [5], [6]. Obviously, if one exceeds with the consumption of this beverage, its effects could turn into harmful for human health.

Multiple factors contribute to give coffee its unmistakable taste and aroma; in fact, more than 1000 compounds occur in a cup of espresso, among them caffeine is the best-known compound and its recognition and attraction are probably due to the stimulating effects on the central nervous system [7]. Caffeine also influences the coffee flavour since, together with other compounds, such as trigonelline, thermally generated compounds (e.g., pyrazines, piperazine) and derivatives of phenolic acids (e.g., chlorogenic acid), it affects the bitterness of coffee. The bitterness is an important attribute of EC that drives the consumer acceptance [8]. In addition, several evidences have demonstrated that phenolic acids and chlorogenic

acids possess antioxidant, anti-inflammatory and anticarcinogenic activities [9]–[11]. Another revered taste of coffee flavour is the acidity (sourness); organic acids, such as acetic, citric and tartaric acid, seem to be the main responsible for this sensation in the oral mucosa [12]. Regarding the aroma, lipids play a key role because they retain lipophilic compounds that sensibly contribute to the aroma of the beverage. Obviously, all these nuances in coffee flavor are not the product of chance, but they are the result of a complex process to which coffee beans undergo and which gives coffee powder its peculiar physical-chemical characteristics. Numerous factors, such as type of coffee blend, roasting and grinding degree and preparation method (i.e., coffee extraction technique) can influence the levels of chemical compounds that arrive in cup and, accordingly, the final coffee flavour and quality [13], [14]. There are different possible manufacturing processes that eliminate the pulp of the coffee berries from the internal beans. For instance after harvesting the berries from the coffee plant, one of these methods provides that the fruit is separated from the seeds, and the beans are washed and dried in the open air. Then it follows the roasting phase in which the beans are introduced into a proper machine, that quickly brings them to a very high temperature. During this phase, over 600 chemical reactions take place in the bean, the result of which is a change in color (from green to brown), nutritional content and flavor (particularly sweetness and acidity), as well as weight loss and volume increase. At this point the coffee bean is more crumbly, perfect to be ground. The grinding phase produces a coffee powder with a granulometry that greatly affects the extraction, since the shape and size of the coffee powder particles play a fundamental role in the extraction speed of the chemical compounds and determine, together with the pressing operation, a key feature of the coffee pod: its porosity. In fact, the grinding phase together with the pressing operation create the coffee pod where the extraction process will take place by a percolation process.

As a consequence, one of the main future goals of the coffee industry is the customised coffee preparation, because the personal preferences depend on people's culture and traditions but also on health issues and temporary needs. For instance, a strong coffee usually aids concentration after a poor night's sleep or a light drink

is usually preferred after a heavy meal. Moreover, the success of coffee poses a new challenge for the environmental sustainability of the coffee industry: reduce the pressure to the agricultural and forestry sector below the equatorial zone. In other words, the raw material used in the preparation phase has to be minimised, whereas the quality and reproducibility of the beverage should be kept as high as possible. For this purpose, an important concept in the coffee industry to describe the efficiency of an extraction system is the Extraction Yield (EY), which is defined as the mass of extracted solubles driven into the cup over the mass of coffee powder. This indicator can be related with the amount of the Total Dissolved Solids (TDS), which is defined as the mass of dissolved substances over the mass of the beverage. Thus, the EY is obtained multiplying the TDS by the ratio between the mass of the beverage and the mass of the coffee powder. The TDS can be measured by a digital refractometer or by drying a portion of espresso coffee (EC) and weighting the remaining solids. The Specialty Coffee Association adopted a reference document, called brewing chart [13], which prescribes for EY the following optimal range $18\% - 22\%$; values lower than 18% lead to the so-called under-extracted coffees too acidic and sweet, whereas values larger than 22% lead to the so-called over-extracted coffees too bitter and astringent. In literature, EY and TDS are used for multiple purposes, see [15], [16] for a detailed description of their application.

The process of coffee extraction is complex both from the physical and chemical point of view, thus a complete description of such a process by a mathematical model is challenging. A limited number of studies has been developed in the physico-chemical modelling of coffee extraction. Among them, the model provided in [17] describes dissolution and transport of filtered coffee, using an approach that takes into account the intergranular and intragranular motion of coffee particles. This one-dimensional model has been exploited in [18] to investigate the coffee extraction uniformity. In [19], a one-dimensional percolation model is proposed and used to calculate the EY. A similar percolation model is used in [20], to predict the EY and the proposed numerical approach ensures the positivity of the concentrations and the mass conservation. The same solving strategy is also adopted in [21] where the percolation model is generalised for the prediction of an

arbitrary number of chemical compounds. All these one-dimensional percolation models have the advantage to be simple computational tools to predict the global water flow and extraction dynamics [22]. The three-dimensional model considering the main percolation processes and endowed with numerical simulations and a preliminary experimental validation can be found in [23] and [24].

In this thesis we propose a comprehensive study on the modelling of the EC extraction process and the numerical solution of the resulting problems.

The outline of the thesis is the following. In Chapter 1, we introduce Partial Differential Equations (PDE), their properties and classification, then we focus on Advection-Diffusion-Reaction equations and their features as they are the main governing equations of the espresso extraction process.

Chapter 2 presents two percolation models for the prediction of the dynamics and transport of water within the coffee pod and the physico-chemical characterisation of the extracted coffee. In more details, porous media and their properties are described, and the equations governing the percolation process in porous media are derived; then we analyse the espresso percolation, and discuss the physico-chemical processes occurring during the extraction process. In addition, we introduce and discuss a three-dimensional model for the prediction of the coffee extraction. Finally, we present and analyse a reduced model for coffee percolation.

Chapter 3 focuses on numerical methods for the approximation of initial-boundary values problems. More precisely, we introduce the finite difference method, which allows the solution of a differential equation by approximating the derivatives with finite difference ratios. Then we present the Galerkin Method and the finite element bases. Finally, we consider the Radial Basis Functions (RBFs) and their properties, with particular attention to their applications in PDE discretisation.

Chapter 4 presents the numerical experiments carried out on espresso coffee percolation models of previous chapter. In particular, we propose two different numerical approximations of the reduced model, (i.e., a finite difference approach and an RBF-based approach). The reliability of such a model together with the proposed solving strategies is assessed experimentally in both cases, by comparing real and

simulated extractions conducted under the same physico-chemical conditions. The results show that the proposed tools can help the coffee industry in the control of the extraction efficiency, and, consequently, in its sustainability goals. Then, we discuss the reliability of the three dimensional model; in more details, it is tested through a wide campaign of chemical laboratory analyses on espresso coffee samples extracted under different conditions. The results of laboratory analyses on the considered chemical substances are compared with those of the numerical simulations. The comparison shows the potential of such a model in coffee industry applications, paving the way to tools allowing the customisation of the coffee beverage taste. In addition, we propose a RBF-based numerical approximation for the three dimensional model of the water flow; more precisely, we consider only the equation describing the hydraulic head dynamics. The reliability of the considered model, together with the proposed solving strategy is experimentally assessed by simulating the hydraulic head behaviour with different initial pressures of the incoming water. The preliminary and promising results suggest a further investigation of such a tool in order to discretise the full percolation model. Also, we discuss and compare the results presented in the chapter.

Finally, in the last Chapter we discuss the achieved results and we give some final remarks and further developments.

Chapter 1

Fundamentals of mathematical physics

The term mathematical physics refers to the development of mathematical methods to be applied to physical problems. Mathematical physics needs the powerful tool of differential equations. These equations express relationships between physical quantities and their rates of change, providing a mathematical description of dynamic systems.

In this chapter we discuss Partial Differential Equations (PDEs) and their properties. In more details, this chapter is organised as follows. In Section 1.1 we introduce PDEs, and their classification. Then, in Section 1.2 we focus on Advection-Diffusion-Reaction equations and their features.

1.1 Partial Differential Equations

Partial Differential Equations (PDEs) are powerful mathematical tools for describing complex phenomena in physics [25], engineering [26], medicine [27], economy [28] and other application fields [29]. A partial differential equation gives a relation between an unknown function of several variables and its partial derivatives. Such relations are quite natural in many physical phenomena, such as for example the electromagnetic field generated by charged object, the wave propagation, the

heat diffusion. So, the PDE theory provides an indispensable resource to deal with models in several application fields such as physics, engineering, biology, and finance. In this thesis they are used to model the espresso coffee percolation problem.

The general form of a linear second order PDE in the unknown $u : \Omega \to \mathbb{R}$ is given by:

$$\sum_{i,j=1}^{d} a_{i,j}(\boldsymbol{x}) \frac{\partial^2 u}{\partial x_i \partial x_j} + \sum_{i=1}^{d} b_i(\boldsymbol{x}) \frac{\partial u}{\partial x_i} + c(\boldsymbol{x}) u = f(\boldsymbol{x}), \tag{1.1}$$

where $\boldsymbol{x} = (x_1, x_2, \ldots, x_d)^t \in \Omega \subseteq \mathbb{R}^d$ is the vector of the independent variables, coefficients $a_{i,j}(\boldsymbol{x}), b_i(\boldsymbol{x})$, $c(\boldsymbol{x})$, and $f(\boldsymbol{x})$ are given functions. In the case these coefficients depend also on the solution $u(\boldsymbol{x})$ the equation is nonlinear. A function $u(\boldsymbol{x})$ is said *particular solution* or *integral* of Equation (1.1) if, replaced in this equation together with all its derivatives, it makes (1.1) an identity. The set of all solutions of (1.1) is said *general integral*.

PDEs can be classified in three different families: elliptic, parabolic and hyperbolic equations. Such a classification is based on the coefficients of the highest order derivatives in the equation itself. Thus, let $A(\boldsymbol{x}) = (a_{ij}(\boldsymbol{x}))_{ij}$, $i, j = 1, 2, \ldots, d$, be the matrix of the coefficients of the second order derivatives of Equation (1.1). We note that from Schwarz's theorem [30] on the equality of mixed partial derivatives we can suppose matrix $A(\boldsymbol{x})$ symmetric. Let $\bar{\boldsymbol{x}} \in \Omega$, and we denote $A = A(\bar{\boldsymbol{x}})$. From the symmetry of A we have that its eigenvalues are real and we say that at $\bar{\boldsymbol{x}} \in \Omega$ the equation (1.1) is:

- *elliptic* if the eigenvalues of A are all positive or all negative.
- *parabolic* if the eigenvalues of A are all positive or all negative except one that is equal to zero.
- *hyperbolic* if A has only one negative eigenvalue and the others are positive, or if A has only one positive eigenvalue and the others are negative.

Elliptic, parabolic, and hyperbolic partial differential equations of order two have been widely studied, below we give some examples of such equations.

The simplest examples of elliptic PDEs are the Laplace's and Poisson's equations, respectively:

$$\Delta u = 0,$$
$$\Delta u = f(\boldsymbol{x}),$$

where u is the unknown function, $f : \Omega \subset \mathbb{R}^d \to \mathbb{R}$ is a given function, and Δ denotes the (spatial) Laplace operator, i.e., $\Delta u = \sum_{i=1}^{d} \frac{\partial^2 u}{\partial x_i^2}$. In general, Laplace's equation describes situations of equilibrium, or also those situations in which the variable of interest does not depend explicitly on the time variable.

Let us consider the function $u : \Omega \times [0, +\infty) \subset \mathbb{R}^{d+1} \to \mathbb{R}$, $u \in C^2(\Omega)$. Parabolic PDEs are used to describe a wide variety of time-dependent phenomena, including heat conduction. In fact, the most famous example of parabolic equation is the heat equation:

$$\frac{\partial u}{\partial t} - \Delta u = 0.$$

Besides heat conduction, parabolic equations can describe other situations, including particle diffusion phenomena, and pricing of derivative investment instruments.

Finally, the model of hyperbolic equations is the wave equation:

$$\frac{\partial^2 u}{\partial t^2} - \Delta u = 0.$$

Many equations in mechanics are hyperbolic, so their study is of particular interest nowadays. The solutions of hyperbolic equations are 'wave-like'. If there is a perturbation in the initial data of a hyperbolic equation, not all points of the domain feel the perturbation at the same time. This feature differs hyperbolic equations from parabolic and elliptic equations. In fact, a perturbation in the initial, or boundary, data of an elliptic or parabolic equation is felt simultaneously by all points in the domain.

1.2 Advection-Diffusion-Reaction Equations

Advection-Diffusion-Reaction (ADR) equations are a class of PDEs that describe phenomena where it is present at the same time advection, diffusion, and reaction

processes. These equations find widespread applications in various scientific disciplines, including fluid dynamics, chemical engineering, environmental science, and mathematical biology [31], [32].

Advection describes the process of transport of a conserved quantity, e.g., mass or heat, due to fluid motion. Advection requires a fluid flow to transport the quantity under consideration; thus, it can not happen in rigid solids [33].

Diffusion usually describes the spread of chemical species from regions of higher concentration to regions of lower concentration or the heat diffusion between regions with different temperature. It can occur both in fluids and solids. Diffusion in a moving fluid does not depend on the flow direction. Diffusion can be thought as a spreading mechanism driven by gradients of one or more quantities. For instance, thermal diffusion is driven by a temperature gradient, mass diffusion is driven by a concentration gradient, and momentum diffusion is driven by a gradient of velocity [33].

Reaction is a process that leads to the transformation of one set of chemicals to another, through creation or destruction of the substances under consideration [34].

Let $d = 3$, the general form of an advection-diffusion-reaction equation in the unknown function $u : \Omega \times [0, \infty) \to \mathbb{R}$ can be expressed as [35], [36]:

$$\frac{\partial u}{\partial t} = -\nabla \cdot (\boldsymbol{v}u) + \nabla \cdot (D \nabla u) + R(u), \tag{1.2}$$

where $u(\boldsymbol{x}, t)$ is the quantity of interest, $\boldsymbol{v}$ is a function of time and space and describes the velocity field that the quantity $u(\boldsymbol{x}, t)$ is moving with, determining a direction of preferred transport. D is the diffusion coefficient that may be dependent on spatial coordinates, governing the spreading or smoothing of u. $R(u)$ is the reaction term, describing any chemical or biological processes affecting u; it describes sources or sinks of the quantity u. For example, when u is the concentration of a chemical species, $R > 0$ means that a chemical reaction is creating more of the species, while $R < 0$ means that a chemical reaction is destroying the species. Finally, ∇ represents the gradient operator and $\nabla\cdot$ denotes the divergence operator.

The right-hand side of Equation (1.2) is the sum of three contributions.

- The first contribution, $-\nabla \cdot (\boldsymbol{v}u)$ describes the advective movement of the quantity of interest u that has been transported with velocity $\boldsymbol{v}$.

- The second contribution $\nabla \cdot (D\nabla u)$ describes diffusion processes. If u is the concentration of a chemical substance, then if the concentration in a region is low compared to the surrounding areas, the substance diffuses in from the surroundings, so the concentration will increase. Conversely, if concentration is high compared to the surroundings, then the substance diffuses out and the concentration will decrease.

- The third contribution $R(u)$ describes the creation or destruction of the quantity u by reaction processes. For example, if u is the concentration of a substance, then R describes how the substance can be created or destroyed by chemical reactions.

ADR equations describes different behaviors depending on the values of parameters and the nature of the underlying physical system. Thus, understanding their classification and properties is crucial for interpreting the solutions and predicting the system's evolution.

Advection-Dominated Regime is characterized by an advection process that dominates over diffusion; the equation describes a system where the transport of the quantity u is primarily due to advection.

Diffusion-Dominated Regime Conversely, in the diffusion-dominated regime the diffusion term prevails, leading to a smoother spreading of u over space. This scenario is relevant in contexts such as heat conduction, where diffusion plays a dominant role in the redistribution of temperature.

Reaction-Influenced Dynamics The reaction term R can depend on u, thus the reaction term can introduce non-linearity in the system.

Chapter 2

Coffee percolation models

Brewing an espresso coffee means to fill with roasted, ground and tamped coffee a filter basket, then let the hot water at high pressure enters the filter basket and pass through it. This extraction method of coffee from the pod can be described as a process of percolation of a fluid (water) into a porous medium (the coffee pod). In fact, the espresso coffee is extracted from the coffee powder, obtained by grinding the previously roasted coffee bean. Then, the powder is inserted in the filter basket where it is tamped. These operations together create the coffee pod, i.e. the place where the extraction process will occur, that is the porous medium. Percolation in porous media can occur in a variety of ways, depending on the properties of the medium and the forces driving the fluid flow. One common type of percolation is gravity-driven flow, which occurs when a fluid flows downward through a porous medium under the influence of gravity. This type of flow is important in many natural systems, such as groundwater recharge and discharge, and can also be used in engineering applications such as groundwater remediation. In this chapter we present two different percolation models for the prediction of the dynamics and transport of water within the coffee pod and the consequent physico-chemical characterisation of the coffee extracted. In particular, in Section 2.1 porous media and their properties are described, and the equations governing the percolation process in porous media are derived; in Section 2.2 we analyse the espresso percolation, and discuss the physico-chemical processes occurring during

the espresso extraction process. In Section 2.3 we introduce and discuss a three-dimensional model for the prediction of the coffee extraction. Finally, in Section 2.4 we present and analyse a reduced model, for the same purposes. For both models in Sections 2.3, 2.4 we will discuss benefits and disadvantages of using such a kind of model.

2.1 Percolation in porous media

Porous media can be defined as collections of solid bodies (grains) with enough open space around them to allow a fluid to pass through it. These are materials containing interconnected void spaces, called pores, which are usually filled up with one or more fluids, be them liquid or gas, while the skeleton, formed by the solid part, is called solid matrix. Therefore, they are multiphase materials in the sense that they consist in the solid phase, i.e. the solid matrix, and in the fluid phase, since the pore space is occupied by at least a fluid. Some examples of natural porous media are rocks, aquifers, polymer materials, as well as biological tissues such as bones, wood and cork. Their relevant role in science and industrial applications makes easy to understand why they are of such significant interest in scientific literature.

Percolation in porous media is the movement of a fluid, usually the water, flowing through the interconnected pores or void spaces, driven by forces such as gravity, capillary action, and pressure gradients. During this flow mass transport and dissolution phenomena can occur. With the term dissolution we mean that chemical process in which a substance, usually in the solid state, melts into the liquid. At the end of this process, the chemicals are dispersed in the liquid, so mass transport by the fluid flow occurs. In the following we deepen in the main properties that characterise porous media since it is helpful to understand how percolation in porous media works, then we derive the general equations governing the phenomena occurring during the percolation process in porous media.

2.1.1 Porosity

Porosity is a scalar quantity that expresses the capacity of the medium to contain fluids inside; it is defined as:

$$\varepsilon = \frac{V_p}{V_m}, \tag{2.1}$$

where V_p denotes the volume of the voids while V_m denotes the total volume of the medium. We observe that $0 < V_p < V_m$, so we have $0 < \varepsilon < 1$. Porosity is typically expressed as a percentage and can range from very low values, as in the case of dense rocks, to very high values as in the case of foams. Formula (2.1) defines total porosity; in fact, since in real porous media not all pores are connected to each other, we can define the actual porosity as

$$\varepsilon_a = \frac{V_{pi}}{V_m}, \tag{2.2}$$

where V_{pi} is the volume of the interconnected voids contained in the volume V_m. Therefore it expresses the ability of the medium to contain moving fluids inside. Obviously, we have $0 < \varepsilon_a < \varepsilon < 1$.
Moreover, if we define the voids index as

$$e = \frac{V_p}{V_s}, \tag{2.3}$$

where V_s is the volume of the solid matrix, and then $V_s = V_m - V_p$ we have the relationship that links the voids index to porosity:

$$\frac{1}{e} = \frac{V_s}{V_p} = \frac{V_m - V_p}{V_p} = \frac{1}{\varepsilon} - 1 = \frac{1-\varepsilon}{\varepsilon},$$

from which we have:

$$e = \frac{\varepsilon}{1-\varepsilon}, \qquad \varepsilon = \frac{e}{1+e}.$$

2.1.2 Permeability and hydraulic conductivity

Another important concept is permeability, which is a measure of how easily fluids can flow through a porous medium. Permeability depends on factors such as

the size and shape of the pores and the degree of connectivity between the pores. Intrinsic (or absolute) permeability is defined as the capacity of a porous medium to let a fluid pass through it. It is a property of the medium independent of the fluid. It has the dimensions of a squared length and, therefore, is measured in m^2 in the International System of Units (SI). But, since the values found in nature are much lower in order of magnitude than the m^2, in practical applications the permeability is usually measured in *darcy*, a unit of measurement that, despite is not part of the SI is widely used in geology. In particular,

$$1\, darcy = 0.987 \cdot 10^{-12}\, m^2.$$

Whereas the absolute permeability is an intrinsic and exclusive property of the porous medium, the hydraulic conductivity, often called the permeability coefficient, can be defined as the volumetric flow rate of water flowing through a porous medium of unitary section under the effect of a hydraulic gradient of unit value, at the temperature of 20 °C. It has the dimensions of a velocity and, consequently, in the SI is measured in m/s. Unlike absolute permeability, hydraulic conductivity also depends on the properties of the fluid that passes through the porous medium, such as density and viscosity, and not only on the medium itself. The relationship between absolute permeability k and hydraulic conductivity K is as follows:

$$K = \frac{\rho_0 g k}{\mu_0}, \tag{2.4}$$

where g is the gravity acceleration, ρ_0 and μ_0 are reference density and reference dynamic viscosity of the fluid, respectively. Since the hydraulic conductivity measures the fluid ability to flow through the porous medium, it can have different values for different directions of flow. When the flow is uniform in all directions, there is a unique value of K and the medium is said *isotropic*. While the medium is called *anisotropic* when the hydraulic conductivity changes for different directions of flow; in this case we have to extend it from a scalar to a tensor and we denote with the symbol $\mathbf{K}$. Therefore, the hydraulic conductivity tensor for a three-dimensional

system will be a 3×3 matrix:

$$\mathbf{K} = \begin{pmatrix} K_{xx} & 0 & 0 \\ 0 & K_{yy} & 0 \\ 0 & 0 & K_{zz} \end{pmatrix}. \tag{2.5}$$

The out diagonal elements are nonzero in the case in which a pressure change in one direction also produces flow in other directions, so the $\mathbf{K}$ matrix will be:

$$\mathbf{K} = \begin{pmatrix} K_{xx} & K_{xy} & K_{xz} \\ K_{yx} & K_{yy} & K_{yz} \\ K_{zx} & K_{zy} & K_{zz} \end{pmatrix}$$

where $K_{xy} = K_{yx}$, $K_{xz} = K_{zx}$ e $K_{yz} = K_{zy}$.

In addition, we call *homogeneous* a porous medium that has constant properties (such as porosity, hydraulic conductivity, etc.) in all points of the domain, otherwise we call it *heterogeneous*.

2.1.3 From the miscroscopic to the macroscopic behaviour through the continuum hypothesis

Porous media can be analysed with two different levels of description. We define a *material point* as a neighbourhood of a point belonging to the medium. Thus according with the size of the neighbourhood we can consider at least two levels of accuracy for its description. The *microscopic level*, where every point in the domain is occupied by only one phase (solid, liquid or gaseous), that is when the size of the neighbourhood tends to zero and the *macroscopic level*, where every material point consists in all the different phases[33], that is when the size of the neighbour is sufficiently large to contains several molecules/particles of the phases under study. The study of the fluid flow into the medium at the microscopic level means to consider the dynamics of the particles occurring in each phase and also the complex inter-phases geometry. This is usually excessively expensive and almost impracticable, at least with the current computational resources available nowadays,

however, some strategies can be considered to speed-up this approach, see for example the Lattice Boltzmann method [37] and the cellular automata models [38].

Therefore, a macroscopic description is helpful to overpass these difficulties and the *continuum hypothesis* is assumed. It states that the macroscopic behavior of a porous medium can be described in the same way of a continous medium. So that we can consider quantities such as velocity, temperature, etc. ... as continuous functions in space and time, and usual mathematical analysis tools of differential and integral calculus can be applied. There are three main approaches to transform the microscopic physical laws that describe the flow behaviour into their macroscopic counterparts: the REV averaging procedure, the homogenization approach and the mixture theory. In this thesis the REV averaging procedure is presented, see [39] and [40] for further details on the other two techniques.

The development of the macroscopic description from the microscopic properties of the medium implies neglecting information not relevant for the fluid flow at macroscopic level. In the REV averaging approach this disregarded information is incorporated into averaged coefficients that help to describe the medium in a realistic way. These macroscopic averaged quantities are related to the microscopic quantities by averaging operators acting on an averaging volume. This means that this spatial averaging procedure is referred to a certain elementary volume of the porous medium and the characteristics of the material are averaged, this is called REV (representative elementary volume). The REV dV has to be larger than the dimension of a single pore in such a way that it can include a sufficient number of voids to show changes on a microscopic scale. At the same time dV has to be much smaller than the size of the medium in order to reflect the local variability of macroscopic properties. Therefore, the continuum hypothesis implies that the obtained averaged quantities are independent from the dimension of the averaging volume dV and that they are continuous over space and time.

Let us assume that the REV dV exists, in the following we introduce average operators that will be exploited in the derivation of the macroscopic balance principle 2.1.4. Let $\boldsymbol{x}$ be the position vector of the centroid of dV, and let us consider the point P within dV. We denote with $\boldsymbol{r}$ the position vector of P, and

with $\boldsymbol{y}$ the position of P with respect to the centroid of dV, as shown in Figure 2.1. Thus, we have:

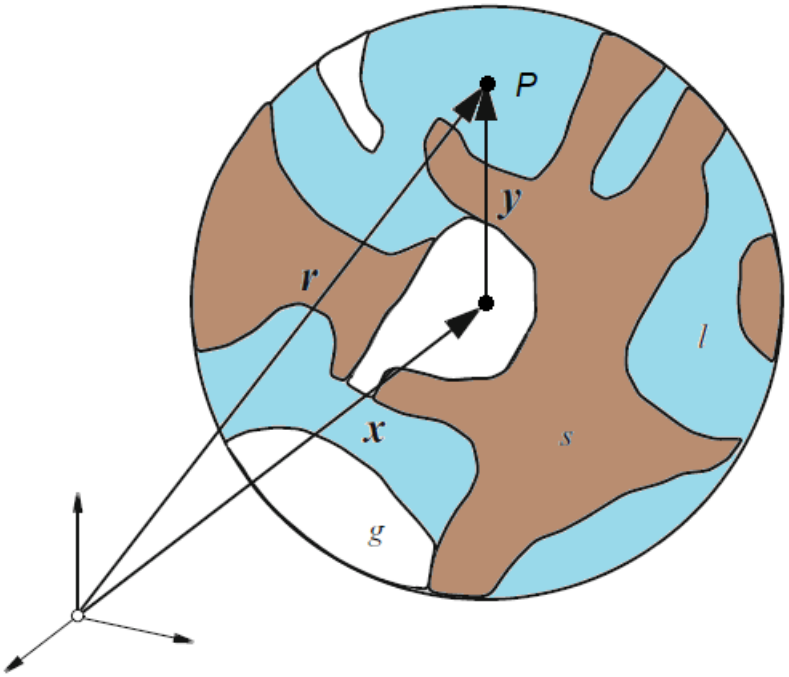

Figure 2.1: Representation of a REV dV with one liquid phase l shown in light blue, the gaseous phase g in white and the solid phase s in brown. The centroid of dV and a point P are highlighted.

$$\boldsymbol{r} = \boldsymbol{x} + \boldsymbol{y}. \tag{2.6}$$

We define the distribution function γ_α of the α-phase, establishing if the position vector $\boldsymbol{r}$ in dV lies or not to the α-phase, where $\alpha \in \{l, g, s\}$. This is:

$$\gamma_\alpha(\boldsymbol{r}, t) = \begin{cases} 1 & \text{if } \boldsymbol{r} \text{ lies in the } \alpha\text{-phase,} \\ 0 & \text{otherwise,} \end{cases} \qquad \forall t. \tag{2.7}$$

Thus, for the point P in Figure 2.1 $\gamma_l = \gamma_s = 1$, but $\gamma_g = 0$. In the following, we denote with dv the microscopic differential volume of the REV dV, independently of the fixed coordinate system, that is in our case $dv = dv(\boldsymbol{y})$. In addition we denote with ε_α the volume fraction of the α-phase defined as:

$$\varepsilon_\alpha(\boldsymbol{x}, t) = \frac{dV_\alpha(\boldsymbol{x}, t)}{dV} = \frac{1}{dV} \int_{dV} \gamma_\alpha(\boldsymbol{x} + \boldsymbol{y}, t) dv. \tag{2.8}$$

It represents the fraction of the macroscopic REV volume dV covered by the α-phase. Obviously the quantities defined in (2.8) satisfy the following relations:

$$\sum_{\alpha} \varepsilon_\alpha = 1, \quad \text{and} \quad 0 \leq \varepsilon_\alpha \leq 1.$$

For a given REV we define three different averaging operators all satisfying the following criteria. For more details see [41]:

Criterion I: The integrand of averaging operators multiplied by the infinitesimal element of integration is an additive quantity.

Criterion II: The macroscopic quantity has to exactly correspond to the total amount of the microscopic one.

Criterion III: Proper definitions of the macroscopic quantities are needed. They have to be given according to the ones of the microscopic quantities.

Criterion IV: The macroscopic averaged quantity must be the same function most widely observed from experience.

Volume average operator:

$$\langle \cdot \rangle_\alpha(\boldsymbol{x}, t) = \frac{1}{dV} \int_{dV} (\cdot)\gamma_\alpha(\boldsymbol{x} + \boldsymbol{y}, t) dv. \tag{2.9}$$

Intrinsic volume average operator:

$$\langle \cdot \rangle^\alpha(\boldsymbol{x}, t) = \frac{1}{dV_\alpha(\boldsymbol{x}, t)} \int_{dV} (\cdot)\gamma_\alpha(\boldsymbol{x} + \boldsymbol{y}, t) dv. \tag{2.10}$$

Intrinsic mass average operator:

$$\overline{(\cdot)}^\alpha(\boldsymbol{x}, t) = \frac{1}{\langle \rho \rangle_\alpha dV} \int_{dV} (\cdot)\rho(\boldsymbol{x} + \boldsymbol{y}, t)\gamma_\alpha(\boldsymbol{x} + \boldsymbol{y}, t) dv, \tag{2.11}$$

where ρ denotes the mass density. Let ψ be a scalar quantity, from (2.8), (2.9) and (2.10) it holds:

$$\varepsilon_\alpha(\boldsymbol{x}, t)\langle \psi \rangle^\alpha(\boldsymbol{x}, t) = \frac{dV_\alpha(\boldsymbol{x}, t)}{dV} \frac{1}{dV_\alpha(\boldsymbol{x}, t)} \int_{dV} \psi(\boldsymbol{x} + \boldsymbol{y}, t)\gamma_\alpha(\boldsymbol{x} + \boldsymbol{y}, t) dv = \langle \psi \rangle_\alpha(\boldsymbol{x}, t). \tag{2.12}$$

Moreover, from (2.11) we have:

$$\langle\rho\rangle_\alpha\overline{\psi}^\alpha = \langle\rho\rangle_\alpha \frac{1}{\langle\rho\rangle_\alpha dV}\int_{dV}\psi(\boldsymbol{x}+\boldsymbol{y},t)\rho(\boldsymbol{x}+\boldsymbol{y},t)\gamma_\alpha(\boldsymbol{x}+\boldsymbol{y},t)dv = \langle\rho\psi\rangle_\alpha \quad (2.13)$$

In addition, we can define the *fluctuation* $\tilde{\psi}^\alpha$ of the microscopic quantity ψ, as the *deviation* of ψ at the point $\boldsymbol{r}$ from its mass average at the point $\boldsymbol{x}$, i.e.:

$$\tilde{\psi}^\alpha(\boldsymbol{x},\boldsymbol{y},t) = \psi(\boldsymbol{x}+\boldsymbol{y},t) - \overline{\psi}^\alpha(\boldsymbol{x},t). \quad (2.14)$$

Furthermore, since $\overline{\psi}^\alpha(\boldsymbol{x},t)$ is constant in dV, for the two microscopic scalar quantity, ψ, ϕ it follows:

$$\begin{aligned}\overline{\tilde{\psi}^\alpha}^\alpha &= 0,\\ \overline{\tilde{\psi}^\alpha\overline{\phi}^\alpha}^\alpha &= \overline{\tilde{\psi}^\alpha}^\alpha\overline{\phi}^\alpha = 0,\\ \overline{\psi\phi}^\alpha &= \overline{\psi}^\alpha\overline{\phi}^\alpha + \overline{\tilde{\psi}^\alpha\tilde{\phi}^\alpha}^\alpha.\end{aligned} \quad (2.15)$$

2.1.4 The balance principle

Our intent is to describe the motion of a fluid in a porous medium. The laws that describe this motion all derive from the balance statement of some extensive property of this multi-component system (mass, momentum, mass, energy ...). Thus in this section we derive the general balance principle for a porous medium containing N chemical substances and only one liquid phase l. This assumption has been made for the simplicity of notation and does not compromise the generality of the discussion.

An extensive property of a chemical substance is a property that depends on the mass of the substance which such quantity refers to, while an intensive property is a property that does not depend on the size of the sample. Temperature, pressure, density are examples of intensive properties, while volume, mass, momentum, kinetic and internal energy are examples of extensive properties. Extensive and intensive property are quantitative properties, for this reason in this context we use the two terms as synonymous, and we use the same symbol to denote the property and its amount.

In each point it is possible to define intensive and extensive quantities and understand how they vary over time, that is, what their temporal rate of change is.

We consider an extensive property of a chemical species k and we indicate with $\mathcal{F}_k$ its amount. For each extensive property $\mathcal{F}_k$ we can associate an intensive property ψ_k, which is the quantity of that property per unit of mass of the species k. In addition, we can define the volume density f_k of $\mathcal{F}_k$, as the amount of $\mathcal{F}_k$ per unit of volume, i.e.:

$$f_k(\boldsymbol{x}, t) = \rho_k \psi_k(\boldsymbol{x}, t), \tag{2.16}$$

where ρ_k is the mass density of the chemical k, defined as the mass of the species k per unit of volume. We note that the intensive properties can be either scalars or vectors but, for simplicity of notation we denote them as scalars in any case.

For a given volume V containing the REV dV, we have:

$$\mathcal{F}_k(t) = \int_V \rho_k \psi_k(\boldsymbol{x}, t) dV = \int_V f_k(\boldsymbol{x}, t) dV. \tag{2.17}$$

The balance equation of the extensive quantity $\mathcal{F}_k$ in a fixed Eulerian coordinate system is defined as:

$$\frac{D\mathcal{F}_k}{Dt} \equiv \frac{D}{Dt} \int_V f_k dV - \int_V \rho_k F_k dV = \int_V \rho_k G_k dV. \tag{2.18}$$

where F_k denotes an external sink of $\mathcal{F}_k$ and G_k is its net rate of production. The notation $\dfrac{D}{Dt}$ in (2.18) indicates the *material (or substantial) derivative* defined as:

$$\frac{D}{Dt} = \frac{\partial}{\partial t} + (\boldsymbol{v}_k^{\mathcal{F}} \cdot \nabla), \tag{2.19}$$

where $\boldsymbol{v}_k^{\mathcal{F}}$ is the velocity vector of the particle associated with $\mathcal{F}_k$. The first term in formula (2.19) is said *local derivative*, while the second one is called *convective derivative*, it represents the change of the extensive property $\mathcal{F}_k$ due to the convection of the particle from one position to another with a different amount of $\mathcal{F}_k$.

Theorem 1 (Reynolds' transport theorem)**.** *Let $\mathcal{F}$ be the extensive property defined in* (2.17)*, and let $\boldsymbol{v}$ be a fluid vector field. In addition, let $V = V(t)$ be a volume bounded by a closed surface moving with the fluid then*

$$\frac{D\mathcal{F}}{Dt} = \int_V \left[\frac{\partial f}{\partial t} + \nabla \cdot (f\boldsymbol{v}) \right] dV$$

See [42] Chapter 2, for the proof of the theorem. Exploiting the Reynolds' transport Theorem 1 from (2.18) we obtain:

$$\frac{D}{Dt}\int_V f_k dV = \int_V \left[\frac{\partial f_k}{\partial t} + \nabla\cdot\left(f_k\,\boldsymbol{v}_k^{\mathcal{F}}\right)\right] dV = \int_V \rho_k\left(F_k + G_k\right) dV,$$

from the arbitrariness of V we have:

$$\frac{\partial f_k}{\partial t} + \nabla\cdot\left(f_k\,\boldsymbol{v}_k^{\mathcal{F}}\right) = \rho_k\left(F_k + G_k\right), \tag{2.20}$$

Let $\boldsymbol{j}_k^{\mathcal{F}}$ be the diffusive flux of the chemical k corresponding to $\mathcal{F}_k$, defined as:

$$\boldsymbol{j}_k^{\mathcal{F}} = f_k\left(\boldsymbol{v}_k^{\mathcal{F}} - \boldsymbol{v}_k\right),$$

where $\boldsymbol{v}_k$ denotes the particle velocity of the chemical substance k. That gives

$$f_k\boldsymbol{v}_k^{\mathcal{F}} = \boldsymbol{j}_k^{\mathcal{F}} + f_k\,\boldsymbol{v}_k. \tag{2.21}$$

Thus, substituting (2.21) in (2.20), it becomes:

$$\frac{\partial f_k}{\partial t} + \nabla\cdot\left(\boldsymbol{j}_k^{\mathcal{F}} + f_k\,\boldsymbol{v}_k\right) = \rho_k\left(F_k + G_k\right), \tag{2.22}$$

and since the divergence operator is linear we get:

$$\frac{\partial f_k}{\partial t} + \nabla\cdot\left(f_k\,\boldsymbol{v}_k\right) + \nabla\cdot\boldsymbol{j}_k^{\mathcal{F}} = \rho_k\left(F_k + G_k\right). \tag{2.23}$$

Usually the particle velocity $\boldsymbol{v}_k$ of chemical k is not measurable. Thus, summing over chemicals $k = 1, \ldots, N$, we can consider the mass-weighted velocity $\boldsymbol{v}$ of the particle, defined as:

$$\boldsymbol{v} = \frac{1}{\rho}\sum_{k=1}^{N}\rho_k\boldsymbol{v}_k, \qquad\qquad \rho = \sum_{k=1}^{N}\rho_k, \tag{2.24}$$

and introduce the diffusive flux $\boldsymbol{j}_k$ of the species k that relates $\boldsymbol{v}_k$ to the mass-weighted velocity $\boldsymbol{v}$:

$$\boldsymbol{j}_k = \rho_k\left(\boldsymbol{v}_k - \boldsymbol{v}\right),$$

that gives:

$$\rho_k\boldsymbol{v}_k = \boldsymbol{j}_k + \rho_k\boldsymbol{v}. \tag{2.25}$$

Inserting (2.25) in (2.23), and recalling formula (2.16) we obtain the following general balance equation in which we eliminated the particle velocity $\boldsymbol{v}_k$ of the species k:

$$\frac{\partial}{\partial t}\left(\rho_k \psi_k\right) + \nabla \cdot \left(\rho_k \psi_k \, \boldsymbol{v}\right) + \nabla \cdot \left(\boldsymbol{j}_k^{\mathcal{F}} + \psi_k \boldsymbol{j}_k\right) = \rho_k \left(F_k + G_k\right). \tag{2.26}$$

Equation (2.26) involves quantities related to each species k, however it is enough to state the balance principle for barycentric related amounts. Thus, we can sum (2.26) over all the chemicals $k = 1, \ldots, N$ and get:

$$\frac{\partial}{\partial t}\left(\rho \psi\right) + \nabla \cdot \left(\rho \psi \, \boldsymbol{v}\right) + \nabla \cdot \boldsymbol{j} = \rho \left(F + G\right), \tag{2.27}$$

where:

$$\begin{aligned}
\psi &= \frac{1}{\rho} \sum_{k=1}^{N} \rho_k \psi_k, \\
F &= \frac{1}{\rho} \sum_{k=1}^{N} \rho_k F_k, \\
G &= \frac{1}{\rho} \sum_{k=1}^{N} \rho_k G_k, \\
\boldsymbol{j} &= \sum_{k=1}^{N} \left(\boldsymbol{j}_k^{\mathcal{F}} + \psi_k \boldsymbol{j}_k\right).
\end{aligned}$$

The microscopic balance equation (2.27) can be macroscoped exploiting the averaging procedures (2.9)- (2.15), however we also need to provide averages of derivatives with respect to space and time. To this purposes, the following theorem relates the average of the divergence of the microscopic extensive quantity $\mathcal{F}$ to the divergence of its average (i.e. to the divergence of the corresponding macroscopic quantity):

Theorem 2. *Let $\mathcal{F}$ be an extensive quantity, $dA_{\alpha\beta}$ the macroscopic differential interface between the phases α and β in the macroscopic REV volume dV, da a microscopic differential element of $dA_{\alpha\beta}$, $\boldsymbol{n}^{\alpha\beta} = -\boldsymbol{n}^{\beta\alpha}$ a normal vector on $dA_{\alpha\beta}$ pointing from the phase α to β. It holds:*

$$\langle \nabla \cdot \mathcal{F} \rangle_\alpha = \nabla \cdot \langle \mathcal{F} \rangle_\alpha + \frac{1}{dV} \sum_{\beta \neq \alpha} \int_{dA_{\alpha\beta}} \mathcal{F} \cdot \boldsymbol{n}^{\alpha\beta} da.$$

Furthermore, the following theorem expresses the average of the time derivative of the extensive quantity $\mathcal{F}$ to the time derivative of its average:

Theorem 3. *Let $\mathcal{F}$ be an extensive quantity, $dA_{\alpha\beta}$ the macroscopic differential interface between the phases α and β in the macroscopic REV volume dV, da a microscopic differential element of $dA_{\alpha\beta}$, $\boldsymbol{n}^{\alpha\beta} = -\boldsymbol{n}^{\beta\alpha}$ a normal vector on $dA_{\alpha\beta}$ pointing from the phase α to β, and $\boldsymbol{w}$ the velocity of the $\alpha\beta$ interface. It holds:*

$$\left\langle \frac{\partial \mathcal{F}}{\partial t} \right\rangle_\alpha = \frac{\partial}{\partial t} \langle \mathcal{F} \rangle_\alpha - \frac{1}{dV} \sum_{\beta \neq \alpha} \int_{dA_{\alpha\beta}} \mathcal{F} \cdot \left(\boldsymbol{w} \cdot \boldsymbol{n}^{\alpha\beta} \right) da$$

For the detailed proof of these theorems see [43, Sections 2.7.1, 2.7.2].

Exploiting the averaging procedures (2.9)- (2.15) and Theorems 2 and 3 the microscopic balance equation (2.27) can be macroscoped, leading to the macroscopic balance equation for the α-phase:

$$\frac{\partial}{\partial t} \left(\langle \rho \rangle_\alpha \overline{\psi}^\alpha \right) + \nabla \cdot \left(\langle \rho \rangle_\alpha \overline{\psi}^\alpha \overline{\boldsymbol{v}}^\alpha \right) + \nabla \cdot \left(\varepsilon_\alpha \boldsymbol{j}^\alpha \right) - \langle \rho \rangle_\alpha \left[\overline{F}^\alpha + e^\alpha \left(\rho \psi \right) + J^\alpha \right] = \langle \rho \rangle_\alpha \overline{G}^\alpha, \tag{2.28}$$

$\alpha = s, f,\ f = l, g$. For a detailed derivation of this procedure see [41]. In Equation (2.28) $\boldsymbol{j}^\alpha$ is the macroscopic diffusive flux vector for the intrinsic mass averaged intensive quantity associated with the property $\mathcal{F}$, $\overline{\psi}^\alpha$ defined as:

$$\boldsymbol{j}^\alpha = \langle \boldsymbol{j} \rangle^\alpha + \langle \rho \rangle^\alpha \overline{\tilde{\boldsymbol{v}}^\alpha \tilde{\psi}^\alpha}^\alpha,$$

It consists in two addenda; the first one describes the macroscopic diffusion, while the second one is the macroscopic mechanical dispersion. The term $e^\alpha \left(\rho \psi \right)$ represents the exchange of $\overline{\psi}^\alpha$ of the α-phase with the other phases, due to the relative motion of the interfaces among the different phases. It is defined as:

$$e^\alpha \left(\rho \psi \right) = \frac{1}{\langle \rho \rangle_\alpha} \frac{1}{dV} \sum_{\beta \neq \alpha} \int_{dA_{\alpha\beta}} \rho \psi \left(\boldsymbol{w} - \boldsymbol{v} \right) \cdot \boldsymbol{n}^{\alpha\beta} da. \tag{2.29}$$

Finally, J^α expresses the diffusion of $\overline{\psi}^\alpha$ through the interfaces between the phases. This is:

$$J^\alpha = \frac{1}{\langle \rho \rangle_\alpha} \frac{1}{dV} \sum_{\beta \neq \alpha} \int_{dA_{\alpha\beta}} \boldsymbol{j} \cdot \boldsymbol{n}^{\alpha\beta} da. \tag{2.30}$$

Moreover, if we set $F^{\alpha}_{\text{ex}} = e^{\alpha}(\rho\psi) + J^{\alpha}$, and we assume that there is no storing of properties at the phase boundary, we obtain [41]:

$$\sum_{\alpha} \langle\rho\rangle_{\alpha} F^{\alpha}_{\text{ex}} = 0. \tag{2.31}$$

For the reader's convenience, we rewrite equation (2.28) in the following simplified form where we omitted the averaging operators symbols, and we replaced the mass density by its intrinsic average (2.12), i.e.: $\rho_{\alpha} = \langle\rho\rangle_{\alpha} = \varepsilon_{\alpha}\langle\rho\rangle^{\alpha} = \varepsilon_{\alpha}\rho^{\alpha}$:

$$\frac{\partial}{\partial t}\left(\varepsilon_{\alpha}\rho^{\alpha}\psi^{\alpha}\right) + \nabla\cdot\left(\varepsilon_{\alpha}\rho^{\alpha}\psi^{\alpha}\,\boldsymbol{v}^{\alpha}\right) + \nabla\cdot\left(\varepsilon_{\alpha}\boldsymbol{j}^{\alpha}\right) = \varepsilon_{\alpha}\rho^{\alpha}\left(F^{\alpha} + F^{\alpha}_{\text{ex}} + G^{\alpha}\right). \tag{2.32}$$

Equation (2.32) is the balance principle for the intensive quantity ψ^{α}. We highlight that, for conservative quantities such as mass, momentum and energy, it coincides with the conservation principle.

2.1.5 Conservation of mass

Let $\mathcal{M}^{\alpha}_{k}$ denotes the mass of chemicals k in the α-phase, the conservation of the mass $\mathcal{M}^{\alpha}_{k}$ is obtained from (2.32) where the definitions of the general quantities in (2.32) are listed in Table 2.1.

terms	**description**
$\psi^{\alpha} = \omega^{\alpha}_{k} = \dfrac{\rho^{\alpha}_{k}}{\rho^{\alpha}}$	mass fraction of species k
$\boldsymbol{j}^{\alpha} = \boldsymbol{j}^{\alpha}_{k}$	diffusive flux of species k
$F^{\alpha} = \dfrac{r^{\alpha}_{k}}{\rho^{\alpha}}$	mass-weighted homogeneous (intraphase) reaction rate of species k
$F^{\alpha}_{\text{ex}} = \dfrac{R^{\alpha}_{k}}{\rho^{\alpha}}$	mass-weighted heterogeneous (interphase) reaction rate of species k
$G^{\alpha} = 0$	since $\mathcal{M}^{\alpha}_{k}$ is conservative

Table 2.1: Definitions of the general quantities in equation (2.32) for mass species conservation (i.e. $\mathcal{F}^{\alpha} = \mathcal{M}^{\alpha}_{k}$ and $\psi^{\alpha} = \omega^{\alpha}_{k}$) with a brief description.

Thus, for $k = 1, \ldots, N^\alpha$, $\alpha = s, f$, $f \in \{l, g\}$ we get:

$$\frac{\partial}{\partial t}\left(\varepsilon_\alpha \rho^\alpha \omega_k^\alpha\right) + \nabla \cdot \left(\varepsilon_\alpha \rho^\alpha \omega_k^\alpha \boldsymbol{v}^\alpha\right) + \nabla \cdot \left(\varepsilon_\alpha \boldsymbol{j}_k^\alpha\right) = \varepsilon_\alpha \left(r_k^\alpha + R_k^\alpha\right), \tag{2.33}$$

where N^α denotes the number of chemicals k in the α-phase.

In order to ensure global mass conservation, equations (2.33) are subjected to the following constrains:

i) the sum of the mass fluxes of all chemicals into the α-phase has to be equal to the mass change in the selected phase. If Q^α denotes the internal supply of mass of the α-phase and Q_{ex}^α represents the phase change of mass this lead to:

$$\sum_{k=1}^{N^\alpha} \left(r_k^\alpha + R_k^\alpha\right) = \rho^\alpha \left(Q^\alpha + Q_{\text{ex}}^\alpha\right) \tag{2.34}$$

ii) The diffusive fluxes summed over all the substances vanish in the phase α, i.e.:

$$\sum_{k=1}^{N^\alpha} \boldsymbol{j}_k^\alpha = \boldsymbol{0}. \tag{2.35}$$

Each on of the Equations (2.33) states the balance principle for the mass fraction of the species k in the α-phase. It can be equivalently expressed for the mass concentration C_k^α of the chemical k, which represents the mass of substance k per unit volume of α-phase and it is equal to the mass density ρ_k^α, i.e.: $C_k^\alpha = \rho_k^\alpha = \rho^\alpha \omega_k^\alpha$. Therefore, for $k = 1, \ldots, N^\alpha$, $\alpha = s, f$, $f \in \{l, g\}$ we get:

$$\frac{\partial}{\partial t}\left(\varepsilon_\alpha C_k^\alpha\right) + \nabla \cdot \left(\varepsilon_\alpha C_k^\alpha \boldsymbol{v}^\alpha\right) + \nabla \cdot \left(\varepsilon_\alpha \boldsymbol{j}_k^\alpha\right) = \varepsilon_\alpha \left(r_k^\alpha + R_k^\alpha\right). \tag{2.36}$$

The diffusive mass flux $\boldsymbol{j}_k^s$ of chemicals in the solid phase is meaningless, so we formally consider $\boldsymbol{j}_k^s = \boldsymbol{0}$. Thus, Equations (2.33) for the solid phase become:

$$\frac{\partial}{\partial t}\left(\varepsilon_s \rho^s \omega_k^s\right) + \nabla \cdot \left(\varepsilon_s \rho^s \omega_k^s \boldsymbol{v}^s\right) = \varepsilon_s \left(r_k^s + R_k^s\right), \tag{2.37}$$

for $k = 1, \ldots, N^s$.

For the diffusive mass flux vector $\boldsymbol{j}_k^f$ of the species k in the fluid phase f, we consider the Fick's law:

$$\boldsymbol{j}_k^f = -\rho^f \boldsymbol{D}_k^f \cdot \nabla \omega_k^f, \tag{2.38}$$

where $\boldsymbol{D}_k^f$ is the hydrodynamic dispersion tensor consisting in two parts, a molecular diffusion $D_k^f \boldsymbol{I}$ and a mechanical diffusion $\boldsymbol{D}^f$mech, i.e:

$$\boldsymbol{D}_k^f = D_k^f \boldsymbol{I} + \boldsymbol{D}_{\text{mech}}^f = \left(D_k^f + \beta_T^f ||\boldsymbol{v}^{fs}||\right)\boldsymbol{I} + \left(\beta_L^f - \beta_T^f\right)\frac{\boldsymbol{v}^{fs} \otimes \boldsymbol{v}^{fs}}{||\boldsymbol{v}^{fs}||}, \tag{2.39}$$

where $\otimes$ denotes the tensor product, D_k^f is the molecular diffusion coefficient, β_T^f, β_L^f are the transverse and longitudinal dispersion coefficients, respectively, and $\boldsymbol{I}$ is the identity matrix. In addition, the relative velocity $\boldsymbol{v}^{\alpha s}$ of the α-phase is defined as:

$$\boldsymbol{v}^{\alpha s} = \boldsymbol{v}^{\alpha} - \boldsymbol{v}^{s}, \qquad \alpha = s, f,\ f \in \{l, g\}. \tag{2.40}$$

However, when high concentrations of solubles occur non linear effects have to be considered and the definition (2.39) of $\boldsymbol{j}_k^f$ should be replaced by an extended nonlinear non-Fickian dispersion law[44], [45]. Therefore, Equations (2.33) for the fluid phase becomes:

$$\frac{\partial}{\partial t}\left(\varepsilon_f \rho^f \omega_k^f\right) + \nabla \cdot \left(\varepsilon_f \rho^f \omega_k^f \, \boldsymbol{v}^f\right) + \nabla \cdot \left(\varepsilon_f \boldsymbol{j}_k^f\right) = \varepsilon_f \left(r_k^f + R_k^f\right), \tag{2.41}$$

for $k = 1, \ldots, N^f$.

Let $\mathcal{M}^\alpha$ denotes the global mass of the α-phase, the global conservation of mass $\mathcal{M}^\alpha$ is obtained by summing (2.33) over all substances k, and taking into account constrains (2.34), (2.35) and recalling that:

$$\sum_{k=1}^{N^\alpha} \omega_k^\alpha = 1. \tag{2.42}$$

For $\alpha = s, f,\ f \in \{l, g\}$ we have:

$$\frac{\partial}{\partial t}\left(\varepsilon_\alpha \rho^\alpha\right) + \nabla \cdot \left(\varepsilon_\alpha \rho^\alpha \, \boldsymbol{v}^\alpha\right) = \varepsilon_\alpha \rho^\alpha \left(Q^\alpha + Q_{\text{ex}}^\alpha\right). \tag{2.43}$$

In addition, in Table 2.2 the definitions of the general quantities for $\mathcal{F}^\alpha = \mathcal{M}^\alpha$ of (2.32) are listed.

Finally, since mass is a conservative quantity, we have to require that the mass created over all phases is null, i.e.:

$$\sum_{\alpha = s,l,g} \varepsilon_\alpha \rho^\alpha Q_{\text{ex}}^\alpha = 0. \tag{2.44}$$

terms	description
$\psi^\alpha = 1$	since equation (2.42) holds
$\boldsymbol{j}^\alpha = 0$	since equation (2.35) holds
$F^\alpha = Q^\alpha$	internal supply of mass of the α-phase
$F^\alpha_{\text{ex}} = Q^\alpha_{\text{ex}}$	change of mass of the α-phase
$G^\alpha = 0$	since $\mathcal{M}^\alpha$ is conservative.

Table 2.2: Definitions of the general quantities in equation (2.32) for mass conservation (i.e: $\mathcal{F}^\alpha = \mathcal{M}^\alpha$) with a brief description.

If we denote with Q_α the bulk source term, i.e: $Q_\alpha = \varepsilon_\alpha(Q^\alpha + Q^\alpha_{\text{ex}})$ Equation (2.43) becomes:

$$\frac{\partial}{\partial t}\left(\varepsilon_\alpha \rho^\alpha\right) + \nabla \cdot \left(\varepsilon_\alpha \rho^\alpha \, \boldsymbol{v}^\alpha\right) = \rho^\alpha Q_\alpha, \tag{2.45}$$

for $\alpha = s, f,\ f \in \{l, g\}$. It states the global conservation of mass for the α-phase.

2.1.6 Conservation of momentum

Let $\mathcal{V}^\alpha$ denotes the momentum of the α-phase, the conservation of the momentum is obtained from (2.32) where the definitions of the general quantities are listed in Table 2.3, where the interfacial drag term $\boldsymbol{f}^\alpha_\sigma$ represents the exchange of momentum between the phase α and the other phases, due to mass exchange and mechanical interactions. We recall the abuse of notation in the symbol of intensive properties; they can be either scalars or vectors but, for simplicity of notation we denoted them as scalars in any case. Thus, for $\alpha = s, f,\ f \in \{l, g\}$ we get:

$$\frac{\partial}{\partial t}\left(\varepsilon_\alpha \rho^\alpha \boldsymbol{v}^\alpha\right) + \nabla \cdot \left(\varepsilon_\alpha \rho^\alpha \left(\boldsymbol{v}^\alpha \, \boldsymbol{v}^\alpha\right)\right) + \nabla \cdot \left(\varepsilon_\alpha \boldsymbol{\sigma}^\alpha\right) = \varepsilon_\alpha \rho^\alpha \left(\boldsymbol{g}^\alpha + \boldsymbol{f}^\alpha_\sigma\right), \tag{2.46}$$

see [33] for a detailed discussion on equation (2.46).

terms	description
$\psi^\alpha = \boldsymbol{v}^\alpha$	mass-weighted velocity of the α-phase
$\boldsymbol{j}^\alpha = \boldsymbol{\sigma}^\alpha$	stress tensor of the α-phase
$F^\alpha = \boldsymbol{g}^\alpha$	external supply of momentum due to gravity of the α-phase
$F^\alpha_{\text{ex}} = \boldsymbol{f}^\alpha_\sigma$	interfacial drag term
$G^\alpha = 0$	since $\mathcal{V}^\alpha$ is conservative

Table 2.3: Definitions of the general quantities in equation (2.32) for momentum conservation (i.e. $\mathcal{F}^\alpha = \mathcal{V}^\alpha$) with a brief description.

2.1.7 Conservation of energy

Let $\mathcal{E}^\alpha$, $\mathcal{K}^\alpha$ denote the internal or thermal, and kinetic energy of the α-phase, respectively. The conservation of the total energy $\mathcal{E}^\alpha + \mathcal{K}^\alpha$ is obtained from (2.32) where the definitions of the general quantities are listed in Table 2.4. For $\alpha = s, f$, $f \in \{l, g\}$ we get:

$$\begin{aligned} &\frac{\partial}{\partial t}\left(\varepsilon_\alpha \rho^\alpha \left(E^\alpha + \frac{1}{2}||\boldsymbol{v}^\alpha||^2\right)\right) + \nabla \cdot \left(\varepsilon_\alpha \rho^\alpha \left(E^\alpha + \frac{1}{2}||\boldsymbol{v}^\alpha||^2\right) \boldsymbol{v}^\alpha\right) + \\ &+\nabla \cdot \left(\varepsilon_\alpha \left(\boldsymbol{j}^\alpha_T + \boldsymbol{\sigma}^\alpha \cdot \boldsymbol{v}^\alpha\right)\right) = \varepsilon_\alpha \rho^\alpha \left(H^\alpha + \boldsymbol{g}^\alpha \cdot \boldsymbol{v}^\alpha + H^\alpha_{\text{ex}} + \boldsymbol{f}^\alpha_\sigma \cdot \boldsymbol{v}^\alpha\right), \end{aligned} \tag{2.47}$$

where $||\cdot||$ is the Euclidean norm, and H^α_{ex}, $\boldsymbol{f}^\alpha_\sigma$ represent the exchange of energy and momentum, respectively, between the phase α and the other phases, due to mass exchange and mechanical interactions.

From Equation (2.47), after subtraction of $\boldsymbol{v}^\alpha$ dotted with (2.46), for $\alpha = s, f$, $f \in \{l, g\}$ we get:

$$\frac{\partial}{\partial t}\left(\varepsilon_\alpha \rho^\alpha E^\alpha\right) + \nabla \cdot \left(\varepsilon_\alpha \rho^\alpha \boldsymbol{v}^\alpha E^\alpha\right) + \nabla \cdot \left(\varepsilon_\alpha \boldsymbol{j}^\alpha_T\right) + \varepsilon_\alpha \boldsymbol{\sigma}^\alpha : \nabla \boldsymbol{v}^\alpha = \varepsilon_\alpha \rho^\alpha \left(H^\alpha + H^\alpha_{\text{ex}}\right), \tag{2.48}$$

where the notation $\boldsymbol{A} : \boldsymbol{B}$ means a double dot product between the two second order tensor $\boldsymbol{A}$, $\boldsymbol{B}$ of dimension D; i.e.:

$$\boldsymbol{A} : \boldsymbol{B} = \sum_{i=1}^{D} \sum_{j=1}^{D} A_{ij} B_{ji}.$$

terms	description
$\psi^\alpha = E^\alpha + \frac{1}{2}\|\|\boldsymbol{v}^\alpha\|\|^2$	mass-weighted total energy of the α-phase
$\boldsymbol{j}^\alpha = \boldsymbol{j}_T^\alpha + \boldsymbol{\sigma}^\alpha \cdot \boldsymbol{v}^\alpha$	$\boldsymbol{j}_T^\alpha, \boldsymbol{\sigma}^\alpha$heat flux vector and stress tensor of the α-phase, respectively
$F^\alpha = H^\alpha + \boldsymbol{g}^\alpha \cdot \boldsymbol{v}^\alpha$	H^α external supply of energy of the α-phase
$F_{\text{ex}}^\alpha = H_{\text{ex}}^\alpha + \boldsymbol{f}_\sigma^\alpha \cdot \boldsymbol{v}^\alpha$	exchange of total energy between the α-phase and all the other phases
$G^\alpha = 0$	since energy is conservative

Table 2.4: Definitions of the general quantities in equation (2.32) for total energy conservation (i.e. $\mathcal{E}^\alpha + \mathcal{K}^\alpha$) with a brief description.

The term $\varepsilon_\alpha \boldsymbol{\sigma}^\alpha : \nabla \boldsymbol{v}^\alpha$ in (2.48) represents an energy dissipation term. It is always negative, however in porous media it is usually negligible, thus, for $\alpha = s, f$, $f \in \{l, g\}$ Equation (2.48) becomes:

$$\frac{\partial}{\partial t}\left(\varepsilon_\alpha \rho^\alpha E^\alpha\right) + \nabla \cdot \left(\varepsilon_\alpha \rho^\alpha \boldsymbol{v}^\alpha E^\alpha\right) + \nabla \cdot \left(\varepsilon_\alpha \boldsymbol{j}_T^\alpha\right) = \varepsilon_\alpha \rho^\alpha \left(H^\alpha + H_{\text{ex}}^\alpha\right). \tag{2.49}$$

The heat flux vector of the α-phase is proportional to the gradient of the temperature T^α of the α-phase and it is defined as:

$$\boldsymbol{j}_T^\alpha = -\boldsymbol{\Lambda}^\alpha \cdot \nabla T^\alpha,$$

where the hydrodynamic thermodispersion tensor is:

$$\begin{aligned} \boldsymbol{\Lambda}^\alpha &= \boldsymbol{\Lambda}_0^\alpha + \boldsymbol{\Lambda}_{\text{mech}}^\alpha \\ &= \left(\Lambda^\alpha + \gamma_T^\alpha ||\boldsymbol{v}^{fs}||\right) \boldsymbol{I} + \left(\gamma_L^\alpha - \gamma_T^\alpha\right) \frac{\boldsymbol{v}^{fs} \otimes \boldsymbol{v}^{fs}}{||\boldsymbol{v}^{\alpha s}||}. \end{aligned} \tag{2.50}$$

It consists in two parts; the thermal conductivity tensor $\boldsymbol{\Lambda}_0^\alpha = \Lambda^\alpha \boldsymbol{I}$ and the thermal mechanical diffusion tensor $\boldsymbol{\Lambda}_{\text{mech}}^\alpha$, while γ_L^α and γ_T^α represent the thermal transverse and longitudinal dispersion coefficients of the α-phase, respectively. In addition, we recall that $\boldsymbol{I}$ denotes the identity matrix and the relative velocity $\boldsymbol{v}^{\alpha s}$ of the α-phase has been defined in (2.40). We note that Equation (2.49) states the conservation of total energy for the α-phase, i.e., the first law of thermodynamics , see [33] for a detailed discussion on equation (2.49) and formula (2.50).

2.2 Insights into the physics of espresso coffee

In this section we deepen in the physical and chemical processes that occur during the espresso brewing procedure, in order to fully understand the dynamics of espresso coffee preparation. This consists in hot water, usually at 93 °C, at high pressure, typically 9 bar, that enters the filter basket previously filled with roasted, ground and tamped coffee. This process is referred to as percolation. During the espresso percolation the water dissolves the chemicals contained in the grains and transports them in the cup. This occurs in two main stages: the imbibition phase and the extraction. During the first phase, the water flows through the void spaces among grains of coffee due to gravity and it is absorbed into each grain by capillarity. Whereas, during the second stage the water dissolves the chemicals contained in the coffee powder and transports the dissolved compounds from the interior of the grains to their external surface up to the cup. However, in both the models that we are going to present the initial imbibition phase of wetting is disregarded and only the extraction phase is modelled.

The espresso beverage is extracted in a metal holder, generally called filter basket or simply filter, in which the coffee powder is contained. Figure 2.2 shows a picture of two conventional filter baskets for double portion extraction, with slightly different lateral profile. The filter is usually manufactured in stainless steel and has an almost cylindrical shape and a perforated bottom with holes whose diameter is usually of 0.25 mm [13]. This feature of the filter prevents the passage of larger coffee particles from the pod into the cup, which could be annoying when tasting the espresso. The typical width of double-shot filter is 60 mm, while its height may vary depending on its holding capacity. For example, the 20 g VST© competition filter basket, has an height of 26 mm. It is optimized for use with 20 g of dry coffee powder, that is the usual dose used in specialty coffee bar and in World Barista Championship competitions.

The filter basket gives the shape to the coffee cake. It has been seen that the optimal ratio height-width of the coffee pod is around 0.2. This means that a coffee pod contained in the VST© competition filter basket previously described has an

Figure 2.2: Picture of conventional double-shot filter baskets

height of 12 mm. The remaining empty space is left to prevent over-compacting of the cake that would occur during the wetting phase in which the coffee particles expand. Only small deviations of this ratio can be recommended; in fact, for too larger height-diameter ratio an excessively high pressure is required or, for normal pressure values an extremely coarse grind would be suggested, resulting in a low extraction. Conversely, for too low height-diameter ratios, too fine grounds are required in order to extract coffee in a standard time, this would prejudge the reproducibility of the extraction, because channeling effects could appear [13] with a resulting low quality extraction. The coffee pod is obtained by compacting the ground coffee powder usually with a tamping force of around 20 kgF in the filter. In general, the particle size distribution of an espresso grinding has a bimodal pattern; Figure 2.3 reports the particle size distribution curve of an espresso powder sample analysed with a laser diffraction particle size analyser. The x axis reports the values of the particle diameters and the corresponding value on the y axis is the percentage of volume covered by all particles having that diameter.

We highlight the bimodal trend of the curve that has a local minimum around 100 µm, this allows us to divide the particles into two families: the fines, whose diameter is smaller than 100 µm, and the boulders, with diameter larger than 100 µm. This peculiar feature of the particle size produces a double effect: it forms

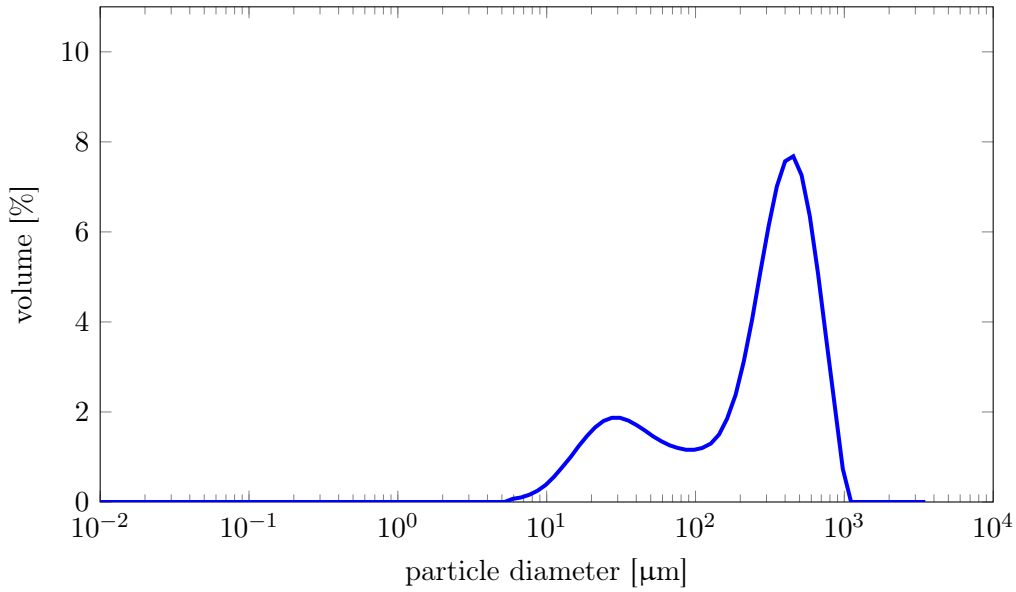

Figure 2.3: Particle size distribution curve of a sample of espresso coffee powder.

a coarse fixed structure of the pod, which allows a correct flow and, at the same time, the large amount of fines allows the extraction of an higher amount of solubles and emulsifier material. From a mathematical point of view, the coffee pod can be modelled as a porous medium. In particular, both the size of the grains and their ratio fines-boulders affects the porous structure of the medium and they determines a relevant property, its porosity ε (cf. Section 2.1.1). Therefore, a mathematical model for the espresso percolation process has to consider at least the feature of the medium, the two phases involved, i.e. the liquid and the solid phases, and the main processes taking place for each of them.

2.3 A 3D model for espresso coffee percolation

We present a three-dimensional model for the prediction of the coffee percolation. The model was firstly proposed in [23], and it is the most complete mathematical model available in literature for such a purpose. In fact, it allows the solution of flow, mass and heat transport simultaneously. In the following we analyse and derive each equation of this model by using fundamental principles described in

Section 2.1.

Up to now, the general percolation model derived in Section 2.1 consists in Equations (2.37), (2.41), (2.45), (2.46), (2.49), where the volumetric flux density, usually called *Darcy velocity* can be introduced, i.e.:

$$\boldsymbol{q}^f = \varepsilon_f(\boldsymbol{v}^f - \boldsymbol{v}^s). \tag{2.51}$$

The following reasonable hypotheses are considered in the formulation of this model:

1. The porous medium is isotropic and homogeneous.

2. Since the percolation process lasts about 25 seconds, but espresso coffee comes out after about 5 seconds, that are necessary for the coffee pod imbibition, the flow is not considered during the first imbibition phase and therefore the porous medium is considered saturated. This means that there is no gaseous phase, i.e: $f = l$.

3. Thermodynamic equilibrium is assumed between the phase, that is the temperatures of all phases are equal at each point of the medium, i.e.: $T^l = T^s = T$. Thus, energy conservation equations (2.49) can be summed up over the phases resulting in only one equation.

4. Solid grains are assumed to be incompressible, thus fluids and solid equations can be decoupled and there is no need to solve mass and momentum equations for the solid phase.

5. The term associated with the solid movement $\varepsilon^f \boldsymbol{v}^s$ is negligible, thus for the volumetric flux density holds: $\boldsymbol{q}^f = \varepsilon^f \boldsymbol{v}^f$.

As consequence of these assumptions we have that the model consists in Equations (2.37), (2.41), and (2.45), (2.46), only for the liquid phase, i.e.: $\alpha = l$, and a unique equation of kind (2.49) since thermodynamic equilibrium is assumed. Moreover, since the medium is saturated by a single liquid, the liquid volume fraction is equal to the medium porosity $\varepsilon^l = \varepsilon$, while the solid volume fraction is $\varepsilon^s = 1 - \varepsilon$. For this reason and the aforementioned hypothesis 5, in the following

we omit the superscript l in the volumetric flux density, i.e.: $\boldsymbol{q} = \boldsymbol{q}^l$, and in general when we refer to the liquid phase.

2.3.1 The Darcy's law

In this Section we analyse the Darcy's law, which describes the motion of a fluid in a porous medium. It was empirically formulated by Darcy in 1856 as the result of his experiments for the construction of the Dijon fountains [46]. Darcy's law is valid in steady-state operations, i.e. the speed of the fluid is egligible and, although varying from point to point, remains approximately constant over time at each point; moreover, we assume the following conditions:

- laminar flux,
- system totally saturated by a unique fluid,
- absence of chemical-physical interactions between fluid and porous medium.

We note that alternative formulations of the Darcy's law can also be given for unsaturated media by making appropriate modifications on the hydraulic conductivity coefficient [33]. Although Darcy's law was formulated for the first time empirically, it can be derived from the conservation equation of the momentum (2.46) for the liquid phase l, where we split the liquid stress tensor $\boldsymbol{\sigma}$ into an equilibrium part, gaining the pressure contribution, and non-equilibrium part, due to viscous forces, $\boldsymbol{\tau}$ called deviatoric fluid stress tensor, according to:

$$\begin{aligned} \boldsymbol{\sigma} &= p\boldsymbol{\delta} - \boldsymbol{\tau}, \\ \varepsilon\rho\boldsymbol{f}_\sigma &= p\nabla\varepsilon + \boldsymbol{f}_\tau \end{aligned} \tag{2.52}$$

where $\boldsymbol{\delta}$ denotes the Kronecker delta function. Introducing (2.52) in (2.46) we get:

$$\frac{\partial}{\partial t}\left(\varepsilon\rho\boldsymbol{v}\right) + \nabla\cdot\left(\varepsilon\rho\left(\boldsymbol{v}\,\boldsymbol{v}\right)\right) + \varepsilon\nabla p - \nabla\cdot\left(\varepsilon\boldsymbol{\tau}\right) = \varepsilon\rho\boldsymbol{g} + \boldsymbol{f}_\tau, \tag{2.53}$$

We observe that in a perfect fluid or in a fluid at rest, $\boldsymbol{\tau}$ vanishes, so that the stresses within it are purely isotropic, i.e., $\boldsymbol{\sigma} = p\boldsymbol{\delta}$, where p is the hydrostatic pressure[47]. Moreover, the velocity $\boldsymbol{v}$ is supposed to be sufficiently small so that the Reynolds

number Re_p [48] based on the typical pore diameter is enough small (in the case of espresso coffee $Re_p \approx 10^{-1}$). As a consequence, the inertial terms in (2.53) can be neglected, i.e.:

$$\frac{\partial}{\partial t}\left(\varepsilon\rho\boldsymbol{v}\right) \approx 0, \qquad \nabla\cdot\left(\varepsilon\rho\left(\boldsymbol{v}\,\boldsymbol{v}\right)\right) \approx 0.$$

Thus, equation (2.53) becomes:

$$\varepsilon\left(\nabla p - \rho\boldsymbol{g}\right) = \boldsymbol{f}_\tau, \tag{2.54}$$

where $\boldsymbol{f}_\tau$ is given by:

$$\boldsymbol{f}_\tau = -\frac{\varepsilon\mu}{\boldsymbol{k}}\boldsymbol{q},$$

where μ denotes the viscosity of the fluid and $\boldsymbol{k}$ is the intrinsic permeability discussed in Section 2.1.2. Equation (2.54) is the Darcy equation, that is usually written in pressure formulation:

$$\boldsymbol{q} = -\frac{\boldsymbol{k}}{\mu}\left(\nabla p - \rho\boldsymbol{g}\right) \tag{2.55}$$

Moreover, Equation (2.55) can be written in its equivalent formulation for the hydraulic head $h = z + \dfrac{p}{\rho_0 g}$ as:

$$\boldsymbol{q} = -\mathbf{K} f_\mu\left(\nabla h + \chi\boldsymbol{e}\right), \tag{2.56}$$

where $f_\mu = \dfrac{\mu_0}{\mu}$, is the viscosity relation function, $\chi = \dfrac{\rho - \rho_0}{\rho_0}$, is the buoyancy coefficient, $\boldsymbol{e} = (0,0,1)^T$, and $\mathbf{K}$ is the hydraulic conductivity tensor discussed in Section 2.1.2. In conclusion, Darcy's law (2.56) describes the flow behaviour through a saturated medium, in laminar flux regime. It states that the flux is proportional to the hydraulic gradient, and the negative sign indicates that the flow of the fluid occurs in the direction that goes from points at higher pressure to those where the pressure is lower.

2.3.2 The Richards' equation

Richards' equation describes the flow of a fluid in a porous medium. Since the extraction of coffee from the pod will be modeled as a flow problem in a porous medium saturated by a single fluid we will derive the Richards' equation for such

a porous medium. See [49] for the derivation of the unsaturated case. Richards' equation can be obtained combining the principle of continuity, namely the mass conservation of the liquid phase (2.45) with the Darcy's law (2.56).

Under the hypothesis of absence of sources or sinks, Equation (2.45) becomes:

$$\frac{\partial(\varepsilon\rho)}{\partial t} + \nabla \cdot (\rho \boldsymbol{q}) = 0, \tag{2.57}$$

where $\boldsymbol{q}$ is given by the Darcy's law (2.56). Furthermore, from the product rule we have:

$$\frac{\partial(\varepsilon\rho)}{\partial t} = \varepsilon\frac{\partial\rho}{\partial t} + \rho\frac{\partial\varepsilon}{\partial t}. \tag{2.58}$$

Let us introduce the two following additional constitutive laws. The first states that particles consolidate when the liquid pressure p decreases, i.e.:

$$\frac{\partial\varepsilon}{\partial t} = \frac{d\varepsilon}{dp}\frac{\partial p}{\partial t} = C_v\frac{\partial p}{\partial t}, \tag{2.59}$$

where $C_v \equiv \dfrac{d\varepsilon}{dp}$ is a coefficient related to the classical coefficient of consolidation used in soil mechanics [50]. The second law relates the water compressibility β with the liquid pressure:

$$\beta = \frac{1}{\rho}\frac{d\rho}{dp}. \tag{2.60}$$

From the chain rule and introducing (2.59) and (2.60) in (2.58) we have:

$$\frac{\partial(\varepsilon\rho)}{\partial t} = \varepsilon\frac{d\rho}{dp}\frac{\partial p}{\partial t} + \rho C_v\frac{\partial p}{\partial t} = \rho(\varepsilon\beta + C_v)\frac{\partial p}{\partial t}. \tag{2.61}$$

In addition, recalling that $h = z + \dfrac{p}{\rho g}$, we have:

$$\frac{\partial h}{\partial t} = \frac{1}{\rho g}\frac{\partial p}{\partial t}, \tag{2.62}$$

that is:

$$\frac{\partial p}{\partial t} = \rho g\frac{\partial h}{\partial t}. \tag{2.63}$$

Moreover, combining (2.57), (2.61) and (2.63) we obtain:

$$g\rho^2(\varepsilon\beta + C_v)\frac{\partial h}{\partial t} + \nabla \cdot (\rho \boldsymbol{q}) = 0. \tag{2.64}$$

If we define the *specific storage* S_0 as the volume of water released from a unit volume of porous medium due to a unit decrease in hydraulic head, i.e. $S_0 = g\rho(\varepsilon\beta + C_v)$, (2.64) becomes:

$$S_0 \frac{\partial h}{\partial t} + \nabla \cdot \boldsymbol{q} = 0. \tag{2.65}$$

We note that in (2.65) we have also replaced $\nabla \cdot (\rho \boldsymbol{q})$ with $\boldsymbol{q} \cdot \nabla\rho + \rho\nabla \cdot \boldsymbol{q}$, and we have assumed that the spatial gradient of ρ is negligible compared to other terms in the equation, so it has been neglected and finally we divided by ρ. We point out that, because the specific storage coefficient S_0 depends on the fluid density, that in turn is a function of the pressure p, and therefore of h, Equation (2.65) is non-linear. However, since in reality S_0 does not change very much when the pressure changes, it is normally given as a constant value, i.e. $S_0 = g\rho_0(\varepsilon\beta + C_v)$, where ρ_0 is a reference mass density of the fluid. We note that Equation (2.65) when the flux $\boldsymbol{q}$ is given by (2.56), it is the Richards' equation valid for a medium completely saturated by a single fluid.

2.3.3 The mass transport equations

During the percolation process the chemical substances can behave in two different ways; i) they can be dissolved by the water flow and therefore they can be transported by the fluid flow; ii) they can remain bounded to the porous medium during all the percolation process. Hence, due to the different nature of the process they are subjected to, we can divide the species in two different groups:

- the dissolved substances that are flowing together with the water and are being transported by the water flow, whose dynamics is described by the mass transport equation for the chemicals species in the liquid phase. For such species we denote with $C_k = C_k^l = \rho^l \omega_k^l$, $k = 1, 2, \ldots, N^l$ their chemical concentration.

- the solid particles that remain bounded to the porous matrix, whose dynamics is described by the mass transport equation for the species in the solid phase.

For such substances we denote with $C_k^s = \rho^s \omega_k^s$, $k = 1, 2, \ldots, N^s$ their chemical concentration.

The dynamics of the dissolved substances

The dynamics of the dissolved substances is described by the mass transport equation for the species in the liquid phase and it derives from Equation (2.41), where we substitute Formula (2.51) and assumption 5. In particular, if the notation of the liquid concentration C_k, $k = 1, 2, \ldots, N^l$ is used, we obtain:

$$\frac{\partial}{\partial t}(\varepsilon C_k) + \nabla \cdot (C_k \, \boldsymbol{q}) + \nabla \cdot \boldsymbol{j}_k = \varepsilon \left(r_k^l + R_k^l \right), \tag{2.66}$$

where

$$\boldsymbol{j}_k = \varepsilon \boldsymbol{j}_k^l. \tag{2.67}$$

Equation (2.66) can be written in his equivalent convective form; in absence of internal sinks or sources of water this is:

$$\varepsilon \frac{\partial C_k}{\partial t} + \boldsymbol{q} \nabla C_k + \nabla \cdot \boldsymbol{j}_k = R_k, \tag{2.68}$$

where R_k denotes the total reaction rate of the species k in the liquid phase. In conclusion, the dynamics in time of the concentration C_k of the chemicals k, $k = 1, 2, \ldots, N^l$ follows the second-order PDE (2.68). In particular, the second-order term $\nabla \cdot \boldsymbol{j}_k$ describes diffusion phenomena that substances undergo to, while the first-order term $\boldsymbol{q} \nabla C_k$ describes convection phenomena to which dissolved chemicals are subjected.

The dynamics of the solid particles

The dynamics of chemicals remaining bounded to the porous matrix is described by the mass transport equation for the species in the solid phase and it derives from Equation (2.37), where from the notation for the solid concentration C_k^s, for $k = 1, 2, \ldots, N^s$, it is obtained:

$$\varepsilon_s \frac{\partial C_k^s}{\partial t} = R_k^s, \tag{2.69}$$

where R_k^s denotes the total reaction rate of the species k in the solid phase. Note that, since we deal with stationary solids, we have that $\nabla \cdot (\varepsilon_s \rho^s \omega_k^s \, \boldsymbol{v}^s) \approx 0$.

2.3.4 The heat transport equation

The dynamic of the heat transport follows Equation (2.49), that is given for the internal Energy E^α of the α-phase . Neglecting density, solid strain and chemical effects, the internal energy is related to the temperature T^α of the α-phase through the following relation:

$$dE^\alpha = c^\alpha dT^\alpha, \qquad \alpha = s, f, \tag{2.70}$$

where c^α is the specific heat capacity of the α-phase, that we suppose independent from the temperature. So that, if we denote with $E_0^\alpha = E_0^\alpha(T_0^\alpha)$ a constant reference value of internal energy corresponding to the reference value of temperature T_0^α, we have:

$$E^\alpha(T^\alpha) = E_0^\alpha + \int_{T_0^\alpha}^{T^\alpha} c^\alpha dT^\alpha, \qquad \alpha = s, f,$$

from which follows:

$$E^\alpha = E_0 + c^\alpha \left(T^\alpha - T_0^\alpha\right), \qquad \alpha = s, f. \tag{2.71}$$

Thus, exploiting relation (2.71), in Equation (2.49) and supposing the thermodynamic equilibrium of assumption 3, i.e., summing up over the phases Equation (2.49), we get the following convective form for heat transport in porous media:

$$\left(\varepsilon\rho c + \varepsilon_s \rho^s c^s\right) \frac{\partial T}{\partial t} + \rho c \boldsymbol{q} \cdot \nabla T + \nabla \cdot \boldsymbol{j}_T = H_e, \tag{2.72}$$

where H_e denotes a total source/sink of internal energy and $\boldsymbol{j}_T$ is the heat flux vector defined by:

$$\boldsymbol{j}_T = -\boldsymbol{\Lambda} \cdot \nabla T, \tag{2.73}$$

where $\boldsymbol{\Lambda}$ is the thermal hydrodynamic conductivity tensor defined by:

$$\begin{aligned} \boldsymbol{\Lambda} &= (\varepsilon\Lambda + \varepsilon_s \Lambda^s)\mathbf{I} + \rho c \boldsymbol{\Lambda}_{\text{mech}} \\ &= \Big(\varepsilon\Lambda + \varepsilon_s\Lambda^s + \rho c \gamma_T ||\boldsymbol{q}||\Big)\boldsymbol{I} + \rho c \Big(\gamma_L - \gamma_T\Big)\frac{\boldsymbol{q} \otimes \boldsymbol{q}}{||\boldsymbol{q}||}, \end{aligned} \tag{2.74}$$

where $\boldsymbol{\Lambda}_{\text{mech}}$ is the thermal mechanical diffusion tensor, Λ, Λ^s are the thermal conductivities of the fluid and solid phases, respectively, while γ_L, γ_T are the thermal transverse and longitudinal dispersion coefficients, respectively [33].

2.3.5 The 3D coffee percolation model

As already described in the introduction of this chapter, the extraction process of espresso coffee consists in hot water that enters the filter basket presviously filled with ground, roasted and tamped coffee. Then the water flows through the empty spaces between the grains, dissolving various chemicals substances and removing some fine particles from the wet coffee powder. This process is called coffee percolation.

Now, we are in a position to precisely define the complete percolation model for espresso coffe extraction. This model has been proposed in [23] and [24]. It divides the substances involved in the percolation process in liquid and solid species. Among the first ones there are the carrier fluid, i.e. the water, together with the dissolved and oily substances, while the solid species include all the particles that belong to the porous medium.

Moreover, some simplifying hypotheses are assumed that sound reasonable for the espresso coffee extraction, also in relation to analogous phenomena [33], [51], [52]. We used these hypotheses in the previous sections, for the derivation of the main parts of the model, however, for the reader's convenience, we recap the most important assumptions below, see [23] for more details.

- The porous medium is isotropic and homogeneous. In particular, the homogeneity property has been assumed since the coffee powder is grounded with different size of coffee grains, however their physical and chemical properties are the same in each grain independently of their size and location.

- The momentum equation for the liquid phase is simplified by the Darcy's law since the pore Reynolds number is sufficiently small, in fact $Re_p \approx 10^{-1}$ [23].

- A species appears in the liquid or solid phase depending on its involvement or not in the transport process. This means that a fine solid particle that is involved in the mass transport by the fluid flow is considered liquid, despite being a solid species from the physical point of view; similarly a soluble species that is bounded to the porous medium is considered solid.

- Each species belongs to both the liquid phase and the solid phase, where the liquid portion accounts for the quantity of that chemicals which is in solution or in suspension in the water, while the solid portion accounts for the amount of the same chemicals that is bounded to the porous matrix. This means that we have the same number of liquid N^l and solid N^s species to be monitored that we denote with $N_{l-s} := N^l = N^s$.

- Oberbeck-Boussinesq approximation [53], [54] is assumed, that is all the thermophysical properties are considered constant except for the fluid density in the buoyancy term ($\rho \boldsymbol{g}$ in (2.55) or $\chi \boldsymbol{e}$ in (2.56), respectively).

- Since the percolation process lasts about 25 seconds, but espresso coffee comes out after about 5 seconds, that are necessary for the porous medium imbibition, the flow is disregarded during the first imbibition phase and so the porous medium is considered saturated.

- The expansion of the coffee particles due to the wetting process is discarded.

- After the initial imbibition, local thermal balance is assumed between liquid and solid phase.

- There are no internal sinks or sources of water, heat, and chemical substances in the coffee pod.

The spatial domain of the percolation model is a circular cylinder $\mathcal{C}$, with height H, whose top circular face Γ_1, of radius R, lays on the plane $z = 0$ of the three-dimensional Cartesian coordinate system and its center is on the origin of the xy plane. So that, the bottom face Γ_3 lays on the $z = -H$ plane, we denote with Γ_2

h	hydraulic head
p	pressure
$\boldsymbol{q}$	fluid flux
C_k	mass concentration of liquid/solid species k
C_k^s	mass concentration of solid species k
ε	porosity
ε_s	solid volume fraction, $\varepsilon_s = (1-\varepsilon)$
S_0	specific storage coefficient
$\mathbf{K}$	hydraulic conductivity tensor
f_μ	viscosity relation function
χ	buoyancy coefficient
$\boldsymbol{e}$	$(0,0,1)^T$
$\boldsymbol{j}_k$	hydrodynamic diffusion/dispersion vector of species k
$\boldsymbol{j}_T$	heat flux vector
R_k	total reaction rate of species k
R_k^s	total reaction rate of solid species k
T	temperature
T_0	reference temperature
ρc	volumetric heat capacity of the fluid
$\rho^s c^s$	volumetric heat capacity of the solid
H_e	sources/sinks of internal energy

Table 2.5: Description of the symbols occurring in the model (2.75)

the lateral face. The complete model for the espresso coffee percolation is:

$$\begin{cases} S_0 \dfrac{\partial h}{\partial t} + \nabla \cdot \boldsymbol{q} = 0, \\ \boldsymbol{q} = -\mathbf{K} f_\mu \left(\nabla h + \chi \boldsymbol{e} \right) \\ \varepsilon \dfrac{\partial C_k}{\partial t} + \boldsymbol{q} \nabla C_k + \nabla \cdot \boldsymbol{j}_k = R_k, & k = 1, 2, \ldots, N_{l-s}, \\ \varepsilon_s \dfrac{\partial C_k^s}{\partial t} = R_k^s, & k = 1, 2, \ldots, N_{l-s}, \\ \left(\varepsilon \rho c + \varepsilon_s \rho^s c^s \right) \dfrac{\partial T}{\partial t} + \rho c \boldsymbol{q} \cdot \nabla T + \nabla \cdot \boldsymbol{j}_T = H_e, \end{cases} \tag{2.75}$$

where each equation is prescribed in $\mathcal{C}$, and for $t \in (0, \tau)$, where $\tau > 0$ denotes the percolation time. The unknowns of system (2.75) are the flux $\boldsymbol{q}$, the hydraulic head h, the mass concentration of the liquid and solid chemical species C_k, C_k^s, respectively, and the temperature T. The symbols appearing in problem (2.75) are reported in Table 2.5. We note that the first equation of model (2.75), is the Richards' equation (2.65), where the flux $\boldsymbol{q}$ is given by the second equation that is the Darcy's law (2.56). The third equation is the transport equation (2.68) for the species k; there are N_{l-s} equation of this type, one for each species to be monitored. The fourth equation states the mass conservation (2.69) for the solid species k that is not involved in the diffusion-transport process; there are N_{l-s} equation of this type, one for each species to be monitored. Finally, the last equation is the heat equation (2.72) in the porous medium.

The boundary and initial conditions for problem (2.75) are shown below. For the hydraulic head it holds:

$$\begin{cases} h = h_{z0}, & \text{on } \Gamma_1, t > 0, \\ \dfrac{\partial h}{\partial \mathbf{n}} = 0, & \text{on } \Gamma_2, t > 0, \\ \boldsymbol{q} \cdot \mathbf{n} = -\Phi_h \min\{h_C - h, 0\}, & \text{on } \Gamma_3, t > 0, \\ p = p_0(z), & \text{in } \mathcal{C}, t = 0, \end{cases} \tag{2.76}$$

where, the first equation prescribes a given profile for the hydraulic head at the entrance of the coffee pod and $\mathbf{n}$ denotes the outward normal unit vector. In particular the third equation of system (2.76) allows an external flux with rate $\Phi_h(h - h_C)$ when $h > h_C$, where Φ_h is a prescribed transfer coefficient accounting for a kind of conductivity of the filter placed at the lower base of the coffee pod, and h_C a proper value for the hydraulic head; this condition states that the coffee start to exit when h is greater than h_C nearby the filter. Finally, the last equation in system (2.76) is the initial condition. It is given for the pressure p and it automatically prescribes an initial condition for h. Here, p_0 is the prescribed pressure profile when percolation starts, thus for the compatibility condition it must be $h_{z0} = \dfrac{p_0(z)|_{z=0}}{\rho_0 g}$.

For the concentration C_k $k = 1, 2, \ldots, N_{l-s}$ of the liquid-solid species we have:

$$\begin{cases} \nabla C_k \cdot \mathbf{n} = 0, & \text{on } \Gamma_1, \Gamma_2, t > 0, \\ -(\boldsymbol{D}_k \cdot \nabla C_k) \cdot \mathbf{n} = -\Phi_k \min\{C_{kC} - C_k, 0\}, & \text{on } \Gamma_3, t > 0, \\ C_k = 0, & \text{in } \mathcal{C}, t = 0, \end{cases} \tag{2.77}$$

where C_{kC} is a known value for the concentration and $\boldsymbol{D}_k$ is the hydrodynamic dispersion tensor defined in (2.39). If $C_k > C_{kC}$ a mass outward flux occurs with rate $\Phi_k(C_k - C_{kC})$; again, as for the hydraulic head, Φ_k can be read as the admittance of the filter at the bottom of the coffee pod, for the species k. Moreover, on the top and lateral faces Neumann condition is prescribed since flux through these surfaces is not permitted.

For the solid species only the initial condition is needed:

$$C_k^s = C_{k0}^s, \quad \text{in } \mathcal{C}, t = 0, \qquad\qquad k = 1, 2, \ldots, N_{l-s}, \tag{2.78}$$

where C_{k0}^s is the concentration of the species k in the coffee powder before the percolation process.

Finally, for the temperature we prescribe:

$$\begin{cases} T = T_{z0}, & \text{on } \Gamma_1, t > 0, \\ \nabla T \cdot \mathbf{n} = 0, & \text{on } \Gamma_2, \Gamma_3, t > 0, \\ T = T_0, & \text{in } \mathcal{C}, t = 0, \end{cases} \tag{2.79}$$

where T_{z0} is the incoming water temperature, and T_0 is the initial temperature, i.e. after the imbibition, of the system water-coffee powder. Besides, on the lateral and bottom faces Neumann condition is prescribed.

In conclusion, the complete three-dimensional model for the prediction of espresso coffee percolation is given by system (2.75) equipped with initial-boundary conditions (2.76), (2.77) (2.78), and (2.79). It is the most complete model available in literature for such a purpose. In fact, it allows the prediction of the water dynamics, the transport of the dissolved substances, the dynamics of the solid particles, and the energy balance between the liquid and the coffee pod.

2.4 A reduced model for the espresso extraction

In this section we present and discuss a reduced model previously presented in [19] for the prediction of the extraction efficiency, and later generalised in [21] to forecast the extraction of an arbitrary number of chemical substances. This is a one-dimensional model having the advantage to be a simple prediction tool taking into account quantities that are averaged over the whole domain or over some its sections. In the following, we discuss the mathematical model in [19], [21], [55] to simulate the espresso coffee percolation, discarding also in this case the initial imbibition phase. This means that we suppose that, at the initial time, each grain has been wetted and the porous medium saturated. The detailed derivation of this model can be found in [17]–[19].

The preparation process of espresso coffee takes place when the hot and pressurised water goes inside the filter basket, filled with the tamped coffee powder previously roasted. During the percolation process, the water flows through the interconnected void spaces among the coffee grains and dissolves the chemical substances contained in the powder. In particular, during the extraction phase the pressurised hot water transports the previously dissolved chemicals from the grains up to the cup. Moreover, most dissolved solubles of a coffee beverage comes from the dissolution of the substances contained in the small grains, instead, the substances within the big grains are only partially dissolved [22]. Therefore, the proposed mathematical model describes the transport of chemicals from the interior of the grains to their external surfaces, their dissolution into the liquid and the transport process due to the fluid flow through the coffee pod. This model also takes into account the two physical phases involved in this process, i.e., the liquid and the solid phase, and the main physico-chemical processes occurring for each of them. These are the advective transport and the diffusion of chemicals in the liquid phase, and the diffusion phenomena of the species within each grain of the solid phase. Here the grains of the coffee powder are approximated through spheres of two distinct radii a^f, a^b, for fine and coarse grains, usually called fines and boulders, respectively. Note that this assumption agrees with the bimodality feature of coffee

powder granulometry produced by usual grinding machines, see Section 2.2 for details.

Figure 2.4 shows a sketch of the coffee pod, which is assumed to be a circular cylinder of radius R_0 and height L, whose top circular face lays on the plane $z = 0$ and its bottom face lays on the plane $z = L$. In the coffee extraction, the water

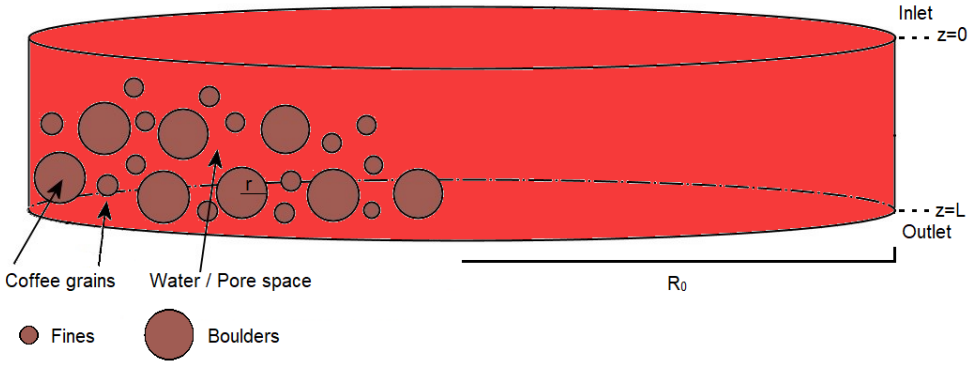

Figure 2.4: A graphic representation of the coffee cake. The coffee grains forming the solid matrix are shown in brown, and the inter-granular pore space is shown in red.

flow develops mainly along the vertical direction; in particular, a uniform inlet flow is provided to the top face and, due to the low flow velocity, no (lateral) boundary effects are assumed. So, this uniform flow from the top face to the bottom face can be described with a one-dimensional model along the z-axis; at the same time, the dissolution processes for chemicals in the coffee grains develop mainly along the radial direction, therefore, the dynamics of the solid phase are described through a one-dimensional model along the radial direction for each fixed z-level. In more detail, the vertical direction is related to the inter-grain flow and transport, while the radial direction corresponds to the intra-grain transport. Let N_{l-s} be the number of the substances whose concentration has to be computed. We denote with c_i^l the concentration of the i-th liquid chemical substance outside the grains that has been already dissolved and is being transported by the water flow. Similarly, we denote with c_i^f and c_i^b the concentration of the i-th chemical substance into the fines and boulders, respectively, that has not yet been involved in the transport

process outside the coffee grains. So, $\boldsymbol{c}^l$, $\boldsymbol{c}^f$, $\boldsymbol{c}^b \in \mathbb{R}^{N_{l-s}}$ are the vectors of the liquid, fine solid and coarse solid concentrations, respectively.

We consider the following initial-boundary value problem describing the dynamics of the concentration c_i^l of chemical substance i in the liquid phase:

$$\begin{cases} (1-\phi)\,\dfrac{\partial c_i^l}{\partial t}(z,t) = D\dfrac{\partial^2 c_i^l}{\partial z^2}(z,t) - q\dfrac{\partial c_i^l}{\partial z}(z,t) + b^f G_i^f(\boldsymbol{c}^l,\boldsymbol{c}^f,z,t) + b^b G_i^b(\boldsymbol{c}^l,\boldsymbol{c}^b,z,t), \\ -D\dfrac{\partial c_i^l}{\partial z}(0,t) + q c_i^l(0,t) = 0, \\ -D\dfrac{\partial c_i^l}{\partial z}(L,t) = 0, \\ c_i^l(z,0) = 0, \end{cases} \tag{2.80}$$

for $i = 1, 2, \ldots, N_{l-s}$, $z \in (0, L), t \in (0, \tau)$, where $\tau > 0$ is the percolation time, D is the effective diffusivity, q is Darcy's flux, ϕ is the local volume fraction occupied by grains, which is defined as the sum of the volume fractions associated with each kind of solid particles, i.e.,

$$\phi = \phi^f + \phi^b, \quad \phi^f = b^f\frac{a^f}{3}, \quad \phi^b = b^b\frac{a^b}{3},$$

here b^f and b^b are the so-called Brunauer-Emmett-Teller parameters [56] and a^f and a^b are the radii of fines and boulders, respectively. For $i = 1, 2, \ldots, N_{l-s}$, in (2.80) the differential equation gives a one-dimensional version of model (2.68) and the right-hand side consists of a diffusive term, an advective term and two reactive terms G_i^f and G_i^b. They are described at the end of this section since they relate the dynamics of liquid and solid species. The second and third equations in (2.80) are the boundary conditions at the inlet and outlet of the coffee pod, respectively. In particular, they prescribe no flux of solubles across the inlet, and no diffusive flux at the outlet, respectively. Finally, the initial condition prescribes a zero liquid concentration of solubles at the initial time $t = 0$.

The dynamics of the concentrations of chemical species i, for $i = 1, 2, \ldots, N_{l-s}$,

in the solid phase is modeled by the following initial-boundary value problem:

$$\begin{cases} \dfrac{\partial c_i^s}{\partial t}(r,z,t) = \dfrac{D_i^f}{r^2}\dfrac{\partial}{\partial r}\left(r^2\dfrac{\partial c_i^s}{\partial r}(r,z,t)\right), \\ -D_i^f\dfrac{\partial c_i^s}{\partial r}(0,z,t) = 0, \\ -D_i^f\dfrac{\partial c_i^s}{\partial r}(a^s,z,t) = G_i^s(\boldsymbol{c}^l,\boldsymbol{c}^s,z,t), \\ c_i^s(r,z,0) = c_{0_i}, \end{cases} \tag{2.81}$$

for $s = f, b$, $r \in (0, a^s), t \in (0, \tau)$, and $z \in (0, L)$. Problem (2.81) is given for fines, i.e. $s = f$, and for boulders, i.e. $s = b$. Here, D_i^f is the diffusivity of substance i inside the grain, and it is assumed to be independent of the particle dimension, and c_{0_i} is the initial solid concentration. The first equation of problem (2.81) is the diffusion equation in spherical coordinates in the case of spherical symmetry. It describes the transport of species occurring inside the coffee grains. The second and third equations are the boundary conditions, in particular the third equation describes the flux of soluble of type i per unit area occurring through the interface between the small grains and the inter-granular space, that is $G_i^s(\boldsymbol{c}^l, \boldsymbol{c}^s, z, t)$, $s = f, b$. In addition, we highlight that $G_i^s(\boldsymbol{c}^l, \boldsymbol{c}^s, z, t) = G^i\left(\boldsymbol{c}^l(z,t), \boldsymbol{c}^s(a^s, z, t), z, t\right)$, since it describes the exchange of solubles occurring on the surface of small grains, where $r = a^s$, $s = f, b$. Finally, the last one is the initial condition, prescribing an initial value, c_{0_i} of chemical i in the coffee powder. We highlight that, $c_i^s = c_i^s(r, z, t)$, this means that, for each i, $i = 1, 2, \ldots, N_{l-s}$, we have one problem of type (2.80), which for each z-level is coupled with two problems of kind (2.81), one for the solid concentrations c_i^f and the other for c_i^b. The coupling is given by the terms G_i^s, modelling the mass transfer of the chemical i extracted from the grains going into the liquid phase, i.e., the fluid moving among the grains. In fact, G_i^s, for $s = f, b$, gives the flux per unit area of substances through the surface of the grains and the void spaces among them. Moreover, in the reactive terms, we introduce the substances interaction. In particular, we suppose that the amount of the extracted substance i at the time t depends on the amount of the already dissolved species j,

$j = 1, \ldots, N_{l-s}$, $j \neq i$ at that time. They are defined as follows:

$$G_i^s(\boldsymbol{c}^l, \boldsymbol{c}^s, z, t) = k_r^i c_i^s(a^s, z, t) \max(c_i^s(a^s, z, t) - c_i^l(z, t), 0) \max(c_{\text{sat}}^i - c_i^l(z, t), 0) \cdot \cdot \prod_{\substack{j=1, \\ j \neq i}}^{N_{l-s}} \max(c_j^l(,t) - c_{\text{dis}}^{i,j}, 0), \tag{2.82}$$

for $s = f, b$, where c_{sat}^i is the concentration of saturation of the liquid with respect to the substance i, and k_r^i is the reaction rate of the substance i, and $\max(x, 0)$ is the continuous, non-differentiable function that selects the maximum non-negative argument. Formula (2.82) is highly non-linear, and the numerical results of previous works present in the literature [19], [21], [55], [57] justify its use. In particular $G_i^s(\boldsymbol{c}^l, \boldsymbol{c}^s, z, t)$ is zero when the liquid near the grains is saturated, or when it is at the same concentration as the dissolved chemicals at the grain surface, or when all solubles inside the grain have been dissolved. Furthermore, $c_{\text{dis}}^{i,j}$ is the threshold above which the dissolved amount of substance j influences the dissolution of substance i. Thus, the flux is zero also when the substance j into the liquid immediately near the grains has a concentration lower than the threshold $c_{\text{dis}}^{i,j}$.

Therefore, the complete mathematical model consists of the coupled problems (2.80) and (2.81), where the unknown solutions are the concentrations c_i^l, c_i^f, c_i^b, $i = 1, \ldots, N_{l-s}$.

We recall that this model can be used to forecast the extraction of an arbitrary number of chemical substances, and also for the prediction of the extraction efficiency. In the latter case we have $N_{l-s} = 1$. Thus, we are assuming a common behavior for the different chemical substances. Note that this agrees with the aim of calculation of the EY, i.e., the total amount of extracted substances.

The mass conservation principle asserts that the total mass of the system must be conserved, i.e., it must be constant during the percolation process, or equivalently its time rate of change must be null. More precisely, the total mass is given by the sum of the mass $\mathcal{M}^l$ of the dissolved chemical species in the liquid phase, the mass $\mathcal{M}^i$ of the species not yet dissolved in the solid phase, and the mass $\mathcal{M}^{\text{cup}}$ of the dissolved substances already dropped into the cup. The total amount $\mathcal{M}^l$ of

dissolved substances in the liquid phase at time t is given by:

$$\mathcal{M}^l = \pi R_0^2 \int_0^L (1-\phi) c^l dz. \tag{2.83}$$

Differentiating (2.83) with respect to time, substituting the governing equation of problem (2.80), evaluating the integral over each term and exploiting the boundary conditions in (2.80), we obtain:

$$\frac{d\mathcal{M}^l}{dt} = -\pi R_0^2 q c^l|_{z=L} + \pi R_0^2 \int_0^L \left(b^f G^f + b^b G^b\right) dz. \tag{2.84}$$

The total amount $\mathcal{M}^s$ of substances within the grain of type s, at time t, is given by:

$$\mathcal{M}^s = \pi R_0^2 \int_0^L \frac{b^s}{4\pi (a^s)^2} \int_0^{a^s} 4\pi c^s r^2 dr dz, \qquad s = f, b. \tag{2.85}$$

In particular, $\dfrac{b^s}{4\pi(a^s)^2}$ represents the number of particles of type s per volume inside the cake. Moreover, in (2.85) the integral with respect to the variable r is the total solid concentration within the particles of type s. Differentiating (2.85) with respect to time, exploiting the governing equation of problem (2.81), and using its boundary conditions, we have:

$$\frac{d\mathcal{M}^s}{dt} = -\pi R_0^2 \int_0^L b^s G^s dz. \tag{2.86}$$

So, considering the sum of (2.84) and (2.86), for both fines and boulders, we obtain:

$$\frac{d}{dt}(\mathcal{M}^l + \mathcal{M}^f + \mathcal{M}^b) = -\pi R_0^2 q c^l\big|_{z=L}.$$

Since the model (2.80),(2.81) has to obey the mass conservation principle, we have

$$\frac{d\mathcal{M}^{\text{cup}}}{dt} = \pi R_0^2 q c^l\big|_{z=L}. \tag{2.87}$$

where $\mathcal{M}^{\text{cup}}$ is the mass of dissolved substances dropped into the cup. By integrating Eq. (2.87) with respect to time, and exploiting the initial condition of system (2.80) we have:

$$\mathcal{M}^{\text{cup}} = \pi R_0^2 q \int_0^t c^l(L, s) ds. \tag{2.88}$$

In particular, let $\bar{\mathcal{M}}^{\text{cup}} = \mathcal{M}^{\text{cup}}|_{t=\tau}$ be the mass of the total chemicals in cup at $t = \tau$, i.e., at the end of the extraction. In addition, let $\mathcal{M}^{\text{in}}$ be the mass of dry ground coffee powder in the filter basket, we have:

$$\mathcal{M}^{\text{in}} = \phi\rho\pi R_0^2 L, \tag{2.89}$$

where ρ is the coffee grain density. Furthermore, we recall that the EY is defined as the ratio between the mass of the total dissolved substances inside the cup and the mass of the dry ground coffee, i.e.:

$$\begin{aligned} EY &= \frac{\bar{\mathcal{M}}^{\text{cup}}}{\mathcal{M}^{\text{in}}} \\ &= \frac{q}{\phi\rho L}\int_0^\tau c^l(L,t)dt, \end{aligned} \tag{2.90}$$

where formulas (2.88),(2.89) have been used. Finally, once the solution of problem (2.80)-(2.81) is obtained, the EY can be calculated exploiting formula (2.90).

Chapter 3

Numerical methods for differential equations

The espresso extraction models presented in Sections 2.3 and 2.4do not have an explicit analytic solution, so, we need some numerical methods that allows us to determine an approximate solution of the corresponding continuous problems.

We recall that a PDE (cf. Chapter 1) relates the unknown function of several independent variables, with its partial derivatives. For example

$$\sum_{i,j=1}^{d} a_{i,j}(\boldsymbol{x})\frac{\partial^2 u}{\partial x_i \partial x_j} + \sum_{i=1}^{n} b_i(\boldsymbol{x})\frac{\partial u}{\partial x_i} + c(\boldsymbol{x})u = f(\boldsymbol{x}), \tag{3.1}$$

is a second order partial differential equation, in the unknown $u : \Omega \to \mathbb{R}$, where $\boldsymbol{x} \in \Omega \subseteq \mathbb{R}^d$.

In general, it is not always possible to determine, with analytical methods, a solution of a differential equation, since the known analytical methods are of limited applicability. Furthermore, even knowing the general integral, this does not mean that a particular solution can then be determined; in fact, in order to identify this solution, it is necessary to assign boundary conditions on u (and / or on its derivatives) at the boundary of the domain Ω. Therefore, the theoretical study of such equations often concerns only with the existence and uniqueness of the solution. Thus, it is clear the importance of having numerical methods that allows the construction of approximate problems (of finite dimension N) whose solution

u_N is an approximation of the exact solution u of the continuous problem.

In the following of this chapter we present different numerical methods for the solution of PDE. Here we recall some general features common to all methods. Let $\mathcal{P}(u, g) = 0$ denotes a boundary value problem, composed of a PDE and boundary conditions, in the unknown function u, and depending on the set of data g. We recall that a problem is said to be *well-posed* if it admits a unique solution which continuously depends on the data; in the following we always restrict our attention to well-posed problems. In addition, let $\mathcal{P}_N(u_N, g_N) = 0$ denotes an approximation of $\mathcal{P}(u, g) = 0$ with some numerical method, whose solution is u_N, and depending on the approximation g_N of the data set g. If both problems admit a unique solution, we have: $u = u(g)$ and $u_N = u_N(g_N)$. In addition, let $||\cdot||$ denotes some suitable norm, a numerical method is said to be *convergent* if the numerical solution converges to the exact solution, that is, if

$$||u - u_N|| \to 0 \text{ for } N \to \infty.$$

In particular, the method is convergent if and only if:

$$\forall \varepsilon > 0 \ \exists N_\varepsilon < 0, \ \exists \delta_{\varepsilon, N_\varepsilon} \text{ such that } \forall N > N_\varepsilon, \ \forall g_N : ||g - g_N|| < \delta_{\varepsilon, N_\varepsilon},$$

$$||u(g) - u_N(g_N)|| \leq \varepsilon,$$

where the norm used for the solutions may be different from the one used for the data. Verifying the convergence of a numerical method may not be easy. Usually, it is better to move on to verifying its consistency and stability properties. In particular, a numerical method is said to be *consistent* if the numerical scheme tend to the differential equation, i.e., if

$$\mathcal{P}_N(u, g) \to 0 \text{ for } N \to \infty,$$

or equivalently if

$$\mathcal{P}_N(u, g) - \mathcal{P}(u, g) \to 0 \text{ for } N \to \infty.$$

Moreover, let $u_N + \delta u_N$ be the solution of the problem $\mathcal{P}_N(u_N + \delta u_N, g_N + \delta g_N) = 0$ with perturbed data. The numerical method is said to be *stable* if small perturba-

tions on the data induce small variations of the solution, that is:

$$\forall \varepsilon > 0 \ \exists \delta_\varepsilon > 0 \text{ such that } \forall ||\delta g_N|| < \delta_\varepsilon \Rightarrow ||\delta u_N|| < \varepsilon, \ \forall N.$$

As already mentioned, the convergence property is usually the most difficult to verify by direct analysis. However, for consistent schemes applied to linear well-posed initial value problems, the Lax-Richtmyer Equivalence Theorem states that a numerical method is stable if and only if it is convergent. A rigorous proof of this theorem for such a kind of problems is available in [58] and [59].

This chapter is organized as follows. In Section 3.1 we introduce the finite difference method (FDM), which allows the solution of a differential equation by approximating the derivatives with finite difference ratios. FDM has application in many different areas of applied science; in [60], [61] is applied for the solution of the diffusion equation, in [62], is used for the approximation of the gas dynamics equations and in [63] is applied to the equations of continuum mechanics.

In Section 3.2 we present the Galerkin Method and the finite element basis. Galerkin Method is a popular classical finite element method (FEM) for approximating initial-boundary value problems. Its fields of application are multiple, from computational fluid dynamics [33] to medicine [64], [65].

Then, in Section 3.3 we deal with Radial Basis Functions (RBFs) and their properties, focusing our attention to their applications in PDEs discretisation using collocation method in Section 3.3.1. RBFs are powerful tools in applied mathematics. This is a meshfree method having application in many different areas of applied science and engineering. In particular, RBFs are useful in functions approximation, and in the solution of many engineering problems [66], including applications in image processing [67], [68]. In addition, they are a suitable tool for scattered data interpolation problems [69], machine learning techniques [70], solution of differential equations [71], and other applications [66].

3.1 Finite Difference Method

The *finite difference method* transforms a partial differential equation in an algebraic system having a finite number of equations and unknowns. In particular, the derivatives of a function $f(x)$ on the point x are approximated by an expression involving only a finite set of values of the function in a neighbourhood of such a point.

Let $f : [a, b] \to \mathbb{R}$ be a sufficiently regular function, let us suppose $f \in C^4([a, b])$, in such a way that simple convergence results for the finite difference method are guaranteed. If we consider for the function f the Taylor formula at the point x until the second order, we have:

$$f(x+h) = f(x) + hf'(x) + \frac{h^2}{2}f''(x) + O(h^3),\ h \to 0, \tag{3.2}$$

and similarly:

$$f(x-h) = f(x) - hf'(x) + \frac{h^2}{2}f''(x) + O(h^3),\ h \to 0, \tag{3.3}$$

where $O(\cdot)$ is the Landau symbol. Subtracting the (3.3) from (3.2) we get:

$$f(x+h) - f(x-h) = 2hf'(x) + O(h^3), \tag{3.4}$$

from which we have:

$$f'(x) = \frac{f(x+h) - f(x-h)}{2h} + O(h^2). \tag{3.5}$$

Similarly, from the Taylor formula at the point x until the third order, we have:

$$f(x+h) = f(x) + hf'(x) + \frac{h^2}{2}f''(x) + \frac{h^3}{3!}f'''(x) + O(h^4),\ h \to 0, \tag{3.6}$$

and similarly:

$$f(x-h) = f(x) - hf'(x) + \frac{h^2}{2}f''(x) - \frac{h^3}{3!}f'''(x) + O(h^4),\ h \to 0, \tag{3.7}$$

If we sum the (3.6) and (3.7) we get:

$$f''(x) = \frac{f(x+h) - 2f(x) + f(x-h)}{h^2} + O(h^2). \tag{3.8}$$

Our aim is to approximate the derivative of a function f in the given interval $[a, b]$, thus, we define a partition of $[a, b]$, of step $h = \dfrac{b-a}{N}$ i.e., the set of $N+1$ nodes $\{x_n\}_{n=0,1,\ldots,N}$, such that $x_0 = a$, $x_N = b$ and $x_{n+1} = x_n + h$, $n = 0, 1, \ldots, N-1$. We denote with u_n the approximation of $f(x_n)$, i.e.: $u_n \approx f(x_n)$, $n = 0, 1, \ldots, N$. With this notation and from formula (3.5), for $n = 1, \ldots, N-1$ we can express the approximation u'_n of the derivative of f calculated in the point x_n as:

$$u'_n = \frac{u_{n+1} - u_{n-1}}{2h}, \tag{3.9}$$

that is called *centered finite difference*. The truncation error made in the approximation (3.9) corresponds to the remainder terms in formula (3.5), so it is given by $O(h^2)$. Thus formula (3.9) is second-order accurate.

Similarly, from formula (3.8), for $n = 1, \ldots, N-1$ we can express the approximation u''_n of the second derivative of f calculated in the point x_n as:

$$u''_n = \frac{u_{n+1} - 2u_n + u_{n-1}}{h^2}, \tag{3.10}$$

that is called *centered second finite difference*, again it is affected by a truncation error given by $O(h^2)$, thus it is second-order accurate. Finally, we note that in case of a multivariate function an analogous approach can be used to approximate the partial derivatives of this function, see [72] for a detailed discussion.

3.1.1 Approximation of a boundary value problem

We describe the use of finite difference quotients in the numerical solution of the linear boundary value problem:

$$\begin{cases} -f''(x) + p(x)f'(x) + q(x)f(x) = r(x), \quad x \in (a, b) \\ a_0 f(a) - a_1 f'(a) = \alpha \\ b_0 f(b) + b_1 f'(b) = \beta, \end{cases} \tag{3.11}$$

where $p, q, r \in C([a, b])$ and exists some positive constants P^*, Q_*, Q^* such that:

$$|p(x)| \leq P^*, \quad Q_* \leq q(x) \leq Q^*, \quad x \in [a, b], \tag{3.12}$$

we also suppose that $a_0a_1 \geq 0, b_0b_1 \geq 0$ and at least one of the constant a_0, b_0 is non-zero, suppose $a_0 \neq 0$. These conditions ensure the existence and the uniqueness of the solution of (3.11), see [73], pag. 19.

Let us consider a uniform partition of the interval $[a, b]$:

$$x_n = a + nh, \qquad n = -1, 0, 1, \ldots, N, N+1, \qquad h = \frac{b-a}{N}, \tag{3.13}$$

where x_{-1}, x_{N+1} are auxiliary points outside the interval.

We want to approximate the boundary-value problem (3.11) by an auxiliary problem on the discrete function $\{u_n\}_{-1 \leq n \leq N+1}$. For this purpose, for $n = 0, 1, \ldots, N$ we consider the approximation of the first and second derivatives of f by finite different ratios (3.9) and (3.10). Thus, for $x = x_n$, we have:

$$-\frac{u_{n+1} - 2u_n + u_{n-1}}{h^2} + p(x_n)\frac{u_{n+1} - u_{n-1}}{2h} + q(x_n)u_n = r(x_n) \quad n = 0, \ldots, N. \tag{3.14}$$

Multiplying by $\dfrac{h^2}{2}$, we have:

$$\begin{aligned} \left(p(x_n)\frac{h}{4} - \frac{1}{2}\right)u_{n+1} + \left(q(x_n)\frac{h^2}{2} + 1\right)u_n + \left(-p(x_n)\frac{h}{4} - \frac{1}{2}\right)u_{n-1} \\ = r(x_n)\frac{h^2}{2} \qquad\qquad n = 0, \ldots, N. \end{aligned} \tag{3.15}$$

For the boundary conditions, i.e. for $n = 0$ and $n = N$, we have:

$$\begin{cases} a_0u_0 - a_1\dfrac{u_1 - u_{-1}}{2h} = \alpha \\ b_0u_N + b_1\dfrac{u_{N+1} - u_{N-1}}{2h} = \beta, \end{cases} \tag{3.16}$$

So (3.11) can be approximated by the finite difference scheme of $N + 3$ equations in $N + 3$ unknowns $u_{-1}, u_0, u_1, \ldots, u_N, u_{N+1}$:

$$\begin{cases} \left(p(x_n)\dfrac{h}{4} - \dfrac{1}{2}\right)u_{n+1} + \left(q(x_n)\dfrac{h^2}{2} + 1\right)u_n + \left(-p(x_n)\dfrac{h}{4} - \dfrac{1}{2}\right)u_{n-1} \\ \qquad\qquad = r(x_n)\dfrac{h^2}{2} \qquad n = 0, \ldots, N \\ a_0u_0 - a_1\dfrac{u_1 - u_{-1}}{2h} = \alpha \\ b_0u_N + b_1\dfrac{u_{N+1} - u_{N-1}}{2h} = \beta. \end{cases} \tag{3.17}$$

From (3.17) it is possible to obtain a finite difference scheme of $N+1$ equations in $N+1$ unknowns $u_0, u_1, \ldots, u_N$ by replacing the value of u_{-1} and u_{N+1}, obtained from (3.16), in the first equation, i.e. the one for $n=0$, and in the last one, i.e. the one for $n=N$, respectively. Thus we obtain the following linear system:

$$A\mathbf{u} = \mathbf{r}, \tag{3.18}$$

where $\mathbf{u} = (u_0, u_1, \ldots, u_N)^T$,
$\mathbf{r} = \dfrac{h^2}{2}(r(x_0), \ldots, r(x_N))^T + \left(\dfrac{h}{a_1}\alpha\Big[1 + \dfrac{h}{2}p(x_0)\Big], 0, \ldots, 0, \dfrac{h}{b_1}\beta\Big[1 + \dfrac{h}{2}p(x_N)\Big]\right)^T$,

$$A = \begin{pmatrix} d_0 & c_0 & 0 & \cdots & \cdots & \cdots & 0 \\ e_1 & d_1 & c_1 & 0 & \cdots & \cdots & 0 \\ 0 & \ddots & \ddots & \ddots & & & \vdots \\ \vdots & & \ddots & \ddots & \ddots & & \vdots \\ \vdots & & & \ddots & \ddots & \ddots & 0 \\ 0 & \cdots & \cdots & 0 & e_{N-1} & d_{N-1} & c_{N-1} \\ 0 & \cdots & \cdots & \cdots & 0 & e_N & d_N \end{pmatrix}, \tag{3.19}$$

$$c_n = \begin{cases} -1, & n = 0, \\ -\dfrac{1}{2}\Big[1 - \dfrac{h}{2}p(x_n)\Big], & n = 1, \ldots, N-1, \end{cases} \tag{3.20a}$$

$$d_n = 1 + \frac{h^2}{2}q(x_n) + \begin{cases} h\dfrac{a_0}{a_1}\Big[1 + \dfrac{h}{2}p(x_0)\Big], & n = 0, \\ 0, & n = 1, \ldots, N-1, \\ h\dfrac{b_0}{b_1}\Big[1 - \dfrac{h}{2}p(x_N)\Big], & n = N, \end{cases} \tag{3.20b}$$

$$e_n = \begin{cases} -\dfrac{1}{2}\Big[1 + \dfrac{h}{2}p(x_n)\Big], & n = 1, \ldots, N-1, \\ -1, & n = N. \end{cases} \tag{3.20c}$$

Obviously this finite difference scheme holds only if $a_1 \neq 0$ and $b_1 \neq 0$.
Can be verified that the tridiagonal matrix A is non-singular and the following result holds:

Theorem 4. *Let p, q be two functions satisfying the condition* (3.12)*, we also suppose that $a_0 a_1 \geq 0, b_0 b_1 \geq 0$ and $|a_0| + |b_0| \neq 0$. Let h be the discretization step of the finite difference scheme* (3.17) *such that $h < \frac{2}{P^*}$. Then the finite difference scheme* (3.17) *has a unique solution.*

Proof. See [73], pag. 96. □

Finally, we note that this procedure can be generalised with analogous arguments also in the case of PDE, as illustrated in [72].

3.2 The Galerkin Method

Given an initial-boundary value problem, composed of a partial differential equation and initial/boundary conditions the Galerkin method requires a different formulation of the problem. Thus, instead of looking for the classical solution, we have to define the so-called *weak solution*, having in principle lower regularity properties. These solutions naturally belong to Sobolev spaces, which are very extensive spaces of functions, widely used in functional analysis and characterized by weak derivatives, rather than derivatives understood in the classical sense. Moreover, important advantages of the weak formulation are that problems derived from physical applications with non-smooth data can be taken into account

In this Section we deep in the Galerkin finite element method, a classical technique for the discretisation of PDEs. In particular, we face the discretisation of an abstract boundary value problem in Section 3.2.1. Then, in Section 3.2.2 we also present time discretisation for initial boundary value problems. Finally, in Section 3.2.3 we provide some basic features of the finite element approximation.

3.2.1 Approximation of a boundary value problem

We consider the following boundary value problem

$$\begin{cases} \mathcal{L}u = f, & \text{in } \Omega, \\ \mathcal{B}u = 0, & \text{on } \partial\Omega^*, \end{cases} \tag{3.21}$$

where $\Omega \subseteq \mathbb{R}^d$, $d = 2, 3$, is a bounded open set, whose boundary is $\partial\Omega$ and $\partial\Omega^* \subseteq \partial\Omega$ (possibly the whole boundary). We denoted with $\mathcal{L}$ a linear differential operator, with $\mathcal{B}$ an affine boundary operator and with f a given function. Most often, $\mathcal{L}$ is an unbounded operator in a space H that can be either $L^2(\Omega)$ or the weighted Hilbert space $L^2_w(\Omega) \coloneqq \left\{ g : \Omega \to \mathbb{R} \;\middle|\; \int_\Omega g^2(\boldsymbol{x}) w(\boldsymbol{x}) d\boldsymbol{x} < \infty \right\}$. The unknown solution u is searched in a subspace $X \subset H$, where H is an Hilbert space and the operators $\mathcal{L}$, $\mathcal{B}$ can be defined for functions belonging to X.

Problem (3.21) can be reformulated in its *weak form*. This can be obtained by multiplying the differential equation by a suitable set of test functions v and integrating over the whole domain. In this procedure, to reduce the order of differentiation of the solution u, the following integration by parts formula is definitely useful

$$\int_\Omega \frac{\partial u}{\partial x_i} v d\boldsymbol{x} = -\int_\Omega u \frac{\partial v}{\partial x_i} d\boldsymbol{x} + \int_{\partial\Omega} uvn_i d\gamma, \qquad i = 1, \ldots, d, \tag{3.22}$$

where $\mathbf{n} = (n_1, \ldots, n_d)$ denotes the outward unit normal vector on $\partial\Omega$. Solutions of the weak formulation are not required to solve equations in system (3.21) pointwise, but they have to solve the aforementioned integral equation for every $v \in X$. Such a formulation is convenient to define approximation methods, such as the Galerkin method.

As a result, the weak formulation of system (3.21) is:

$$\text{find } \tilde{u} \in W \text{ such that } \mathcal{A}(\tilde{u}, v) = \mathcal{F}(v), \qquad \text{for all } v \in V, \tag{3.23}$$

where W is the space of admissible solutions and V is the space of test functions, both can be considered to be Hilbert spaces; $\mathcal{A}(\cdot, \cdot)$ is the bilinear form obtained by the operator $\mathcal{L}$ and the above mentioned integration; $\mathcal{F} \in V'$, where V' is the dual space of V, thus $\mathcal{F}$ is a linear functional on V that accounts for the right-hand side f and for possible non-homogeneous boundary terms. In fact, boundary conditions on u can be enforced in two ways: they can be included in the definition of the space W, and they are called *essential*; or they can be applied while transforming the problem into its weak form, yielding suitable expressions for $\mathcal{A}$ and $\mathcal{F}$, in such a case they are called *natural*.

The existence and uniqueness of the solution to (3.23) if $W = V$ is guaranteed by the Lax-Milgram Theorem, under proper hypothesis for the bilinear form $\mathcal{A}$. Instead, in the more general case $W \neq V$, the existence and uniqueness are guaranteed by an extension of the Lax-Milgram Theorem. A complete presentation of these results can be found in [74]. Now, we turn into the numerical approximation of problem (3.23). Let $h > 0$ be a discretisation parameter (for example the mesh spacing) and

$$\{V_h : h > 0\}$$

be a family of finite dimensional subspaces of V. Suppose that, for all $v \in V$,

$$\inf_{v_h \in V_h} ||v - v_h|| \to 0, \qquad \text{as } h \to 0, \tag{3.24}$$

meaning that, as h becomes smaller, every function belonging to V can be well approximated with some function in V_h. Thus, if $W = V$, the Galerkin approximation to (3.23) is:

$$\text{find } u_h \in V_h \text{ such that } \mathcal{A}(u_h, v_h) = \mathcal{F}(v_h), \qquad \text{for all } v_h \in V_h. \tag{3.25}$$

For the analysis of problem (3.25), we have the following theorem.

Theorem 5. *Let V be a real Hilbert space, endowed with the norm $||\cdot||$, $\mathcal{A}(w, v) : V \times V \to \mathbb{R}$ a bilinear form and $\mathcal{F}(v) : V \to \mathbb{R}$ a linear continuous functional. Assume moreover that $\mathcal{A}$ is continuous, i.e. there exists $\gamma > 0$ such that:*

$$|\mathcal{A}(w, v)| \leq \gamma ||w||\, ||v||, \quad \text{for all } w, v \in V,$$

and coercive, i.e. there exists $\alpha > 0$ such that:

$$\mathcal{A}(v, v)| \geq \alpha ||v||^2, \quad \text{for all } v \in V.$$

Then, there exists a unique solution u_h to (3.25), which furthermore is stable since

$$||u_h|| \leq \frac{||\mathcal{F}||_{V'}}{\alpha}.$$

Moreover, if u is the solution to (3.23) with $W = V$, it follows

$$||u - u_h|| \leq \frac{\gamma}{\alpha} \inf_{v_h \in V_h} ||u - u_h||,$$

hence u_h converges to u, as $h \to 0$.

Let $\{\phi_j\}_{1\leq j\leq N_h}$ be a basis for the vector space V_h. Then, any function u_h in V_h admits a representation over this basis as follows

$$u_h(\boldsymbol{x}) = \sum_{j=1}^{N_h} \xi_j \phi_j(\boldsymbol{x}),$$

and choosing the basis functions ϕ_j also as test functions v_h and using linearity, we obtain a linear system of N_h equations in N_h unknowns, i.e.:

$$A\boldsymbol{\xi} = \boldsymbol{F}, \tag{3.26}$$

where $\boldsymbol{\xi} = (\xi_j), \boldsymbol{F} = (\mathcal{F}(\phi_j))$, and A is the *stiffness matrix* whose entries are $A_{ij} = \mathcal{A}(\phi_j, \phi_i)$, $i, j = 1, \ldots, N_h$..

The Galerkin method has been defined for the case in which $W = V$. However, if some constraint requires to keep the two spaces different, then the Petrov-Galerkin method can be defined in similar way.

3.2.2 Approximation of an initial boundary value problem

Now, we turn our attention to time-dependent problems. We consider the following initial boundary value problem

$$\begin{cases} \dfrac{\partial u}{\partial t} + \mathcal{L}u = f, & \text{in } (0,\bar{t}) \times \Omega, \\ \mathcal{B}u = 0, & \text{on } (0,\bar{t}) \times \partial\Omega^*, \\ u = u_0, & \text{on } \Omega, \text{ for } t = 0, \end{cases} \tag{3.27}$$

where $\bar{t} > 0$ is the observation time, $u \in H$, u and f are functions of the space variables $\boldsymbol{x}$, and the time variable t, $u_0 = u_0(\boldsymbol{x})$ is the initial datum, the operators $\mathcal{L}$, $\mathcal{B}$, defined as in problem (3.21), may depend on t. For each Hilbert space W, H with norm $||\cdot||_W, |||\cdot||_H$, respectively, we define the following spaces:

$$L^2(0,\bar{t};W) = \left\{ v : (0,\bar{t}) \to W : v \text{ is measurable and } \int_0^{\bar{t}} ||v(t)||_W^2 dt < \infty \right\},$$

$$C^0([0,\bar{t}];H) = \left\{ v : [0,\bar{t}] \to H : v \text{ is continuous and } ||v(t)||_H < \infty \right\}.$$

With the same procedure already described for problem (3.21), we suppose that problem (3.27) has a unique solution that can be computed by the weak formulation of problem (3.27): find $\tilde{u} \in L^2(0,\bar{t};W) \cap C^0([0,\bar{t}];H)$ such that

$$\frac{d}{dt}(\tilde{u}(\boldsymbol{x},t),v) + \mathcal{A}(\tilde{u}(\boldsymbol{x},t),v) = \mathcal{F}(t,v), \qquad \text{for all } v \in V, \tag{3.28}$$

and $\tilde{u} = u_0$ at $t = 0$, where $\mathcal{A}(\cdot,\cdot)$ is a bilinear form that corresponds to the operator $\mathcal{L}$ and $\mathcal{F} \in V'$.

The numerical approximation of problem (3.28) must be performed both in space and in time. First, we deal with the time discretisation. We divide the time interval $[0,\bar{t}]$ in N_t subintervals of length $\Delta t = \dfrac{\bar{t}}{N_t} : [t_n, t_{n+1}], n = 0,\dots,N_t - 1$. A possible method to obtain the time discretisation is the finite difference scheme, which consists in replacing the time derivative with a quotient obtained from the Taylor expansion of u, see Section 3.1 or [72]. The basic idea is illustrated on the following Cauchy problem

$$\begin{cases} \dfrac{dy}{dt} = \psi(t,y(t)), \quad t \in (0,\bar{t}), \\ y(0) = y_0, \end{cases} \tag{3.29}$$

where ψ is a continuous function from $[0,\bar{t}] \times \mathbb{R}$ in $\mathbb{R}$ which is also Lipschitz continuous with respect to y, uniformly in $t \in [0,\bar{t}]$. There are many possible finite difference schemes with different order of accuracy, however, we limit our interest on the *θ-scheme*, which is probably the most used. The Cauchy problem (3.29) discretised by means of the θ-scheme becomes

$$\frac{1}{\Delta t}(y^{n+1} - y^n) = \theta\psi(t_{n+1}, y^{n+1}) + (1-\theta)\psi(t_n, y^n),$$

for $n = 0,\dots,N_t - 1$, with $y^0 = y_0$ and y^n approximation of $y(t_n)$. The choice for the parameter θ must fall in $[0,1]$; the extreme cases, $\theta = 0$ and $\theta = 1$, define the well-known explicit forward and implicit backward Euler schemes, respectively, which are first order accurate with respect to the time step Δt; the scheme with $\theta = 1/2$ is known as the Crank-Nicolson scheme, which is potentially second order accurate; for any value of $\theta \neq 0$, the scheme is implicit.

The θ-scheme applied to (3.28), together with the Galerkin method for spatial discretisation, gives the following fully discrete problem: for each $n = 0, \ldots, N_t - 1$ find $u_h^{n+1} \in V_h$ such that

$$\frac{1}{\Delta t}(u_h^{n+1} - u_h^n, v_h) + \mathcal{A}\left(\theta u_h^{n+1} + (1-\theta)u_h^n, v_h\right) = \theta\mathcal{F}(t_{n+1}, v_h) + (1-\theta)\mathcal{F}(t_n, v_h), \qquad \text{for all } v_h \in V_h, \quad (3.30)$$

where we denote with u_h^n the approximation of $u(\boldsymbol{x}, t)$ at each time step n and by u_h^0 a convenient approximation to $u_0(\boldsymbol{x})$. To complete the discretisation procedure, we provide the algebraic restatement of (3.30) with the same basis definition made for (3.26). Setting

$$u_h^n(\boldsymbol{x}, t) = \sum_{j=1}^{N_h} \xi_j(t)\phi_j(\boldsymbol{x}), \qquad u_h^0(\boldsymbol{x}, 0) = \sum_{j=1}^{N_h} \xi_j^0\phi_j(\boldsymbol{x}),$$

the following system of N_h equations in N_h unknowns is obtained

$$M\boldsymbol{\xi}^{n+1} + \theta\Delta t A\boldsymbol{\xi}^{n+1} = \boldsymbol{\eta}^{n+1}, \qquad n = 0, \ldots, N_t - 1 \quad (3.31)$$

where $\boldsymbol{\xi}^{n+1} = (\xi_j^{n+1})$, in particular, $\boldsymbol{\xi}^0 = (\xi_j^0)$, $M_{ij} = (\phi_i, \phi_j)$, and

$$\boldsymbol{\eta}^{n+1} = \theta\Delta t F(t_{n+1}) + (1-\theta)\Delta t F(t_n) + M\boldsymbol{\xi}^n - (1-\theta)\Delta t A\boldsymbol{\xi}^n,$$

for $j = 1, \ldots, N_h, n = 0, \ldots, N_t - 1$. The stiffness matrix A is the same as that introduced in the steady case, unless it depends on t that happens when the operator $\mathcal{L}$ in (3.27) is time-dependent. The same argument holds for the vector F with respect to the operator $\mathcal{B}$ in (3.27). The symmetric and positive-definite matrix M, which is always time-independent, is called *mass matrix*. Finally, we note that the order in which spatial and temporal discretisation are applied is not relevant for the purposes of the final algebraic system.

3.2.3 The Finite Element Method

In the previous sections we have defined the Galerkin method to discretise with respect to space variables both steady and time-dependent problems, as well as

the finite difference θ-scheme to discretise with respect to time when necessary. Although the Galerkin method can work well with a generic Riesz basis of the Hilbert space H, this method becomes particularly efficient when a finite element basis is employed. Thus, in the following of this section, we present the main properties of such base of functions: the existence of a triangulation of Ω, the construction of a finite dimensional subspace, and the existence of a basis of functions having small support with respect to the whole set Ω.

Triangulation

As usual, let $\Omega \subset \mathbb{R}^d, d = 2, 3$ be the domain. For the sake of simplicity, we restrict our discussion to domains with piecewise polygonal boundaries, i.e., $\bar{\Omega}$ can be exactly covered by a finite union of polyhedra. However, if the domain is not polygonal, it can always be approximated by a polygonal domain. In this case, the accuracy of this operation increases as the diameter of the polyhedra becomes smaller. We begin with a preliminary definition.

A *d-simplex* $\mathcal{K}$ is the convex envelope of $d+1$ points $\boldsymbol{a}_j \in \mathbb{R}^d, j = 1, 2, \ldots, d+1$, called vertices of $\mathcal{K}$, that are not all lying in the same hyperplane. It is the smallest convex passing through all these points. Consider the set $\mathcal{T}_h$ of non degenerated d-simplices $\mathcal{T}_h = \{\mathcal{K}_j : j = 1, 2, \ldots, N\}$. This is called *triangulation* or *triangular mesh* of $\bar{\Omega}$ if:

1. $\mathcal{K}_j \subset \bar{\Omega}, j = 1, \ldots, N$ and $\bar{\Omega} = \bigcup_{j=1}^{N} \mathcal{K}_j$;

2. for any two distinct simplices $\mathcal{K}_i, \mathcal{K}_j \in \mathcal{T}_h$, $\mathcal{K}_i \cap \mathcal{K}_j$ is a k-simplex, $0 \leq k \leq d-1$, such that all its vertices are also vertices of $\mathcal{K}_i$ and $\mathcal{K}_j$; in particular, $\overset{\circ}{\mathcal{K}}_i \cap \overset{\circ}{\mathcal{K}}_j = \emptyset$.

3. $diam(\mathcal{K}_j) \leq h$ for all $\mathcal{K}_j \in \mathcal{T}_h$, where $diam(\mathcal{K}_j)$ is the longest edge of $\mathcal{K}_j$.

Where h denotes the diameter of the triangulation.

This definition tells us that, in the space the intersection of two tetrahedra can be either empty, or reduced to a single common entity, such as a vertex, an edge or

a face. Such a mesh is often referred as *conforming mesh*. Its *vertices* or *nodes* are the vertices of the d-simplices $\mathcal{K}_j$ that form the mesh.

Piecewise polynomial spaces

The second basic property of a finite element method consists in determining a finite dimensional space that is a suitable approximation of the infinite dimensional space X to which the exact solution of the differential problem belongs. Such finite dimensional space is where the approximated solution is sought. To this end, we consider the set $\mathbf{\Pi}_m^d$ of the polynomials p with coefficients in $\mathbb{R}$ of degree less than or equal to m:

$$\mathbf{\Pi}_m^d = \left\{ p(\boldsymbol{x}) = \sum_{\substack{0 \le i_1,\dots,i_d \le m \\ i_1+\cdots+i_d \le m}} \alpha_{i_1\dots i_d} x_1^{i_1} \cdots x_d^{i_d}, \quad \alpha_{i_1\dots i_d} \in \mathbb{R}, \boldsymbol{x} = (x_1,\dots,x_d) \right\}.$$

Hence, in a three dimensional space we obtain

$$\mathbf{\Pi}_m^3 = \left\{ p(x_1,x_2,x_3) = \sum_{\substack{0 \le i,j,l \le m \\ i+j+l \le m}} \alpha_{ijl} x_1^i x_2^j x_3^l, \quad \alpha_{ijl} \in \mathbb{R} \right\}.$$

It can be verified that $\mathbf{\Pi}_m^d$ is a vector space of dimension

$$dim(\mathbf{\Pi}_m^d) = \binom{d+m}{m}. \tag{3.32}$$

Then, we can define the finite dimensional functional space X_h^m as

$$X_h^m = \left\{ v_h \in C^0(\bar{\Omega}) : v_h|_{\mathcal{K}_j} \in \mathbf{\Pi}_m \text{ for all } \mathcal{K}_j \in \mathcal{T}_h \right\}. \tag{3.33}$$

Such X_h^m is the desired approximation of X.

A triangular Lagrange finite element $\mathbf{\Pi}_m^d$ is locally defined by the triad $(\mathcal{K}, P_m, \Sigma_m)$, where:

1. $\mathcal{K}$ is a d- simplex associated with the triangulation $\mathcal{T}_h$,

2. P_m is a vector space of polynomials of degree less than or equal to m on $\mathcal{K}$,

3. Σ_m is the principal lattice of order m of the simplex $\mathcal{K}$.

The principal lattice of a d-simplex is a set made of a finite number of points belonging to the simplex $\mathcal{K}$. In particular, when $m = 1$, Σ_m is composed of the vertices of the simplex, when $m = 2$, it is composed of the vertices and the edge midpoints of the simplex. In addition, Σ_m is called the set of nodes corresponding to the degrees of freedom of the finite element $(\mathcal{K}, P_m, \Sigma_m)$.

Degrees of freedom and basis functions

A final necessary ingredient for the finite element method is to construct a basis for the space X_h^m in such a way that the basis functions are easy to be defined. An important aspect is the choice of a set of degrees of freedom on each d-simplex $\mathcal{K}$. We define the *degrees of freedom* associated with the d-simplex $\mathcal{K}$ as the number of values necessary to the function $v_h \in X_h^m$ for being uniquely determined in $\mathcal{K}$. The number of degrees of freedom is directly given by the dimension of the vector space $\mathbf{\Pi}_m^d$, reported in formula (3.32). Let us analyse few cases of special interest. If

$d = 2$ and

$m = 1$, $dim(\mathbf{\Pi}_1^2) = 3$, meaning that we have three degrees of freedom. Thus, we have to choose three values on each 2-simplex $\mathcal{K}$ that allow us to describe uniquely a function $v_h|_{\mathcal{K}}$. The simplest and usual choice is the values at the vertices of each $\mathcal{K}$. In addition, we note that such a choice satisfies the requirement of continuity of v_h in $\bar{\Omega}$.

$m = 2$, $dim(\mathbf{\Pi}_2^2) = 6$, thus the degrees of freedom are given by the number of the vertices and the middle points of each edge. Let us remark once again that this choice guarantees that $v_h \in C^0(\bar{\Omega})$, since the degrees of freedom on each edge uniquely identify the restriction of v_h on that edge, in fact, we have three values describing a quadratic function in one variable.

$d = 3$ and

$m = 1,\ dim(\mathbf{\Pi}_1^3) = 4$, thus a typical choice for the unique description of a function $v_h \in X_h^1$ is the values at the four vertices of each 3-simplex $\mathcal{K}$.

$m = 2,\ dim(\mathbf{\Pi}_2^3) = 10$, so the degrees of freedom are usually determined by the four vertices and the six middle points of the edges of each simplex $\mathcal{K}$.

Let us describe a procedure for the construction of a basis for X_h^m. We denote with $(\sigma_j)_{1\leq j\leq N_h}$ the global set of nodes in $\bar{\Omega}$, thus N_h accounts for the total number of degrees of freedom of $\mathbf{\Pi}_m^d$. It can be shown that the space X_h^m is a subspace of $H^1(\Omega)$ of finite dimension corresponding to N_h; Moreover, there exists a basis $\{\phi_i\}_{1\leq i\leq N_h}$ of X_h^m defined by

$$\phi_i(\sigma_j) = \delta_{ij}, \qquad i, j = 1, \ldots, N_h, \tag{3.34}$$

where δ_{ij} is the Kronecker function. Every function $v_h \in X_h^m$ can be uniquely written as

$$v_h(\boldsymbol{x}) = \sum_{i=1}^{N_h} v_h(\sigma_i)\phi_i(\boldsymbol{x}).$$

The basis functions ϕ_i are usually called *shape functions*. We note that the support of each shape function is small, in the sense that it is made of a few d-simplices of the triangulation $\mathcal{T}_h$. More precisely, the support of the shape function ϕ_i is made of the only d-simplices that share the node σ_i.

3.3 RBF Method

We exploit RBFs to solve the initial-boundary values problems predicting the espresso extraction of Sections 2.3, 2.4. Since solution of differential equations include function approximation as fundamental component, we begin our discussion about RBFs with the multivariate scattered data interpolation problem. The usual situation we have to face is the following: given a set of measurements, and the corresponding set of locations at which these measurements were achieved, we have to find a relation which allows us to obtain information also about other

locations. Thus, we have to find a function which is a "good" in some sense to fit the given data. This is called *data interpolation*, and if the locations do not lie on a regular grid, then it is called *scattered data interpolation*. More precisely, let $\mathcal{X} = \{\boldsymbol{x}_i\}_{i=1,2,\ldots,n}$, $\boldsymbol{x}_i \in \Omega \subseteq \mathbb{R}^d$ be the set of locations, usually called *data sites*, and let $\{f_i\}_{i=1,2,\ldots,n}$, $f_i \in \mathbb{R}$ the corresponding set of measurements, usually called *data values*. In addition, we assume that the data are obtained by sampling some unknown function f at the data sites, i.e., $f_i = f(\boldsymbol{x}_i)$, $i = 1, 2, \ldots, n$. The following discussion is restricted to scalar-valued data, however, it can be easily generalized to vector-valued data.

The interpolation problem consists in finding a continuous function $\tilde{f}$ such that $\tilde{f}(\boldsymbol{x}_i) = f_i,\ i = 1, 2, \ldots, n$. A usual approach to solve such a kind of problem is to assume the function $\tilde{f}$ is a linear combination of certain basis functions B_j, i.e.,

$$\tilde{f}(\boldsymbol{x}) = \sum_{j=1}^{n} \lambda_j B_j(\boldsymbol{x}), \qquad \boldsymbol{x} \in \mathbb{R}^d, \tag{3.35}$$

where λ_j are unknown coefficients which can be determined by imposing the interpolation conditions $\tilde{f}(\boldsymbol{x}_i) = f(\boldsymbol{x}_i)$, $i = 1, 2, \ldots, n$. This leads to the following linear system

$$A\boldsymbol{\lambda} = \boldsymbol{f},$$

where A is the interpolation matrix whose entries are given by $a_{ij} = B_j(\boldsymbol{x}_i)$, $i, j = 1, 2, \ldots, n$, $\boldsymbol{\lambda} = [\lambda_1, \lambda_2, \ldots, \lambda_m]^T$, and $\boldsymbol{f} = [f_1, f_2, \ldots, f_n]^T$. The interpolation problem is well-posed, i.e., a solution exists and it is unique, if and only if the matrix A is non-singular.

In the univariate case, i.e., $d = 1$, one can interpolate to n distinct data sites using a polynomial of degree $n - 1$. Unfortunately, the situation is not as favorable in the multivariate case.

Let the finite-dimensional linear function space $\mathcal{B} \subseteq C(\Omega)$ have a basis $\{B_1, B_2, \ldots, B_n\}$. Then $\mathcal{B}$ is an *Haar space* on Ω if

$$\det A \neq 0$$

for any set of distinct point $\{\boldsymbol{x}_1\boldsymbol{x}_2, \ldots, \boldsymbol{x}_n\}$ in Ω, where A denotes the matrix whose entries are $a_{ij} = B_j(\boldsymbol{x}_i)$·

Note that the existence of a Haar space guarantees the invertibility of the interpolation matrix A, i.e., the existence and uniqueness of an interpolant of the form (3.35). In the multivariate case the following theorem forbids the existence of Haar space of continuous functions of dimension greater than one.

Theorem 6 (Mairhuber-Curtis)**.** *If $\Omega \subset \mathbb{R}^d$, $d \geq 2$ contains an interior point, then there exist no Haar spaces of continuous functions on Ω except those of dimension one.*

Proof. See [75], [76]. □

The Mairhuber-Curtis Theorem tells us that for the interpolation problem of arbitrary scattered data in the multivariate case, i.e, $d \geq 2$, if we want to have a well-posed problem we can not decide before the set of basis functions we plan to use, instead we have to choose the basis functions to depend on the interpolation points. In some sense, RBFs give a solution to the problem arising from the Mairhuber-Curtis theorem.

A function $\Phi : \mathbb{R}^d \to \mathbb{R}$ is called *radial* if there exists a univariate function $\varphi : [0, \infty) \to \mathbb{R}$ such that:

$$\Phi(\boldsymbol{x}) = \varphi(||\boldsymbol{x}||),$$

where $|| \cdot ||$ denotes some norm on $\mathbb{R}^d$, usually the Euclidean norm.

Thus, we can use a RBF expansion to solve the interpolation problem (3.35). In particular, it becomes:

$$\tilde{f}(\boldsymbol{x}) = \sum_{j=1}^{n} \lambda_j \Phi(\boldsymbol{x} - \boldsymbol{x}_j) \equiv \sum_{j=1}^{n} \lambda_j \Phi_j(\boldsymbol{x}), \qquad \boldsymbol{x} \in \mathbb{R}^d. \tag{3.36}$$

If we think at $\Phi(\boldsymbol{x})$ as a function with center at the origin, for $j = 1, 2, \ldots, n$, the shifts $\Phi_j(\boldsymbol{x}) = \Phi(\boldsymbol{x} - \boldsymbol{x}_j)$ are functions centered at $\boldsymbol{x}_j$. For this reason we often call $\boldsymbol{x}_j$ a center. In particular, the radial basis function $\Phi_j(\boldsymbol{x})$ is said to be centered at x_j. As before, unknown coefficients λ_j in (3.36) can be determined by imposing the interpolation conditions $\tilde{f}(\boldsymbol{x}_i) = f(\boldsymbol{x}_i)$, $i = 1, 2, \ldots, n$. Thus, we have the following

linear system

$$\underbrace{\begin{pmatrix} \Phi_1(\boldsymbol{x}_1) & \dots & \Phi_n(\boldsymbol{x}_1) \\ \vdots & & \vdots \\ \Phi_1(\boldsymbol{x}_n) & \dots & \Phi_n(\boldsymbol{x}_n) \end{pmatrix}}_{A} \underbrace{\begin{pmatrix} \lambda_1 \\ \vdots \\ \lambda_n \end{pmatrix}}_{\boldsymbol{\lambda}} = \underbrace{\begin{pmatrix} f(\boldsymbol{x}_1) \\ \vdots \\ f(\boldsymbol{x}_n) \end{pmatrix}}_{\boldsymbol{f}}. \tag{3.37}$$

The interpolation problem is well-posed, if and only if the matrix A is non-singular. Therefore, now the question is for what kind of RBFs the matrix is non-singular. To this purpose, we recall that a positive definite matrix has all the eigenvalues positive, and therefore it is non-singular. Thus, if we consider a basis functions that can generate a positive definite interpolation matrix, we would always have a well-posed interpolation problem. To this aim let us introduce *positive definite function.*

A continuous function $\Phi : \mathbb{R}^d \to \mathbb{C}$ is called positive definite if for all $n \in \mathbb{N}$, all sets of pairwise distinct centers $\mathcal{X} = \{\boldsymbol{x}_1, \boldsymbol{x}_2, \dots, \boldsymbol{x}_n\} \subset \mathbb{R}^d$, and all $\boldsymbol{\lambda} \in \mathbb{C}^n$, we have

$$\sum_{i=1}^{n} \sum_{j=1}^{n} \lambda_i \bar{\lambda}_j \Phi(\boldsymbol{x}_i - \boldsymbol{x}_j) \geq 0.$$

The function is called *strictly positive definite* if the quadratic form is zero only for $\boldsymbol{\lambda} \equiv 0$. The previous definition of (strictly) positive definite functions is given for complex coefficients and complex-valued functions. The following theorem states the elementary properties of a positive definite function.

Theorem 7. *Let Φ be a positive definite function. The following properties are satisfied.*

1. $\Phi(0) \geq 0$.
2. $\Phi(-\boldsymbol{x}) = \overline{\Phi(\boldsymbol{x})}, \ \forall \ \boldsymbol{x} \in \mathbb{R}^d$,
3. *Any positive definite function is bounded. In fact:* $|\Phi(\boldsymbol{x})| < \Phi(0)$.
4. $\Phi(0) = 0$ *if and only if* $\Phi \equiv 0$.
5. *The product of (strictly) positive definite functions is (strictly) positive definite.*

6. *Non-negative finite linear combinations of positive definite functions are positive definite. If* $\Phi_1, \Phi_2, \ldots, \Phi_n$ *are positive definite on* $\mathbb{R}^d$ *and* $\lambda_j \geq 0$, $j = 1, 2, \ldots, n$, *then* $\Phi(\boldsymbol{x}) = \sum_{j=1}^{n} \lambda_j \Phi_j(\boldsymbol{x})$, $\boldsymbol{x} \in \mathbb{R}^d$,*is also positive definite. Moreover, if at least one of the* Φ_j *is strictly positive definite and the corresponding* $\lambda_j > 0$, *then* Φ *is strictly positive definite.*

Proof. See [76]. □

The previous Theorem 7 shows the elementary property of complex-valued positive definite function, however, in usual applications we concern with real-valued functions. From Theorem 7 it is clear that a positive definite function is real-valued if and only if it is even In addition, the following theorem characterizes real-valued strictly positive definite functions.

Theorem 8. *Let* $\Phi : \mathbb{R}^d \to \mathbb{R}$ *be a continuous function. Then* Φ *is strictly positive definite if and only if it is even and we have, for all* $n \in \mathbb{N}$, *for all* $\boldsymbol{\lambda} \in \mathbb{R}^n$, *and for all pairwise of distinct* $\boldsymbol{x}_1, \boldsymbol{x}_2, \ldots, \boldsymbol{x}_n$,

$$\sum_{i=1}^{n} \sum_{j=1}^{n} \lambda_i \lambda_j \Phi(\boldsymbol{x}_i - \boldsymbol{x}_j) \geq 0.$$

In addition, Φ *is strictly positive definite on* $\mathbb{R}^d$ *if the quadratic form is zero only for* $\boldsymbol{\lambda} \equiv 0$.

Proof. See [76]. □

Thus, to get a well-posed interpolation problem of kind (3.37) one can use positive definite functions. Unfortunately, not all the most popular radial basis functions fit into this characterisation. However, in the following we generalise the notion of positive definite functions to that of (strictly) conditionally positive definite functions of order m, in such a way we cover all the relevant choices for RBFs.

A complex-valued continuous function Φ is called *conditionally positive definite of order* m on $\mathbb{R}^d$ if for all $n \in \mathbb{N}$, all sets of pairwise distinct centers $\mathcal{X} =$

$\{\boldsymbol{x}_1, \boldsymbol{x}_2, \ldots, \boldsymbol{x}_n\} \subset \mathbb{R}^d$, and all $\boldsymbol{\lambda} \in \mathbb{C}^n$, satisfying

$$\sum_{j=1}^{n} \lambda_j p(\boldsymbol{x}_j) = 0$$

for any complex-valued polynomial p of degree at most $m-1$, we have

$$\sum_{i=1}^{n} \sum_{j=1}^{n} \lambda_i \bar{\lambda}_j \Phi(\boldsymbol{x}_i - \boldsymbol{x}_j) \geq 0.$$

The function Φ is called *strictly conditionally positive definite of order m* on $\mathbb{R}^d$ if the quadratic form is zero only for $\boldsymbol{\lambda} \equiv 0$.

An immediate observation is the following

Lemma 9. *A function that is (strictly) conditionally positive definite of order m on $\mathbb{R}^d$ is also (strictly) conditionally positive definite of any higher order. In addition, a (strictly) positive definite function is always (strictly) conditionally positive definite of any order.*

Proof. See [75]. □

As earlier, we can restrict ourselves to real-valued, even functions.

Theorem 10. *A real-valued continuous even function Φ is conditionally positive definite of order m on $\mathbb{R}^d$ if and only if for all $n \in \mathbb{N}$, all sets of pairwise distinct centers $\mathcal{X} = \{\boldsymbol{x}_1, \boldsymbol{x}_2, \ldots, \boldsymbol{x}_n\} \subset \mathbb{R}^d$, and all $\boldsymbol{\lambda} \in \mathbb{R}^n$, satisfying*

$$\sum_{j=1}^{n} \lambda_j p(\boldsymbol{x}_j) = 0$$

for any real-valued polynomial p of degree at most $m-1$, we have

$$\sum_{i=1}^{n} \sum_{j=1}^{n} \lambda_i \lambda_j \Phi(\boldsymbol{x}_i - \boldsymbol{x}_j) \geq 0.$$

In addition, Φ is strictly conditionally positive definite of order m on $\mathbb{R}^d$ if the quadratic form is zero only for $\boldsymbol{\lambda} \equiv 0$.

Sometimes there is the need to have an interpolant that can reproduces certain types of functions. For example when data are constant, or when they come from a linear function, then it would be desirable that also the interpolant has such properties. Moreover, when we have to face numerical solution of partial differential equations, sometimes it is important that the interpolant can reproduce linear functions. Thus, what we can do is to modify the interpolant by adding certain polynomials to the expansion (3.36), i.e., we can consider the following approximation of f:

$$\hat{f}(\boldsymbol{x}) = \sum_{j=1}^{n} \lambda_j \Phi_j(\boldsymbol{x}) + \sum_{j=1}^{M} \mu_j p_j(\boldsymbol{x}), \tag{3.38}$$

where $m \in \mathbb{N}$, $M = \begin{pmatrix} m-1+d \\ m-1 \end{pmatrix}$, and $\{p_j(\boldsymbol{x})\}_{j=1,2,\ldots,M}$ is a base of the M-dimensional linear space $\boldsymbol{\Pi}^d_{m-1}$ of polynomials in $\boldsymbol{x} \in \mathbb{R}^d$, with real coefficients, of degree at most $m-1$. The interpolation conditions $\hat{f}(\boldsymbol{x}_i) = f(\boldsymbol{x}_i)$, $i = 1, 2, \ldots, n$, leads to a system of n linear equations, but now we have $n + M$ unknowns, $\lambda_1, \lambda_2, \ldots, \lambda_n$, $\mu_1, \mu_2, \ldots, \mu_M$, so in order to ensure a unique solution we also require the polynomial basis $\{p_j(\boldsymbol{x})\}_{j=1,2,\ldots,M}$ to be orthogonal to the RBF coefficients $\boldsymbol{\lambda}$, i.e.:

$$\sum_{j=1}^{n} \lambda_j p_k(\boldsymbol{x}_j) = 0, \; k = 1, 2, \ldots, M. \tag{3.39}$$

As before, if we denote with $P_{ij} = p_j(\boldsymbol{x}_i)$ and $\boldsymbol{\mu} = (\mu_1, \mu_2, \ldots, \mu_M)^T$, imposing the interpolation conditions $\hat{f}(\boldsymbol{x}_i) = f(\boldsymbol{x}_i)$, $i = 1, 2, \ldots, n$, and the orthogonality conditions (3.39), we obtain:

$$\underbrace{\begin{pmatrix} A & P \\ P^T & 0 \end{pmatrix}}_{\hat{A}} \begin{pmatrix} \boldsymbol{\lambda} \\ \boldsymbol{\mu} \end{pmatrix} = \begin{pmatrix} \boldsymbol{f} \\ \boldsymbol{0} \end{pmatrix}, \tag{3.40}$$

whose solution, if $\hat{A}$ is invertible, is

$$\begin{pmatrix} \boldsymbol{\lambda} \\ \boldsymbol{\mu} \end{pmatrix} = \hat{A}^{-1} \begin{pmatrix} \boldsymbol{f} \\ \boldsymbol{0} \end{pmatrix}. \tag{3.41}$$

In the following, we refer to $\hat{A}$ as the polynomially augmented RBF (PA-RBF) interpolation matrix associated to the interpolation nodes $\boldsymbol{x}_i$, $i = 1, 2, \ldots, n$. The following theorem states that to guarantee the invertibility of $\hat{A}$ we have to require the matrix P to have full rank, or equivalently that the interpolation nodes $\boldsymbol{x}_1, \boldsymbol{x}_2, \ldots, \boldsymbol{x}_n$ has to be unisolvent for polynomials of degree $m-1$. We recall that, the set of points $\mathcal{X} = \{\boldsymbol{x}_1, \boldsymbol{x}_2, \ldots, \boldsymbol{x}_n\} \subseteq \mathbb{R}^d$ is said to be $(m-1)$-*unisolvent* if the only polynomial of total degree at most $m-1$ interpolating zero data on $\mathcal{X}$ is the zero polynomial.

Theorem 11. *Let Φ be a real-valued even function, strictly conditionally positive definite of order m on $\mathbb{R}^d$, if the points $\{\boldsymbol{x}_1, \boldsymbol{x}_2, \ldots, \boldsymbol{x}_n\}$ form an $(m-1)$-unisolvent set, then the system of linear equations* (3.40) *is uniquely solvable.*

Proof. See [75]. □

3.3.1 RBF Collocation

We consider the following boundary value problem

$$\begin{cases} \mathcal{L}u = f, & \text{in } \Omega, \\ u = g, & \text{on } \partial\Omega, \end{cases} \tag{3.42}$$

where $\Omega \subseteq \mathbb{R}^d$, is a bounded set, whose boundary is $\partial\Omega$. We denote with $\mathcal{L}$ a linear elliptic partial differential operator and with f and g given functions. For the sake of simplicity, we consider Dirichlet boundary conditions. We represent the approximate solution $\hat{u}$ by a RBF expansion analogous to that used for scattered data interpolation. In particular, for the following discussion we assume the interpolant of the form (3.38), since this is the form we use in the numerical simulations. However, an analogous approach can be used also in the case of an approximated solution with the form (3.36). In addition, for the same reason, we restrict ourselves to the case in which the set of the centers coincides with those of the *collocation points*, and we denote this set with $\mathcal{X} = \{\boldsymbol{x}_1, \boldsymbol{x}_2, \ldots, \boldsymbol{x}_n\}$.

Let us suppose that $\boldsymbol{u} = (u(\boldsymbol{x}_1), u(\boldsymbol{x}_2), \ldots, u(\boldsymbol{x}_n))^T$ and Theorem 11 holds, applying the operator $\mathcal{L}$ to $\hat{u}$, and using the following notation $\boldsymbol{a}(\boldsymbol{x})^{\mathcal{L}} = (\mathcal{L}\varphi_1(\boldsymbol{x}), \ldots, \mathcal{L}\varphi_n(\boldsymbol{x}))$,

$\boldsymbol{p}(\boldsymbol{x})^{\mathcal{L}} = (\mathcal{L}p_1(\boldsymbol{x}), \ldots, \mathcal{L}p_m(\boldsymbol{x}))$, we have:

$$\mathcal{L}\hat{u}(\boldsymbol{x}) = \underbrace{\begin{pmatrix} \boldsymbol{a}(\boldsymbol{x})^{\mathcal{L}} & \boldsymbol{p}(\boldsymbol{x})^{\mathcal{L}} \end{pmatrix}}_{\boldsymbol{b}(\boldsymbol{x})^{\mathcal{L}}} \begin{pmatrix} \boldsymbol{\lambda} \\ \boldsymbol{\mu} \end{pmatrix} = \boldsymbol{b}(\boldsymbol{x})^{\mathcal{L}} \hat{A}^{-1} \begin{pmatrix} \boldsymbol{u} \\ \boldsymbol{0} \end{pmatrix} = (\boldsymbol{b}(\boldsymbol{x})^{\mathcal{L}} \hat{A}^{-1})_{1:n} \boldsymbol{u}, \quad (3.43)$$

where in the second equality we exploited relation (3.41) for $\hat{u}$, and the notation $(\cdot)_{1:n}$ denotes the first n components of the vector $(\cdot)$. Therefore, equation (3.43) allows us to compute the action of the operator $\mathcal{L}$ on the function $\hat{u}$ at the point $\boldsymbol{x}$ as a linear combination of the values of u in the nodal points.

Let us split the n collocation points in $\mathcal{X}$ in n_I interior points collected in $\mathcal{X}_I$ and n_B boundary points collected in $\mathcal{X}_B$; i.e., $\mathcal{X} = \mathcal{X}_I \cup \mathcal{X}_B$ and $n = n_I + n_B$. In addition, we reorder the points in such a way that we have first all the n_I interior points and then all the n_B boundary points, this means that the vector $\boldsymbol{u}$ can be reordered as $\boldsymbol{u} = (\boldsymbol{u}_I, \boldsymbol{u}_B)^T$, where $\boldsymbol{u}_I = (u(\boldsymbol{x}_1), u(\boldsymbol{x}_2), \ldots, u(\boldsymbol{x}_{n_I}))$, and $\boldsymbol{u}_B = (u(\boldsymbol{x}_{n_I+1}), u(\boldsymbol{x}_{n_I+2}), \ldots, u(\boldsymbol{x}_n))$. The collocation problem is obtained by imposing the differential equation at the interior points $\mathcal{X}_I$ and the boundary condition at the boundary points $\mathcal{X}_B$. That is:

$$\begin{cases} \mathcal{L}\hat{u}(\boldsymbol{x_i}) = f(\boldsymbol{x}_i), & \boldsymbol{x}_i \in \mathcal{X}_I, \\ \hat{u}(\boldsymbol{x_i}) = g(\boldsymbol{x}_i), & \boldsymbol{x}_i \in \mathcal{X}_B. \end{cases} \quad (3.44)$$

Exploiting (3.43) the differential equation of problem (3.44) becomes:

$$(\boldsymbol{b}(\boldsymbol{x}_i)^{\mathcal{L}} \hat{A}^{-1})_{1:n} \boldsymbol{u} = f(\boldsymbol{x}_i), \qquad \boldsymbol{x}_i \in \mathcal{X}_I, \quad (3.45)$$

Let $\boldsymbol{f}$ be the vector containing the given function f evaluated at the interior points in $\mathcal{X}_I$. Similarly, let $\boldsymbol{g}$ be the vector containing the given function g evaluated at the boundary points in $\mathcal{X}_B$. Problem (3.44) written in matrix form is:

$$\begin{pmatrix} L \\ B \end{pmatrix} \boldsymbol{u} = \begin{pmatrix} \boldsymbol{f} \\ \boldsymbol{g} \end{pmatrix} \quad (3.46)$$

where $L \in \mathbb{R}^{n_I \times n}$ has rows $L_{i,:} = (\boldsymbol{b}(\boldsymbol{x}_i)^{\mathcal{L}} \hat{A}^{-1})_{1:n}$, $\boldsymbol{x}_i \in \mathcal{X}_I$, and $B \in \mathbb{R}^{n_B \times n}$, $B \equiv \left(\hat{A}\hat{A}^{-1}\right)_{n_I+1:n,1:n}$. Thus, if $\begin{pmatrix} L \\ B \end{pmatrix}$ is non singular, the collocation problem (3.46)

has a unique solution $\boldsymbol{u} = \begin{pmatrix} L \\ B \end{pmatrix}^{-1} \begin{pmatrix} \boldsymbol{f} \\ \boldsymbol{g} \end{pmatrix}$. For further in-depth analysis on RBF collocation see [75], [76].

Chapter 4

Numerical simulations

In this chapter we present and discuss the numerical experiments carried out on espresso coffee percolation models of Sections 2.3 2.4.

In particular, in Section 4.1 we describe two numerical approximations of problem (2.80), (2.81). The reliability of such a model together with the proposed solving strategies is assessed experimentally in both cases, by comparing a set of real extractions and simulated extractions conducted under the same physico-chemical conditions. The results show a good predictive power of the reduced percolation model, which can help the coffee industry in the control of the extraction efficiency, and, consequently, in its sustainability goals.

In Section 4.2 we discuss the reliability of the three dimensional model presented in Section 2.3. This model has been tested through a wide campaign of chemical laboratory analyses on espresso coffee samples extracted under different conditions; 8 chemical substances among the most relevant ones in affecting the beverage taste have been considered. The results of such laboratory analyses are compared with those of the numerical simulations obtained using the aforementioned model. Such a model has been implemented in the simulation tool for porous media and groundwater movement FeFlow Demo 7.2 [77]. The comparison between the real and simulated EC shows the potential of such a model in coffee industry applications, paving the way to tools allowing the customisation of the coffee beverage taste.

In Section 4.3 we present a RBF-based numerical approximation for the three

dimensional model. More precisely, in the numerical experiment we focus on the prediction of the flow and we consider the equation describing the hydraulic head dynamics. The reliability of the considered model together with the proposed solving strategy is experimentally assessed by simulating the hydraulic head with different initial pressures of the incoming water. The preliminary results show a reasonable behaviour of the simulated quantity. Such a scheme deserves further investigation in order to discretise the full percolation model.

Finally in Section 4.4 we discuss and compare the results presented in the previous sections.

4.1 The experiment with the reduced percolation model

In this Section we describe the numerical approximation methods proposed for the reduced percolation model (2.80), (2.81). In more details, Section 4.1.1 describes a finite difference based approximation scheme for such a model. Besides, Section 4.1.2 presents a RBF-based approximation scheme for the same model. In both sections, we assess experimentally the reliability of such a model together with each proposed solving strategy, by comparing real and simulated extractions. The presented results show the potential of such a model in coffee industry applications.

4.1.1 A Finite Differences approximation

In this Section we present an approximation scheme based on the Crank–Nicolson method for the numerical solution of problem (2.80), (2.81). This method is a nested fixed-point iteration strategy for the solution of the resulting nonlinear system of algebraic equations. As already described in Section 2.4, the reduced percolation model can be used for multiple purposes of coffee industry, in fact, it can be used both for the EY (Extraction Yield) prediction i.e., when the number of total monitored chemical substances is $I = 1$, and for the flavour prediction i.e., $I > 1$; so, we performed two different experiments, testing the predictive power of

the model in both cases. For each of them we describe the experimental procedure used for the coffee samples extraction, then we present the results of the numerical simulations. Finally we show the comparisons between experimental and numerical results.

The numerical results of the two cases of study shown in this section, together with the proposed approximation scheme has been presented for the first time in [55] and [21], respectively.

Numerical approximation

The numerical approximation scheme of the problem (2.80), (2.81) is based on the Crank-Nicolson method [78]. For the reader's convenience below we report the reduced model. The problem modelling the liquid concentration is:

$$\begin{cases} (1-\phi)\,\dfrac{\partial c_i^l}{\partial t}(z,t) = D\dfrac{\partial^2 c_i^l}{\partial z^2}(z,t) - q\dfrac{\partial c_i^l}{\partial z}(z,t) + b^f G_i^f(\boldsymbol{c}^l,\boldsymbol{c}^f,z,t) + b^b G_i^b(\boldsymbol{c}^l,\boldsymbol{c}^b,z,t), \\ -D\dfrac{\partial c_i^l}{\partial z}(0,t) + q c_i^l(0,t) = 0, \\ -D\dfrac{\partial c_i^l}{\partial z}(L,t) = 0, \\ c_i^l(z,0) = 0, \end{cases}$$

for $i = 1, 2, \ldots, N_{l-s}$, $z \in (0, L), t \in (0, \tau)$. The problem modelling the solid concentration is

$$\begin{cases} \dfrac{\partial c_i^s}{\partial t}(r,z,t) = \dfrac{D_i^f}{r^2}\dfrac{\partial}{\partial r}\left(r^2\dfrac{\partial c_i^s}{\partial r}(r,z,t)\right), \\ -D_i^f\dfrac{\partial c_i^s}{\partial r}(0,z,t) = 0, \\ -D_i^f\dfrac{\partial c_i^s}{\partial r}(a^s,z,t) = G_i^s(\boldsymbol{c}^l,\boldsymbol{c}^s,z,t), \\ c_i^s(r,z,0) = c_{0_i}, \end{cases}$$

for $i = 1, 2, \ldots, N_{l-s}$, $s = f, b$, $r \in (0, a^s), t \in (0, \tau)$, and $z \in (0, L)$.

In the following, we describe all the details of this approximation scheme.

Let N be a positive integer, $h_z = L/N$ and $z_j = (j-1)h_z$, $j = 1, \ldots, N+1$. Similarly, let M be a positive integer, $h_f = a^f/M$ and $h_b = a^b/M$, respectively, and $r_k = (k-1)h_s$, $k = 1, \ldots, M+1$, where $s = f, b$. Let N_t be a positive integer,

$h_t = \tau/N_t$, and $t_n = nh_t$, $n = 0, 1, \ldots, N_t$. Using the Crank-Nicolson method together with the first-order upwind scheme for the spatial discretisation of the advective term, the discretised form of problem (2.80) is

$$
\begin{cases}
\left(\varepsilon + 2\beta + 3\delta + h_t\dfrac{q^2}{D}\right) c^{l,i}_{1,n+1} - (2\beta+\delta)\, c^{l,i}_{2,n+1} = -\left(-\varepsilon + 2\beta + 3\delta + h_t\dfrac{q^2}{D}\right) c^{l,i}_{1,n} + \\
\qquad + (2\beta+\delta)\, c^{l,i}_{2,n} + \dfrac{h_t}{2} G^{f,i}_{1,n+1} + \\
\qquad + \dfrac{h_t}{2} G^{b,i}_{1,n+1} + \dfrac{h_t}{2} G^{f,i}_{1,n} + \dfrac{h_t}{2} G^{b,i}_{1,n}, \qquad n = 0, 1, \ldots, N_t - 1, \\
\\
-(\beta+\delta)\, c^{l,i}_{j-1,n+1} + (\varepsilon + 2\beta + \delta)\, c^{l,i}_{j,n+1} - \beta c^{l,i}_{j+1,n+1} = (\beta+\delta)\, c^{l,i}_{j-1,n} + \\
\qquad - (-\varepsilon + 2\beta + \delta)\, c^{l,i}_{j,n} + \beta c^{l,i}_{j+1,n} + \dfrac{h_t}{2} G^{f,i}_{j,n+1} + \\
\qquad + \dfrac{h_t}{2} G^{b,i}_{j,n+1} + \dfrac{h_t}{2} G^{f,i}_{j,n} + \dfrac{h_t}{2} G^{b,i}_{j,n}, \qquad j = 2, 3, \ldots, N, n = 0, 1, \ldots, N_t - 1, \\
\\
-(2\beta+\delta)\, c^{l,i}_{N,n+1} + (\varepsilon + 2\beta + \delta)\, c^{l,i}_{N+1,n+1} = (2\beta+\delta)\, c^{l,i}_{N,n} + \\
\qquad - (-\varepsilon + 2\beta + \delta)\, c^{l,i}_{N+1,n} + \dfrac{h_t}{2} G^{f,i}_{N+1,n+1} + \\
\qquad + \dfrac{h_t}{2} G^{b,i}_{N+1,n+1} + \dfrac{h_t}{2} G^{f,i}_{N+1,n} + \dfrac{h_t}{2} G^{b,i}_{N+1,n}, \qquad n = 0, 1, \ldots, N_t - 1, \\
\\
c^{l,i}_{j,0} = 0, \qquad j = 1, 2, \ldots, N+1,
\end{cases}
\tag{4.1}
$$

for $i = 1, 2, \ldots, I$. Where $\varepsilon = 1 - \phi$, $\beta = h_t D/(2h_z^2)$, $\delta = h_t q/(2h_z)$, $c^{l,i}_{j,n} \approx c^l_i(z_j, t_n)$, and $G^{s,i}_{j,n} \approx G^s_i(\boldsymbol{\lambda}^i_n, \mathbf{c}^{s,i}_{M+1,n}, z_j, t_n)$, $s = f, b$ with vectors $\boldsymbol{\lambda}^i_n$, $\mathbf{c}^{s,i}_{M+1,n}$ defined as

$$
\begin{aligned}
\boldsymbol{\lambda}^i_n &= \left(c^{l,i}_{1,n}, c^{l,i}_{2,n}, \ldots, c^{l,i}_{N+1,n}\right)^T, \\
\mathbf{c}^{s,i}_{M+1,n} &= \left(c^{s,i}_{M+1,1,n}, c^{s,i}_{M+1,2,n}, \ldots, c^{s,i}_{M+1,N+1,n}\right)^T, \quad s = f, b,
\end{aligned}
\tag{4.2}
$$

$i = 1, 2, \ldots, I$. Moreover, for the approximations $G^{s,i}_{j,n}$, of the reaction terms we used

$$
G^{s,i}_{j,n} = b^s k^i_r c^{s,i}_{M+1,j,n} f_p(c^{s,i}_{M+1,j,n} - c^{l,i}_{j,n}) f_p(c^i_{\text{sat}} - c^{i,l}_{j,n}) \prod_{\substack{k=1 \\ k\neq i}}^{I} f_p(c^{l,k}_{j,n} - c^{i,k}_{\text{dis}}), \quad s = f, b, \tag{4.3}
$$

where, for $i = 1, 2, \ldots, I$, we denote with $c^{s,i}_{M+1,j,n}$ the approximated solid concentrations, defined below, and

$$f_p(x) = \begin{cases} \exp\left(\frac{x}{p} + \log(p) - 1\right), & x \leq p \\ x, & x > p, \end{cases} \tag{4.4}$$

where $p > 0$ sufficiently small, provides a continuous and derivable approximation of the $\max(x, 0)$ function. Similarly, using the Crank-Nicolson method where the spatial discretisation is obtained by using the half step symmetric scheme, the discretised form of problem (2.81) is

$$\begin{cases} \left(1 + 6\alpha^{s,i}\right) c^{s,i}_{1,j,n+1} - 6\alpha^{s,i} c^{s,i}_{2,j,n+1} = \left(1 - 6\alpha^{s,i}\right) c^{s,i}_{1,j,n} + \\ \qquad + 6\alpha^{s,i} c^{s,i}_{2,j,n}, \qquad j = 1, 2, \ldots, N+1, n = 0, 1, \ldots, N_t - 1, \\ \\ -\alpha^{s,i} \dfrac{k_-^2}{(k-1)^2} c^{s,i}_{k-1,j,n+1} + \left(1 + \alpha^{s,i} \dfrac{k_-^2 + k_+^2}{(k-1)^2}\right) c^{s,i}_{k,j,n+1} - \alpha^{s,i} \dfrac{k_+^2}{(k-1)^2} c^{s,i}_{k+1,j,n+1} = \\ \qquad = \alpha^{s,i} \dfrac{k_-^2}{(k-1)^2} c^{s,i}_{k-1,j,n} + \left(1 - \alpha^{s,i} \dfrac{k_-^2 + k_+^2}{(k-1)^2}\right) c^{s,i}_{k,j,n} + \\ \qquad + \alpha^{s,i} \dfrac{k_+^2}{(k-1)^2} c^{s,i}_{k+1,j,n}, \quad k = 2, 3, \ldots, M, j = 1, 2, \ldots, N+1, n = 0, 1, \ldots, N_t - 1, \\ \\ -\alpha^{s,i} \dfrac{\tilde{M}_-^2 + \tilde{M}_+^2}{M^2} c^{s,i}_{M,j,n+1} + \left(1 + \alpha^{s,i} \dfrac{\tilde{M}_-^2 + \tilde{M}_+^2}{M^2}\right) c^{s,i}_{M+1,j,n+1} = \alpha^{s,i} \dfrac{\tilde{M}_-^2 + \tilde{M}_+^2}{M^2} c^{s,i}_{M,j,n} + \\ \qquad + \left(1 - \alpha^{s,i} \dfrac{\tilde{M}_-^2 + \tilde{M}_+^2}{M^2}\right) c^{s,i}_{M+1,j,n} - \dfrac{h_t}{h_s} \dfrac{\tilde{M}_+^2}{M^2} G^{s,i}_{j,n+1} + \\ \qquad - \dfrac{h_t}{h_s} \dfrac{\tilde{M}_+^2}{M^2} G^{s,i}_{j,n}, \qquad j = 1, 2, \ldots, N+1, n = 0, 1, \ldots, N_t - 1, \\ \\ c^{s,i}_{k,j,0} = c_{0_i}, \qquad k = 1, 2, \ldots, M+1, j = 1, 2, \ldots, N+1, \end{cases} \tag{4.5}$$

for $i = 1, 2, \ldots, I$, where $\alpha^{s,i} = h_t D_i^f / \left(2h_s^2\right)$, $s = f, b$, $k_- = k - 3/2$, $k_+ = k - 1/2$, $\tilde{M}_- = M - 1/2$, $\tilde{M}_+ = M + 1/2$, $c^{s,i}_{k,j,n} \approx c^{s,i}(r_k, z_j, t_n)$, and $G^{s,i}_{j,n}$ has been

defined in (4.3). We note that at $r = 0$ we used the De L'Hôpital rule that gives:

$$\begin{aligned}\frac{\partial c_i^s}{\partial t}(0,z,t) &= \lim_{r\to 0}\left(\frac{2}{r}D_i^f\frac{\partial c_i^s}{\partial r}(r,z,t) + D_i^f\frac{\partial^2 c_i^s}{\partial r^2}(r,z,t)\right) = \\ &= 3D_i^f\frac{\partial^2 c_i^s}{\partial r^2}(0,z,t), \qquad i = 1,2,\ldots,I.\end{aligned} \tag{4.6}$$

For $i = 1,2,\ldots,I$, systems (4.1),(4.5) are coupled through the functions $G^{s,i}$. Moreover, in system (4.5) the concentrations $c_{k,j,n}^{s,i}$, for $s = f,b$ depend on z_j, therefore such systems must be solved for each $z_j, j = 1,2,\ldots,N+1$.

The discretised systems (4.1),(4.5) can be written in matrix form as follows:

$$A^i\boldsymbol{\sigma}_{n+1}^i = C^i\boldsymbol{\sigma}_n^i + \boldsymbol{\varphi}_{n+1}^i + \boldsymbol{\varphi}_n^i, \qquad n = 0,1,\ldots,N_t-1,\ i = 1,2,\ldots,I, \tag{4.7}$$

$$B^i\boldsymbol{\lambda}_{n+1}^i = E^i\boldsymbol{\lambda}_n^i + \boldsymbol{\psi}_{n+1}^i + \boldsymbol{\psi}_n^i, \qquad n = 0,\ldots,N_t-1,\ i = 1,2,\ldots,I, \tag{4.8}$$

where

$$\begin{aligned}&A^i, C^i \in \mathbb{R}^{2(N+1)(M+1)\times 2(N+1)(M+1)},\\ &B^i, E^i \in \mathbb{R}^{N+1\times N+1},\\ &\boldsymbol{\sigma}_n^i \in \mathbb{R}^{2(N+1)(M+1)}, \boldsymbol{\lambda}_n^i \in \mathbb{R}^{N+1},\\ &\boldsymbol{\varphi}_n^i \in \mathbb{R}^{2(N+1)(M+1)}, \boldsymbol{\psi}_n^i \in \mathbb{R}^{N+1};\end{aligned}$$

for $n = 0,1,\ldots,N_t-1$ and $i = 1,2,\ldots,I$. The liquid unknown vector has been defined in (4.2), and solid unknown vector is defined as

$$\boldsymbol{\sigma}_n^i = \begin{pmatrix}\mathbf{c}_n^{f,i}\\ \mathbf{c}_n^{b,i}\end{pmatrix}, \tag{4.9}$$

with

$$\begin{aligned}\mathbf{c}_n^{f,i} = \Big(&c_{1,1,n}^{f,i}, c_{2,1,n}^{f,i},\ldots,c_{M+1,1,n}^{f,i}, c_{1,2,n}^{f,i}, c_{2,2,n}^{f,i},\ldots,c_{M+1,2,n}^{f,i},\ldots,\\ &c_{1,N+1,n}^{f,i}, c_{2,N+1,n}^{f,i},\ldots,c_{M+1,N+1,n}^{f,i}\Big)^T,\end{aligned}$$

and analogously for the vector $\mathbf{c}_n^{b,i}$, $i = 1,2,\ldots,I$. The vectors with the non-linear terms are defined as

$$\boldsymbol{\varphi}_n^i = \begin{pmatrix}\mathbf{F}_n^{f,i}\\ \mathbf{F}_n^{b,i}\end{pmatrix},$$

$$\boldsymbol{\psi}_n^i = \left(\frac{h_t}{2}G_{1,n}^{f,i} + \frac{h_t}{2}G_{1,n}^{b,i}, \frac{h_t}{2}G_{2,n}^{f,i} + \frac{h_t}{2}G_{2,n}^{b,i},\ldots,\frac{h_t}{2}G_{N+1,n}^{f,i} + \frac{h_t}{2}G_{N+1,n}^{b,i}\right)^T,$$

with

$$\mathbf{F}_n^{s,i} = \left(0, \ldots, 0, -\frac{h_t \tilde{M}_+^2}{h_f M^2} G_{1,n}^{s,i}, 0, \ldots, 0, -\frac{h_t \tilde{M}_+^2}{h_f M^2} G_{2,n}^{s,i}, 0, \ldots, 0, -\frac{h_t \tilde{M}_+^2}{h_f M^2} G_{N+1,n}^{f,i}\right)^T,$$

$s = f, b$, $i = 1, 2, \ldots, I$. We note that non-zero elements in $\boldsymbol{\varphi}_n^i$ are in positions that are multiples of $M + 1$; matrices A^i are block diagonal matrices of order $2(N + 1)(M + 1)$,

$$A^i = \begin{pmatrix} A^{f,i} & 0 & \ldots & & & 0 \\ 0 & \ddots & 0 & & & \vdots \\ \vdots & 0 & A^{f,i} & 0 & & \vdots \\ \vdots & & 0 & A^{b,i} & 0 & \vdots \\ \vdots & & & 0 & \ddots & 0 \\ \vdots & & & & 0 & A^{b,i} \end{pmatrix},$$

$i = 1, 2, \ldots, I$, where each block is a three-diagonal matrix of order $M + 1$, that is

$$A^{s,i} = \begin{pmatrix} A_{1,:}^{s,i} \\ A_{2,:}^{s,i} \\ \vdots \\ A_{M+1,:}^{s,i} \end{pmatrix},$$

whose rows are:

$$A_{1,:}^{s,i} = \begin{pmatrix} 1 + 6\alpha^{s,i} & -6\alpha^{s,i} & 0 & \ldots & 0 \end{pmatrix},$$
$$A_{k,:}^{s,i} = \begin{pmatrix} 0 & \ldots & 0 & -\alpha^{s,i} \dfrac{k_-^2}{(k-1)^2} & 1 + \alpha^{s,i} \dfrac{k_-^2 + k_+^2}{(k-1)^2} & -\alpha^{s,i} \dfrac{k_+^2}{(k-1)^2} & 0 & \ldots & 0 \end{pmatrix},$$
$k = 2, 3, \ldots, M$,
$$A_{M+1,:}^{s,i} = \begin{pmatrix} 0 & \ldots & 0 & -\alpha^{s,i} \dfrac{\tilde{M}_-^2 + \tilde{M}_+^2}{M^2} & 1 + \alpha^{s,i} \dfrac{\tilde{M}_-^2 + \tilde{M}_+^2}{M^2} \end{pmatrix},$$

for $s = f, b$. B is a three-diagonal matrix of order $N+1$,

$$B^i = \begin{pmatrix} \varepsilon + 2\beta + 3\delta + \dfrac{h_t q^2}{D} & -2\beta - \delta & 0 & \dots & & & 0 \\ \ddots & \ddots & \ddots & 0 & & & \vdots \\ 0 & \ddots & \ddots & \ddots & 0 & & \vdots \\ \vdots & 0 & -\beta - \delta & \varepsilon + 2\beta + \delta & -\beta & 0 & \vdots \\ \vdots & & 0 & \ddots & \ddots & \ddots & \vdots \\ \vdots & & & 0 & \ddots & \ddots & \ddots \\ \vdots & \dots & & & 0 & -2\beta - \delta & \varepsilon + 2\beta + \delta \end{pmatrix}.$$

Similarly, the right-hand side matrices in (4.7),(4.8) are

$$C^i = \begin{pmatrix} C^{f,i} & 0 & \dots & & & 0 \\ 0 & \ddots & 0 & & & \vdots \\ \vdots & 0 & C^{f,i} & 0 & & \vdots \\ \vdots & & 0 & C^{b,i} & 0 & \vdots \\ \vdots & & & 0 & \ddots & 0 \\ \vdots & & & & 0 & C^{b,i} \end{pmatrix},$$

where

$$C^{s,i} = \begin{pmatrix} C^{s,i}_{1,:} \\ C^{s,i}_{2,:} \\ \vdots \\ C^{s,i}_{M+1,:} \end{pmatrix},$$

whose rows are:

$$C^{s,i}_{1,:} = \begin{pmatrix} 1 - 6\alpha^{s,i} & 6\alpha^{s,i} & 0 & \dots & 0 \end{pmatrix},$$

$$C^{s,i}_{k,:} = \begin{pmatrix} 0 & \dots & 0 & \alpha^{s,i}\dfrac{k_-^2}{(k-1)^2} & 1 - \alpha^{s,i}\dfrac{k_-^2 + k_+^2}{(k-1)^2} & \alpha^{s,i}\dfrac{k_+^2}{(k-1)^2} & 0 & \dots & 0 \end{pmatrix},$$

$k = 2, 3, \dots, M,$

$$C^{s,i}_{M+1,:} = \begin{pmatrix} 0 & \dots & 0 & \alpha^{s,i}\dfrac{\tilde{M}_-^2 + \tilde{M}_+^2}{M^2} & 1 - \alpha^{s,i}\dfrac{\tilde{M}_-^2 + \tilde{M}_+^2}{M^2} \end{pmatrix},$$

for $i = 1, 2, \ldots, I$, and $s = f, b$.

$$E^i = \begin{pmatrix} \varepsilon - 2\beta - 3\delta - \dfrac{h_t q^2}{D} & 2\beta + \delta & 0 & \ldots & & & 0 \\ \ddots & \ddots & \ddots & 0 & & & \vdots \\ 0 & \ddots & \ddots & \ddots & 0 & & \vdots \\ \vdots & 0 & \beta + \delta & \varepsilon - 2\beta - \delta & \beta & 0 & \vdots \\ \vdots & & 0 & \ddots & \ddots & \ddots & \vdots \\ \vdots & & & 0 & \ddots & \ddots & \ddots \\ \vdots & \ldots & & & 0 & 2\beta + \delta & \varepsilon - 2\beta - \delta \end{pmatrix}.$$

Note that, the matrices $C^{s,i}$ and E^i have the same structure of $A^{s,i}$ and B^i, respectively. In addition, except for the sign of the terms involving h_t, they have also the same elements. This feature is determined by the trapezoidal rule used for the time discretisation.

The solution to system (4.7),(4.8) is based on a two-step procedure. More precisely, from (4.7),(4.8), we consider a nested fixed-point iteration for each time step. It consists in solving consecutively such linear systems for a given $n = 0, \ldots, N_t - 1$:

$$A^i \boldsymbol{\sigma}_{n+1}^{i,\mu,\nu} = C^i \boldsymbol{\sigma}_n^i + \boldsymbol{\varphi}_{n+1}^{i,\mu,\nu-1} + \boldsymbol{\varphi}_n^i, \tag{4.10}$$

$$B^i \boldsymbol{\lambda}_{n+1}^{i,\mu,\nu} = E^i \boldsymbol{\lambda}_n^i + \boldsymbol{\psi}_{n+1}^{i,\mu,\nu-1} + \boldsymbol{\psi}_n^i, \tag{4.11}$$

$i = 1, 2, \ldots, I$, where the index ν stands for the inner fixed-point iteration and μ for the outer fixed-point iteration, relatively to the time step $n + 1$; moreover, $\boldsymbol{\varphi}_{n+1}^{i,\mu,\nu}, \boldsymbol{\psi}_{n+1}^{i,\mu,\nu}$ mean that the concentrations of the substance i are evaluated at those inner ν and outer μ iterations, respectively. The stages of the solving strategy are outlined in Algorithm 1.

Algorithm 1: Given the initial value c_{0_i}, for $i = 1, \dots, I$, and the parameters $maxit_1$, $maxit_2$, tol_1, tol_2 compute the solution $\boldsymbol{\sigma}_n^i$, $\boldsymbol{\lambda}_n^i$, $n = 1, \dots, N_t$, of system (4.7),(4.8), by the following steps.

for $n = 0, 1, \dots, N_t - 1$ **do**
  for $i = 1, 2, \dots, I$ **do**
    $\boldsymbol{\sigma}_0^i = (c_{0_i}, \dots, c_{0_i})^T$; $\boldsymbol{\lambda}_0^i = (0, \dots, 0)^T$;
    $\boldsymbol{\sigma}_{n+1}^{i,1,1} = \boldsymbol{\sigma}_n^i$; $\boldsymbol{\lambda}_{n+1}^{i,1,1} = \boldsymbol{\lambda}_n^i$;
    for $\mu = 2, 3, \dots, maxit_2$ **do**
      $\boldsymbol{\sigma}_{n+1}^{i,\mu,1} = \boldsymbol{\sigma}_{n+1}^{i,\mu-1,\bar{\nu}}$;
      for $\nu = 2, 3, \dots, maxit_1$ **do**
        $\boldsymbol{\lambda}_{n+1}^{i,\mu,\nu-1} = \boldsymbol{\lambda}_{n+1}^{i,\mu-1,\tilde{\nu}}$;
        Compute $\boldsymbol{\sigma}_{n+1}^{i,\mu,\nu}$ from $A\boldsymbol{\sigma}_{n+1}^{i,\mu,\nu} = C\boldsymbol{\sigma}_n^i + \boldsymbol{\varphi}_{n+1}^{i,\mu,\nu-1} + \boldsymbol{\varphi}_n^i$;
        if $\max\left(\left|\boldsymbol{\sigma}_{n+1}^{i,\mu,\nu} - \boldsymbol{\sigma}_{n+1}^{i,\mu,\nu-1}\right|\right) \leq tol_1$ **then**
          $\boldsymbol{\sigma}_{n+1}^{i,\mu,\bar{\nu}} = \boldsymbol{\sigma}_{n+1}^{i,\mu,\nu}$;
          break;
        end
      end
      $\boldsymbol{\lambda}_{n+1}^{i,\mu,1} = \boldsymbol{\lambda}_{n+1}^{i,\mu-1,\tilde{\nu}}$;
      for $\nu = 2, \dots, maxit_1$ **do**
        $\boldsymbol{\sigma}_{n+1}^{i,\mu,\nu-1} = \boldsymbol{\sigma}_{n+1}^{i,\mu,\bar{\nu}}$;
        Compute $\boldsymbol{\lambda}_{n+1}^{i,\mu,\nu}$ from $B\boldsymbol{\lambda}_{n+1}^{i,\mu,\nu} = E\boldsymbol{\lambda}_n^i + \boldsymbol{\psi}_{n+1}^{i,\mu,\nu-1} + \boldsymbol{\psi}_n^i$;
        if $\max\left(\left|\boldsymbol{\lambda}_{n+1}^{i,\mu,\nu} - \boldsymbol{\lambda}_{n+1}^{i,\mu,\nu-1}\right|\right) \leq tol_1$ **then**
          $\boldsymbol{\lambda}_{n+1}^{i,\mu,\tilde{\nu}} = \boldsymbol{\lambda}_{n+1}^{i,\mu,\nu}$;
          break;
        end
      end
      if $\max\left(\left|\boldsymbol{\sigma}_{n+1}^{i,\mu,\bar{\nu}} - \boldsymbol{\sigma}_{n+1}^{i,\mu-1,\bar{\nu}}\right|\right) \leq$
       tol_2 *and* $\max\left(\left|\boldsymbol{\lambda}_{n+1}^{i,\mu,\tilde{\nu}} - \boldsymbol{\lambda}_{n+1}^{i,\mu-1,\tilde{\nu}}\right|\right) \leq tol_2$ **then**
        $\boldsymbol{\sigma}_{n+1}^{i,\bar{\mu},\bar{\nu}} = \boldsymbol{\sigma}_{n+1}^{i,\mu,\bar{\nu}}$; $\boldsymbol{\lambda}_{n+1}^{i,\bar{\mu},\tilde{\nu}} = \boldsymbol{\lambda}_{n+1}^{i,\mu,\tilde{\nu}}$;
        break;
      end
    end
    $\boldsymbol{\sigma}_{n+1}^i = \boldsymbol{\sigma}_{n+1}^{i,\bar{\mu},\bar{\nu}}$; $\boldsymbol{\lambda}_{n+1}^i = \boldsymbol{\lambda}_{n+1}^{i,\bar{\mu},\tilde{\nu}}$
  end
end

We observe that $maxit_1$ is the maximum number of steps for the inner iterate, and $maxit_2$ is the maximum number for the outer iterate. For each $i = 1, 2, \ldots, I$, the final inner iteration on system (4.10) yields $\boldsymbol{\sigma}_{n+1}^{i,\mu,\bar{\nu}}$, while the last inner iteration on system (4.11) gives $\boldsymbol{\lambda}_{n+1}^{i,\mu,\tilde{\nu}}$. These iterations satisfy the corresponding stopping criteria reported in Algorithm (1), see lines 19 and 24, where max function gives the maximum component of the vector argument and $tol_1 > 0$ is a prescribed tolerance. Moreover, the outer iteration serves to refine the results produced by the inner iterate, where coupling between systems is neglected. The final outer iteration satisfies a stopping criterion where $tol_2 > 0$ is a prescribed tolerance. Besides, this final iteration gives $(\boldsymbol{\sigma}_{n+1}^{i,\bar{\mu},\bar{\nu}}, \boldsymbol{\lambda}_{n+1}^{i,\bar{\mu},\tilde{\nu}})$ that is the approximated solution at time t_{n+1} of the original system (4.7),(4.8). We note that the convergence of the inner steps can be improved by relaxed iterations with a proper parameter ω, which also helps to have a positive solution at initial time steps. The following algorithm sums up the ideas on the solving strategy for systems (4.7),(4.8).

Experimental measurements

In this Section we present the results of the two experimental campaigns of espresso extractions. More precisely, in Extraction Procedure 1 we describe the equipment, the procedures and the physical parameters of the extraction campaign, as well as the results obtained in terms of EY. While in Extraction Procedure 2 we describe the equipment, the procedures and the physical parameters used in the experiment we performed for the prediction of the beverage taste. In particular, we considered two types of chemicals that affect the most the espresso taste, namely caffeine and total amount of chlorogenic acids (CQAs).

Extraction Procedure 1. The samples were prepared using the grinding machine Mythos 1 [79] to prepare the coffee powder, which was tamped with the dynamometric tamper PUQ® PRESS M2 [80]. The espresso samples were extracted with the professional espresso coffee machine Victoria Arduino VA388 Black Eagle [81]. The grinder, the tamper and the espresso machine were provided by the espresso machine manufacturer Simonelli Group SpA (Belforte del Chienti, Italy). The

experiments were performed with two types of Arabica coffee: the single origin Cibao Altura (HMC, origin - Dominican Republic, variety - typica, caturra, process - fully washed), and the Arabica mix Modœtia (HMC, origin - Brazil, variety - mundo novo & catuai, process - natural; origin - India Plantation, variety - kent, process - washed; origin - Ethiopia Yirgacheffe, variety - heirloom, process - washed). The extraction of the samples was performed following this procedure: 20 ± 0.1 g of coffee powder were used to fill the VST© Competition filter basket, with inner radius 29.25 mm and height 26 mm; the coffee powder was tamped with a constant tamping force set at 20 kgF; the mass of extracted espresso coffee was kept constant at 40 ± 2 g, in such a way that the brew ratio between grams of coffee powder and grams of extracted coffee was kept constant at 1:2. The extractions differ in the values of water pressure, water temperature and granulometry of the coffee powder for both the coffee types; all these parameters were modified one at a time within a grid of prescribed values. Each parameter has been properly set in the espresso machine by an experienced professional barista. The extraction grid consists in these parameters and values: coffee type - Cibao Altura and Modœtia; water temperature - $90.4, 93.4$ °C; water pressure - $6, 9$ bar, and 12 bar applied only to the extra fine and extra coarse granulometries; granulometry - optimal, fine, coarse, extra fine, extra coarse for Cibao Altura, and optimal, fine, coarse for Modœtia. We note that with optimal granulometry we mean the granulometry that yields about 40 g of coffee in cup extracted in 25 s at 93.4 °C and 9 bar. Taking this granulometry as reference, the finer granulometries are obtained by reducing the distance between the burrs of the grinder, whereas the coarser by increasing the distance between the burrs. Clearly, fixed the brew ratio, the extraction times vary depending on the granulometry. We report the mean times τ in Table 4.1. They were calculated as the average of the extraction times recorded for the corresponding granulometry, as the water temperature and pressure vary. Table 4.1 also shows the mean height L of the tamped coffee powder into the filter basket.

In addition, the coffee powder obtained with different grinding settings was analysed by the laser diffraction granulometer Mastersizer 3000, Malvern Instru-

Coffee type	Optimal		Fine		Coarse		Extra Fine		Extra Coarse	
	L[mm]	τ[s]	L[mm]	τ[s]	L[mm]	τ [s]	L[mm]	τ[s]	L[mm]	τ[s]
Cibao Altura	13.04	28	13.27	42	14.20	21	12.60	75	14.20	16
Modœtia	13.00	26	13.27	41	14.20	21	–	–	–	–

Table 4.1: Heights L of the tamped coffee powder and extraction times τ for the different granulometries and types of coffee.

ments [82]. This device measures the volume of the sample particles and calculates the diameter of equivalent spheres, so the particles are uniquely classified by their diameter, regardless of their actual shape. Figures 4.1, 4.2 show the particle size distribution curves for the Cibao Altura and Modœtia, respectively. For each values of diameter in the x-axis, the corresponding value in the y-axis represents the volume percentage covered by all the particles having that equivalent diameter. We point out the bimodal trend of the curves presenting a local minimum around 100 µm. This justifies the usual choice of dividing the coffee particles into two families: the boulders, whose diameter is bigger than 100 µm, and the fines, whose diameter is smaller than 100 µm; in addition, as representative radius for boulders and fines, i.e., a^b, a^f, we choose the two modes for each granulometry profile. In Figure 4.1, we report the optimal, extra fine and extra coarse granulometries, for the Cibao Altura. We observe that these three profiles of granulometry are sensibly far from each other. In fact, in the extra coarse powder there is a higher amount of boulders and their average size is the biggest with respect to the optimal and extra fine powder. Similarly, the extra fine powder has the highest percentage of fines and the least of boulders, furthermore, the boulder particles have a smaller average diameter. Figure 4.2, shows the granulometry profiles of Modœtia samples; it reflecets the same trend observed in Figure 4.1 but with less evident differences, since the three grinding levels are closer.

TDS Measurement Procedure 1. The TDS measurements were obtained following this procedure: a small amount of coffee sample, after properly cooled down

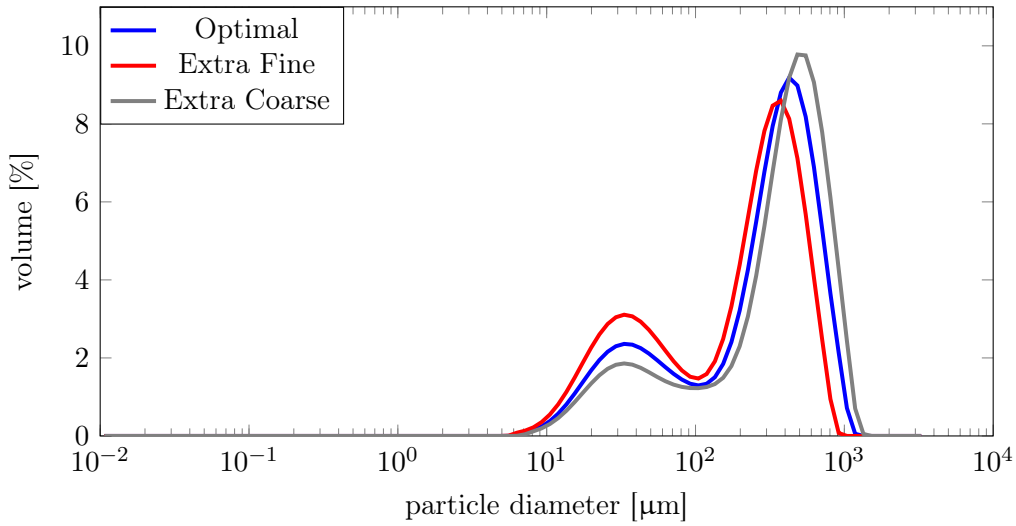

Figure 4.1: Particle size distribution curves of the Cibao Altura ground coffee.

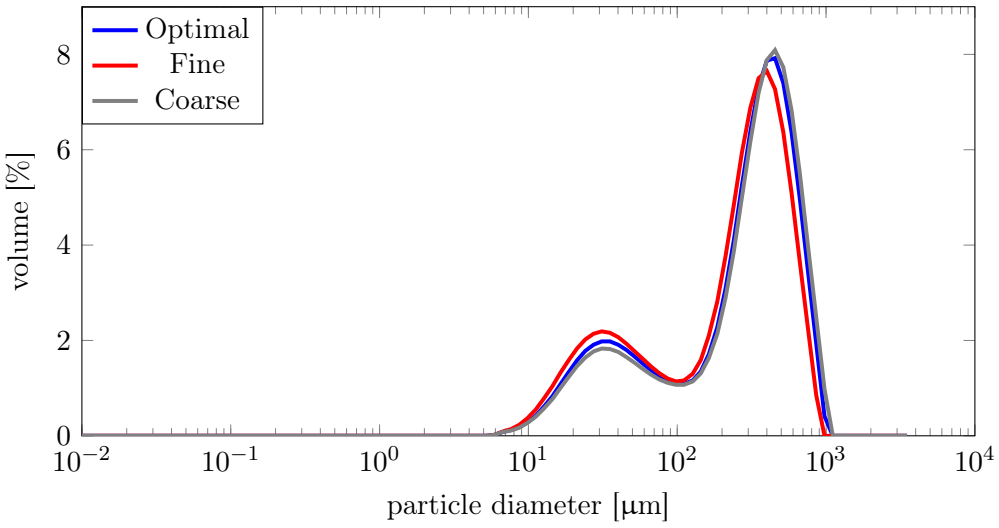

Figure 4.2: Particle size distribution curves of the Modœtia ground coffee.

and stirred, was inserted in a digital refractometer manufactured by VST inc. then the TDS value was recorded. Samples for each extraction configuration were tripled and the total number of the samples is 90. Then, the EY has been calculated for each sample using the following relation:

$$\text{EY} = \frac{\text{TDS}}{\text{brew ratio}}.$$

Tables 4.2, 4.3 show the values of TDS and EY recorded for each sample of

the Cibao Altura and Modœtia coffee, respectively; TDS and EY values have been averaged over the three repeated extractions. We highlighted the maximum and minimum values of EY inside each granulometry, since they are useful for the numerical results. The parameters configuration that globally maximises the EY is: 93.4 °C, 6 bar and fine granulometry, closely followed by the 93.4 °C, 6 bar and extra fine granulometry, for Cibao Altura; 90.4 °C, 6 bar and fine granulometry, for Modœtia.

T [°C]	p [bar]	τ [s]	**granulometry**	**TDS** [%] (σ)	**EY** [%]
93.4	9	25	Optimal	10.3 (0.00)	20.77
93.4	6	31	Optimal	10.5 (0.20)	**21.35**
90.4	9	26	Optimal	10.3 (0.15)	20.53
90.4	6	32	Optimal	10.0 (0.17)	**20.34**
93.4	9	42	Fine	10.2 (0.27)	20.90
93.4	6	42	Fine	10.7 (0.15)	**21.86**
90.4	9	42	Fine	10.4 (0.21)	21.21
90.4	6	44	Fine	10.2 (1.04)	**20.43**
93.4	9	19	Coarse	9.6 (0.25)	19.91
93.4	6	24	Coarse	10.1 (0.17)	**20.20**
90.4	9	19	Coarse	9.4 (0.30)	**19.42**
90.4	6	24	Coarse	9.8 (0.29)	19.83
93.4	9	74	Extra Fine	10.9 (0.16)	21.77
93.4	6	73	Extra Fine	10.9 (0.42)	**21.80**
93.4	12	81	Extra Fine	11.0 (0.14)	**21.45**
93.4	9	15	Extra Coarse	8.9 (0.14)	18.24
93.4	6	21	Extra Coarse	9.5 (0.07)	**19.14**
93.4	12	14	Extra Coarse	8.9 (0.00)	**18.02**

Table 4.2: TDS measurements equipped with the standard deviation (σ) and EY calculation for the samples of Cibao Altura coffee extracted with Procedure 1.

The experimental measurements confirm that a finer particle size increases the TDS and the EY. Moreover, they show that the optimal pressure configuration is 6 bar.

T [°C]	p [bar]	τ [s]	**granulometry**	**TDS** [%] (σ)	**EY** [%]
93.4	9	26	Optimal	10.4 (0.28)	**20.87**
93.4	6	26	Optimal	10.0 (0.12)	**20.43**
90.4	9	26	Optimal	10.2 (0.06)	20.81
90.4	6	25	Optimal	10.2 (0.06)	20.53
93.4	9	39	Fine	10.9 (0.23)	22.09
93.4	6	39	Fine	10.8 (0.25)	**22.07**
90.4	9	42	Fine	11.0 (0.3)	22.18
90.4	6	41	Fine	11.2 (0.26)	**22.58**
93.4	9	18	Coarse	9.6 (0.50)	19.44
93.4	6	22	Coarse	9.7 (0.31)	**20.11**
90.4	9	19	Coarse	9.5 (0.06)	**19.09**
90.4	6	22	Coarse	10.0 (0.29)	20.10

Table 4.3: TDS measurements equipped with the standard deviation (σ) and EY calculation for the samples of Modœtia coffee extracted with Procedure 1.

In addition, we considered two types of substances among the most relevant ones affecting the beverage taste, namely caffeine and total amount of chlorogenic acids (CQAs), given by 3-Caffeoylquinic acid (3-CQA), 3,5-Dicaffeoylquinic acid (3,5-CQA), and 5-Caffeoylquinic acid (5-CQA). In this case the extraction of coffee samples followed this procedure:

Extraction Procedure 2. The coffee variety used is the pure Arabica coffee named Cibao Altura (HMC): origin – Dominican Republic; region – Juncalito Montains; producer – Finca Nunez; variety – typica, caturra; process – fully washed; altitude – 900 masl; descriptive notes – cashew nuts, cane sugar, dried apricot. The coffee beans were ground using the grinding machine Mythos 2 [83]. Then, 20 ± 0.1 g of coffee powder were used to fill the VST© Competition filter basket, with height 26 mm and inner radius 29.25 mm; the coffee powder was tamped with a constant tamping force set at 20 kg F, using the dynamometric tamper PUQ® PRESS M2 [80]. The espresso samples were extracted with the traditional espresso coffee machine Victoria Arduino 388, Black Eagle [81]. Also in this case the equipment was supplied by the manufacturing company Simonelli Group SpA (Belforte del Chienti, Italy). The mass of extracted espresso coffee was kept constant at 40 ± 2 g, and also in this case the brew ratio between grams of dry coffee and grams of extracted coffee was kept constant at 1:2. The samples were extracted at different values of water temperature and water pressure; these parameters were modified one at a time within a set of prescribed values by an experienced professional barista. Each sample was collected into a ceramic coffee cup and, after being properly cooled down, was transferred into a test tube. Samples for each extraction configuration were duplicated. The total number of the extracted samples is 18.

The extraction grid consists in the following values: water temperature - 88, 93, 98 °C; water pressure - 7, 9, 11 bar. The coffee powder was ground in such a way that with 20 g of dry coffee, we can brew 40 g of coffee beverage in 25 ± 1 s. In addition, we measured the averaged height of the coffee pod that is 13.88 mm.

Again, the coffee powder was analysed by the laser diffraction granulometer Mastersizer 3000, Malvern Instruments [82]. Figure 4.3, shows the particle size

distribution curve. The values of the particle diameters are shown on the x axis. The corresponding value on the y axis represents the percentage of volume covered by all particles having that diameter. Again, as representative radii for fines and boulders, a^f and a^b, we choose the half of the two modes.

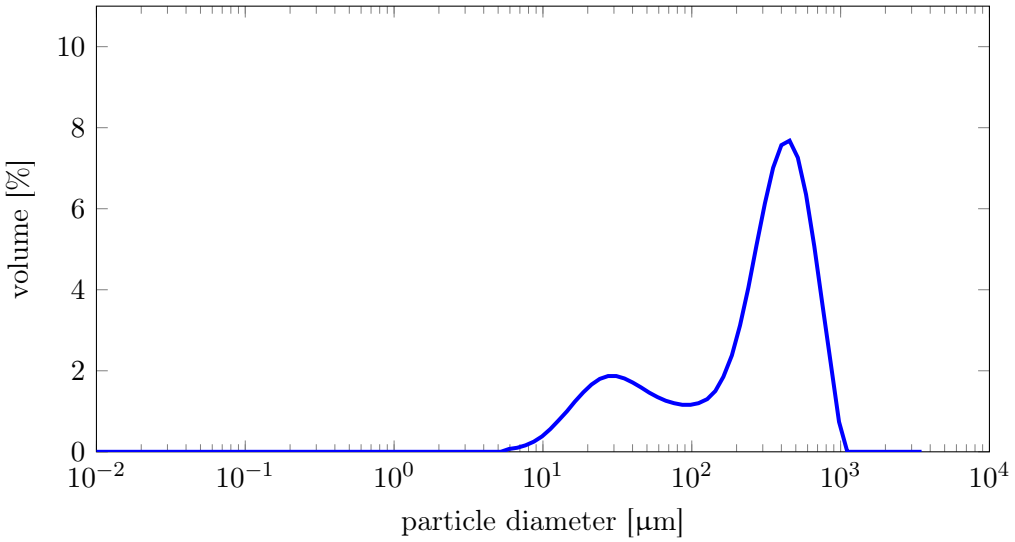

Figure 4.3: Particle size distribution curve of the coffee powder for the granulometry used in the experimental extractions.

Caffeine and CQAs were quantified in the ground coffee and in extracted samples. The results of the chemical analyses, with the relative standard deviations, RSD (expressed in percentage), are shown in Tables 4.4-4.5. Moreover, in Table 4.5 the highest and lowest amount of the analysed substances in cup have been highlighted, when varying water temperature and pressure.

caffeine [g/kg]	**CQAs** [g/kg]
16.24 (7.0)	37.17 (0.1)

Table 4.4: Concentrations of caffeine and CQAs contained in the coffee powder extracted with Procedure 2, it reports also the percentage RSD value that is (RSD).

Conditions	**caffeine**		**CQAs**	
p [bar], T [°C]	mg/40mL	mg/mL (RSD) [%]	mg/40mL	mg/mL (RSD) [%]
7, 88	224.85	5.62 (4.3)	140.67	3.52 (3.9)
9, 88	236.56	5.91 (3.5)	136.17	3.40 (1.6)
11, 88	**222.95**	5.57 (4.5)	**128.56**	3.21 (7.7)
7, 93	235.41	5.89 (0.4)	134.98	3.37 (0.6)
9, 93	**253.17**	6.33 (1.5)	**150.75**	3.77 (4.1)
11, 93	240.35	6.01 (1.0)	139.92	3.50 (3.6)
7, 98	226.45	5.66 (0.9)	141.94	3.55 (1.4)
9, 98	235.94	5.90 (3.6)	137.94	3.45 (3.0)
11, 98	230.25	5.76 (1.7)	133.12	3.33 (0.9)

Table 4.5: Total caffeine and CQAs concentration for samples extracted with Procedure 2.

The extraction configuration that maximises the amount of extracted chemicals is 9 bar, 93 °C, while the configuration that minimises the amount of extracted chemicals is 11 bar, 88 °C.

Numerical results

In this section we present the numerical results of model (2.80),(2.81) obtained by the approximation scheme and the iterative procedure described in Algorithm 1. We discuss two case of study. In the first one we have $I = 1$, so that we can compare experimental and numerical results in terms of the EY. These results have been presented for the first time in [55]. In the second case we set $I = 2$, and we compared the in-silico extractions with real extractions in terms of extracted substances. This case of study has been presented for the first time in [21].

Extraction Yield prediction

The numerical solution of model (2.80),(2.81) with $I = 1$ is obtained by the approximation scheme (4.10), (4.11) and the iterative procedure described in Algorithm 1. This method has been implemented in MATLAB together with the mass computation formulas of Section 2.4 to show the mass conservation of the model, and also the EY, i.e., formula (2.90), to compare the numerical results with the experimental results described in the previous section.

In the numerical simulations, the physico-chemical parameters of the model are the same used in literature; in particular, the solid diffusivity $D^f = 6.25 \cdot 10^{-10}$ m^2/s [19], the liquid diffusivity $D = 1.0 \cdot 10^{-8}$ m^2/s [19], the concentration of saturation $c_{\text{sat}} = 212.4$ kg/m^3 [19], the initial solid concentration $c_{s0} = 200$ kg/m^3 [22] considering the extractable mass of coffee grains at 90°C reaching about 30% of the coffee bed, the total solid fraction $\phi = 0.8272$ [19], whereas the reaction rate $k_r = 6.0 \cdot 10^{-9}$ m^7/kg^2 has been fitted to the experiments. Regarding the parameters of the discretisation scheme, we choose $N = 4, M = 5$ thus the orders of the length of space steps are $h_z \approx 10^{-3}, h_f \approx 10^{-6}, h_b \approx 10^{-5}$; time steps are $N_t = 1000$ thus $h_t \approx 10^{-2}$; the parameter p in (4.4) is 0.1. The relaxation parameter ω depends on the time step, in particular, $\omega = 0.8$, if $n = 1$; $\omega = 0.1$, otherwise. Finally, in Algorithm 1 the tolerances are $tol_1 = tol_2 = 10^{-10}$ and the maximum number of allowed iterations are $maxit_1 = maxit_2 = 1000$. We note that, although the rough spatial discretisation with $N = 4$ and $M = 5$, they seem sufficient to describe the dynamics of the process. In fact, we have also performed similar simulations with doubled parameters, i.e., $N = 8, M = 10$, obtaining the same behaviour of the results described below.

Moreover, with this model the temperature and pressure control is indirect, in fact temperature and pressure are not parameter of the model. However, their control is indirectly allowed by acting on the Darcy's flux. On the other hand, we observe that the granulometry is the parameter of the model with the major impact on the simulated EY.

In the following, we show the results of the model calibration. We select these

six extractions: EF_{CA}, F_M, O_M, O_{CA}, C_M, EC_{CA}, where the normal-size letters are the acronym of the granulometry (EF extre fine, F fine, O optimal C coarse and EC extra coarse) and the subscript letters identify the coffee type (CA Cibao Altura, M Modoetia). In Table 4.6 we summarized the geometrical and physical parameters due to the granulometry of each sample. In more details, a^f, a^b come from the granulometry analyses reported in Figures 4.1,4.2, while ϕ^f is obtained from the volume percentage covered by all the fine particles and the total solid fraction ϕ. In Figure 4.4, we show the values of the Darcy's flux q, on the y-axis,

Sample	a^f [µm]	a^b [µm]	ϕ^f	τ [s]
EF_{CA}	16.6	187.4	0.27	75
F_M	15.5	200.0	0.24	41
O_M	16.6	227.0	0.22	26
O_{CA}	16.6	213.0	0.22	28
C_M	15.6	227.0	0.20	21
EC_{CA}	16.5	242.0	0.17	16

Table 4.6: Geometrical and physical parameters of the simulated extractions with $I = 1$.

as function of granulometry obtained from the model calibration. In particular, the granulometry is represented by the solid fraction of fines ϕ^f, shown on the x-axis. The fines radius is reported on the legend. Markers of the same shape and colour identify a unique value of Darcy's flux. Figure 4.4 shows five different values for q corresponding to the granulometry types taken into account. In particular, the extra coarse granulometry corresponds to the value of Darcy's flux $q = 7 \cdot 10^{-4}$ m/s; the coarse granulometry to $q = 5.3 \cdot 10^{-4}$ m/s; the optimal granulometry to $q = 4.5 \cdot 10^{-4}$ m/s; the fine granulometry to $q = 3.0 \cdot 10^{-4}$ m/s; the extra-fine granulometry to $q = 1.5 \cdot 10^{-4}$ m/s. We note that, if we read the picture from smaller to bigger values of ϕ^f, we can identify five vertical regions, divided by the dashed lines, corresponding to granulometries with increasing fineness and for which

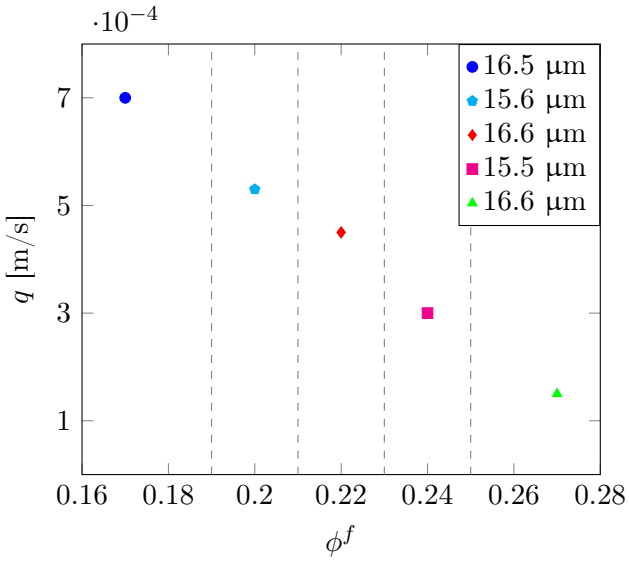

Figure 4.4: Distribution of the Darcy's flux values on the y-axis, as function of granulometry data: ϕ^f on the x-axis and a^f reported in the legend.

a decreasing value of q has to be prescribed. Thus, q is inversely proportional to the granulometry. In fact, as we expect, the coarser the granulometry the lower the resistance of the porous medium and the higher the value of q. In addition, the point $q = 4.5 \cdot 10^{-4}$ in Figure 4.4, is given by the superposition of samples $\mathrm{O_M}$ and $\mathrm{O_{CA}}$, which have very similar granulometry features and so the same Darcy's flux value. This result confirms what we expected from the experimental campaign: if grinded in a similar way, different types of coffee can produce beverages with similar EY values.

Table 4.7, reports the EY values computed by using Eq. (2.90), where the integral has been approximated by the trapezoidal rule. We reported the Darcy's flux values and the corresponding EY ranges from the laboratory experiments as well, for the reader's convenience. The simulated EY values are in agreement with those calculated from the TDS measurements in Tables 4.2,4.3. In particular, the samples $\mathrm{O_{CA}}$, $\mathrm{C_M}$, $\mathrm{EC_{CA}}$ show a numerical EY falling in the range values of the measured EY for the corresponding samples in Tables 4.2,4.3. On the other hand, the remaining samples have a numerical EY that is very close to the range identified by the measured EY, in more details, the EY of $\mathrm{EF_{CA}}$, $\mathrm{F_M}$ and $\mathrm{O_M}$ underestimate

Sample	$q\,[10^{-4}\mathrm{m/s}]$	**EY** [%]	**Experimental EY range** [%]
$\mathrm{EF_{CA}}$	1.5	21.03	$21.45 - 21.80$
$\mathrm{F_M}$	3.0	21.79	$22.07 - 22.58$
$\mathrm{O_M}$	4.5	19.75	$20.43 - 20.87$
$\mathrm{O_{CA}}$	4.5	20.92	$20.34 - 21.35$
$\mathrm{C_M}$	5.3	19.36	$19.09 - 20.11$
$\mathrm{EC_{CA}}$	7.0	18.37	$18.02 - 19.14$

Table 4.7: Numerical results of the EY with the corresponding Darcy's flux values.

the measured EY of about 2.0%, 1.3% and 3.3%, respectively.

The proposed method preserves the two main features of mass transport: the mass conservation and the positivity of the solution. We show some numerical evidence of these features in Table 4.8 and Figure 4.5, respectively. Table 4.8 shows the numerical mass conservation of system (4.10),(4.11). We denote with $\mathcal{M}_t$ the total mass of the system at time t,

$$\mathcal{M}_t = \left(\mathcal{M}^l + \mathcal{M}^f + \mathcal{M}^b + \mathcal{M}^{\mathrm{cup}}\right)\Big|_t,$$

where the liquid and solid phase mass and the mass of substances already dropped into the cup have been defined in Section 2.4. We denote with $\mathcal{M}_0$ the total mass at time $t = 0$. Obviously, at $t = 0$, only $\mathcal{M}^f, \mathcal{M}^b > 0$. Similarly, we denote with $\mathcal{M}_\tau$ the total mass at the end of the extraction. As it can be seen in Table 4.8, $\mathcal{M}_0$ and $\mathcal{M}_\tau$ are strictly close to each other and within a difference of less than 3.4%. Some oscillation in the total mass occurs at the initial time steps, but, at the end of the simulation, we have mass conservation. This initial oscillatory behaviour is due to the fact that the numerical simulation needs some initial steps before reaching stability.

Finally, Figure 4.5 reports the qualitative behaviour of the liquid and solid concentrations over time at about half the height of the coffee powder, i.e., $L/2$, for the sample $\mathrm{O_M}$, other samples showed similar behaviours. In both Figures 4.5(a), 4.5(b), the black line correspond to the liquid concentration c^l, which is null at the initial

Sample	$\mathcal{M}_0$ [g]	$\mathcal{M}_\tau$ [g]
EF_{CA}	5.7	5.6
F_M	6.0	5.9
O_M	5.9	5.7
O_{CA}	5.9	5.8
C_M	6.4	6.2
EC_{CA}	6.4	6.2

Table 4.8: Mass conservation of the numerical scheme: comparison between the initial mass $\mathcal{M}_0$ and the final mass $\mathcal{M}_\tau$.

time and it soon undergoes a steep increase due to the dissolution of substances. Then, for increasing times, as the amount of coffee in the cup increases, the liquid concentration into the filter basket decreases. The red and blue curves in Figure 4.5(a) are the solid concentration of fines c^f at the centre of the particles and at the boundary, respectively. The fine particle releases its soluble material very quickly and it is rapidly depleted by dissolution and diffusion. The three lines, after few initial seconds, closely follow each other, in particular, the corresponding values show that the red line is slightly above the blue line, which is slightly above the black one. Moreover, since the blue and red curves of the fines external layer and inner core, respectively, almost coincide with the curve of liquid concentration, G^f is small, meaning that after an initial peak the contribution of the fines decreases. We note the constant trend of the fines concentration between 1 s and 5 s. Here $G^f \equiv 0$ since $c^f < c^l$, thus the dissolution of fines stops and their concentration remains constant. Figure 4.5(b) shows the behaviour of the solid concentration of boulders c^b at the centre of the particle and at the boundary, respectively corresponding to the cyan and violet curves. Here the external layer feels the dissolution much more than the core, which initially remains quite unmodified. Besides, the violet line always follows the black line from above, thus the external layer of boulders resists the dissolution better than fines and its contribution lasts till the end of the

extraction.

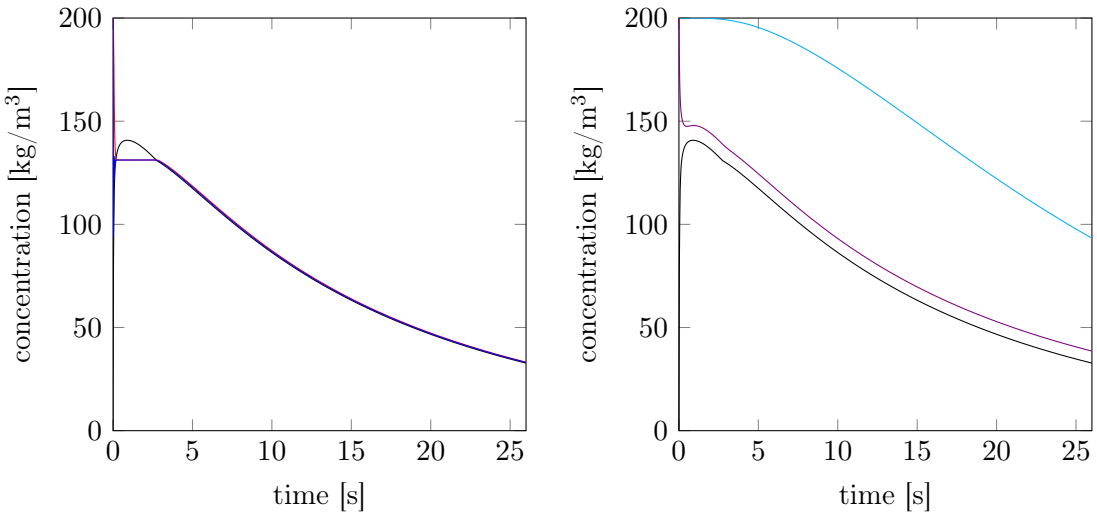

Figure 4.5: Concentration curves during the simulated extraction of O_M sample at half height of the coffee powder: (a) concentrations of liquid (black), fine's centre (red), fine's boundary (blue), (b) concentrations of liquid (black), boulder's centre (cyan), boulder's boundary (violet).

Prediction of the extracted chemicals substances

The numerical solution of problem (2.80),(2.81) with $I = 2$ is obtained by the approximation scheme (4.10), (4.11) and iterative procedure described in Algorithm 1. We implemented this procedure in a MATLAB program.

In the numerical simulations the physico-chemical parameters used in the model are in good agreement with those used in [19], [55] and [23]. Table 4.9 shows the configuration of these parameters for the in-silico extractions, whose value depends on the substance.

Moreover, the liquid diffusivity is $D = 1.0 \cdot 10^{-8}$ m^2/s, and the total solid fraction is $\phi = 0.7$. The discretisation parameters are the same used for the EY prediction. In more details, we set $N = 4, M = 5$ in such a way that $h_z \approx 10^{-3}, h_f \approx 10^{-6}, h_b \approx$

substance	k_r [m^7/kg^2]	D^f [m^2/s]	c_{sat} [kg/m^3]	c_{s0} [kg/m^3]	c_{dis} [kg/m^3]
caffeine	$9.6 \cdot 10^{-10}$	$9.0 \cdot 10^{-10}$	212.4	16.24	0.5
CQAs	$1.7 \cdot 10^{-9}$	$1.0 \cdot 10^{-10}$	75.0	37.17	0.1

Table 4.9: Parameters configuration used in the numerical simulation, for each traced chemical substance.

10^{-5}; the time steps are $N_t = 1000$, thus $h_t \approx 10^{-2}$; the parameter p in (4.4) is 0.1. Furthermore, the relaxation parameter $\omega = 0.8$, if $n = 1$; $\omega = 0.1$, otherwise. Finally, in Algorithm (1), the chosen tolerances are $tol_1 = tol_2 = 10^{-10}$ and the maximum number of allowed iterations are $maxit_1 = maxit_2 = 1000$, but only in the first time step is required such a large number of sub-iterations.

The geometrical and physical parameters due to the granulometry of the samples are reported in Table 4.10. In particular, a^f, a^b come from the granulometry analyses shown in Figure 4.3, again the fine solid fraction ϕ^f is obtained considering the volume percentage covered by all the particles smaller than 100 µm and the total solid fraction ϕ.

a^f [µm]	a^b [µm]	ϕ^f	q [m/s]
14.63	227	0.18	$q = 4.5 \cdot 10^{-4}$

Table 4.10: Geometrical and physical parameters of the simulated extractions.

In Table 4.11 we show the results of the numerical simulations performed with the discussed parameters setting.

The concentration of the substances obtained by numerical simulation are in completely agreement with those coming from laboratory analyses. Figure 4.6

caffeine [mg/mL]	**CQAs** [mg/mL]
5.78	3.48

Table 4.11: Results of the numerical simulation for the prediction of the extracted chemicals substances.

shows the comparison between the numerical and experimental results, where the chemicals are reported along the x-axis. In particular, the black vertical bars identify the range spotted by the chemical analyses. The lighter-colour circular markers represent the expected value, calculated as the average of the experimental data, while the darker-colour square markers are the results of the numerical simulations. In more details, the simulated value for the caffeine is very close to the corresponding

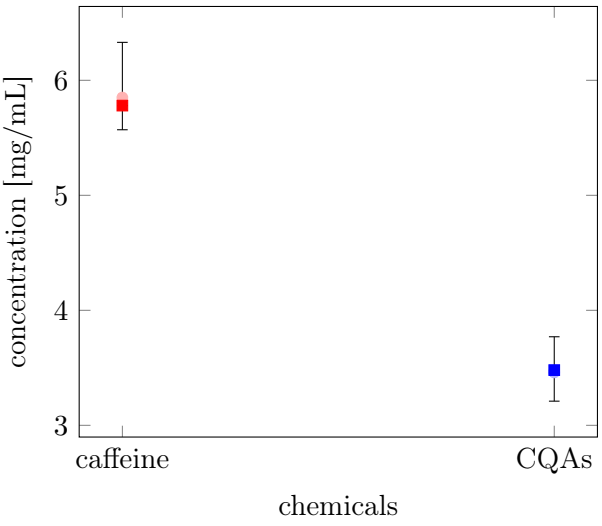

Figure 4.6: Comparison between simulated and extracted caffeine and CQAs, in the case of interaction among species.

expected value, while the simulated value for the CQAs is completely superposed on the corresponding expected value.

Finally, in Table 4.12 we report the simulated caffeine and CQAs values under varying the discretisation parameters N and M, in the case of interaction among species. Moreover, we added the absolute error between the simulated and extracted

values in brackets, to give some numerical evidence of the accuracy of the proposed solving strategy. Also, in Table 4.12 we report the execution time of Algorithm 1. The results have been obtained on a PC equipped with an Intel(R) Core(TM) i7-10510U CPU @ 1.80GHz 2.30GHz, operative system Windows 10.

N, M	**caffeine** (E) [mg/mL]		**CQAs** (E) [mg/mL]		**execution time** [s]
3, 4	5.64	(0.21)	3.49	(0.03)	4.2
4, 5	5.78	(0.07)	3.48	(0.02)	5.3
5, 6	5.85	(0.00)	3.45	(0.01)	6.3

Table 4.12: Comparison of the numerical simulations under varying discretisation parameters.

4.1.2 An RBF-based approximation

In this section, we describe an RBF-based numerical approximation of problem (2.80)-(2.81). This approximation scheme is based on the Crank-Nicolson method, as in the previous approach, but now the spatial derivatives are approximated via RBFs. Then, with the results of the same experimental extraction campaign presented in Extraction Procedure 1 we describe the corresponding numerical simulations. In particular, since such simulations have the same operative parameters of the real extractions, we make a comparison between them in terms of the EY. Such numerical results together with the approximation scheme discussed in this section, has been presented for the first time in [84]. Before proceeding, we would like to point out that, since the purpose of numerical simulations is the prediction of EY, i.e., $I = 1$. For the sake of simplicity, in presenting the numerical scheme we omit all indexes species-related.

Numerical approximation

Let $\mathcal{Z} = \{z_j\}_{j=0,1,\dots,N} \subseteq [0, L]$ be a set of distinct discretisation nodes along the vertical direction, such that $z_0 = 0$ and $z_N = L$. Let z_{-1} be a node in a left neighbourhood of 0 and z_{N+1} be a node in a right neighbourhood of L, we choose $\bar{\mathcal{Z}} = \mathcal{Z} \cup \{z_{-1}, z_{N+1}\}$ as the set of the approximation nodes. In Figure 4.7, we show the points of $\mathcal{Z}$ in blue, and the points of $\bar{\mathcal{Z}} \setminus \mathcal{Z}$ in red.

Similarly, for $s = b, f$, let $\mathcal{R}^s = \{r_k^s\}_{k=0,1,\dots,M^s} \subseteq [0, a^s]$ be a set of distinct discretisation nodes along the radial direction in fines and boulders, respectively, we use $\bar{\mathcal{R}}^s = \mathcal{R}^s \cup \{r_{-1}^s, r_{M^s+1}^s\}$ as the set of approximation nodes in the radial direction, where r_{-1}^s is a point in a left neighbourhood of 0 and $r_{M^s+1}^s$ in a right neighbourhood of a^s.

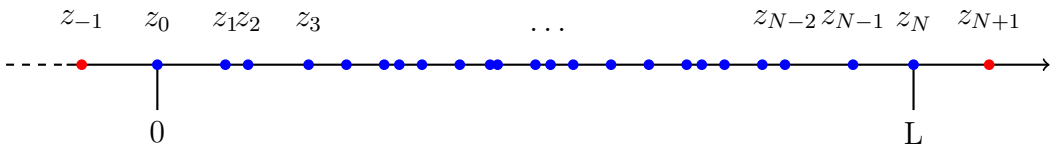

Figure 4.7: Graphical representation of points in $\bar{\mathcal{Z}}$.

Let Z and R^s, $s = f, b$, be the polynomially augmented RBF (PA-RBF) interpolation matrices associated with the nodes $\bar{\mathcal{Z}}$ and $\bar{\mathcal{R}}^s$, respectively. We note that these matrices are such that equations (3.40) hold and $d = 1$. Thus, for a fixed time t, if we collect in the vector $\boldsymbol{c}^l(t)$ the values of the liquid concentration $c^l(z, t)$ calculated at the points of $\bar{\mathcal{Z}}$, that is $\boldsymbol{c}^l(t) = \left(c^l(z_j, t)\right)_{j=-1,0,\dots,N+1}$, the analogue of relation (3.43) for the liquid concentration c^l, is:

$$\mathcal{L}\hat{c}^l(z, t) = \left(\boldsymbol{b}(z)^{\mathcal{L}} Z^{-1}\right)_{-1:N+1} \boldsymbol{c}^l(t), \tag{4.12}$$

where $\hat{c}^l(z, t)$ denotes the approximation of $c^l(z, t)$ with formula (3.38). Similarly, for fixed t and z, if we collect the values of the solid concentrations $c^s(r, z, t)$, $s = f, b$, calculated at the points of $\bar{\mathcal{R}}^s$ in the vectors $\boldsymbol{c}^s(z, t)$, that is $\boldsymbol{c}^s(z, t) = (c^s(r_k^s, z, t))_{k=-1,0,\dots,M^s+1}$, the analogue of relation (3.43) for the solid concentrations c^s are:

$$\mathcal{L}\hat{c}^s(r, z, t) = \left(\boldsymbol{b}(r)^{\mathcal{L}} (R^s)^{-1}\right)_{-1:M^s+1} \boldsymbol{c}^s(z, t), \tag{4.13}$$

where $\hat{c}^s(z,t)$ denotes the approximation of $c^s(z,t)$ with formula (3.38).

We denote with $\mathcal{L}_0$ the identity operator and with $\mathcal{L}_1$ and $\mathcal{L}_2$ the first and second derivative operators respect to z, respectively. For each of these operators, we can consider relation (4.12) at each point of $\mathcal{Z}$. For instance, for the first derivative, this leads to:

$$\left(\mathcal{L}_1\hat{c}^l(z_j,t)\right)_{j=0,1,\dots,N} = \left(Z_z Z^{-1}\right)_{:,-1:N+1} \boldsymbol{c}^l(t) \equiv Z^z \boldsymbol{c}^l(t), \tag{4.14}$$

where $Z_z \equiv \left(\boldsymbol{b}(z_j)^{\mathcal{L}_1}\right)_{j=0,1,\dots,N}$ has $N+1$ rows, moreover, $Z^z = (Z_z Z^{-1})_{:,-1:N+1}$ is called differentiation matrix of first order. Similarly, for $\mathcal{L}_0$ and $\mathcal{L}_2$ with matrices Z_0 and Z_{zz}, respectively.

Similarly, for fixed z_j we can consider relation (4.13) in each point of $\mathcal{R}^s$. For the second order differential operator respect to r, that with an abuse of notation we denote with $\mathcal{L}_2$, this leads to:

$$(\mathcal{L}_2\hat{c}^s(r_k^s,z_j,t))_{k=0,1,\dots,M^s} = \left(R^s_{rr}\left(R^s\right)^{-1}\right)_{:,-1:M^s+1} \boldsymbol{c}^s(z_j,t) \equiv R^{s,rr}\boldsymbol{c}^s(z_j,t), \tag{4.15}$$

where $R^s_{rr} \equiv \left(\boldsymbol{b}(r_k^s)^{\mathcal{L}_2}\right)_{k=0,1,\dots,M^s}$, $s=f,b$, defines the differentiation matrices of second order in the radial direction $R^{s,rr}$. Similarly, for $\mathcal{L}_0$ and $\mathcal{L}_1$ with matrices R^s_0 and R^s_r, respectively, for $s=f,b$.

In more detail, we have the following matrices:

$$\begin{aligned}
I^z &= \left(Z_0 Z^{-1}\right)_{:,-1:N+1},\\
Z^z &= \left(Z_z Z^{-1}\right)_{:,-1:N+1},\\
Z^{zz} &= \left(Z_{zz} Z^{-1}\right)_{:,-1:N+1},\\
I^s &= \left(R^s_0\left(R^s\right)^{-1}\right)_{:,-1:M^s+1}, \quad s=f,b,\\
R^{s,r} &= \left(R^s_r\left(R^s\right)^{-1}\right)_{:,-1:M^s+1}, \quad s=f,b,\\
R^{s,rr} &= \left(R^s_{rr}\left(R^s\right)^{-1}\right)_{:,-1:M^s+1}, \quad s=f,b.
\end{aligned}$$

We define some useful notations for the following approximation scheme. A matrix endowed with the subscript j denotes the single j-th row of the corresponding original matrix (i.e., the matrix without the subscript j). This means that, regardless of the vertical or radial coordinate, the subscript 0 denotes the first row of the matrix that corresponds to the point $z_0 = 0$ or $r^s_0 = 0$, $s=f,b$, respectively. Similarly,

the subscripts N and M^s, $s = f, b$ denote the row of the matrix corresponding to the boundary points $z_N = L$ and $r^s_{M^s} = a^s$, $s = f, b$, respectively. Moreover, in the following solid systems, we use this notation: a matrix equipped with the subscript I is the sub-matrix that consists of all the rows of the corresponding original matrix except the ones corresponding to the left boundary point, $z_0 = 0$ or $r^s_0 = 0$, $s = f, b$, that is for instance: $R^{s,r}_I = (R^{s,r})_{1:M^s,:}$.

With the aforementioned notations, we can express the liquid phase system as:

$$\begin{cases} (1-\phi)\, I^z \dfrac{\partial \boldsymbol{c}^l(t)}{\partial t} &= DZ^{zz}\boldsymbol{c}^l(t) - qZ^z\boldsymbol{c}^l(t) + b^f\boldsymbol{G}^f(t) + b^b\boldsymbol{G}^b(t), \\ -DZ^z_0\boldsymbol{c}^l(t) + qI^z_0\boldsymbol{c}^l(t) &= 0, \\ -DZ^z_N\boldsymbol{c}^l(t) &= 0, \\ \boldsymbol{c}^l(0) &= 0, \end{cases} \tag{4.16}$$

where for each vertical level z_j, $j = 0, 1, \ldots, N$, we collect the reactive terms into vectors $\boldsymbol{G}^s(t)$, $s = f, b$, whose components are given by:

$$G^s(z_j, t) = k_r I^s_{M^s}\boldsymbol{c}^s(z_j, t) \max\left(I^s_{M^s}\boldsymbol{c}^s(z_j, t) - I^z_j\boldsymbol{c}^l(t), 0\right) \max\left(c_{\text{sat}} - I^z_j\boldsymbol{c}^l(t), 0\right).$$

For each vertical level z_j, $j = 0, 1, \ldots, N$, there are two problems of kind (2.81) for the solution of the solid phase, coupled to the liquid phase through the non-linear source terms. For $s = f, b$, they are given by:

$$\begin{cases} I^s_I \dfrac{\partial \boldsymbol{c}^s(z_j, t)}{\partial t} &= D^f\left(\dfrac{2}{r}R^{s,r}_I\boldsymbol{c}^s(z_j, t) + R^{s,rr}_I\boldsymbol{c}^s(z_j, t)\right), \\ I^s_0 \dfrac{\partial \boldsymbol{c}^s}{\partial t}(z_j, t) &= 3D^f R^{s,rr}_0\boldsymbol{c}^s(z_j, t), \\ -D^f R^{s,r}_0\boldsymbol{c}^s(z_j, t) &= 0, \\ -D^f R^{s,r}_{M^s}\boldsymbol{c}^s(z_j, t) &= G^s(z_j, t), \\ \boldsymbol{c}^s(z_j, 0) &= c_0. \end{cases} \tag{4.17}$$

We note that at $r = 0$, the discretisation (4.6) based on De L'Hôpital rule has been used.

Now we can apply the time discretisation to problems (4.16), (4.17) similarly as we did in the finite differences approximation. In more details, we use the Crank-Nicolson method for both linear and non-linear parts where the boundary

conditions are implemented at the new time level. Note that when we indicate a discrete time level, we use the time index as a superscript.

We start with the time discretisation of the PDE for the liquid phase. Let N_t be a positive integer and $h_t = \tau/N_t$; for $n = 0, 1, \ldots, N_t - 1$ we have:

$$(1-\phi)\, I^z(\boldsymbol{c}^{l,n+1} - \boldsymbol{c}^{l,n}) =$$
$$\frac{h_t}{2}\left(DZ^{zz}\boldsymbol{c}^{l,n+1} - qZ^z\boldsymbol{c}^{l,n+1} + b^f\boldsymbol{G}^{f,n+1} + b^b\boldsymbol{G}^{b,n+1} + DZ^{zz}\boldsymbol{c}^{l,n} - qZ^z\boldsymbol{c}^{l,n} + b^f\boldsymbol{G}^{f,n} + b^b\boldsymbol{G}^{b,n}\right),$$

where $\boldsymbol{c}^{l,n} \approx \boldsymbol{c}^l(t_n)$, $n = 0, 1, \ldots, N_t$. Thus, we get:

$$\begin{cases} \left[(1-\phi)\, I^z - \dfrac{h_t}{2}\left(DZ^{zz} - qZ^z\right)\right]\boldsymbol{c}^{l,n+1} &= \left[(1-\phi)\, I^z + \dfrac{h_t}{2}\left(DZ^{zz} - qZ^z\right)\right]\boldsymbol{c}^{l,n} \\ & \quad + \dfrac{h_t}{2}\left(b^f\boldsymbol{G}^{f,n+1} + b^b\boldsymbol{G}^{b,n+1}\right) + \\ & \quad + \dfrac{h_t}{2}\left(b^f\boldsymbol{G}^{f,n} + b^b\boldsymbol{G}^{b,n}\right), \\ -DZ_0^z\boldsymbol{c}^{l,n+1} + qI_0^z\boldsymbol{c}^{l,n+1} &= 0, \\ -DZ_N^z\boldsymbol{c}^{l,n+1} &= 0, \\ \boldsymbol{c}^{l,0} &= 0. \end{cases} \tag{4.18}$$

We do the same for the solid phases; so for $s = f, b$, we get

$$I_I^s\left(\boldsymbol{c}^{s,n+1}(z_j) - \boldsymbol{c}^{s,n}(z_j)\right) =$$
$$= \frac{h_t}{2}D^f\left(\frac{2}{r}R_I^{s,\,r}\boldsymbol{c}^{s,n+1}(z_j) + R_I^{s,\,rr}\boldsymbol{c}^{s,n+1}(z_j) + \frac{2}{r}R_I^{s,\,r}\boldsymbol{c}^{s,n}(z_j) + R_I^{s,\,rr}\boldsymbol{c}^{s,n}(z_j)\right),$$

where $\boldsymbol{c}^{s,n}(z_j) \approx \boldsymbol{c}^s(z_j, t_n)$, $j = 0, \ldots, N$, $n = 0, 1, \ldots, N_t$. Thus, we get:

$$\begin{cases} \left[I_I^s - \dfrac{D^f h_t}{2}\left(\dfrac{2}{r}R_I^{s,\,r} + R_I^{s,\,rr}\right)\right]\boldsymbol{c}^{s,n+1}(z_j) &= \left[I_I^s + \dfrac{D^f h_t}{2}\left(\dfrac{2}{r}R_I^{s,\,r} + R_I^{s,\,rr}\right)\right]\boldsymbol{c}^{s,n}(z_j), \\ \left[I_0^s - \dfrac{3D^f h_t}{2}R_0^{s,\,rr}\right]\boldsymbol{c}^{s,n+1}(z_j) &= \left[I_0^s + \dfrac{3D^f h_t}{2}R_0^{s,\,rr}\right]\boldsymbol{c}^{s,n}(z_j), \\ -D^f R_0^{s,r}\boldsymbol{c}^{s,n+1}(z_j) &= 0, \\ -D^f R_{M^s}^{s,r}\boldsymbol{c}^{s,n+1}(z_j) &= G^{s,n+1}(z_j), \\ \boldsymbol{c}^{s,0}(z_j) &= c_0, \end{cases} \tag{4.19}$$

In systems (4.19), the concentrations $\boldsymbol{c}^{s,n}(z_j)$, $s = f, b$ depend on z_j, therefore such systems must be solved for each vertical level z_j. Moreover, systems (4.18), (4.19) are coupled through the reactive terms G^s, whose approximations $G^{s,n}(z_j)$, $s = f, b$, are obtained from

$$G^{s,n}(z_j) = k_r I^s_{M^s} \boldsymbol{c}^{s,n}(z_j) f_p\left(I^s_{M^s}\boldsymbol{c}^{s,n}(z_j) - I^z_j \boldsymbol{c}^{l,n}\right) f_p\left(c_{\text{sat}} - I^z_j \boldsymbol{c}^{l,n}\right),$$

where, for $p > 0$ sufficiently small, f_p is the continuous and differentiable approximation of the function $\max(x, 0)$ defined in (4.4).

In matrix form, the complete system can be written as

$$A\boldsymbol{\sigma}_{n+1} = C\boldsymbol{\sigma}_n + \boldsymbol{\varphi}_{n+1}, \qquad n = 0, \ldots, N_t - 1, \tag{4.20}$$

$$B\boldsymbol{\lambda}_{n+1} = E\boldsymbol{\lambda}_n + \boldsymbol{\psi}_{n+1} + \boldsymbol{\psi}_n, \qquad n = 0, \ldots, N_t - 1, \tag{4.21}$$

where

$$\begin{aligned}
&A, C \in \mathbb{R}^{(N+1)(M^f+M^b+6)\times(N+1)(M^f+M^b+6)},\\
&B, E \in \mathbb{R}^{(N+3)\times(N+3)},\\
&\boldsymbol{\sigma}_n \in \mathbb{R}^{(N+1)(M^f+M^b+6)}, \boldsymbol{\lambda}_n \in \mathbb{R}^{N+3}, \qquad n = 0, \ldots, N_t - 1,\\
&\boldsymbol{\varphi}_n \in \mathbb{R}^{(N+1)(M^f+M^b+6)}, \boldsymbol{\psi}_n \in \mathbb{R}^{N+3}, \qquad n = 0, \ldots, N_t - 1.
\end{aligned}$$

The vectors $\boldsymbol{\sigma}_n$ and $\boldsymbol{\lambda}_n$ are defined as:

$$\begin{aligned}
\boldsymbol{\sigma}_n &= \begin{pmatrix} \mathbf{c}^{f,n} \\ \mathbf{c}^{b,n} \end{pmatrix},\\
\boldsymbol{\lambda}_n &= \left(c^{l,n}_{-1}, c^{l,n}_0, \ldots, c^{l,n}_{N+1}\right)^T,
\end{aligned} \tag{4.22}$$

with

$$\begin{aligned}
\mathbf{c}^{f,n} = \Big(&c^{f,n}_{-1}(z_0), c^{f,n}_0(z_0), \ldots, c^{f,n}_{M^f+1}(z_0), c^{f,n}_{-1}(z_1), c^{f,n}_0(z_1), \ldots, c^{f,n}_{M^f+1}(z_1), \ldots,\\
&c^{f,n}_{-1}(z_N), c^{f,n}_0(z_N), \ldots, c^{f,n}_{M^f+1}(z_N), \Big)^T,
\end{aligned}$$

and analogously for the vector $\mathbf{c}^{b,n}$. In particular $\boldsymbol{\sigma}_n$ and $\boldsymbol{\lambda}_n$ are unknown for $n \geq 1$, instead $\boldsymbol{\lambda}_0$ is the null vector and, for $s = f, b$, $\boldsymbol{c}^{s,0}$ are the vectors having all entries equal to c_0.

The vectors with the non-linear terms are defined as

$$\boldsymbol{\varphi}_n = \begin{pmatrix} \mathbf{F}_n^f \\ \mathbf{F}_n^b \end{pmatrix},$$

$$\boldsymbol{\psi}_n = \left(0, \frac{h_t}{2} b^f G^{f,n}(z_0) + \frac{h_t}{2} b^b G^{b,n}(z_0), \ldots, \frac{h_t}{2} b^f G^{f,n}(z_N) + \frac{h_t}{2} b^b G^{b,n}(z_N), 0\right)^T,$$

with

$$\mathbf{F}_n^s = (0, \ldots, 0, G^{s,n}(z_0), 0, \ldots, 0, \ldots, 0, G^{s,n}(z_N), 0)^T,$$

$s = f, b$. Thus, the unique non-zero elements of $\mathbf{F}_n^s$ are in the positions given by $M^s + 2 + k(M^s + 3)$, $k = 0, \ldots, N$. For the solution of system (4.20), (4.21) we apply the nested fixed-point iteration procedure resumed in Algorithm 1.

More in detail, for each time step $n = 0, \ldots, N_t - 1$, we consider the following nested fixed-point iteration:

$$A\boldsymbol{\sigma}_{n+1}^{\mu,\nu} = C\boldsymbol{\sigma}_n + \boldsymbol{\varphi}_{n+1}^{\mu,\nu-1}, \tag{4.23}$$

$$B\boldsymbol{\lambda}_{n+1}^{\mu,\nu} = E\boldsymbol{\lambda}_n + \boldsymbol{\psi}_{n+1}^{\mu,\nu-1} + \boldsymbol{\psi}_n, \tag{4.24}$$

where the index ν stands for the inner fixed-point iteration and μ for the outer fixed-point iteration, both relative to the time step $n+1$. We note that, discretising the model with such a scheme, leads to a slightly different solid system to solve than that resulting from the finite difference approximation, since the vector $\boldsymbol{\varphi}_n$ is nedeed only at time $n + 1$. Finally, we note that the convergence of the inner steps has been improved by relaxed iterations with proper parameters ω_l and ω_s, $s = f, b$, which also helps the positivity of the solution at the initial time steps.

Experimental measurements

The experimental campaign of the espresso extraction samples is the same described in Extraction Procedure 1 where we described the equipment, the procedures and the physical parameters of the extraction campaign, as well as the results obtained in terms of EY. Here, for the sake of brevity, we have considered a reduced expeimental campaign with respect to the previous section

Numerical results

The numerical solution of problem (2.80),(2.81) is obtained by the approximation scheme (4.23), (4.24) and the iterative procedure described in Algorithm 1. This method has been implemented in MATLAB together with the EY computation formula (2.90) to compare the numerical and experimental results described in Extraction Procedure 1, where only samples of Modœtia coffee powder have been considered.

In the numerical simulations, the physico-chemical parameters are the same used for the EY prediction in Section 4.1.1, and they are in good agreement with those used in [19], [22]: the reaction rate $k_r = 6.0 \cdot 10^{-9}$ m^7/kg^2 [55], the solid diffusivity $D^f = 6.25 \cdot 10^{-10}$ m^2/s [19], [55], the liquid diffusivity $D = 1.0 \cdot 10^{-8}$ m^2/s [19], [55], the concentration of saturation $c_{\text{sat}} = 212.4$ kg/m^3 [19], [55], the initial solid concentration $c_0 = 200$ kg/m^3 [22], [55], the total solid fraction $\phi = 0.8272$ [19], [55].

Regarding the parameters of the discretisation scheme, the points in $\mathcal{Z}$ are distributed as half of a Chebyshev nodes set in such a way that we have more points near $z = 0$. Instead, the point in $\mathcal{R}^s$ are uniformly distributed. Moreover, as RBFs we choose the polyharmonic splines of exponent 3. That is:

$$\Phi_j(z) = \varphi\left(||z - z_j||\right) = |z - z_j|^3, \quad z_j \in \bar{\mathcal{Z}},$$

$$\Phi_j(r^s) = \varphi\left(||r^s - r_j^s||\right) = |r^s - r_j^s|^3, \quad r_j^s \in \bar{\mathcal{R}}^s,\ s = f, b.$$

The maximum degree of the polynomial basis is $m = 3$. Moreover, we choose $N = 100$, $M^f = 4$, and $M^b = 40$; the numbers of time steps are $N_t = 800, 1000, 1500$, for coarse, optimal and fine granulometry, respectively. Thus $h_t \approx 10^{-2}$; the parameter p in (4.4) is 0.1. The relaxation parameters ω_l and ω_s, $s = f, b$ depend on the time step. In particular, $\omega_l = 0.9$ and $\omega_s = 0.75$, if $n \leq 15$; $\omega_l = \omega_s = 0.1$, $s = f, b$, otherwise. Finally, in Algorithm 1 the tolerances are $tol_1 = 10^{-7}$ and $tol_2 = 10^{-6}$ and the maximum allowed iterations are $maxit_1 = maxit_2 = 500$.

Table 4.13 reports the parameters depending on the granulometry. In particular, a^f and a^b come from the granulometry analyses of Figure 4.2, ϕ^f is calculated considering the volume percentage covered by all the fine particles with respect to the total solid fraction ϕ, the Darcy's flux q is inversely proportional to the

Sample	a^f [µm]	a^b [µm]	ϕ^f	q [10^{-4}m/s]	τ [s]
Fine	15.5	200.0	0.24	3	40
Optimal	16.6	227.0	0.22	4.5	26
Coarse	15.6	227.0	0.20	5.3	20

Table 4.13: Geometrical and physical parameters of the simulated extractions.

granulometry. In fact, the finer the granulometry the higher the resistance of the porous medium, thus the smaller the value of q. Finally, the percolation time τ is obtained as the average of the real extraction times reported in Table 4.3.

In Table 4.14, we show the results of the numerical simulations performed with the previously discussed parameters setting. The EY values are obtained by using Eq. (2.90), where the integral has been approximated by the trapezoidal rule. Also the corresponding EY ranges from the laboratory experiments have been reported. For all the samples, there is a good agreement between numerical and

Sample	**EY** [%]	**Experimental EY range** [%]
Fine	22.53	22.07 – 22.58
Optimal	20.44	20.43 – 20.87
Coarse	19.30	19.09 – 20.11

Table 4.14: Numerical results of the EY with the corresponding EY ranges from the laboratory experiments.

experimental data. In fact, the simulated values fall in the range identified by the experimental data. Figure 4.8 shows the comparison between the numerical and experimental results. In more detail, the granulometry is reported along the x-axis; the black vertical bars represent the EY ranges spotted by the laboratory experiments, instead, the coloured square markers are the values of the simulated EY.

In addition, Figure 4.9 shows the qualitative behaviour of the simulated liquid

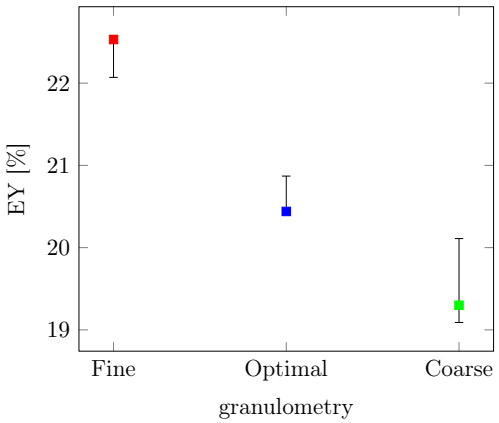

Figure 4.8: Comparison between simulated and real EY values.

concentration over time, for the optimal granulometry sample; similar behaviours are observed for the other granulometries. From Fig. 4.9 we can see that the liquid concentration is null at the initial time and it immediately increases due to the dissolution of substances. Then, for later times, as the amount of the beverage in the cup increases, the liquid concentration in the coffee pod decreases. Figures 4.10, 4.11(a)

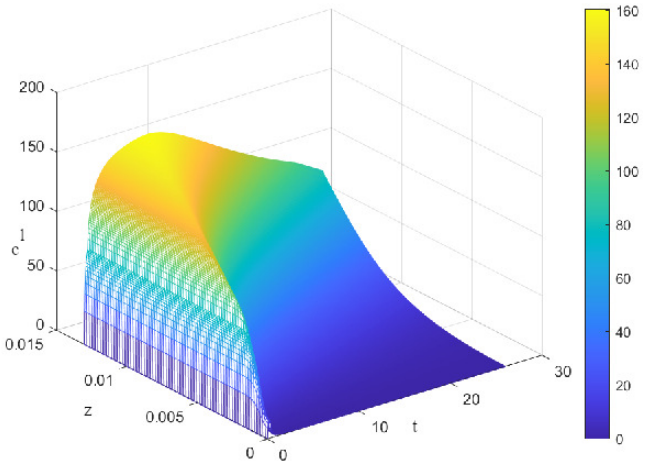

Figure 4.9: Liquid concentration, c^l during the simulated extraction of the sample with optimal granulometry.

show the qualitative behaviour of the simulated solid concentration of boulders and fines respectively, over time at about half the height of the coffee pod, i.e. $L/2$,

for the optimal granulometry sample. From Fig. 4.10 we can see that in boulder particles the external layer is more affected by dissolution than the core, which initially remains quite unmodified. From Fig 4.11(a) we can see that in the first

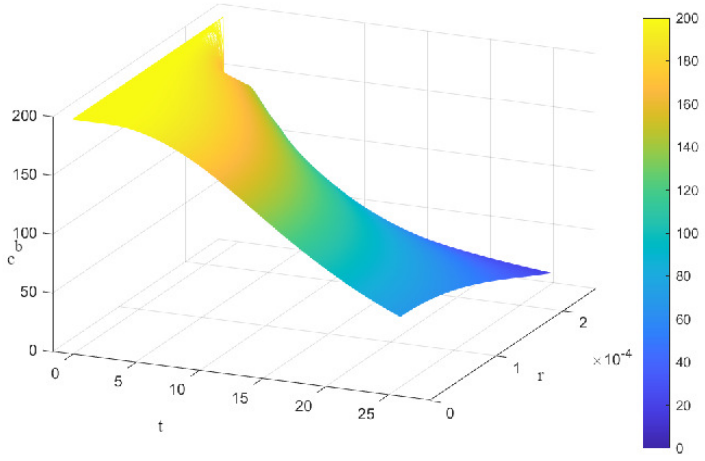

Figure 4.10: Solid concentration of boulders c^b at half the height of the coffee pod, i.e. $z = L/2$, during the simulated extraction of the sample with optimal granulometry.

moments of the extraction the concentration of fine particles immediately decreases due to the dissolution, then for about the next five seconds, the concentration remains constant and finally decreases again, releasing the fines soluble material very quickly. This constant trend is very interesting and it can be easily analysed with Figure 4.11(b), where the liquid and fine solid concentration curves are shown in blue and orange, respectively, over time at about half the height of the coffee powder, i.e., $L/2$. Here we plot the solid concentration of fines at the center of the particle, however, analogous behaviour has been observed also at the boundary. When $c^f < c^l$, then G^f=0, this means that the dissolution of fines stops and their concentration remains constant.

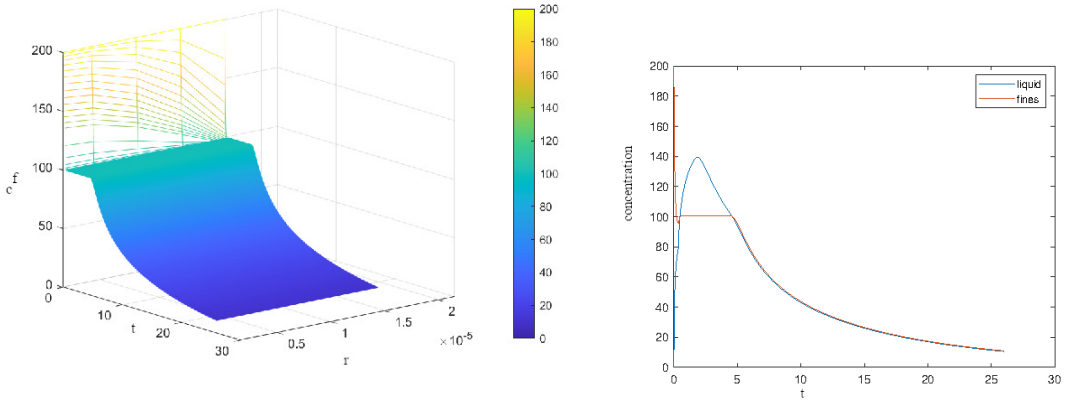

(a) (b)

Figure 4.11: (a) Solid concentration of fines c^f, and (b) Liquid (in blue) and solid concentration of fines at the center of the particle (in orange) at half the height of the coffee pod, i.e. $z = L/2$, during the simulated extraction of the sample with optimal granulometry.

4.2 The 3D model

In this section we describe a numerical experiment for the solution of the model discussed in Section 2.3.5. Such a model predicts the amount of the chemicals substances of interest at the end of the extraction. The numerical experiment we propose consists of two steps. The first step is making the numerical simulations corresponding with the real EC obtained with the Extraction Procedure 3, described below, and used for the chemical analysis. This means that both the real and simulated extraction processes are conducted under the same extraction conditions. The second step is the comparison of the numerical results with the laboratory results. Such kind of numerical experiment is used for the calibration and then validation of the model, over different sets of extractions. In Section 4.2.1 the model used in the numerical experiment is further detailed with the nomenclature of the chemical species of interest, and the numerical scheme for the model approximation is outlined. Then, the results of the experimental extraction campaign are presented in Section 4.2.2. In addition, the settings of the numerical simulations are described

in Section 4.2.3. Finally, the results of the numerical experiment are presented and discussed in Section 4.2.4; the results shown in this section has been presented for the first time in [24].

4.2.1 Numerical approximation

The percolation model takes into account all the species analysed in the chemical analyses; i.e., caffeine (CF), chlorogenic acids (CQAs), trigonelline (TR), citric acid (CA), acetic acid (AA), tartaric acid (TA), ferulic acid (FE), lipids (LP). For greater clarity, instead of using a numeric index for each species, we prefer the use of an alphabetic index corresponding with the acronym of the species. Note that CQAs accounts for the total amount of different derivatives of chlorogenic acids. The model described in Section 2.3.5 can easily consider fines; however, from numerical experiments not reported here, we have that their erosion and transport do not significantly interfere with the other species. Moreover, chemical analyses for fines are not available, given their extreme complexity. Thus, we choose to discard fines, taking in mind the possibility to add them in a future analysis without compromising the validity of the current work. System (2.75) has $N_{l\text{-}s} = 8$ equations for the liquid/solid and solid species. In fact, we recall that each species must be considered both in the liquid and solid phase, because the liquid component $C_k, k =$ CF, CQA, TR, CA, AA, TA, FA, LP, accounts for the amount of that species which is affected by the diffusion and transport phenomena, while the solid component $C_k^s, k =$ CF, CQA, TR, CA, AA, TA, FA, LP accounts for the amount of the same species bound to the porous matrix.

The numerical approximation of model (2.75) is based on the Galerkin method presented in Section 3.2. In the following, we briefly present such a scheme considering a representative PDE for the flow and transport processes: the advection-dispersion equation for the scalar state variable ϕ endowed with the boundary and

initial conditions of interest, that is

$$\begin{cases} \dfrac{\partial \phi}{\partial t} + \boldsymbol{q} \cdot \nabla \phi - \nabla \cdot (\boldsymbol{D} \cdot \nabla \phi) + \phi \nabla \cdot \boldsymbol{q} - Q = 0, & \text{in } \Omega, t \in [0, \tau], \\ \phi = \phi_D, & \text{on } \Gamma_D, t \in [0, \tau], \\ \nabla \phi \cdot \mathbf{n} = q_N & \text{on } \Gamma_N, t \in [0, \tau], \\ -(D \cdot \nabla \phi) \cdot \mathbf{n} = -\Phi \min\{\phi_c - \phi, 0\}, & \text{on } \Gamma_C, t \in [0, \tau], \\ \phi = \phi_0, & \text{on } \Omega, t = 0, \end{cases} \tag{4.25}$$

where Ω is the spatial domain, Q is a source/sink term, ϕ_D is the known value of ϕ on the Dirichlet boundary Γ_D, q_N is the flux at the Neumann boundary Γ_N, Φ, ϕ_c are the transfer coefficient and a reference value for ϕ, respectively, prescribed on the Cauchy boundary Γ_C, finally, ϕ_0 is the value of the initial condition for ϕ. We suppose that the spatial domain Ω is discretised through an unstructured mesh made of N_e triangular prisms Ω^e, $e = 1, \ldots, N_e$. The solution ϕ is approximated by $\hat{\phi}$:

$$\phi(\boldsymbol{x}, t) \approx \hat{\phi}(\boldsymbol{x}, t) = \sum_{i=1}^{N_D} B_i(\boldsymbol{x}) \phi_i^D(t) + \sum_{i=1}^{N} B_i(\boldsymbol{x}) \phi_i(t), \tag{4.26}$$

where B_i, $i = 1, \ldots, N$, denote the basis functions that vanish on the Dirichlet boundary, B_i^D, $i = 1, \ldots, N_D$ denote the basis functions not vanishing on the Dirichlet boundary, and ϕ_i, $i = 1, \ldots, N$, denote the unknown coefficients. The number of nodes is N; it includes the nodes on boundaries except for the Dirichlet one where the function ϕ is known. In fact, $\phi_i^D(t) = \phi_D(\boldsymbol{x}_i, t)$ for nodes $\boldsymbol{x}_i$ in the Dirichlet boundary, where it is supposed that $B_i^D(\boldsymbol{x}_j) = B_i(\boldsymbol{x}_j) = \delta_{i,j}$. We suppose that the basis functions in (4.26) are piecewise linear functions, continuous in Ω and continously differentiable in each prism Ω^e. The problem is reformulated in its weak form. So, we multiply Eq. (4.25) with the base element B_i, $i = 1, \ldots, N$ and, by using the integration by parts, we obtain

$$\sum_{e=1}^{N_e}\int_{\Omega^e} B_i\frac{\partial}{\partial t}\left(\sum_j B_j\phi_j\right)d\Omega^e+\sum_{e=1}^{N_e}\int_{\Omega^e} B_i\boldsymbol{q}\cdot\nabla\left(\sum_j B_j\phi_j\right)d\Omega^e+$$
$$\sum_{e=1}^{N_e}\int_{\Omega^e}\nabla B_i\cdot\left(\boldsymbol{D}\cdot\nabla\left(\sum_j B_j\phi_j\right)\right)d\Omega^e+\sum_{e=1}^{N_e}\int_{\Omega^e} B_i\left(\nabla\cdot\boldsymbol{q}\left(\sum_j B_j\phi_j\right)-Q\right)d\Omega^e+$$
$$\sum_{e=1}^{N_e}\int_{\Gamma_N^e} B_i q_N d\Gamma^e-\sum_{e=1}^{N_e}\int_{\Gamma_C^e} B_i\Phi\left(\phi_C-\left(\sum_j B_j\phi_j\right)\right)d\Gamma^e=0,\quad 1\le i,j\le N, \tag{4.27}$$

where Γ_N^e,Γ_C^e are the Neumann and Cauchy boundaries within the prism Ω^e, respectively. Note that the boundary with Dirichlet condition does not appear since there the basis functions B_i, $i=1,\dots,N$, vanish.

We chose only one set of basis functions $B_i\in C^0$, since in (4.25) the only unknown function is ϕ. However, we need to calculate the Darcy velocity and the mass and heat flux in the solving procedure. If we consider for instance the flux $\boldsymbol{j}=-\boldsymbol{D}\cdot\nabla\phi$, the discrete flux is obtained as

$$\hat{\boldsymbol{j}}=-\sum_{i=1}^{N}\boldsymbol{D}\cdot\nabla B_i(\boldsymbol{x})\phi_j(t),$$

where the first derivatives in $\nabla B_i(\boldsymbol{x})$ are no continuous since the shape function B_i is continuous in Ω and continuously differentiable only in each element Ω^e. Thus, no unique fluxes result at nodal points; this creates inconveniences in the simulation results. To avoid this problems we reformulate Eq. (4.25) and we choose both ϕ and $\boldsymbol{j}$ are unknowns. Usually, the flux $\boldsymbol{j}$ is interpolated by piecewise quadratic shape functions and ϕ by piecewise linear shape functions. This ensures the stability, since the Babuška-Brezzi condition is satisfied [85], [86]. Unfortunately, this procedure increases the computational effort, and it is usually avoided. However, the software used for the simulations also implements some smoothing strategies for the fluxes to avoid the second order interpolation and to reduce the computational effort [33].

The Galerkin approximation of system (2.75) leads to a semi-discrete system, which is fully approximated by a time marching scheme. In particular, a 2nd-order accurate predictor-corrector (Adams-Bashforth/Crank-Nicolson) method is used.

For each time step, the final algebraic linear system has a sparse coefficient matrix and it is solved by using a standard iterative method.

4.2.2 Experimental measurements

Extraction Procedure 3. Two types of coffee were selected for this study, i.e., Arabica and Robusta. Arabica coffee was a blend from Perfero caffè (Fermo, Italy) composed of 50% of natural coffee, Geisha from Peru, variety typica, caturra and 50% of natural coffee from Guatemala (Batch 12-221, Perfero caffè), with a medium roasting degree for EC. Robusta coffee was a blend from Perfero caffè constituted by 50% of Uganda coffee and 50% of Indonesia (Flores island) coffee (Batch 10-221, Perfero caffè), with a medium roasting degree for EC. For the present research, about 4 kg (kilogram) of coffee beans Arabica and 4 kg of Robusta have been used. Coffee beans were ground by Mythos 1 grinder (Simonelli Group S.p.A., Belforte del Chienti, Italy) [87] and the coffee powder was tamped by the automatic tamping machine PuqPress M2 [88]. The preparation of EC samples was performed by a professional barista using the VA388 Black Eagle espresso coffee machine from Victoria Arduino (Simonelli Group S.p.A.) [89]. The EC extraction was carried out by keeping constant the amount of coffee (20 $\pm$ 0.1 g) added in the VST© Competition filter basket and the amount of EC obtained in the cup (40 $\pm$ 2 g). The tamping force (20 kgF – kilogram-force) was kept constant for each sample as well. Then, the experiment was focused on varying three extraction parameters, i.e., granulometry (O, optimal; C, coarse; F, fine), temperature of water (88, 93.4 and 98 °C) and pressure of water (6, 9 and 12 bar), resulting in a grid of 27 different EC samples for Arabica and 27 for Robusta. The time of extraction was fixed at 25 $\pm$ 1 s for EC samples considered optimal (optimal granulometry, water temperature of 93.4 °C and water pressure of 9 bar) and was different for EC samples prepared at different conditions than those optimal, since the brew ratio between mass of coffee pod and mass of EC was kept constant, 1:2. Moreover, other six EC samples were prepared by setting different conditions than those occurring in the previous grid. Hence, a total of 33 EC samples were prepared for Arabica and 33 for Robusta

coffee. Table 4.15 summarises the extraction conditions for each EC sample. All the extractions were performed in duplicate.

The EC samples were analysed for the contents of the aformentioned compound, i.e., total lipids, bioactive compounds such as alkaloids (caffeine and trigonelline), chlorogenic acids (3-caffeoylquinic acid, 3-CQA, 5-caffeoylquinic acid, 5-CQA and 3,5-dicaffeoylquinic acid, 3,5-diCQA), phenolic acids (ferulic acid) and organic acids (acetic, citric and tartaric acid). These classes of compounds affect the coffee taste and flavour hence they participate at the final cup quality. The analysis of total lipids and contents of these different classes of compounds were also performed in roasted and ground (R&G) coffee for both Arabica and Robusta. All the performed analyses were carried out almost in duplicate since the acceptable Relative Standard Deviation (% RSD) was fixed to 20%. The materials and methods used in the laboratory analyses are illustrated in [24], Here, only the obtained results are reported. In more details, Table 4.16 shows the content of total lipids in the analysed espresso samples. The averages of total lipids content in Arabica and Robusta samples are 0.466 g/100 mL and 0.080/100 mL, respectively, which correspond to 93 and 20 mg per cup (20 mL), respectively. These results are in agreement with those reported in the literature (45.0-146.5 mg per cup in Arabica and 13.6-119.2 mg per cup in Robusta) [13]. The lipid content increased with finer particle sizes (0.448 and 0.515 g/100 mL for optimal and fine granulometry in Arabica and 0.068 and 0.094 g/100 mL for optimal and fine granulometry in Robusta) while it is hard to describe how diverse temperatures and pressures of extraction affected the lipid contents in EC. The total content of lipids was also evaluated in R&G coffee. Arabica sample contains 13.87 g/100g (3.4% RSD) while Robusta coffee 9.32 g/100g (2.3% RSD). Similar levels are presented in literature such as about 15 g/100g in Arabica and 10 g/100g in Robusta [13]. In addition, the analysis of 9 bioactive compounds such as alkaloids (caffeine and trigonelline), chlorogenic acids (3,5-dicaffeoylquinic acid – 3,5-diCQA, 3-caffeoylquinic acid – 3-CQA and 5-caffeoylquinic acid – 5-CQA), phenolic acids (ferulic acid) and organic acids (acetic, citric and tartaric acid) has been performed by HPLC-DAD instrument in both EC and R&G coffee. The

content of bioactive compounds in the samples prepared by varying three variables is presented in Tables 4.17, 4.18. The average contents of caffeine, chlorogenic acids, ferulic acid, organic acids and trigonelline are 5.18, 8.35, 0.28, 24.77 and 3.39 g/L, respectively, which correspond to 103.5, 166.9, 5.7, 495.3 and 67.8 mg per cup of Arabica; while in Robusta samples the average contents of the same compounds are 7.48, 6.09, 0.40, 32.33 and 2.74 g/L which coincide to 149.6, 121.8, 8.0, 646.7 and 54.8 mg per cup. Similar levels are reported in literature [12], [90]. For instance, in [12], in espresso coffees prepared by changing perforated disk height, filter basket design and amount of R&G coffee, caffeine and 5-CQA levels go from 3.2 to 5.7 g/L and from 1.8 to 5.0 g/L for Arabica, while from 4.8 to 12.1 g/L and 2.1-6.1 g/L for Robusta. In [90], which analysed 20 commercial coffee samples, the caffeine amount goes from 116.9 to 199.7 mg per cup, while trigonelline from 28.2 to 65.1 mg per cup. On the other hand, higher levels of organic acids are found in the current work with respect to [12], [91] but these variations can be attributed to the complexity of the coffee supply chain. In fact, several factors related to species and plant cultivation, harvesting and processing methods, roasting, grinding and preparation techniques play an important role in coffee quality and its content of volatile and non-volatile compounds [14], [92].

As for total lipids, the content of bioactive compounds increases when finer particles are used. For instance, the averages of caffeine content obtained in all ECs prepared with coarse, optimal and fine granulometry are 4.82, 5.24 and 5.58 g/L in Arabica while 6.86, 7.63 and 7.98 g/L in Robusta. The same behaviour has been observed for all analytes and this inverse increment of compounds levels, with respect to particle sizes, were found also in other scientific papers [15], [16], [93]. Instead, the contribution of water temperature and pressure on the extraction of bioactive compounds is extremely complex and it is not possible to describe it as a linear increment or decrement. However, some small variations in compounds contents have been found. For instance, preparing espresso at 9 bar with optimal particle sizes, higher contents of caffeine, chlorogenic acids and organic acids are obtained at 88 and 93.4 °C.

The contents of bioactive compounds were evaluated in R&G coffee as well. In

Arabica, the following contents are obtained: 12.54 g/kg (7.2%, RSD) of caffeine, 22.13 g/kg (8.6%) of chlorogenic acids, 59.54 g/kg (11.7%) of organic acids, 0.79 g/kg (15.7%) of ferulic acid and 7.97 g/kg (0.2%) of trigonelline; while in Robusta: 18.58 g/kg (9.1%) of caffeine, 16.08 g/kg (8.9%) of chlorogenic acids, 74.79 g/kg (13.1%) of organic acids, 1.06 g/kg (1.5%) of ferulic acid and 5.96 g/kg (6.7%) of trigonelline.

Arabica sample	T [°C]	p [bar]	r	Robusta sample	T [°C]	p [bar]	r
A1	93.4	9	O	R1	93.4	9	O
A2	93.4	6	O	R2	93.4	12	O
A3	93.4	12	O	R3	93.4	6	O
A4	88	9	O	R4	88	9	O
A5	88	6	O	R5	88	12	O
A6	88	12	O	R6	88	6	O
A7	98	12	O	R7	98	9	O
A8	98	9	O	R8	98	12	O
A9	98	6	O	R9	98	6	O
A10	96	9	O	R10	96	9	O
A11	91	8	O	R11	91	8	O
A12	93.4	9	C	R12	93.4	9	C
A13	93.4	6	C	R13	93.4	12	C
A14	93.4	12	C	R14	93.4	6	C
A15	98	9	C	R15	88	9	C
A15	98	9	C	R15	88	9	C
A15	98	9	C	R15	88	9	C
A16	98	12	C	R16	88	12	C
A17	98	6	C	R17	88	6	C
A18	88	9	C	R18	98	9	C
A19	88	12	C	R19	98	12	C
A20	88	6	C	R20	98	6	C
A21	89	10	C	R21	97	7	C
A22	97	7	C	R22	89	10	C
A23	93.4	9	F	R23	93.4	9	F
A24	93.4	6	F	R24	93.4	12	F
A25	93.4	12	F	R25	93.4	6	F
A26	98	12	F	R26	88	9	F
A27	98	6	F	R27	88	12	F
A28	98	9	F	R28	88	6	F
A29	88	9	F	R29	98	6	F
A30	88	12	F	R30	98	9	F
A31	88	6	F	R31	98	12	F
A32	90	8	F	R32	95	11	F
A33	95	11	F	R33	90	8	F

Table 4.15: Extraction conditions of each EC sample. r denotes the type of granulometry: optimal (O), coarse (C), fine (F).

Arabica sample	Total lipids [g/100 mL]	RSD [%]	Robusta sample	Total lipids [g/100 mL]	RSD [%]
A1	0.45	6.6	R1	0.07	16.8
A2	0.53	14.8	R2	0.11	17.1
A3	0.55	16.9	R3	0.14	15.7
A4	0.59	19.2	R4	0.06	13.1
A5	0.38	17.4	R5	0.11	12.0
A6	0.47	15.8	R6	0.08	8.8
A7	0.39	16.0	R7	0.10	6.4
A8	0.41	12.3	R8	0.10	9.6
A9	0.38	18.1	R9	0.06	4.2
A10	0.30	14.5	R10	0.03	19.0
A11	0.29	19.2	R11	0.07	6.5
A12	0.33	11.5	R12	0.11	20.0
A13	0.34	9.0	R13	0.10	8.5
A14	0.44	12.1	R14	0.12	19.9
A15	0.43	17.9	R15	0.07	5.2
A16	0.52	8.3	R16	0.11	18.7
A17	0.55	12.9	R17	0.08	16.9
A18	0.29	3.5	R18	0.09	19.0
A19	0.65	1.1	R19	0.08	1.8
A20	0.43	18.2	R20	0.04	14.2
A21	0.36	0.0	R21	0.06	0.6
A22	0.35	12.1	R22	0.09	10.4
A23	0.52	12.2	R23	0.09	13.1
A24	0.45	8.7	R24	0.07	15.3
A25	0.45	2.1	R25	0.07	18.0
A26	0.41	12.8	R26	0.02	16.2
A27	0.68	4.6	R27	0.09	12.1
A28	0.69	18.2	R28	0.07	17.4
A29	0.66	19.5	R29	0.05	11.5
A30	0.47	8.4	R30	0.05	1.3
A31	0.62	17.8	R31	0.08	9.4
A32	0.59	4.8	R32	0.09	5.4
A33	0.47	14.8	R33	0.09	7.9

Table 4.16: Lipid contents [g/100 mL] found in different EC samples, Arabica and Robusta.

Sample	TR	TA	AA	CA	3-CQA	5-CQA	CF	FA	3,5-diCQA	Tot CQA	Tot OA
A1	3.41	3.45	7.27	16.18	2.95	5.89	5.27	0.27	0.30	9.13	26.89
A2	3.55	3.53	6.98	17.92	3.05	5.74	5.45	0.32	0.32	9.11	28.43
A3	3.55	3.56	7.94	17.40	3.11	6.01	5.40	0.29	0.32	9.44	28.89
A4	3.54	3.54	7.55	16.56	2.94	5.95	5.44	0.30	0.30	9.20	27.66
A5	3.47	3.47	7.75	14.86	2.86	5.44	5.19	0.30	0.30	8.59	26.07
A6	3.28	3.29	5.34	15.58	2.69	5.21	4.77	0.30	0.28	8.17	24.21
A7	3.52	3.53	4.52	11.25	3.02	5.71	5.34	0.34	0.31	9.04	19.31
A8	3.39	3.38	6.11	14.08	2.82	5.24	5.20	0.28	0.30	8.36	23.57
A9	3.36	3.35	7.02	13.65	2.81	5.20	5.10	0.28	0.30	8.31	24.02
A10	3.19	3.19	6.50	13.01	2.66	5.00	4.85	0.27	0.28	7.94	22.70
A11	3.86	3.84	4.67	8.89	3.18	5.93	5.80	0.32	0.32	9.42	17.40
A12	3.13	3.17	6.83	12.98	2.47	4.53	4.76	0.25	0.27	7.26	22.98
A13	3.37	3.38	10.97	16.04	2.58	4.79	5.00	0.27	0.27	7.65	30.39
A14	3.53	3.53	7.12	10.73	2.73	5.00	5.24	0.27	0.29	8.02	21.38
A15	3.20	3.21	3.80	6.32	2.44	4.62	4.85	0.25	0.27	7.32	13.33
A16	3.12	3.11	8.04	10.50	2.37	4.37	4.61	0.23	0.25	7.00	21.65
A17	3.19	3.18	5.92	13.10	2.45	5.76	4.79	0.23	0.21	8.42	22.19
A18	3.23	3.21	11.69	15.90	2.43	4.51	4.71	0.25	0.25	7.19	30.80
A19	2.99	2.98	7.55	13.53	2.26	4.14	4.41	0.23	0.23	6.64	24.07
A20	3.39	3.37	4.57	11.46	2.55	4.77	5.00	0.24	0.27	7.59	19.40
A21	3.32	3.31	13.09	16.42	2.53	4.83	4.82	0.27	0.26	7.62	32.81
A22	3.00	3.01	6.64	10.19	2.37	4.43	4.45	0.24	0.25	7.05	19.84
A23	3.48	3.50	5.42	11.40	2.97	5.51	5.43	0.30	0.32	8.80	20.32
A24	3.54	3.54	4.47	7.94	2.96	5.64	5.53	0.32	0.32	8.93	15.95
A25	3.49	3.48	8.04	16.56	2.93	5.50	5.44	0.31	0.32	8.75	28.08
A26	3.49	3.49	5.53	18.06	2.99	5.64	5.50	0.33	0.33	8.95	27.09
A27	3.71	3.72	7.07	20.49	3.20	5.99	5.98	0.33	0.32	9.51	31.28
A28	3.48	3.49	13.28	17.08	2.98	5.54	5.41	0.32	0.31	8.84	33.86
A29	3.38	3.35	9.53	16.36	2.87	5.30	5.65	0.30	0.30	8.47	29.24
A30	3.46	3.45	5.53	16.51	2.96	5.53	5.49	0.29	0.30	8.80	25.49
A31	3.70	3.69	6.25	18.78	3.15	5.91	5.83	0.34	0.33	9.38	28.73
A32	3.71	3.69	5.68	18.44	3.17	5.88	5.73	0.30	0.32	9.37	27.80
A33	2.75	2.77	4.67	14.02	2.36	4.52	4.40	0.24	0.26	7.14	21.46
Average	3.39	3.39	7.07	14.31	2.78	5.27	5.18	0.28	0.29	8.35	24.77

Table 4.17: Contents of bioactive compounds [g/L] found in Arabica EC samples. TR denotes trigonelline, TA tartaric acid, AA acetic acid, CA citric acid, CF caffeine, FA ferulic acid, CQA chlorogenic acid, OA organic acid. % RSD for all compounds are from 0.3 to 19.7%.

Sample	TR	TA	AA	CA	3-CQA	5-CQA	CF	FA	3,5-diCQA	Tot CQA	Tot OA
R1	2.83	2.75	15.06	18.93	2.28	3.41	7.88	0.39	0.45	6.14	36.74
R2	2.79	2.58	11.55	17.02	2.19	3.21	7.46	0.36	0.48	5.88	31.15
R3	2.66	2.59	7.17	19.07	2.23	3.26	7.46	0.35	0.47	5.96	28.83
R4	2.90	2.72	9.86	20.26	2.44	4.40	8.35	0.42	0.57	7.42	32.84
R5	2.62	2.51	7.17	19.22	2.08	3.01	6.98	0.37	0.45	5.54	28.90
R6	3.17	3.06	14.43	17.95	2.56	4.85	8.54	0.42	0.60	8.01	35.44
R7	2.64	2.52	7.46	18.21	2.09	3.00	6.97	0.36	0.46	5.55	28.18
R8	2.73	2.65	10.01	21.04	2.20	4.27	7.58	0.35	0.50	6.97	33.69
R9	2.76	2.66	10.10	21.15	2.24	3.22	7.48	0.41	0.48	5.95	33.91
R10	2.45	2.41	8.90	19.19	2.02	3.47	6.92	0.39	0.48	5.97	30.50
R11	2.93	2.86	16.94	23.81	2.39	3.46	8.12	0.46	0.51	6.35	43.60
R12	2.50	2.43	13.38	18.44	1.93	2.79	6.82	0.33	0.40	5.12	34.25
R13	2.48	2.40	12.85	18.50	2.23	2.65	6.44	0.36	0.36	5.24	33.74
R14	2.67	2.64	12.32	15.64	2.23	3.15	7.37	0.37	0.44	5.82	30.59
R15	2.68	2.69	11.84	21.81	2.21	3.13	7.22	0.37	0.42	5.75	36.34
R16	2.93	2.75	15.73	19.16	2.23	3.31	7.20	0.38	0.40	5.95	37.64
R17	2.50	2.41	9.57	15.78	2.19	2.87	6.53	0.37	0.39	5.46	27.77
R18	2.56	2.41	9.67	15.73	2.05	2.95	6.57	0.33	0.37	5.36	27.81
R19	2.30	2.26	11.35	14.17	1.93	2.67	6.22	0.32	0.35	4.94	27.79
R20	2.70	2.55	11.14	17.64	2.25	3.04	7.33	0.40	0.44	5.73	31.33
R21	2.67	2.60	12.75	16.10	2.26	3.16	7.31	0.36	0.43	5.84	31.45
R22	2.57	2.56	13.62	16.30	2.40	2.83	6.99	0.35	0.38	5.61	32.48
R23	3.17	2.99	6.54	18.41	2.64	3.92	8.36	0.54	0.51	7.07	27.95
R24	2.82	2.79	12.51	19.56	2.48	3.57	8.28	0.44	0.53	6.58	34.87
R25	2.99	2.40	8.37	16.30	2.21	3.17	7.39	0.45	0.40	5.78	27.08
R26	3.19	3.19	12.70	21.47	3.09	3.85	8.80	0.51	0.52	7.46	37.36
R27	2.85	2.71	14.29	18.76	2.35	3.48	7.81	0.42	0.49	6.32	35.76
R28	3.19	3.14	16.36	20.66	2.83	3.96	9.15	0.46	0.53	7.32	40.16
R29	2.59	2.45	8.71	16.76	2.26	2.99	7.39	0.42	0.51	5.77	27.92
R30	2.70	2.52	10.97	17.52	2.26	3.34	7.51	0.41	0.48	6.08	31.01
R31	2.57	2.46	11.74	16.71	2.33	3.19	7.10	0.42	0.44	5.96	30.90
R32	2.54	2.49	8.80	18.06	2.30	3.26	7.68	0.40	0.45	6.01	29.35
R33	2.78	2.64	9.00	18.09	2.22	3.33	7.58	0.41	0.49	6.05	29.73
Average	2.74	2.63	11.30	18.41	2.29	3.34	7.48	0.40	0.46	6.09	32.33

Table 4.18: Contents of bioactive compounds [g/L] found in Robusta EC samples. TR denotes trigonelline, TA tartaric acid, AA acetic acid, CA citric acid, CF caffeine, FA ferulic acid, CQA chlorogenic acid, OA organic acid. % RSD for all compounds are from 0.1 to 19.2%.

4.2.3 Numerical simulation settings

The numerical and laboratory experiment are performed under the same conditions of the extraction campaign, reported in Table 4.15, and the same extraction protocol: 20 ± 0.1 g in and 40 ± 2 g out; so the parameters of the model used in the numerical simulations are consistent with the corresponding real EC extraction used for laboratory analyses. Starting from the extraction grid used for the model calibration, the same four variables are taken into account: the temperature of the water entering the coffee basket T_{z0} – 88, 93.4, 98 °C; the pressure of the water entering the basket p_{z0} – 6, 9, 12 bar; the granulometry r of the coffee powder – optimal (O), coarse (C) and fine (F); the coffee variety v – Arabica (A) and Robusta (R). Regarding the model validation, the extractions keep the same granulometries and varieties used for the calibrations but take scattered points for temperature and pressure. So the validation is performed on off-grid points to give proof of the model robustness, however, on such points laboratory analyses are clearly available. The extraction is also influenced by other relevant physical or geometrical variables, such as the tamping pressure and extraction equipment, which have been maintained constant. The tamping pressure is fixed at 20 kgF. We note that the tamping operation affects the extraction because together with the granulometry it determines a key feature of the solid matrix, i.e., the porosity ε. Nevertheless, the value considered for the tamping pressure corresponds to the mean tamping usually exerted by a skilled barman, thus we assumed the porosity is only affected by granulometry, which highly influences both the porosity and the accessibility of chemical substances for dissolution. Equipment, common in the world of specialty coffee, has been employed for all the extractions, in particular, the filter basket is the cylindrical VST© with a capacity of 20 g, inner radius $R = 29.25$ mm and height 26 mm. Thus, the domain of the percolation problem is a cylinder with fixed radius R but height H depending on the granulometry of the coffee pod. After measuring the mean height of the coffee pods for each granulometry and each variety, fixed the tamping pressure, it comes out that the different heights have maximum distance less than a millimeter. Besides, using a constant height

$H = 13.88$ mm that corresponds to the mean value, neglecting the phenomena of grain swelling and consolidation occurring at the wetting of ground coffee, very similar results are obtained. The spatial domain $\mathcal{C}$ has been discretised by a mesh made of 3486 triangular prisms and 2160 total nodes, equally distributed on 8 circular cross sections.

The simulation settings are based on the following real data. In more detail, the extraction pressure determines the initial condition and the boundary condition on Γ_1 for the hydraulic head (2.76), and we suppose that the incoming pressurised water imposes the same pressure at the top of the tamped coffee. Besides, we assume that, at the beginning of the extraction, the pressure profile goes from the prescribed value at the top of the coffee powder to the atmospheric pressure value at the bottom by linearly decreasing, that is

$$p_0(z) = \frac{z}{-H}\,(1 - p_{z0}) + p_{z0},$$

where p_{z0} is the incoming water pressure. The values of the other parameters occurring in (2.76) are displayed in Table 4.19. Concerning the boundary and

	p [bar]		
	6	9	12
h_{z0} [m]	61.18	91.78	122.37
Φ_h [1/s]	$6.5 \cdot 10^{-5}$	$6.5 \cdot 10^{-5}$	$6.5 \cdot 10^{-5}$
h_C [m]	0	0	0

Table 4.19: Parameters in the initial and boundary conditions (2.76) of the hydraulic head depending on the pressure of the incoming water.

initial conditions of the temperature in (2.79), the values of the incoming water temperature T_{z0} have been reported above in the definition of the extraction grid, while $T_0 = 70$ °C is the value for the initial condition that is constant for all the cases. Regarding the boundary conditions (2.77) and the initial condition (2.78) for the chemical species, the required parameters are given in Table 4.20. The

	CF	CQA	TR	CA	AA	TA	FA	LP
Φ_k [mm/s]	30	30	30	30	30	30	30	30
C_{kC} [mg/l]	0	0	0	0	0	0	0	0
C^s_{k0A} [mg/l]	12540	22130	7970	39970	11870	7700	790	138700
C^s_{k0R} [mg/l]	18580	16080	5960	40920	27910	5970	1060	96200

Table 4.20: Parameters in the initial and boundary conditions (2.77),(2.78) of the chemical species. C^s_{k0A}, C^s_{k0R} are the initial concentrations for Arabica and Robusta, respectively.

solid concentration at $t = 0$ for Arabica and Robusta, C^s_{k0A}, C^s_{k0A}, respectively, has been taken from the analysis of the ground coffee reported above. Note that the equivalence 1 kg = 1 L is assumed to work.

The remaining parameters have been set by the calibration procedure, exploiting the calibration grid described at the opening of this section. In more detail, these parameters have been fine-tuned relying on the results of the chemical analyses and then an approximation problem has been solved to find the laws that reproduce them properly. Also for the estimation of the admittance Φ_k and the concentration threshold C_{kC}, reported in Table 4.20, a trial-and-error calibration process has been applied. Furthermore, when simulating a percolation process, it is essential to correctly formulate the dissolution or erosion from the porous medium of the chemical species. In system (2.75), the reaction terms R_k, R^s_k account for such modelling. Inspired by groundwater flows and the related dissolution processes, we defined such terms as follows:

$$R_k = -\alpha_k \left(1 - \varepsilon\right) C^s_k, \quad R^s_k = \alpha_k \left(1 - \varepsilon\right) C^s_k, \tag{4.28}$$

where α_k is the dissolution rate. The formulation of the dissolution rate α_k depends on the granulometry r and the coffee variety v in such a way:

$$\alpha^{r,v}_k = A_0 + aT_{z0} + bp_{z0} + cT^2_{z0} + dp^2_{z0} + fT_{z0}p_{z0} + lT^2_{z0}p_{z0} + mT_{z0}p^2_{z0}, \tag{4.29}$$

for k = CF, CQA, TR, CA, AA, TA, FA, LP, r = O, C, F, v = A, R, where also

the coefficients A_0, a, b, c, d, f, l, m depend on k, r, v and are listed in Tables 4.22-4.27.

Another pivotal parameter for a porous medium is the porosity ε, which is largely influenced by the grain size of the coffee powder. As reference value for the optimal granulometry, we choose $\varepsilon_{\mathrm{O}} = 0.305$, which is a mean value among the ones reported in literature [13], [18], [23]. Then, the porosity values $\varepsilon_g, g = \mathrm{C}, \mathrm{F}$, for the remaining granulometries are computed with this simple rule:

$$\varepsilon_g = \varepsilon_{\mathrm{O}} \frac{V_{\mathrm{O}}}{V_g},$$

where $V_g, g = \mathrm{O}, \mathrm{C}, \mathrm{F}$, is the volume percentage associated to the peak of fines in the particle size distribution (PSD) curve. To do this, we assume that the particle size where the peak occurs is almost the same for different granulometries. Considering the PSD curves of some samples with similar granulometries, reported in Figure 4.12, we obtain $\varepsilon_{\mathrm{C}} = 0.330$ and $\varepsilon_{\mathrm{F}} = 0.276$. The hydraulic conductivity tensor $\mathbf{K}$ is another parameter that strongly influences fluid flow; we assume that the coffee pod is an isotropic porous medium, so the tensor $\mathbf{K}$ is associated to a constant diagonal matrix whose elements k_r depend on the pressure of the incoming water p_{z0} and vary with the granulometry r:

$$k_r(p_{z0}) = \begin{cases} 2.60 \cdot 10^{-9} p_{z0}^2 - 6.50 \cdot 10^{-8} p_{z0} + 5.08 \cdot 10^{-7}, & r = \mathrm{O}, \\ 3.90 \cdot 10^{-9} p_{z0}^2 - 1.05 \cdot 10^{-7} p_{z0} + 8.50 \cdot 10^{-7}, & r = \mathrm{C}, \\ 1.20 \cdot 10^{-9} p_{z0}^2 - 3.17 \cdot 10^{-8} p_{z0} + 2.56 \cdot 10^{-7}, & r = \mathrm{F}. \end{cases}$$

We note that this law for the elements of $\mathbf{K}$ has been calculated by interpolating proper values to match the numerical flow rate with the real flow rate. Other simulation parameters are reported in Table 4.21. For some parameters, we have taken our cue from the standard values used in hydrogeology transport processes [33], [94], such as for the molecular diffusivities D_k, the specific storage coefficient S_0, the longitudinal and transverse dispersion coefficients β_L, β_T. Besides, the transverse dispersivity is smaller than the longitudinal dispersivity for 1 or 2 orders of magnitude, as empirically prescribed [95]. Finally, in the heat equation, the choice of the involved parameters resembles the one used in [23], thus more details can be found there.

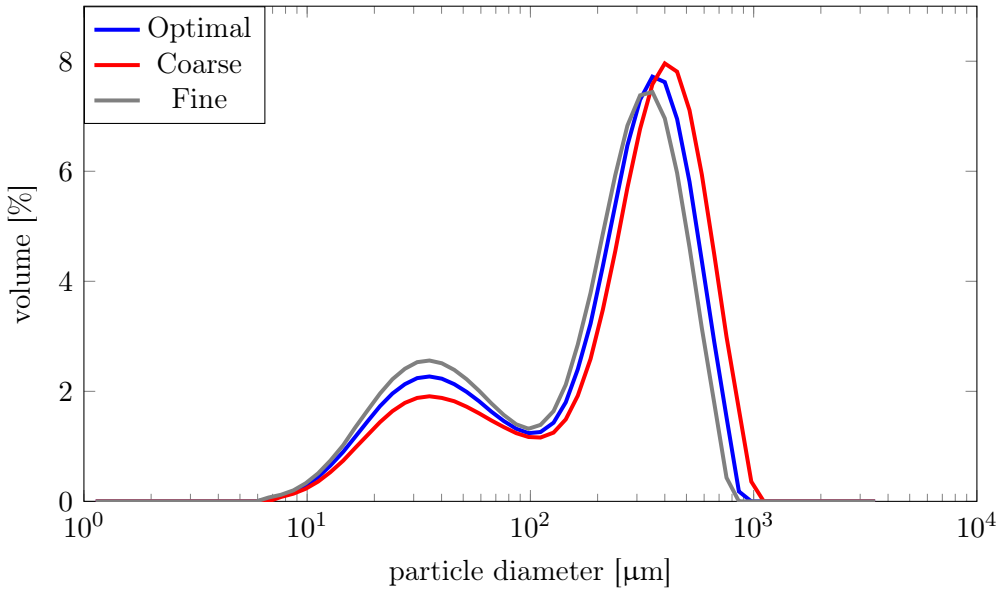

(a) Arabica

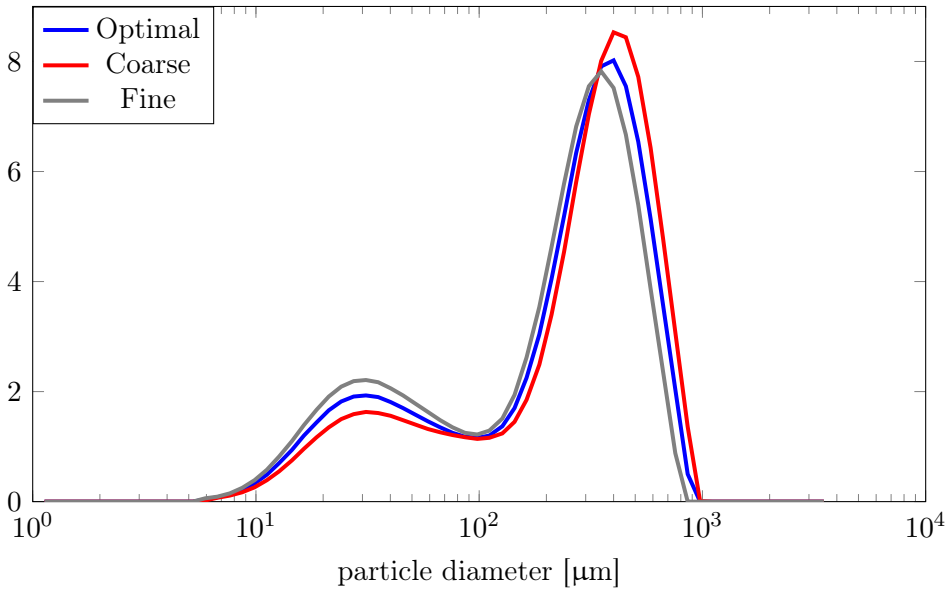

(b) Robusta

Figure 4.12: Particle size distributions of the ground coffee for Arabica variety (a) and Robusta variety (b).

S_0	$1 \cdot 10^{-3}$ 1/m
β_L, β_T	$1, 0.1$ m
D_k	$1 \cdot 10^{-9}$ m^2/s
T_0	100°C
ρc	4.18 MJ/m^3 K
$\rho^s c^s$	3.184 MJ/m^3 K
Λ	0.673 W/m K
Λ^s	0.337 W/m K
$\gamma_L\,, \gamma_T$	$0.5, 0.05$ m
$\tau_{\rm O}, \tau_{\rm C}, \tau_{\rm F}$	$20, 13, 35$ s

Table 4.21: Parameters of model (2.75)-(2.79) varying the species k, k = CF, CQA, TR, CA, AA, TA, FA, LP. These parameters are independent of granulometry, except for the extraction time τ.

	CF	CQA	TR	CA	AA	TA	FA	LP
A_0	$-6.0 \cdot 10^4$	$-5.8 \cdot 10^4$	$3.8 \cdot 10^4$	$-4.4 \cdot 10^5$	$-8.2 \cdot 10^5$	$-2.7 \cdot 10^4$	$1.5 \cdot 10^5$	$-1.2 \cdot 10^4$
a	$1.5 \cdot 10^3$	$5.9 \cdot 10^2$	$-5.7 \cdot 10^2$	$9.4 \cdot 10^3$	$1.9 \cdot 10^4$	$8.4 \cdot 10^2$	$-2.8 \cdot 10^3$	$2.6 \cdot 10^2$
b	$-1.0 \cdot 10^3$	$2.3 \cdot 10^3$	$-1.6 \cdot 10^3$	$1.9 \cdot 10^3$	$-6.3 \cdot 10^3$	$-1.6 \cdot 10^3$	$-2.8 \cdot 10^3$	$6.6 \cdot 10^1$
c	-8.5	$7.0 \cdot 10^{-1}$	2.6	$-5.0 \cdot 10^1$	$-1.1 \cdot 10^2$	-5.2	$1.4 \cdot 10^1$	-1.4
d	$-1.3 \cdot 10^1$	$-1.1 \cdot 10^3$	$2.6 \cdot 10^1$	-6.5	$4.4 \cdot 10^1$	7.4	$5.6 \cdot 10^1$	$-9.3 \cdot 10^{-1}$
f	$1.3 \cdot 10^1$	$1.4 \cdot 10^2$	$1.2 \cdot 10^1$	$-1.9 \cdot 10^1$	$5.4 \cdot 10^1$	$1.5 \cdot 10^1$	$2.0 \cdot 10^1$	$-5.1 \cdot 10^{-1}$
l	0	-1.8	0	0	0	0	0	0
m	0	$1.1 \cdot 10^1$	0	0	0	0	0	0

Table 4.22: Coefficients of the dissolution rate $\alpha_k^{r,v}$, k = CF, CQA, TR, CA, AA, TA, FA, LP, for the optimal granulometry r = O and Arabica variety v = A.

	CF	CQA	TR	CA	AA	TA	FA	LP
A_0	$-1.9 \cdot 10^5$	$7.6 \cdot 10^5$	$-2.3 \cdot 10^5$	$-2.9 \cdot 10^5$	$-4.7 \cdot 10^6$	$-1.7 \cdot 10^5$	$-1.7 \cdot 10^5$	$2.9 \cdot 10^4$
a	$4.3 \cdot 10^3$	$-1.8 \cdot 10^4$	$5.4 \cdot 10^3$	$6.1 \cdot 10^3$	$1.0 \cdot 10^5$	$4.2 \cdot 10^3$	$3.8 \cdot 10^3$	$-6.3 \cdot 10^2$
b	$-1.9 \cdot 10^3$	$-5.6 \cdot 10^4$	$-2.9 \cdot 10^3$	$3.4 \cdot 10^3$	$-6.1 \cdot 10^3$	$-2.2 \cdot 10^3$	$-6.4 \cdot 10^2$	$1.1 \cdot 10^2$
c	$-2.4 \cdot 10^1$	$1.1 \cdot 10^2$	$-3.0 \cdot 10^1$	$-3.2 \cdot 10^1$	$-5.5 \cdot 10^2$	$-2.3 \cdot 10^1$	$-2.1 \cdot 10^1$	3.6
d	$2.8 \cdot 10^1$	$-2.4 \cdot 10^3$	$5.7 \cdot 10^1$	$3.1 \cdot 10^1$	$7.3 \cdot 10^2$	$4.8 \cdot 10^1$	9.3	$1.2 \cdot 10^1$
f	$1.4 \cdot 10^1$	$1.7 \cdot 10^3$	$2.0 \cdot 10^1$	$-4.4 \cdot 10^1$	$-8.6 \cdot 10^1$	$1.4 \cdot 10^1$	5.0	-3.3
l	0	$-1.2 \cdot 10^1$	0	0	0	0	0	0
m	0	$2.5 \cdot 10^1$	0	0	0	0	0	0

Table 4.23: Coefficients of the dissolution rate $\alpha_k^{r,v}$, $k =$ CF, CQA, TR, CA, AA, TA, FA, LP, for the coarse granulometry $r =$ C and Arabica variety $v =$ A.

	CF	CQA	TR	CA	AA	TA	FA	LP
A_0	$5.5 \cdot 10^4$	$1.0 \cdot 10^5$	$-2.9 \cdot 10^3$	$4.0 \cdot 10^5$	$1.6 \cdot 10^6$	$8.5 \cdot 10^3$	$3.2 \cdot 10^4$	$1.2 \cdot 10^4$
a	$-1.1 \cdot 10^3$	$-2.1 \cdot 10^3$	$1.2 \cdot 10^2$	$-8.6 \cdot 10^3$	$-3.8 \cdot 10^4$	$-8.8 \cdot 10^1$	$-5.1 \cdot 10^2$	$-2.6 \cdot 10^2$
b	$-1.1 \cdot 10^2$	$-1.0 \cdot 10^4$	$-6.0 \cdot 10^1$	$-8.8 \cdot 10^2$	$2.0 \cdot 10^4$	$-4.4 \cdot 10^2$	$-1.5 \cdot 10^3$	$1.1 \cdot 10^2$
c	6.0	$1.1 \cdot 10^1$	$-5.1 \cdot 10^{-1}$	$4.6 \cdot 10^1$	$2.0 \cdot 10^2$	$4.7 \cdot 10^{-1}$	2.4	1.4
d	$1.1 \cdot 10^1$	$7.7 \cdot 10^1$	9.3	$4.4 \cdot 10^1$	$-1.0 \cdot 10^3$	$1.8 \cdot 10^1$	$2.8 \cdot 10^1$	-3.3
f	-1.4	$2.0 \cdot 10^2$	-1.4	1.1	$-1.1 \cdot 10^1$	$9.9 \cdot 10^{-1}$	$1.0 \cdot 10^1$	$-6.1 \cdot 10^{-1}$
l	0	-1.0	0	0	0	0	0	0
m	0	$-6.4 \cdot 10^{-1}$	0	0	0	0	0	0

Table 4.24: Coefficients of the dissolution rate $\alpha_k^{r,v}$, $k =$ CF, CQA, TR, CA, AA, TA, FA, LP, for the fine granulometry $r =$ F and Arabica variety $v =$ A.

	CF	CQA	TR	CA	AA	TA	FA	LP
A_0	$6.2 \cdot 10^4$	$5.2 \cdot 10^5$	$1.0 \cdot 10^5$	$2.5 \cdot 10^5$	$-3.1 \cdot 10^5$	$1.1 \cdot 10^5$	$1.4 \cdot 10^5$	$-4.6 \cdot 10^3$
a	$-9.2 \cdot 10^2$	$-1.2 \cdot 10^4$	$-1.7 \cdot 10^3$	$-5.4 \cdot 10^3$	$7.5 \cdot 10^3$	$-1.9 \cdot 10^3$	$-2.8 \cdot 10^3$	$1.0 \cdot 10^2$
b	$-2.3 \cdot 10^3$	$-1.6 \cdot 10^4$	$-3.3 \cdot 10^3$	$7.8 \cdot 10^2$	$-6.3 \cdot 10^3$	$-3.2 \cdot 10^3$	$2.0 \cdot 10^2$	$-4.2 \cdot 10^1$
c	3.2	$6.6 \cdot 10^1$	6.9	$3.0 \cdot 10^1$	$-4.5 \cdot 10^1$	8.5	$1.5 \cdot 10^1$	$-5.6 \cdot 10^{-1}$
d	$-2.1 \cdot 10^1$	$-1.5 \cdot 10^3$	$8.3 \cdot 10^{-13}$	$1.3 \cdot 10^1$	$-7.2 \cdot 10^1$	$1.5 \cdot 10^1$	$-1.9 \cdot 10^1$	1.8
f	$2.8 \cdot 10^1$	$5.7 \cdot 10^2$	$3.4 \cdot 10^1$	$-1.1 \cdot 10^1$	$8.0 \cdot 10^1$	$3.1 \cdot 10^1$	$6.2 \cdot 10^{-1}$	$1.2 \cdot 10^{-1}$
l	0	-4.3	0	0	0	0	0	0
m	0	$1.6 \cdot 10^1$	0	0	0	0	0	0

Table 4.25: Coefficients of the dissolution rate $\alpha_k^{r,v}$, k = CF, CQA, TR, CA, AA, TA, FA, LP, for the optimal granulometry r = O and Robusta variety v = R.

	CF	CQA	TR	CA	AA	TA	FA	LP
A_0	$-2.1 \cdot 10^4$	$-1.5 \cdot 10^5$	$6.7 \cdot 10^4$	$-5.0 \cdot 10^4$	$-2.7 \cdot 10^5$	$9.6 \cdot 10^4$	$4.4 \cdot 10^4$	$-1.2 \cdot 10^4$
a	$3.8 \cdot 10^2$	$3.1 \cdot 10^3$	$-1.6 \cdot 10^3$	$6.0 \cdot 10^2$	$5.3 \cdot 10^3$	$-2.3 \cdot 10^3$	$-1.0 \cdot 10^3$	$2.7 \cdot 10^2$
b	$2.2 \cdot 10^3$	$2.2 \cdot 10^4$	$4.4 \cdot 10^3$	$8.8 \cdot 10^3$	$7.0 \cdot 10^3$	$4.9 \cdot 10^3$	$1.9 \cdot 10^3$	$-1.3 \cdot 10^1$
c	-1.0	$-1.6 \cdot 10^1$	$1.1 \cdot 10^1$	-1.4	$-2.5 \cdot 10^1$	$1.4 \cdot 10^1$	6.8	-1.5
d	-1.9	$-3.7 \cdot 10^1$	$1.1 \cdot 10^1$	$-1.5 \cdot 10^2$	$6.1 \cdot 10^1$	5.6	$4.4 \cdot 10^1$	$-9.3 \cdot 10^{-2}$
f	$-2.4 \cdot 10^1$	$-4.4 \cdot 10^2$	$-4.9 \cdot 10^1$	$-6.4 \cdot 10^1$	$-8.3 \cdot 10^1$	$-5.3 \cdot 10^1$	$-2.9 \cdot 10^1$	$1.9 \cdot 10^{-1}$
l	0	2.2	0	0	0	0	0	0
m	0	$5.1 \cdot 10^{-1}$	0	0	0	0	0	0

Table 4.26: Coefficients of the dissolution rate $\alpha_k^{r,v}$, k = CF, CQA, TR, CA, AA, TA, FA, LP, for the coarse granulometry r = C and Robusta variety v = R.

	CF	CQA	TR	CA	AA	TA	FA	LP
A_0	$-3.9 \cdot 10^4$	$2.9 \cdot 10^5$	$-1.5 \cdot 10^5$	$6.2 \cdot 10^3$	$4.9 \cdot 10^5$	$6.9 \cdot 10^4$	$-1.8 \cdot 10^5$	$-1.9 \cdot 10^3$
a	$9.6 \cdot 10^2$	$-6.9 \cdot 10^3$	$3.6 \cdot 10^3$	$1.6 \cdot 10^2$	$-9.7 \cdot 10^3$	$-1.2 \cdot 10^3$	$4.0 \cdot 10^3$	$4.3 \cdot 10^1$
b	$3.3 \cdot 10^1$	$-3.2 \cdot 10^4$	$-8.6 \cdot 10^2$	$-1.2 \cdot 10^3$	$-6.7 \cdot 10^3$	$-9.0 \cdot 10^2$	$2.6 \cdot 10^2$	$-1.9 \cdot 10^1$
c	-5.7	$4.0 \cdot 10^1$	$-2.1 \cdot 10^1$	-2.4	$4.8 \cdot 10^1$	4.3	$-2.3 \cdot 10^1$	$-2.4 \cdot 10^{-1}$
d	$-2.4 \cdot 10^1$	$-1.0 \cdot 10^3$	$-5.2 \cdot 10^1$	$-4.1 \cdot 10^1$	$8.7 \cdot 10^1$	$-7.0 \cdot 10^1$	$-7.6 \cdot 10^1$	$6.9 \cdot 10^{-1}$
f	4.1	$9.0 \cdot 10^2$	$1.8 \cdot 10^1$	$2.1 \cdot 10^1$	$5.5 \cdot 10^1$	$2.3 \cdot 10^1$	$1.2 \cdot 10^1$	$7.5 \cdot 10^{-2}$
l	0	-5.8	0	0	0	0	0	0
m	0	$1.1 \cdot 10^1$	0	0	0	0	0	0

Table 4.27: Coefficients of the dissolution rate $\alpha_k^{r,v}$, $k =$ CF, CQA, TR, CA, AA, TA, FA, LP, for the fine granulometry $r =$ F and Robusta variety $v =$ R.

4.2.4 Results: comparison and discussion

Problem (2.75) and the initial and boundary conditions (2.76)-(2.79) are implemented in the software FeFlow Demo 7.2 [77], which offers a complete simulation tool for porous media and groundwater movement. FeFlow embeds the numerical approximation of the model, some details of which are given below.

We first show and discuss the results of the model calibration, then the results of the model validation, highlighting the comparison of chemical species between the numerical and laboratory results. Figures 4.13, 4.14, 4.15, 4.16, 4.17, 4.18, 4.19, 4.20 show the extracted amounts of each chemical species in a double cup of about 40 mL, for all the points of the extraction grid used in the calibration, restricting the focus on the Arabica variety. In each figure, the red profiles with square markers display the results from chemical laboratory analyses already described in above, see Tables 4.16, 4.17, 4.18 for details, whereas the blue profiles with circle markers give the results from numerical simulations based on the model (2.75)-(2.79). Besides, in these figures, each row refers to a granulometry – optimal to coarse to fine from top to bottom, each column refers to a temperature and the plots are a function of pressure. The comparison between the red and blue profiles shows a good agreement, especially for the caffeine, chlorogenic acids, trigonelline, tartaric acid and ferulic acid. For the citric acid and the lipids, the correspondence between numerical and analytical results is good, except for some points where peaks occur. In this case, the numerical results give a smooth curve between the maximum and the minimum values of laboratory results. Less correspondence is found for the acetic acid because this species shows a definitely not smooth behaviour of the dissolution coefficient thus the corresponding model of the reactive terms struggles to follow the peaks. However, the general trend of these results is again to smooth the curves of the laboratory results.

Figures 4.21, 4.22, 4.23, 4.24, 4.25, 4.26, 4.27, 4.28 show the extracted amounts of each chemical species in a double cup of about 40 mL for all the points of the extraction grid used in the calibration, restricting the focus on the Robusta variety. These results show similar behaviour to the ones obtained for the Arabica coffee

powder, with an overall correspondence between the red and blue profiles slightly decreased, especially for the lipids, but with improved correspondence in the critical species, like citric acid and acetic acid.

Concerning the amount of simulated liquid coffee, the volumes fall in the interval $[39.4, 40.9]$ cm^3 for all the cases, which completely agrees with 40 ± 2 cm^3 of coffee in a double cup, that is what expected from the real extraction. The equivalence between mass and volume is assumed to be valid.

Tables 4.28, 4.29 show the results of the validation process. In particular, the extraction points are specified along the columns, and the chemical species along the rows. In Table 4.28 for Arabica variety, apart from the citric acid, the acetic acid and the lipids, which have the worst performance even in the calibration process, the other species have most of the percentage errors (shown in brackets) less than 10% (these values are in bold type), some around 20% and very few greater than 20%. Table 4.29 shows the corresponding results for Robusta variety. If we discard the lipids at the point $(96, 9, \mathrm{O})$, the percentage errors are slightly higher on average (but their dispersion is smaller) than in Arabica variety and very high errors are not reached. To sum up, Table 4.30 gives an overview of the predictivity of the model, showing the mean percentage error of each species, averaged over all the validation points.

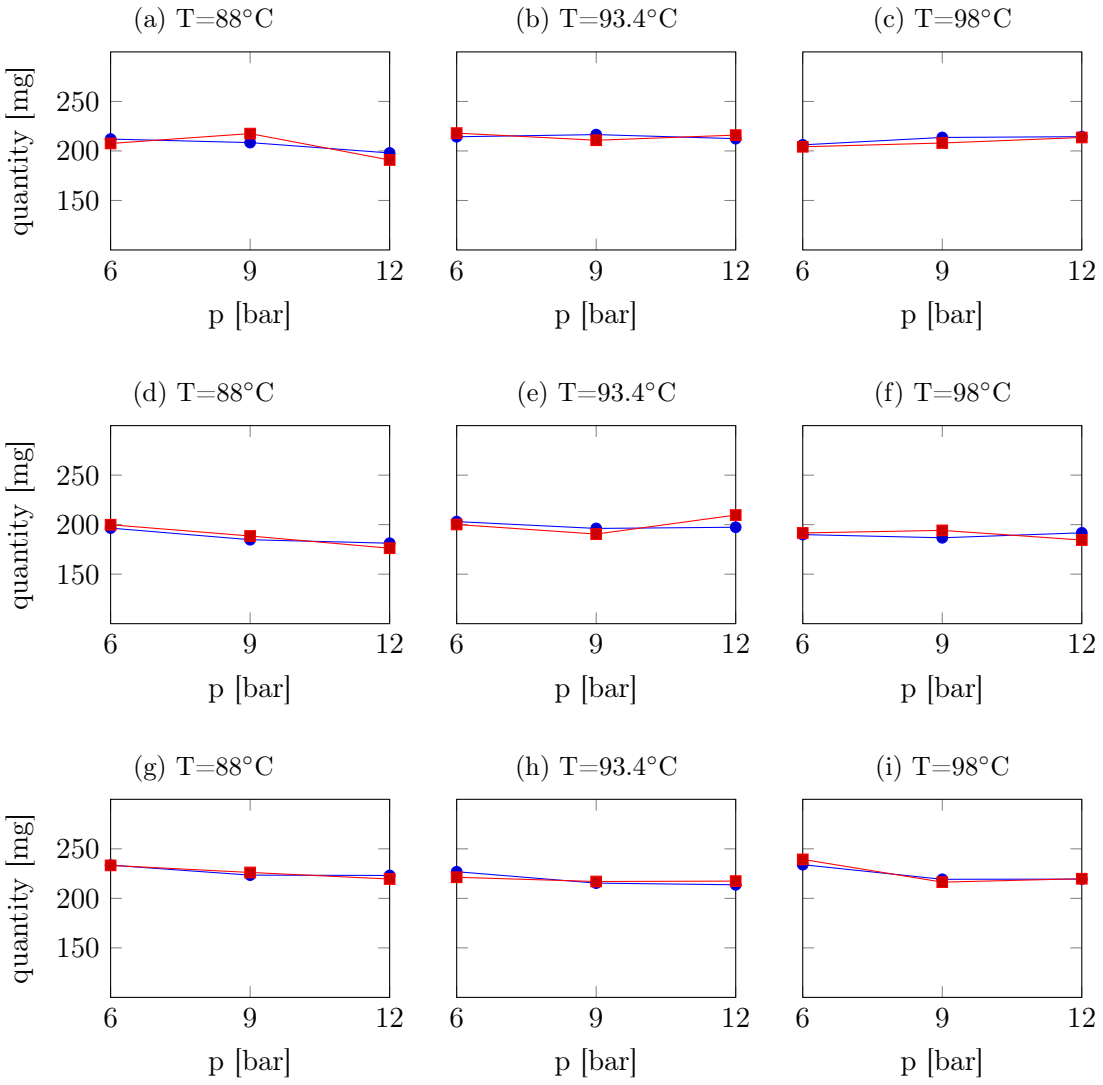

Figure 4.13: Comparison between the caffeine extracted through numerical simulations (blue profile with circles) and laboratory measurements (red profile with squares), with different inlet water temperatures and pressures and different grain size of Arabica coffee powder. Figures (a)-(c) show the results of optimal granulometry, Figures (d)-(f) of coarse granulometry, Figures (g)-(i) of fine granulometry.

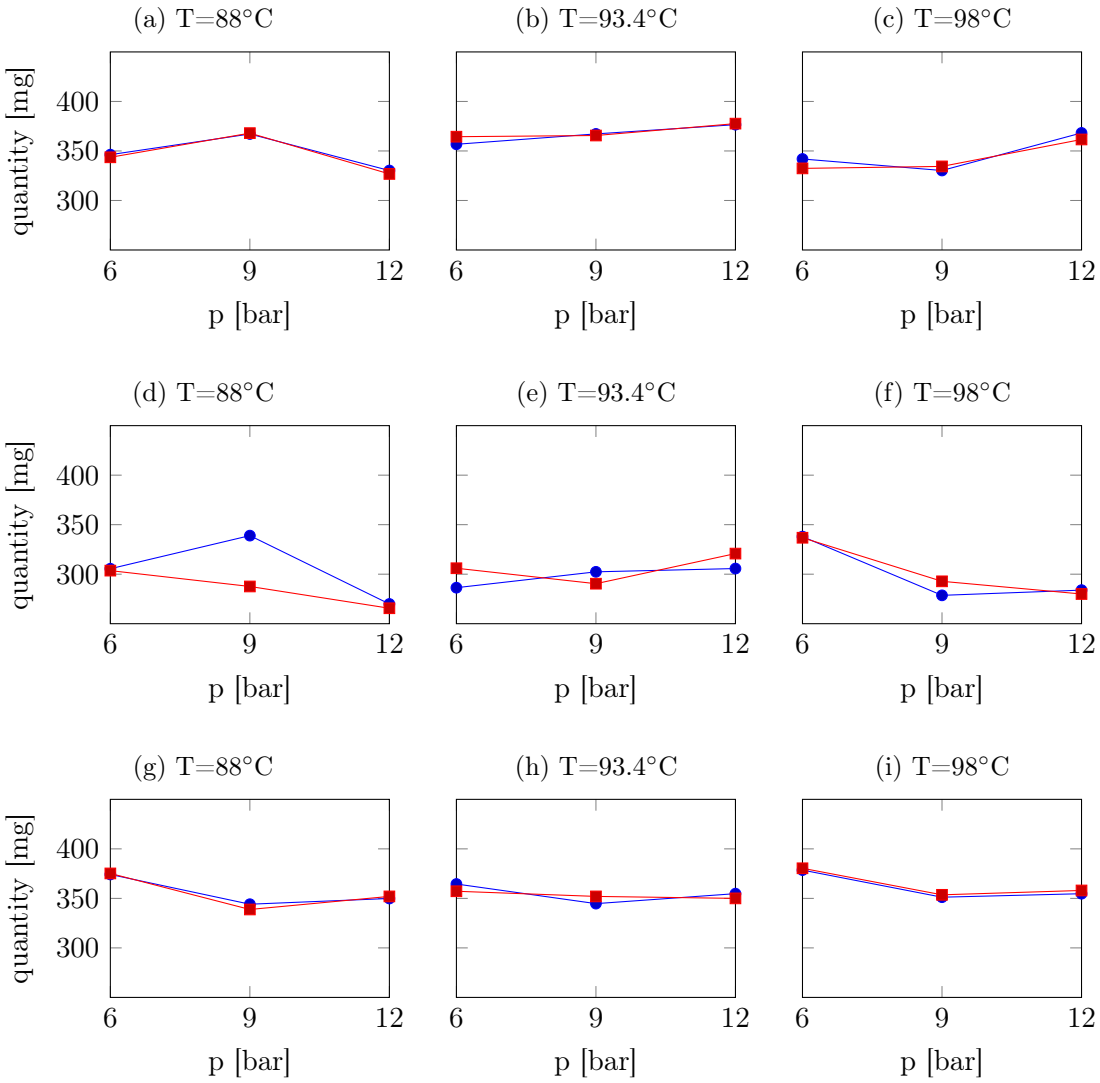

Figure 4.14: Comparison between the chlorogenic acids extracted through numerical simulations (blue profile with circles) and laboratory measurements (red profile with squares), with different inlet water temperatures and pressures and different grain size of Arabica coffee powder. Figures (a)-(c) show the results of optimal granulometry, Figures (d)-(f) of coarse granulometry, Figures (g)-(i) of fine granulometry.

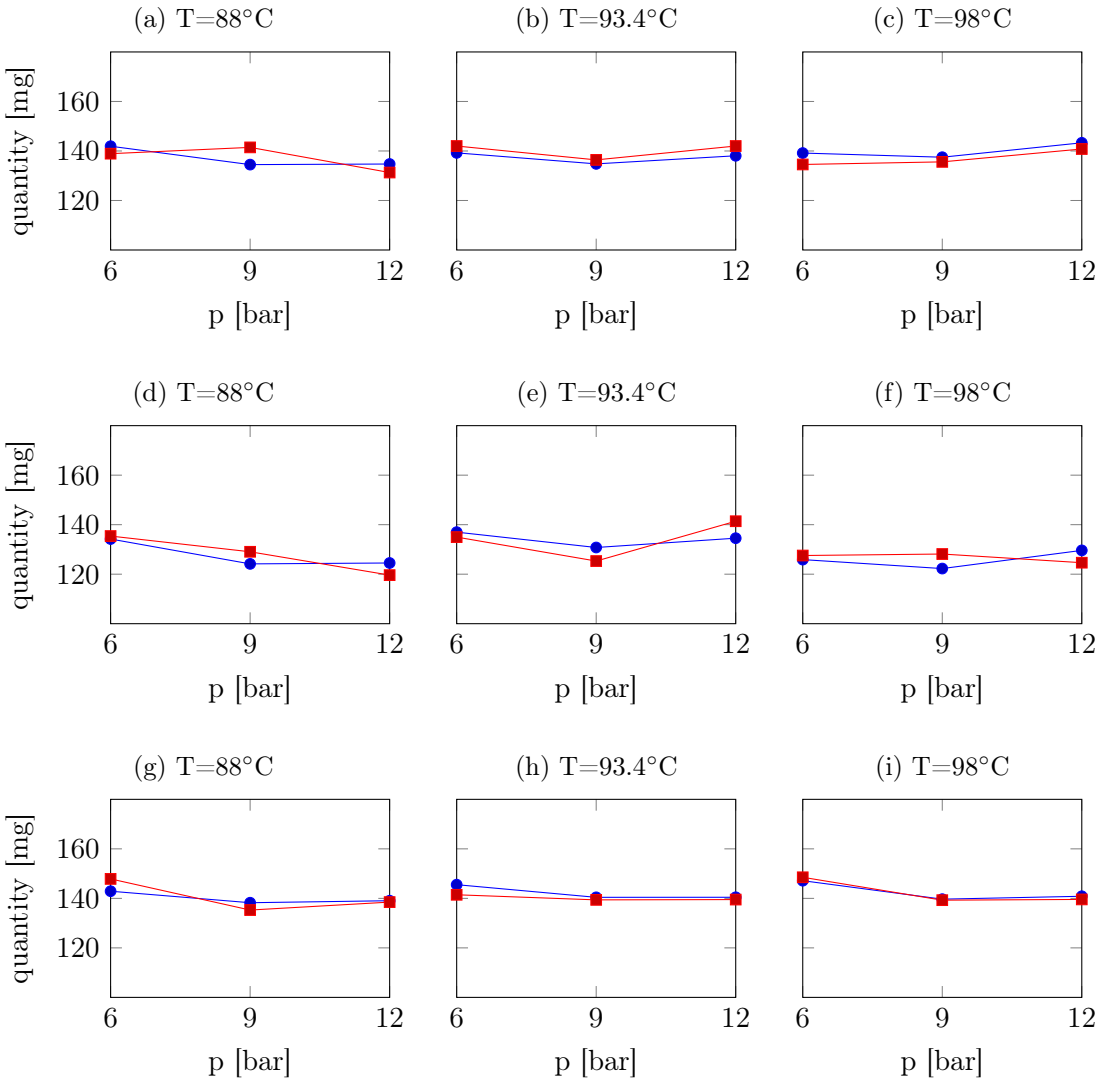

Figure 4.15: Comparison between the trigonelline extracted through numerical simulations (blue profile with circles) and laboratory measurements (red profile with squares), with different inlet water temperatures and pressures and different grain size of Arabica coffee powder. Figures (a)-(c) show the results of optimal granulometry, Figures (d)-(f) of coarse granulometry, Figures (g)-(i) of fine granulometry.

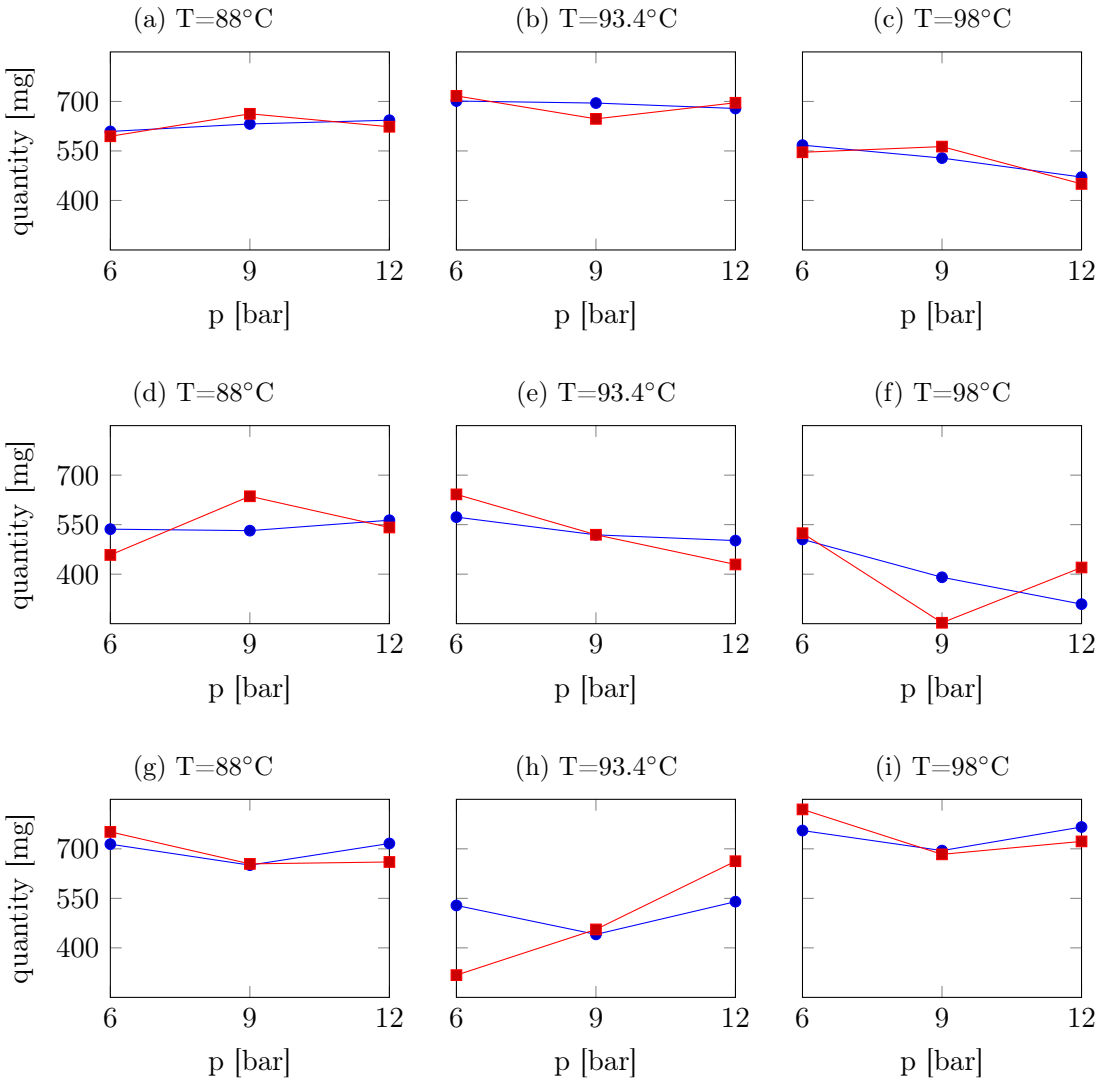

Figure 4.16: Comparison between the citric acid extracted through numerical simulations (blue profile with circles) and laboratory measurements (red profile with squares), with different inlet water temperatures and pressures and different grain size of Arabica coffee powder. Figures (a)-(c) show the results of optimal granulometry, Figures (d)-(f) of coarse granulometry, Figures (g)-(i) of fine granulometry.

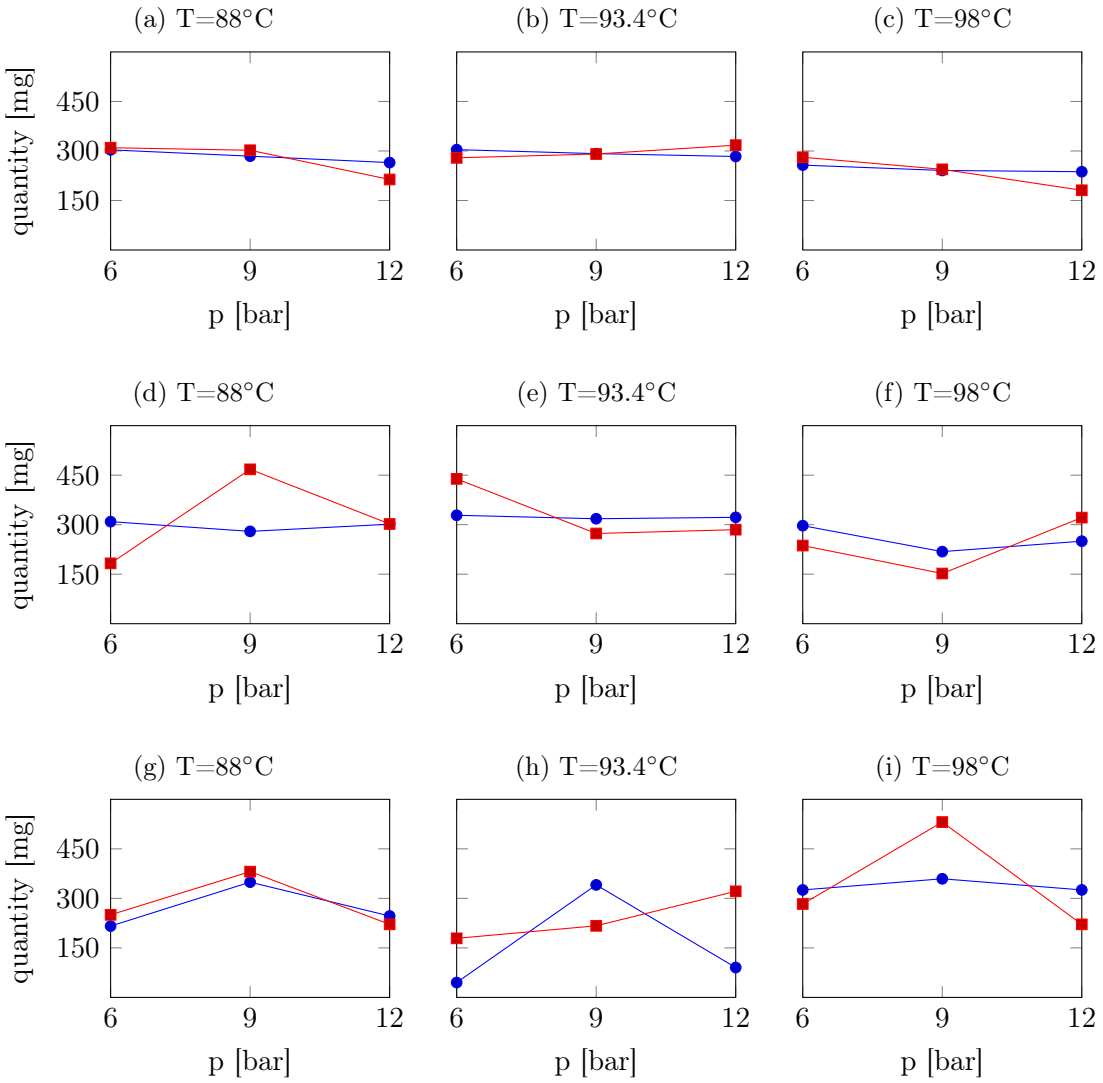

Figure 4.17: Comparison between the acetic acid extracted through numerical simulations (blue profile with circles) and laboratory measurements (red profile with squares), with different inlet water temperatures and pressures and different grain size of Arabica coffee powder. Figures (a)-(c) show the results of optimal granulometry, Figures (d)-(f) of coarse granulometry, Figures (g)-(i) of fine granulometry.

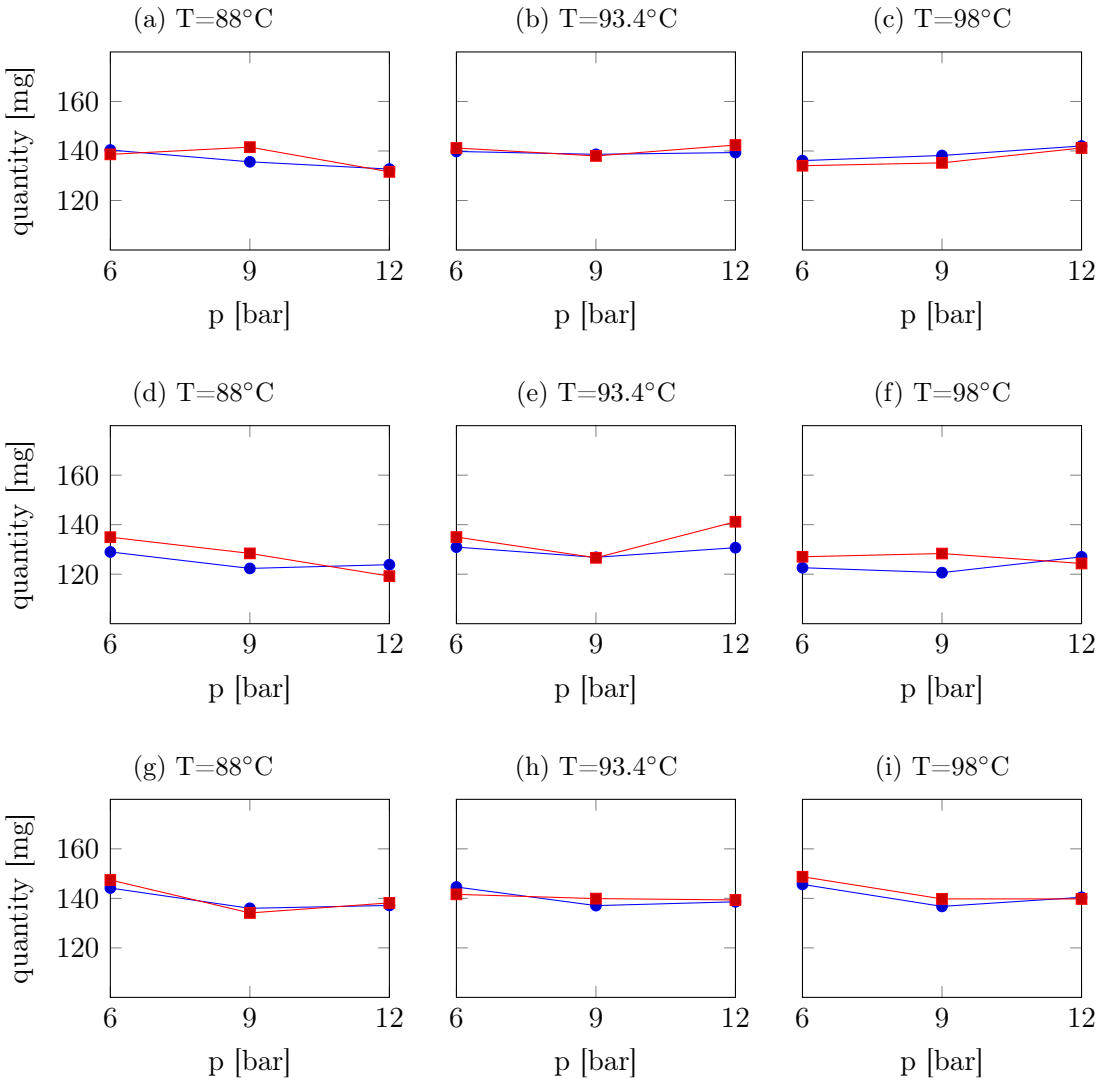

Figure 4.18: Comparison between the tartaric acid extracted through numerical simulations (blue profile with circles) and laboratory measurements (red profile with squares), with different inlet water temperatures and pressures and different grain size of Arabica coffee powder. Figures (a)-(c) show the results of optimal granulometry, Figures (d)-(f) of coarse granulometry, Figures (g)-(i) of fine granulometry.

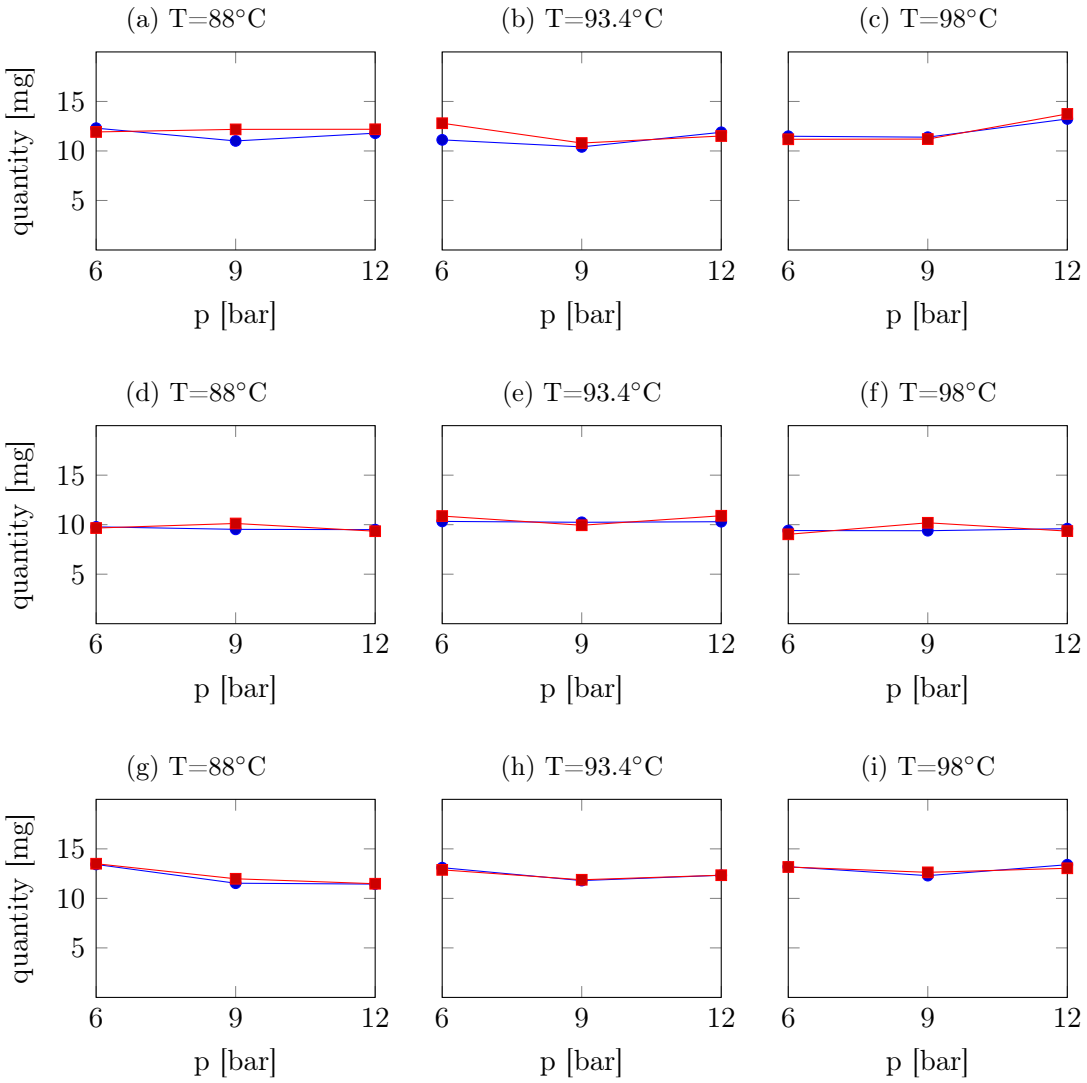

Figure 4.19: Comparison between the ferulic acid extracted through numerical simulations (blue profile with circles) and laboratory measurements (red profile with squares), with different inlet water temperatures and pressures and different grain size of Arabica coffee powder. Figures (a)-(c) show the results of optimal granulometry, Figures (d)-(f) of coarse granulometry, Figures (g)-(i) of fine granulometry.

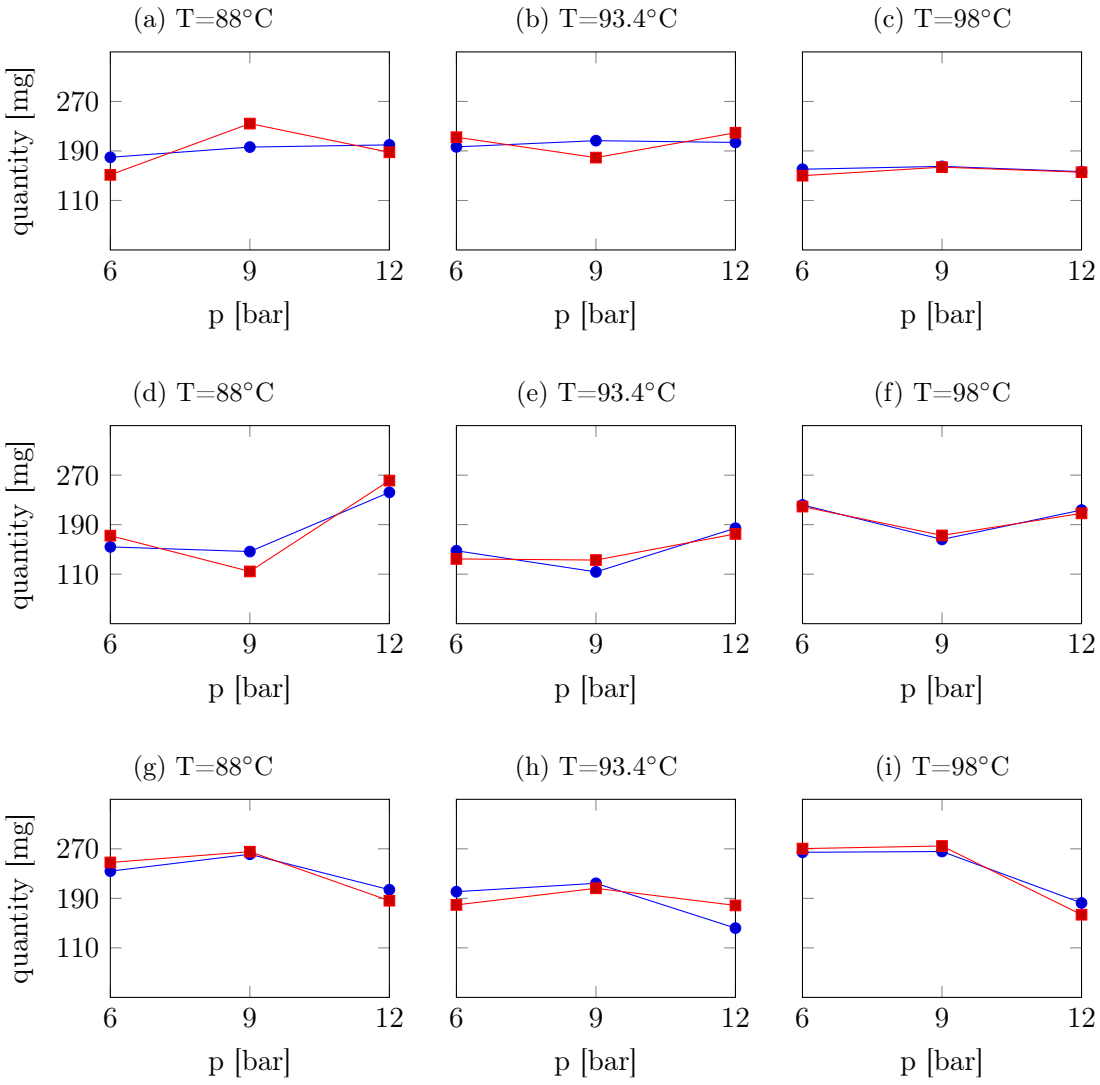

Figure 4.20: Comparison between the lipids extracted through numerical simulations (blue profile with circles) and laboratory measurements (red profile with squares), with different inlet water temperatures and pressures and different grain size of Arabica coffee powder. Figures (a)-(c) show the results of optimal granulometry, Figures (d)-(f) of coarse granulometry, Figures (g)-(i) of fine granulometry.

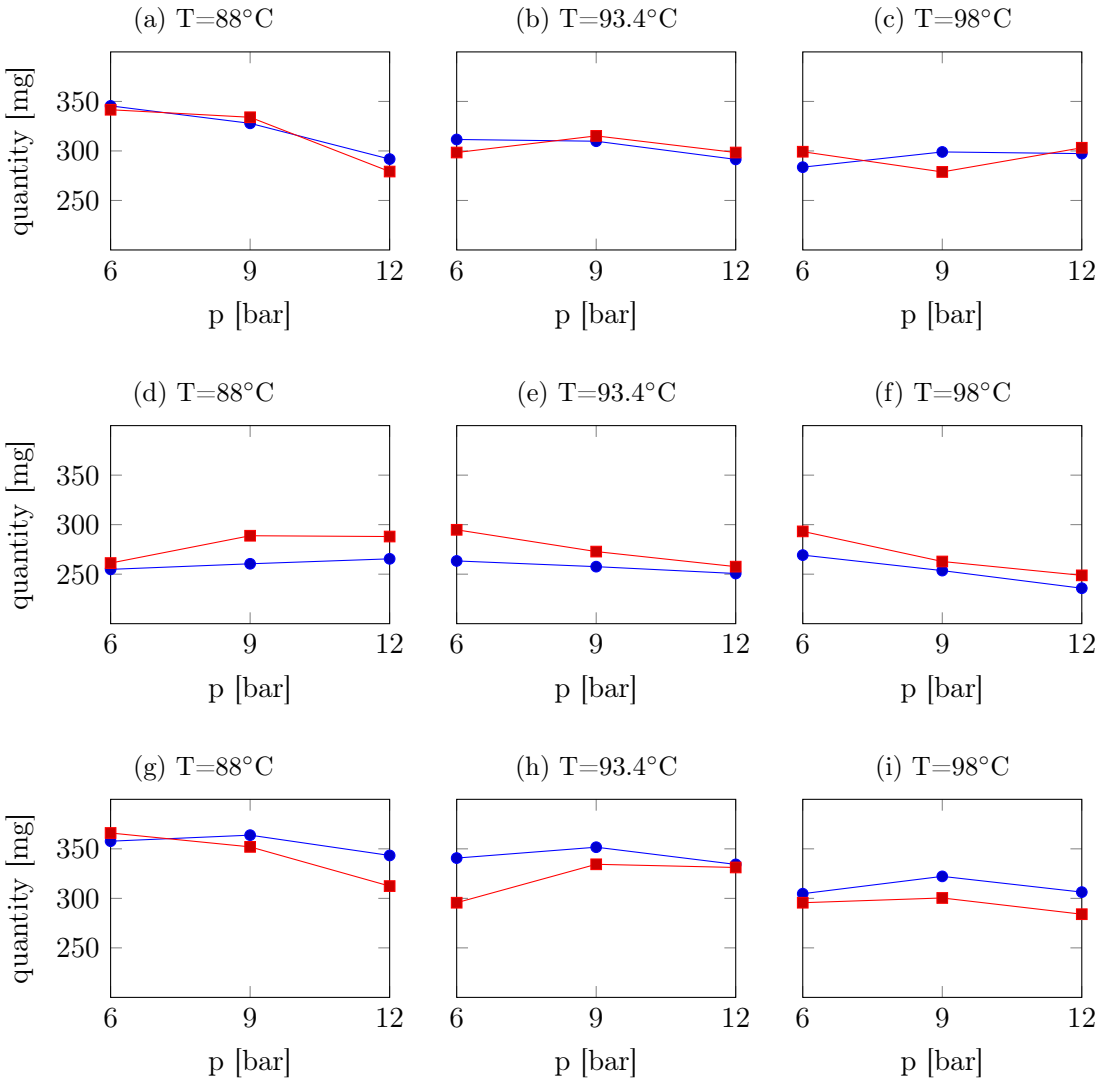

Figure 4.21: Comparison between the caffeine extracted through numerical simulations (blue profile with circles) and laboratory measurements (red profile with squares), with different inlet water temperatures and pressures and different grain size of Robusta coffee powder. Figures (a)-(c) show the results of optimal granulometry, Figures (d)-(f) of coarse granulometry, Figures (g)-(i) of fine granulometry.

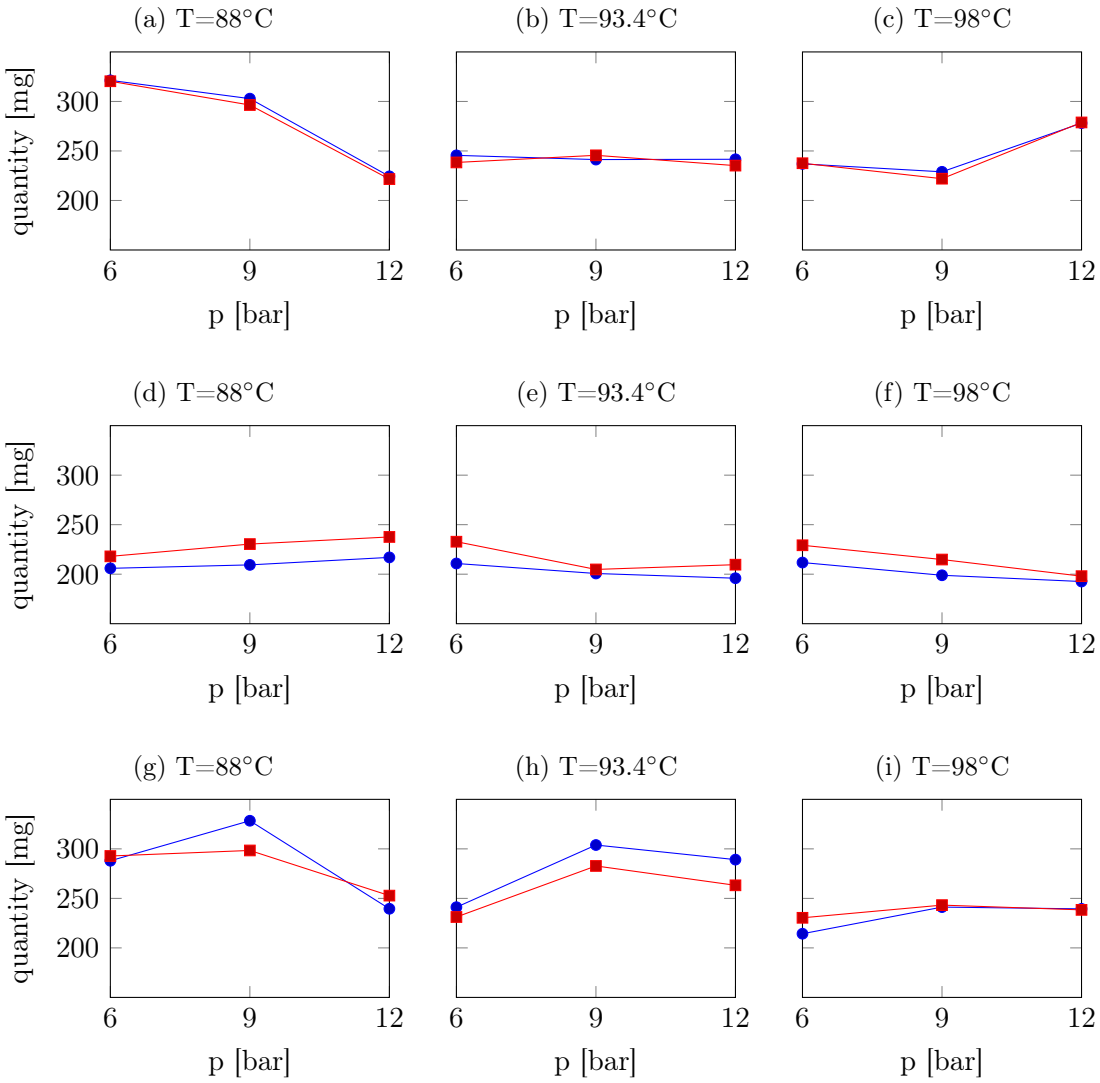

Figure 4.22: Comparison between the chlorogenic acids extracted through numerical simulations (blue profile with circles) and laboratory measurements (red profile with squares), with different inlet water temperatures and pressures and different grain size of Robusta coffee powder. Figures (a)-(c) show the results of optimal granulometry, Figures (d)-(f) of coarse granulometry, Figures (g)-(i) of fine granulometry.

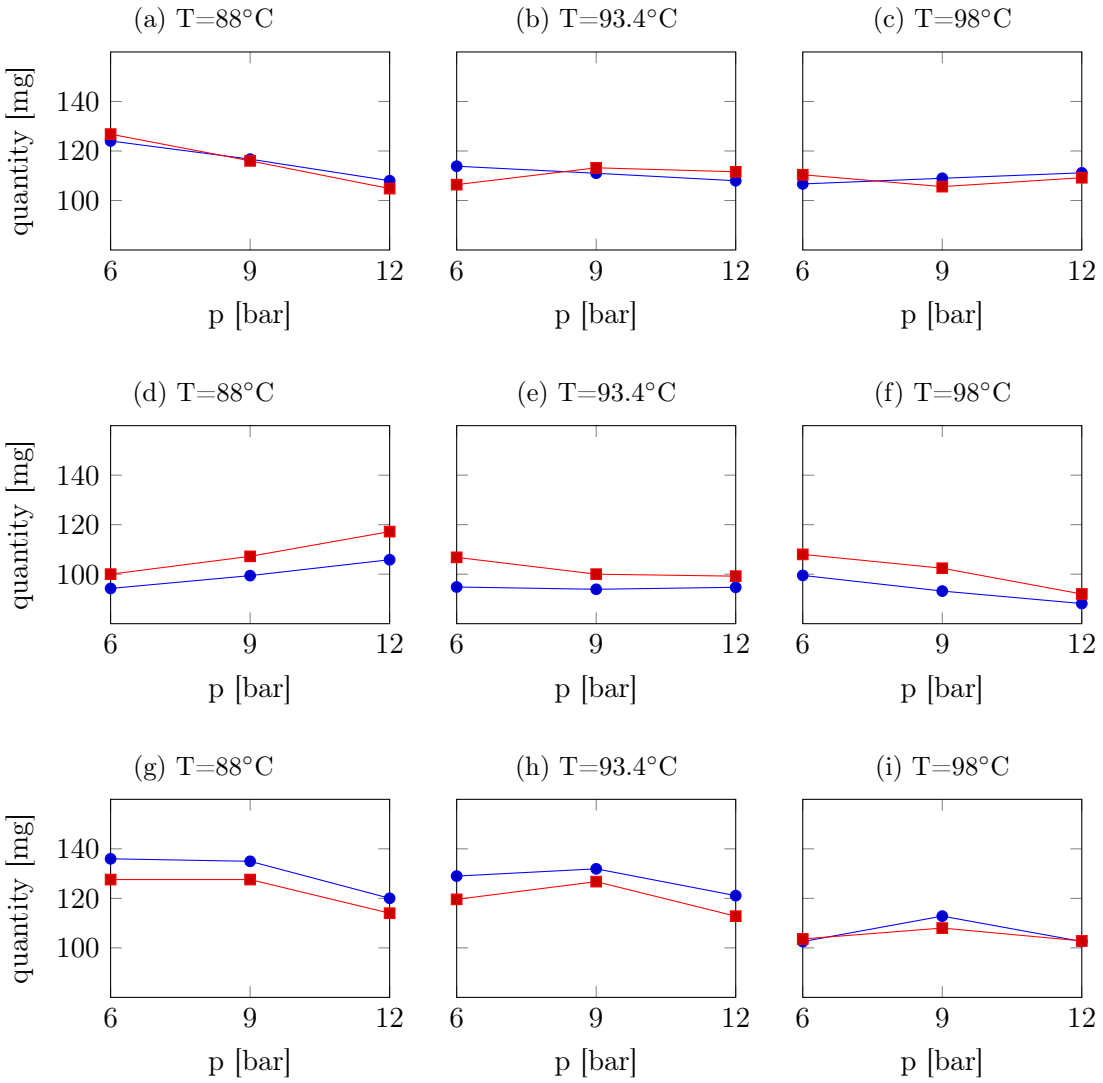

Figure 4.23: Comparison between the trigonelline extracted through numerical simulations (blue profile with circles) and laboratory measurements (red profile with squares), with different inlet water temperatures and pressures and different grain size of Robusta coffee powder. Figures (a)-(c) show the results of optimal granulometry, Figures (d)-(f) of coarse granulometry, Figures (g)-(i) of fine granulometry.

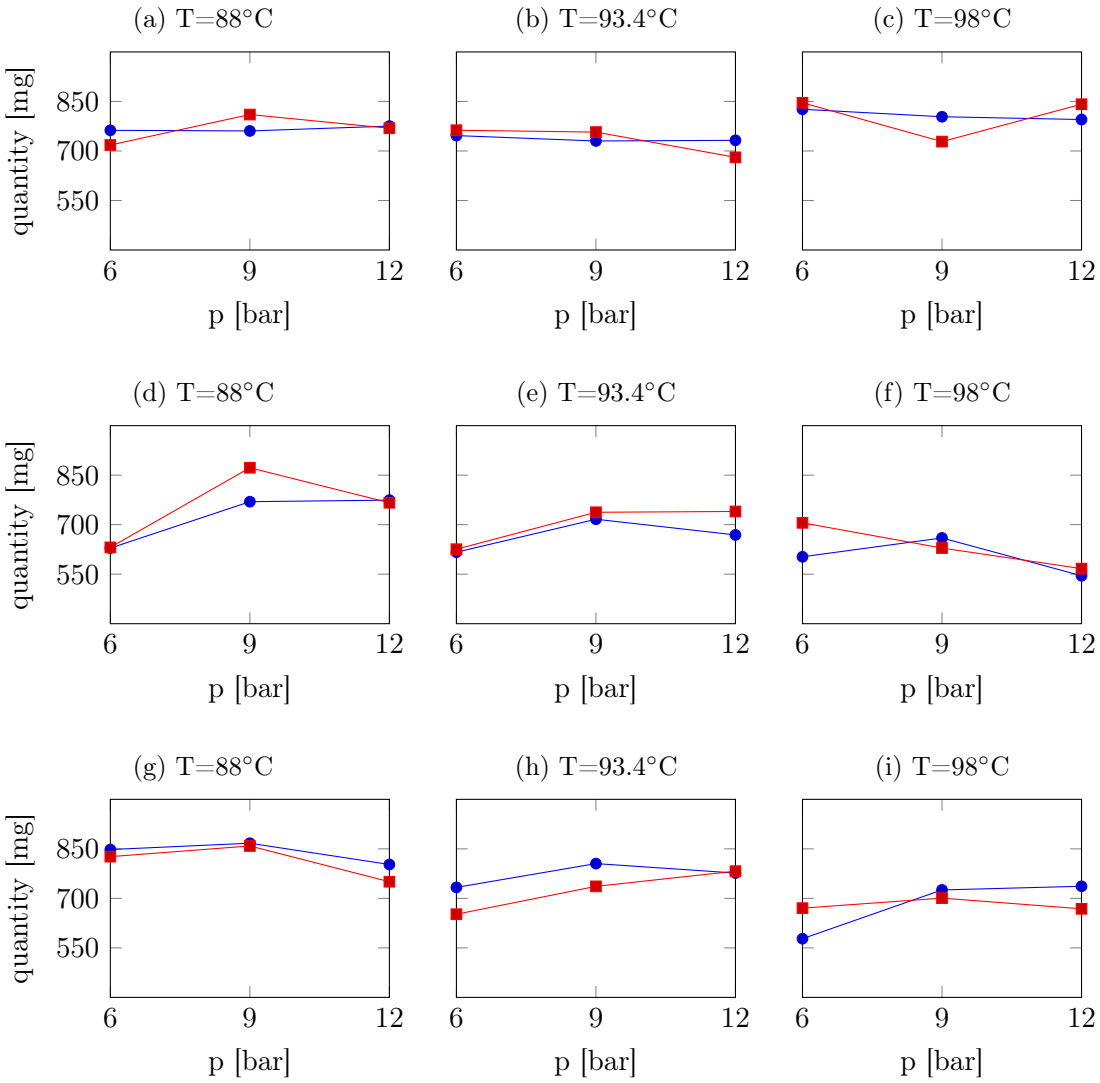

Figure 4.24: Comparison between the citric acid extracted through numerical simulations (blue profile with circles) and laboratory measurements (red profile with squares), with different inlet water temperatures and pressures and different grain size of Robusta coffee powder. Figures (a)-(c) show the results of optimal granulometry, Figures (d)-(f) of coarse granulometry, Figures (g)-(i) of fine granulometry.

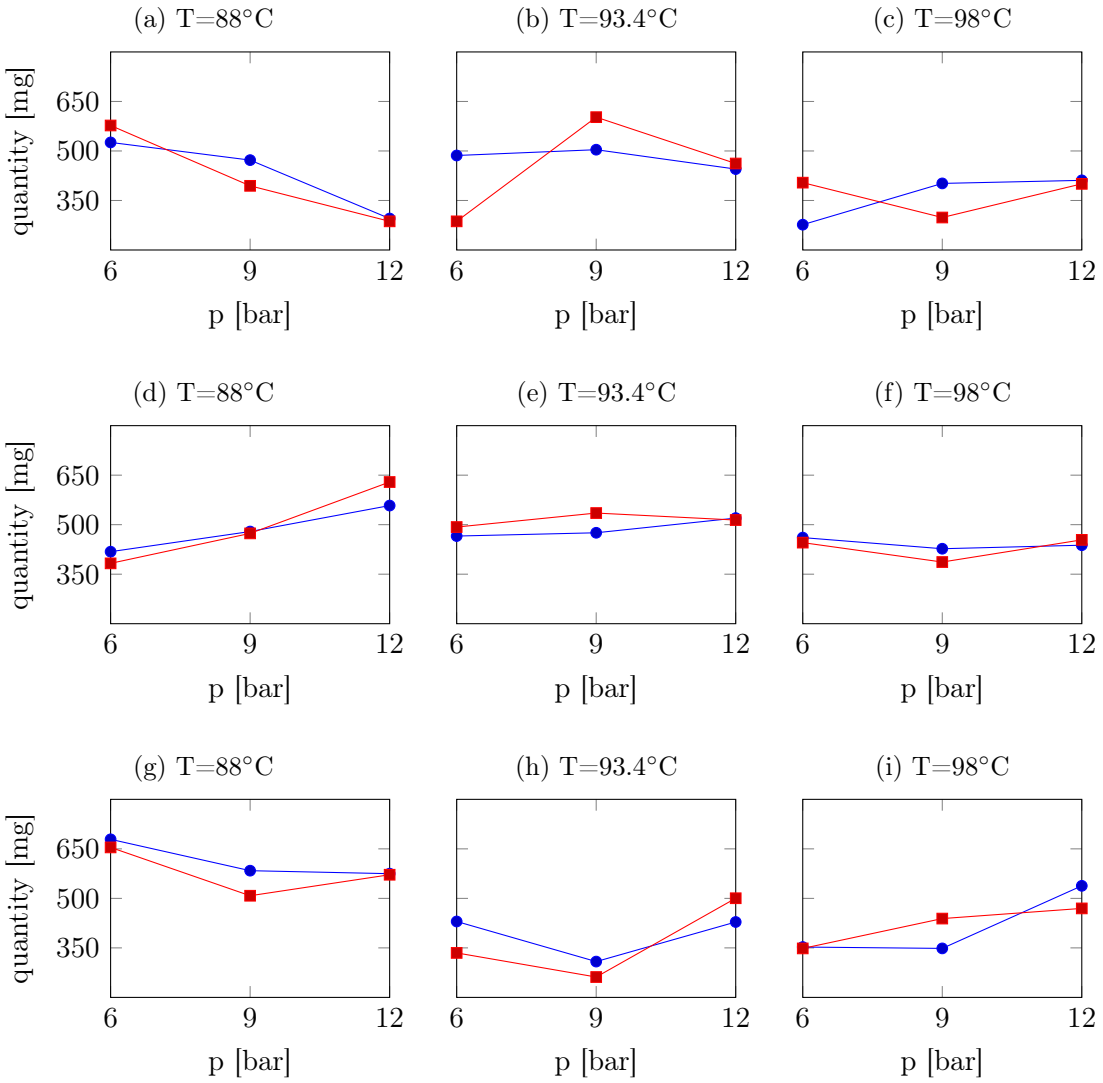

Figure 4.25: Comparison between the acetic acid extracted through numerical simulations (blue profile with circles) and laboratory measurements (red profile with squares), with different inlet water temperatures and pressures and different grain size of Robusta coffee powder. Figures (a)-(c) show the results of optimal granulometry, Figures (d)-(f) of coarse granulometry, Figures (g)-(i) of fine granulometry.

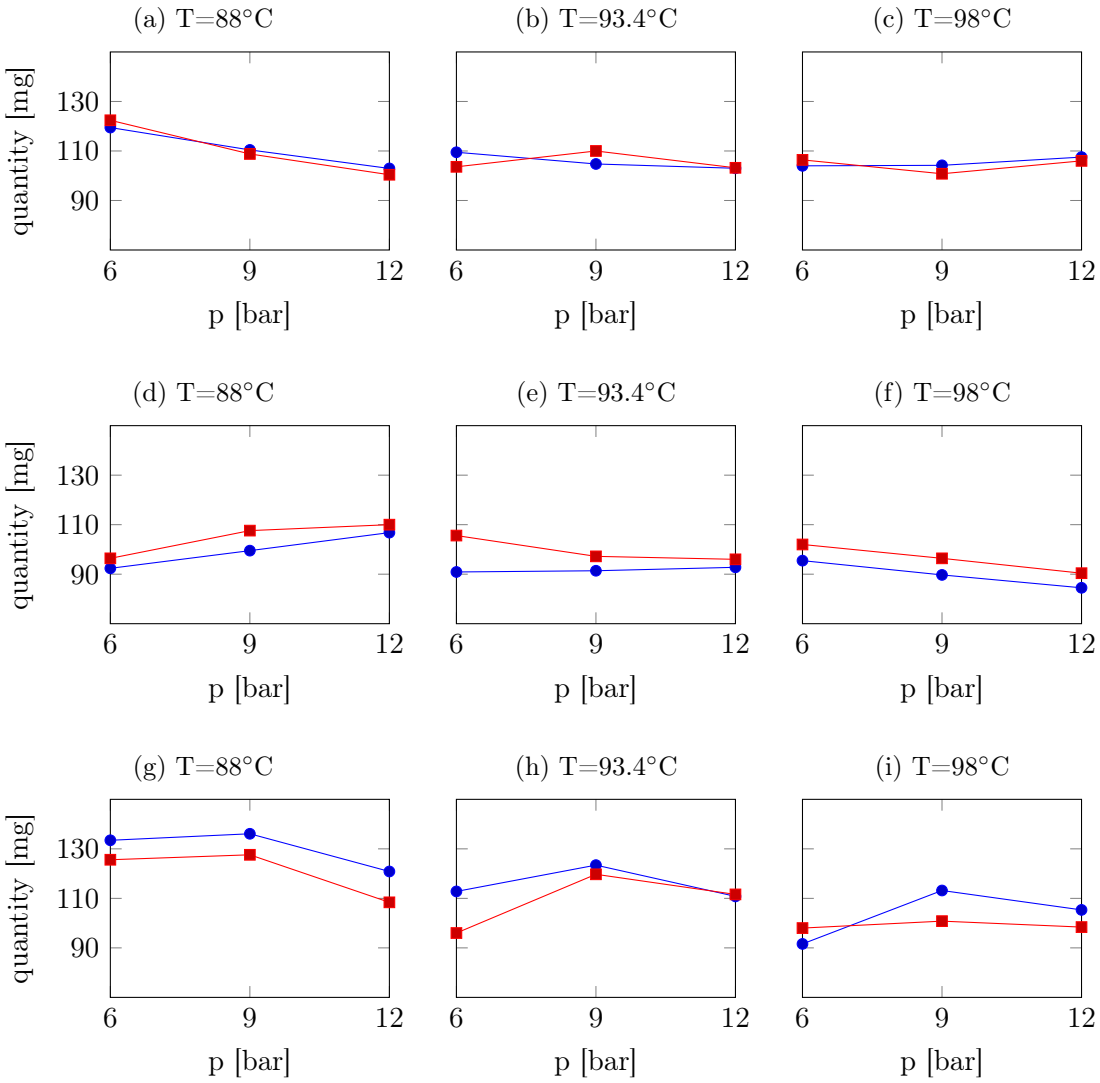

Figure 4.26: Comparison between the tartaric acid extracted through numerical simulations (blue profile with circles) and laboratory measurements (red profile with squares), with different inlet water temperatures and pressures and different grain size of Robusta coffee powder. Figures (a)-(c) show the results of optimal granulometry, Figures (d)-(f) of coarse granulometry, Figures (g)-(i) of fine granulometry.

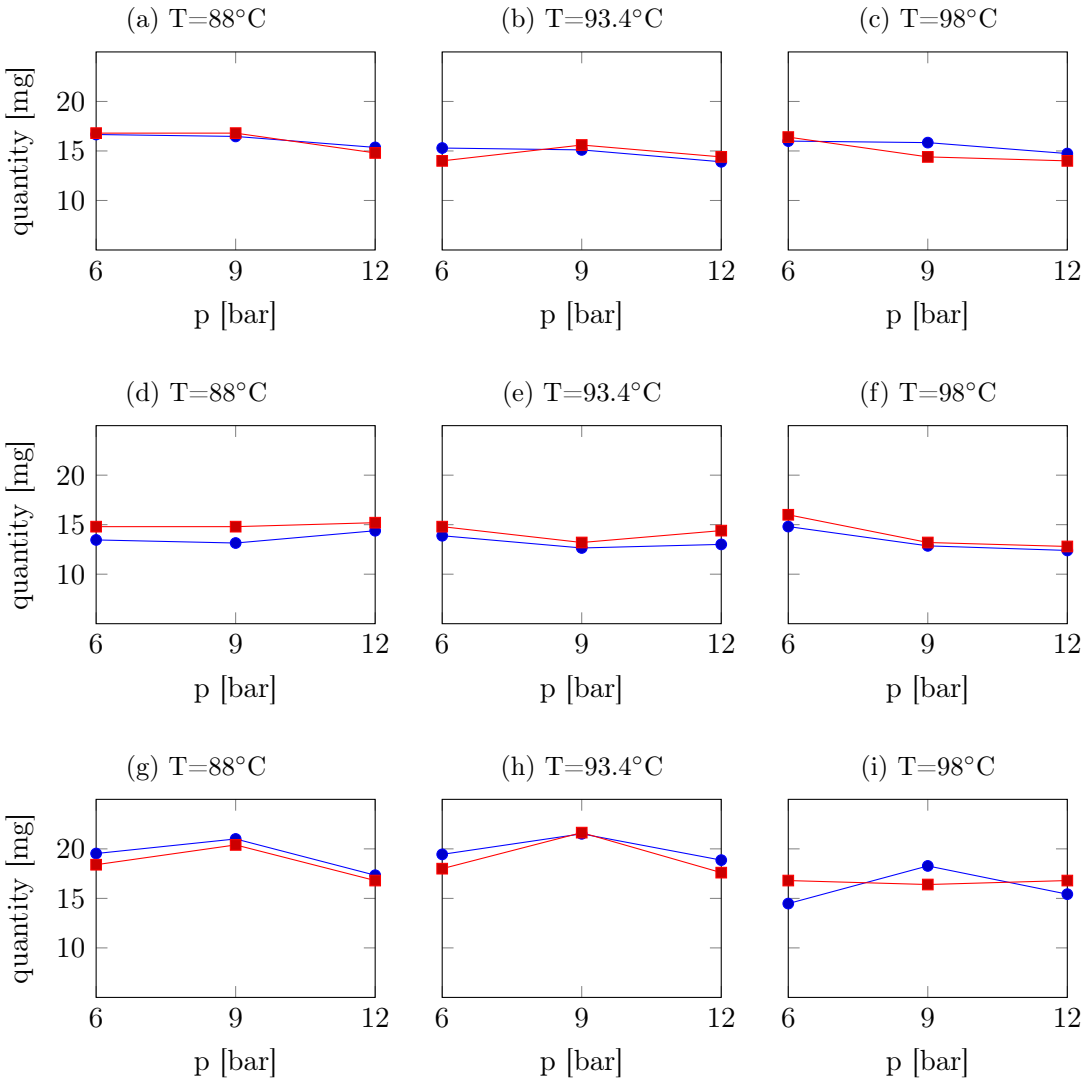

Figure 4.27: Comparison between the ferulic acid extracted through numerical simulations (blue profile with circles) and laboratory measurements (red profile with squares), with different inlet water temperatures and pressures and different grain size of Robusta coffee powder. Figures (a)-(c) show the results of optimal granulometry, Figures (d)-(f) of coarse granulometry, Figures (g)-(i) of fine granulometry.

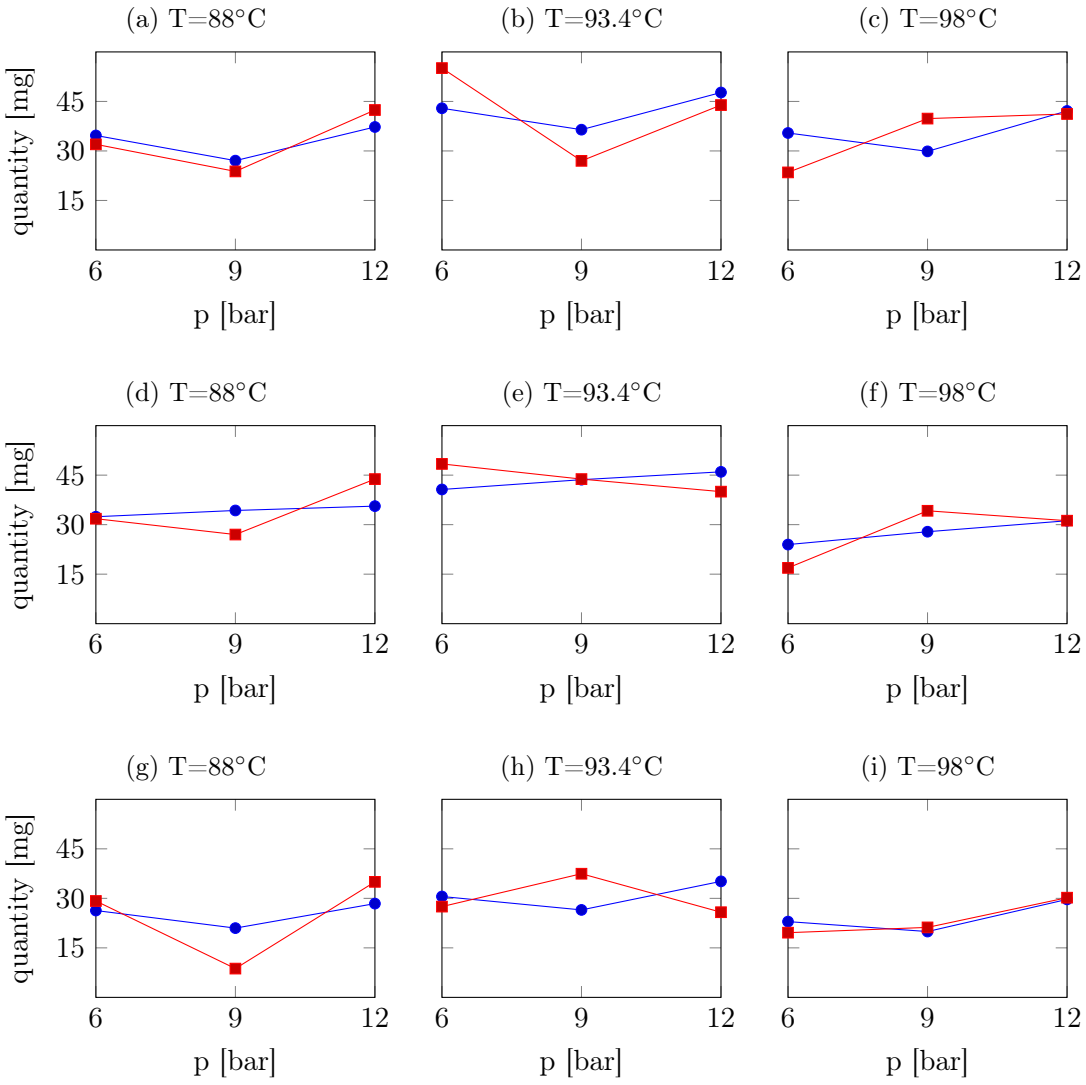

Figure 4.28: Comparison between the lipids extracted through numerical simulations (blue profile with circles) and laboratory measurements (red profile with squares), with different inlet water temperatures and pressures and different grain size of Robusta coffee powder. Figures (a)-(c) show the results of optimal granulometry, Figures (d)-(f) of coarse granulometry, Figures (g)-(i) of fine granulometry.

	$(91, 8, \mathrm{O})$	$(96, 9, \mathrm{O})$	$(89, 10, \mathrm{G})$	$(97, 7, \mathrm{G})$	$(90, 8, \mathrm{F})$	$(95, 11, \mathrm{F})$
CF	215.2 (**7.2**)	216.0 (11.4)	186.9 (**3.0**)	192.0 (**7.9**)	221.2 (**3.5**)	213.9 (21.5)
CQA	369.6 (**1.9**)	351.4 (10.6)	324.8 (**6.6**)	304.5 (**8.0**)	347.6 (**7.3**)	349.5 (22.4)
TR	135.4 (12.2)	136.1 (**6.5**)	125.8 (**5.4**)	126.9 (**5.7**)	140.3 (**5.3**)	140.2 (27.2)
CA	697.2 (96.1)	634.2 (21.8)	542.2 (17.4)	493.4 (21.1)	523.2 (29.0)	541.4 (**3.5**)
AA	297.8 (59.6)	275.2 (**5.9**)	299.0 (42.9)	298.8 (12.5)	336.3 (48.1)	321.4 (72.2)
TA	138.4 (**10.0**)	138.8 (**8.6**)	123.8 (**6.5**)	123.4 (**2.5**)	138.1 (**6.4**)	137.6 (24.3)
FA	10.5 (17.2)	10.8 (**0.3**)	9.8 (**9.7**)	9.7 (**0.2**)	12.0 (**1.4**)	12.3 (30.0)
LP	207.0 (76.0)	188.9 (55.8)	151.9 (**6.7**)	172.2 (24.6)	232.4 (**1.2**)	188.5 (**0.9**)

Table 4.28: Amount [mg] of the chemical species at the end of the percolation process for Arabica variety. The percentage error between numerical and laboratory results is in brackets. The extraction point is denoted by (T, p, r).

	$(91, 8, \mathrm{O})$	$(96, 9, \mathrm{O})$	$(89, 10, \mathrm{G})$	$(97, 7, \mathrm{G})$	$(90, 8, \mathrm{F})$	$(95, 11, \mathrm{F})$
CF	322.5 (**0.7**)	303.3 (**9.6**)	261.2 (**6.6**)	264.0 (**9.7**)	362.0 (19.4)	336.1 (**9.4**)
CQA	270.6 (**6.4**)	228.5 (**4.3**)	208.4 (**7.1**)	207.0 (11.5)	318.1 (31.7)	290.4 (20.8)
TR	115.1 (**1.8**)	109.6 (11.8)	99.8 (**2.9**)	96.5 (**9.7**)	136.7 (22.9)	122.7 (20.8)
CA	729.5 (23.4)	763.7 (**0.5**)	772.4 (18.4)	648.3 (**0.7**)	844.9 (16.8)	781.6 (**8.2**)
AA	520.9 (23.1)	465.3 (30.7)	505.1 (**7.3**)	453.7 (11.0)	503.4 (39.8)	370.3 (**5.2**)
TA	108.9 (**4.8**)	104.0 (**7.9**)	99.7 (**2.6**)	92.6 (10.9)	131.7 (24.7)	115.3 (15.8)
FA	15.6 (15.2)	15.3 (**1.8**)	13.2 (**5.8**)	13.8 (**3.9**)	21.6 (31.9)	19.8 (23.6)
LP	34.9 (29.1)	34.4 (157)	38.9 (14.6)	30.8 (24.5)	24.9 (30.0)	30.0 (18.0)

Table 4.29: Amount [mg] of the chemical species at the end of the percolation process for Robusta variety. The percentage error between numerical and laboratory results is in brackets. The extraction point is denoted by (T, p, r).

	CF	CQA	TR	CA	AA	TA	FA	LP
A	9.1	9.4	10.4	31.0	40.2	9.7	9.8	27.5
R	9.2	13.6	11.7	11.3	19.5	11.1	13.7	45.5

Table 4.30: Mean percentage error among the numerical and laboratory results for each chemical species and Arabica (A) and Robusta (R) varieties.

4.3 Towards a customisation tool for coffee taste

In this section we present an RBF-based numerical approximation for the three dimensional model. In particular, we focus on the prediction of the flow and we consider the equation describing the hydraulic head dynamics.

Section 4.3.1 describes an RBF-based numerical approximation of the three dimensional model discussed in Section 2.3. More precisely, we focus on the equation predicting the water dynamics. This approximation scheme is the same used in the RBF-based approximation scheme of Section 4.1.2 for the reduced percolation model (2.80), (2.81). Then, the reliability of the proposed solving strategy is experimentally assessed through numerical simulations of the hydraulic head behaviour, whose results are shown in Section 4.3.2.

4.3.1 An RBF approximation for the flow prediction in the espresso extraction

For the reader's convenience we recall the problem modelling the water dynamics in the espresso extraction;

$$\begin{cases} S_0 \dfrac{\partial h}{\partial t} + \nabla \cdot \boldsymbol{q} = 0, & \text{in } \mathcal{C},\ t \in [0,\tau], \\ \boldsymbol{q} = -\mathbf{K} f_\mu \cdot (\nabla h + \chi \boldsymbol{e}), & \text{in } \mathcal{C},\ t \in [0,\tau], \\ h = h_{z_0}, & \text{on } \Gamma_1,\ t \in (0,\tau], \\ \dfrac{\partial h}{\partial \mathbf{n}} = 0, & \text{on } \Gamma_2,\ t \in (0,\tau], \\ \boldsymbol{q} \cdot \mathbf{n} = -\Phi_h \min\{h_C - h, 0\}, & \text{on } \Gamma_3,\ t \in (0,\tau], \\ p = p_0(x_3), & \text{in } \mathcal{C},\ t = 0, \end{cases} \tag{4.30}$$

with the same notation introduced in Section 2.3.

The numerical approximation of problem (4.30)is based on the Crank-Nicolson method, where the spatial derivatives are approximated via RBFs.

Let $\bar{\mathcal{X}} = \mathcal{X} \cup \mathcal{X}_1 \cup \mathcal{X}_2 \cup \mathcal{X}_3 = \{\boldsymbol{x}_j\}_{j=1,2,\dots,N} \subseteq \mathcal{C}$ be the set of distinct discretisation nodes, where we denoted with $\mathcal{X}$ the nodes in the interior of $\mathcal{C}$ and with $\mathcal{X}_i$ the nodes belonging to its surfaces Γ_i, $i = 1, 2, 3$, respectively. Let A be the PA-RBF interpolation matrix associated with the interpolation nodes $\bar{\mathcal{X}}$, then equation (3.40) holds with $d = 3$, $f(\boldsymbol{x}) = h(\boldsymbol{x}, t)$ and $t \in [0, \tau]$. Thus, for a fixed t, if $\boldsymbol{h}(t)$ is the column vector of the values of the hydraulic head $h(\boldsymbol{x}, t)$ calculated at the points of $\bar{\mathcal{X}}$, that is $\boldsymbol{h}(t) = (h(\boldsymbol{x}_j, t))^T_{j=1,2,\dots,N}$, the analogue of equation (3.43) for the hydraulic head h, is:

$$\mathcal{L}\tilde{h}(\boldsymbol{x}, t) = \left(\boldsymbol{b}(\boldsymbol{x})^{\mathcal{L}} A^{-1}\right)_{1:N} \boldsymbol{h}(t). \tag{4.31}$$

We denote with $\mathcal{L}_0$ the identity operator, with $\mathcal{L}_{1,i}$, $i = 1, 2, 3$ the first derivative operator respect to the i-th component of $\boldsymbol{x}$ and with $\mathcal{L}_{2,i,s}$ the second derivative operator respect to the components i and s, $i, s = 1, 2, 3$. For each of these operators,

we can impose equation (4.31) at each point of $\mathcal{X}$. For $i, s = 1, 2, 3$ we obtain:

$$\begin{aligned}
&\left(\mathcal{L}_0\tilde{h}(\boldsymbol{x}_j, t)\right)_{j=1,2,\ldots,N}^{T} = (AA^{-1})\,\boldsymbol{h}(t) \equiv I\boldsymbol{h}(t),\\
&\left(\mathcal{L}_{1,i}\tilde{h}(\boldsymbol{x}_j, t)\right)_{j=1,2,\ldots,N}^{T} = (D_{1,i}A^{-1})\,\boldsymbol{h}(t) \equiv D^{1,i}\boldsymbol{h}(t),\\
&\left(\mathcal{L}_{2,i,s}\tilde{h}(\boldsymbol{x}_j, t)\right)_{j=1,2,\ldots,N}^{T} = (D_{2,i,s}A^{-1})\,\boldsymbol{h}(t) \equiv D^{2,i,s}\boldsymbol{h}(t),
\end{aligned} \tag{4.32}$$

where $D_{1,i} \equiv \left(\boldsymbol{b}(\boldsymbol{x}_j)^{\mathcal{L}_{1,i}}\right)_{j=1,2,\ldots,N}$ denotes the differentiation matrix associated to $\mathcal{L}_{1,i}$ and similarly for the other operators in (4.32). With the above described notation we have that the matrix associated to the Laplacian operator is

$$L = D^{2,1,1} + D^{2,2,2} + D^{2,3,3}. \tag{4.33}$$

We define some useful notations for the systems below. A matrix equipped with the subscript I is the sub-matrix that consists of all the rows of the corresponding original matrix related to the points in $\mathcal{X}$. Similarly, a matrix endowed with the subscript $i = 1, 2, 3$ is the sub-matrix that consists of all the rows of the corresponding original matrix related to the point in $\mathcal{X}_i$, $i = 1, 2, 3$. In addition, for $i = 1, 2, 3$ we denote with $\mathbf{n}_i$ the vector containing the i-th components of the unit vectors which are normal to the surface Γ_2 on a point $\boldsymbol{x}_i \in \mathcal{X}_2$, and N_i denotes the diagonal matrix with components $\mathbf{n}_i$. We note that, $\mathbf{n}_i$ has a number of components equal to the number of points in $\mathcal{X}_2$. Moreover, for each $\boldsymbol{x} \in \mathcal{X}_3$, $\mathbf{n}(\boldsymbol{x}) = (0, 0, -1)^T$. With these notations the spatial discretisation of problem (4.30) is:

$$\begin{cases}
S_0 I_I \dfrac{\partial \boldsymbol{h}(t)}{\partial t} - \boldsymbol{K} f_\mu L_I \boldsymbol{h}(t) = 0,\\
I_1 \boldsymbol{h}(t) = \boldsymbol{h}_0,\\
\left(N_1 D_2^{1,1} + N_2 D_2^{1,2} + N_3 D_2^{1,3}\right)\boldsymbol{h}(t) = 0,\\
\boldsymbol{K} f_\mu D_3^{1,3}\boldsymbol{h}(t) = -\Phi_h \min\{\boldsymbol{h}_C - I_3\boldsymbol{h}(t), 0\} - \boldsymbol{K} f_\mu \chi \boldsymbol{e},\\
I\boldsymbol{h}(0) = \dfrac{\boldsymbol{p}_0}{\rho_0 g} + \overline{\boldsymbol{x}}_3,
\end{cases} \tag{4.34}$$

where $\overline{\boldsymbol{x}}_3 = ((\boldsymbol{x}_j)_3)_{j=1,2,\ldots,N}^{T}$, and $(\cdot)_3$ selects the third component of $\cdot$ and $\boldsymbol{p}_0 = p_0(\overline{\boldsymbol{x}}_3)$. Now we can apply the time discretisation to problem (4.34). We use the Crank-Nicolson scheme in the aforementioned spatial discretisation made through RBFs.

The boundary conditions are implemented at the new time level. Note that to state a discrete time level, we use the time index as a superscript. In particular, this procedure for the time discretisation is implemented in the first equation of system (4.34). Let N_t be a positive integer and $h_t = \tau/N_t$, for $k = 0, 1, \ldots, N_t - 1$, for the first equation in (4.34), we have:

$$S_0 I_I \left(\boldsymbol{h}^{k+1} - \boldsymbol{h}^k\right) = \frac{h_t}{2}\left(\boldsymbol{K} f_\mu L_I \boldsymbol{h}^{k+1} + \boldsymbol{K} f_\mu L_I \boldsymbol{h}^k\right), \tag{4.35}$$

where $\boldsymbol{h}^k \approx \boldsymbol{h}(t_k)$. Thus, for $k = 0, 1, \ldots, N_t - 1$, we get:

$$\begin{cases} \left(I_I - \dfrac{h_t \boldsymbol{K} f_\mu}{2S_0} L_I\right) \boldsymbol{h}^{k+1} = \left(I_I + \dfrac{h_t \boldsymbol{K} f_\mu}{2S_0} L_I\right) \boldsymbol{h}^k, \\ I_1 \boldsymbol{h}^{k+1} = \boldsymbol{h}_0, \\ \left(D_2^{1,1}.*\boldsymbol{n}_1 + D_2^{1,2}.*\boldsymbol{n}_2 + D_2^{1,3}.*\boldsymbol{n}_3\right) \boldsymbol{h}^{k+1} = 0, \\ \boldsymbol{K} f_\mu D_3^{1,3} \boldsymbol{h}^{k+1} = -\Phi_h \min\{h_C - I_3 \boldsymbol{h}^k, 0\} - \boldsymbol{K} f_\mu \chi \boldsymbol{e}, \\ I\boldsymbol{h}^0 = \dfrac{\boldsymbol{p}_0}{\rho_0 g} + \overline{\boldsymbol{x}}_3. \end{cases} \tag{4.36}$$

4.3.2 Numerical Experiment

The numerical solution of problem (4.30) is obtained by the approximation scheme described in (4.36). This method has been implemented in MATLAB. Table 4.31 shows the value of the physico-chemical parameters used in the numerical simulations. They are the same used in [23] and they are in good agreement with those used in [24]. Besides, we have chosen the hydraulic conductivity tensor $\boldsymbol{K}$ as

H $[m]$	$13.77 \cdot 10^{-3}$	S_0 $[1/m]$	$1 \cdot 10^{-5}$
Φ_H $[1/s]$	$2.2 \cdot 10^{-5}$	f_μ [ ]	1
τ $[s]$	20	χ [ ]	0
ρ_0 $[kg/m^3]$	997	h_C $[m]$	0

Table 4.31: Parameters configuration used in the numerical experiment.

a constant diagonal matrix with elements value: $K = 1.68 \cdot 10^{-7}$. Finally, for the pressure of the incoming water we choose $p_0 = 6, 9, 11$bar.

Regarding the parameters of the discretisation scheme, we choose $N_t = 5000$, so that $h_t \approx 4 \cdot 10^{-3}$, and $N = 310$ points in $\bar{\mathcal{X}}$. Moreover, as RBF we choose the polyharmonic splines of exponent 3, that is: $\Phi_j(\boldsymbol{x}) = \varphi\left(||\boldsymbol{x} - \boldsymbol{x}_j||\right) = ||\boldsymbol{x} - \boldsymbol{x}_j||_2^3$, $\boldsymbol{x}_j \in \bar{\mathcal{X}}$. The maximum degree of the polynomial basis is $m = 3$.

In Figures 4.29, 4.30 and 4.31 we report a graphic representation of the hydraulic head behaviour inside the coffee pod $\mathcal{C}$ at time $t = \tau$ (left), and in a vertical section of $\mathcal{C}$ (right) at time $t = \tau$, for incoming water pressure value of $p_0 = 6, 9, 11$bar, respectively. Figure 4.29-4.31 shows that inside the coffee pod the hydraulic head linearly decreases along the vertical direction, meaning that the pressurised water, entering the filter at $6, 9, 11$ *bar*, exits respectively with a pressure of $2, 3, 3.5$ bar, approximately. These are quite reasonable results that are in good agreement with laboratory measurements and other simulation results. From this preliminary result, we can conclude that the proposed discretisation technique is a good tool for such a kind of problem and it deserves further explorations in two main directions: i) the discretisation of the full espresso percolation problem, ii) a detailed validation against laboratory measurements and simulation data obtained with other computational tools.

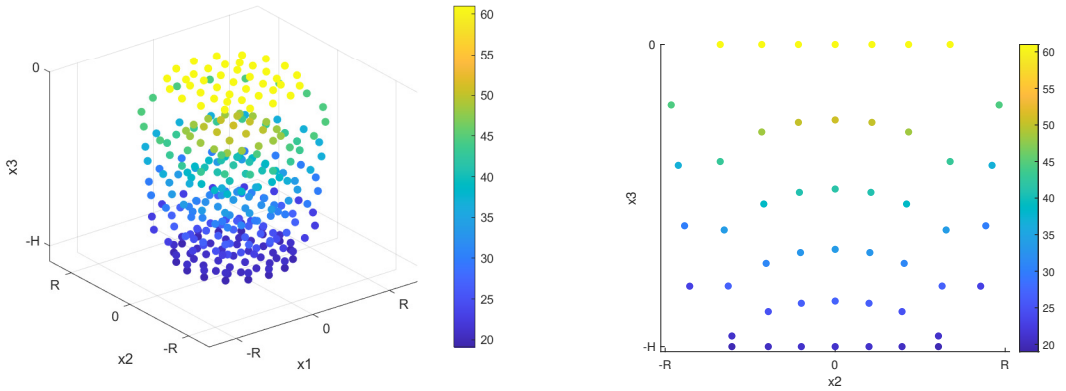

Figure 4.29: Left: representation of the simulated hydraulic head in the coffee pod $\mathcal{C}$, at time $t = \tau$. Right: representation of the simulated hydraulic head in a vertical section of the coffee pod $\mathcal{C}$, at time $t = \tau$. Both the figures refers to incoming water pressurised at 6 bar.

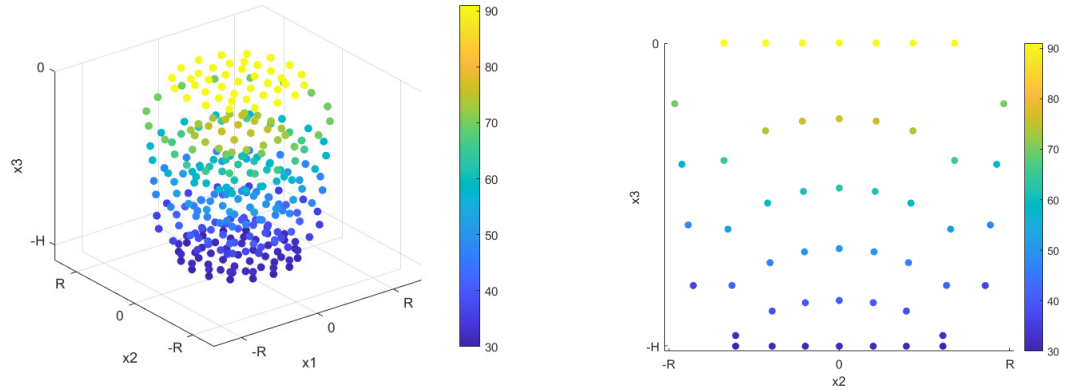

Figure 4.30: Left: representation of the simulated hydraulic head in the coffee pod $\mathcal{C}$, at time $t = \tau$. Right: representation of the simulated hydraulic head in a vertical section of the coffee pod $\mathcal{C}$, at time $t = \tau$. Both the figures refers to incoming water pressurised at 9 bar.

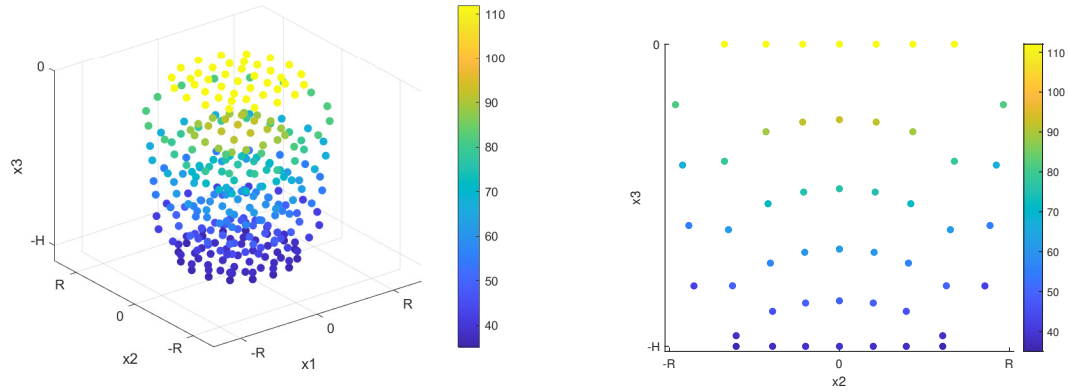

Figure 4.31: Left: representation of the simulated hydraulic head in the coffee pod $\mathcal{C}$, at time $t = \tau$. Right: representation of the simulated hydraulic head in a vertical section of the coffee pod $\mathcal{C}$, at time $t = \tau$. Both the figures refers to incoming water pressurised at 11 bar.

4.4 Analysis and comparison of the results

In this chapter, we presented the results of numerical simulations based on the two models proposed in Sections 2.3, 2.4.

The 3D model detailed in Section 2.3 is a complete model for the prediction of all the main physico-chemical processes occurring during the coffee extraction. This model can describe both the extracted substances at the end of the extraction and the dynamics of the water flow, as well as the heat transport. Being a full model, it has complete predictive power; however, it has the disadvantage of being very complex to implement from scratch. On the contrary, the reduced model described in Section 2.4, has the advantage of an easy implementation but, on the other hand, it can only predict the amount of extracted substances. Furthermore, this model does not take into account the pressure and temperature of the incoming water, so it is suitable for extraction's global predictions such as the EY prediction. Consequently, such a model can be profitably exploited to pursue the coffee industry's sustainability goals. It is instead not appropriate for achieving the beverage customisation, for which the 3D model is particularly suitable.

We proposed two different numerical approximation schemes for the reduced percolation model, whose implementation was fully managed in MATLAB. More precisely, in Section 4.1.1 we described a finite difference approximation scheme and we used such a scheme for the prediction of both EY and extracted substances. In particular, we used two types of coffee for the EY forecasting. The results of the simulations show a quite good agreement between the numerical and real EY, mainly for the Cibao Altura coffee. In addition, we selected two of the most famous substances affecting the health-related properties of espresso coffee: caffeine and chlorogenic acids. In this case, the results of the simulation are very satisfactory showing an interesting predictive power of such a model, meaning that when simulating more than one substance, the modelling of the reaction rate can actually reflects the substances interactions. Then, in Section 4.1.2 we proposed a RBF-based approximation scheme for the EY prediction. Numerical simulations were performed with the same Modœtia coffee samples, as these are the ones for which

the finite difference approach gave the less precise outcomes. The results of the numerical simulations show that the RBF-based scheme provides better accuracy in terms of extraction efficiency.

In Section 4.2 we showed the calibration and validation of the 3D model by comparing the numerical and laboratory results of the extracted chemical species, and using two types of different coffee (Arabica and Robusta). The numerical simulations were performed with the software FeFlow Demo 7.2 [77]. A set of substances between the most affecting the coffee taste and health-related properties has been selected, i.e., caffeine, chlorogenic acids, trigonelline, citric acid, acetic acid, tartaric acid, ferulic acid, and lipids. A large extraction campaign has been dedicated to the model calibration. A dedicated set of extractions has been dedicated to the model validation. The comparison between numerical and laboratory results shows an extremely good correspondence for some species and a generally good behaviour for all the species, with a mean error in the predictive power around 10% in most cases.

Finally, in Section (4.3) we proposed an RBF-based approximation scheme for the equation governing the water dynamics in the 3D study case. More precisely, we simulated the hydraulic head behaviour with diferent values of the initial pressure of the incoming water. The results show that the pressurised water exits the coffee pod at approximately double or triple the atmospheric pressure. These preliminary results are quite reasonable and they are in good agreement with numerical data obtained with the finite element computational tool. Thus, this approximation scheme is a promising tool for flow problems and it deserves further exploration in order to discretise the full espresso coffee percolation problem.

Final discussion and conclusions

The thesis focuses on the study of the espresso coffee extraction process and the corresponding modeling tools. More precisely, we discussed percolation in porous media and we presented two model for the prediction of the coffee extraction. The 3D model takes into account the fluid flow of water into the ground coffee and the consequent dissolution of chemical species, as well as the heat transport. This is a full model capable to predict all the main phenomena occurring in the extraction process. So, such a model is suitable for achieving the beverage personalisation aim of coffee industry. In addition, we studied a reduced percolation model predicting the amount of extracted substances. This model neglects the dynamics of the pressure and of the temperature of the incoming water.

The numerical approximation of the reduced model is based on two different approximation schemes. The finite difference approach is used to predict both the EY and the extracted substances. The comparison of the numerical and real EY shows that the model can follow the real behaviour of the extraction process in terms of extraction efficiency, mainly for the Cibao Altura coffee. Moreover, we predicted two of the most important substances affecting the health-related properties of espresso coffee: caffeine and chlorogenic acids. In this case, the results show that the model is able to predict the amount of the extracted substances with great precision. To this aim, the strength of the reduced model is the reaction terms where the reaction rate can actually reflects the substances interactions. In the other approach, the RBF-based approximation scheme is used to predict the EY on the Modœtia coffee samples for which the finite difference approach gave the less precise results. The results obtained with this second approach show an improved

accuracy in terms of extraction efficiency with respect to the results obtained with the finite difference scheme. Thus, the reduced model is suitable for the global prediction of the extraction, such as the EY prediction. So that it is a good tool for the sustainability purposes of coffee industry. Two main future refinements have to be considered to obtain an effective and reliable simulation tool: (i) improvement of the numerical procedure by taking into account the particular forms of the reaction terms; (ii) improvement of the validation of the percolation model; in particular, it would be interesting to investigate through a wider extraction campaign the correlation between Darcy's flux and variations in pressure and temperature, and to observe the behaviour of the computed EY. The predictive power of the reduced model make this simulation system a strategic tool for the coffee industry, as it could actually support one of the main challenge of the coffee industry, that is the sustainability of the coffee chain by reducing the amount of coffee powder needed for an espresso.

The calibration and validation of the 3D model has been performed by comparing the numerical and laboratory results of 8 extracted substances among the most affecting the coffee taste and using two types of coffees. The comparison between numerical simulations obtained with the software FeFlow Demo 7.2 and laboratory results shows an extremely good agreement for some species and a global good behaviour for all the chemicals, with a mean error around 10% in most cases. The present study considered several extraction conditions and granulometries in proper admissible ranges; however, it has some limitations that should be analysed in future pre-commercial trials. In particular, the following factors influencing the chemical characteristics of EC have been considered stable or of negligible influence during the extraction campaign. The tamping pressure is fixed at a value that is the mean value obtained during coffee preparation by skilled baristas. Coffee extraction is also influenced by environmental factors, whose variability has been reduced as much as possible in this study since samples have been prepared in a few hours and with macroscopic characteristics of the laboratory fairly constant. The repeatability of the results should be tested against larger variability of the environmental factors, such as ambient temperature, air humidity and water quality. Of course, the

extraction equipment also plays a relevant role and a high-quality espresso machine and grinder have been chosen for this study, but other equipment available on the market should also be considered. The whole extraction procedure, involving the proper settings and treatment of the raw material, has been executed by experienced baristas, who significantly limit human error; this is essential to ensure consistency and repeatability of the results. Finally, only pure coffee variety are considered, discarding blends, for which the chemical characterisation is assumed to follow the linear interpolation of the results of this study, but also such an assumption has to be experimentally assessed.

Future studies have to further enhance the predictability of the model by refining some aspects: firstly, the less accurate species such as acetic acid and lipids deserve a deeper investigation on their variability and on the modelling of the corresponding reaction terms; moreover, an in-depth study on fines would enlarge the applicability area of the model, giving information on the appreciated "crema" of EC and providing the capability to simulate the creation of the compact layer and connected critical situations, such as the clog of the filter. The good predictive capabilities of the 3D model make this simulation system a key tool for the coffee market, as it could actually support the one of the current main challenges of the coffee industry, which is the personalisation of the coffee beverage.

An RBF-based approximation scheme has been also proposed and used for the discretisation of the equation modelling the water dynamics in the 3D model. In particular, we predicted the hydraulic head behaviour varying the initial pressure of the incoming water. The preliminary results are quite reasonable and in good agreement with the numerical data obtained with the finite element tool. So, this is a promising approximation strategy that deserves further exploration in order to obtain a proprietary computational tool for the complete 3D model of the coffee percolation process.

Finally, the work of the present thesis, properly tested and validated, represents a really powerful tool for the coffee industry. It paves the way for an effective control strategy of the extraction process. Such tool constitutes the scientific basis for the personalisation of the beverage according to the customers' tastes and for the

optimisation of the consumption of raw materials in order to achieve sustainability goals of coffee market. This, with an even more visionary outlook, can be translated in the realisation of a digital twin controlling all the extractions; the underlying idea of which is the control of all extractions performed by all physical extraction machines remotely connected to the twin.

Bibliography

[1] *E-imports - Espresso Business Solutions*. `http://www.e-importz.com/coffee-statistics.php`. (Visited on 2020) (cit. on p. vii).

[2] *Coffee market*. `https://www.cbi.eu/market-information/coffee/trade-statistics`. (Visited on 2020) (cit. on p. vii).

[3] Ronald B Postuma, Anthony E Lang, Renato P Munhoz, et al. "Caffeine for treatment of Parkinson disease: a randomized controlled trial". In: *Neurology* 79.7 (2012), pp. 651–658 (cit. on p. vii).

[4] Rob M Van Dam and Edith JM Feskens. "Coffee consumption and risk of type 2 diabetes mellitus". In: *The Lancet* 360.9344 (2002), pp. 1477–1478 (cit. on p. vii).

[5] Manami Inoue and Shoichiro Tsugane. "Coffee Drinking and Reduced Risk of Liver Cancer: Update on Epidemiological Findings and Potential Mechanisms". In: *Current nutrition reports* 8.3 (2019), pp. 182–186 (cit. on p. vii).

[6] Charlotte R Kennedy and Sam Abraham. "Association between coffee consumption and different types of cancers: A review of meta-analysis". In: *Cogent Psychology* 4.1 (2017), p. 1392230 (cit. on p. vii).

[7] Melanie A. Heckman, Jorge Weil, and Elvira Gonzalez De Mejia. "Caffeine (1, 3, 7-trimethylxanthine) in foods: a comprehensive review on consumption, functionality, safety, and regulatory matters". In: *Journal of food science* 75.3 (2010), R77–R87 (cit. on p. vii).

[8] Karin Kraehenbuehl, Nicole Page-Zoerkler, Olivier Mauroux, et al. "Selective enzymatic hydrolysis of chlorogenic acid lactones in a model system and in a coffee extract. Application to reduction of coffee bitterness". In: *Food Chemistry* 218 (2017), pp. 9–14 (cit. on p. vii).

[9] Gema Baeza, Miryam Amigo-Benavent, Beatriz Sarriá, et al. "Green coffee hydroxycinnamic acids but not caffeine protect human HepG2 cells against oxidative stress". In: *Food Research International* 62 (2014), pp. 1038–1046 (cit. on p. viii).

[10] Ningjian Liang and David D. Kitts. "Role of chlorogenic acids in controlling oxidative and inflammatory stress conditions". In: *Nutrients* 8.1 (2015), p. 16 (cit. on p. viii).

[11] Narges Tajik, Mahboubeh Tajik, Isabelle Mack, et al. "The potential effects of chlorogenic acid, the main phenolic components in coffee, on health: a comprehensive review of the literature". In: *European journal of nutrition* 56.7 (2017), pp. 2215–2244 (cit. on p. viii).

[12] Gulzhan Khamitova, Simone Angeloni, Lauro Fioretti, et al. "The impact of different filter baskets, heights of perforated disc and amount of ground coffee on the extraction of organics acids and the main bioactive compounds in espresso coffee". In: *Food Research International* 133 (2020), p. 109220 (cit. on pp. viii, 120).

[13] Andrea Illy and Rinantonio Viani. *Espresso coffee: the science of quality*. Academic Press, 2005 (cit. on pp. viii, ix, 26, 27, 119, 129).

[14] Britta Folmer. *The craft and science of coffee*. Academic Press, 2016 (cit. on pp. viii, 120).

[15] Gulzhan Khamitova, Simone Angeloni, Germana Borsetta, et al. "Optimization of espresso coffee extraction through variation of particle sizes, perforated disk height and filter basket aimed at lowering the amount of ground coffee used". In: *Food chemistry* 314 (2020), p. 126220 (cit. on pp. ix, 120).

[16] C Severini, A Derossi, I Ricci, et al. "Roasting conditions, grinding level and brewing method highly affect the healthy benefits of a coffee cup". In: *Int J Clin Nutr Diet* 4.1 (2018), p. 127 (cit. on pp. ix, 120).

[17] K. Moroney, W. Lee, S. Brien, et al. "Asymptotic Analysis of the Dominant Mechanisms in the Coffee Extraction Process". In: *SIAM Journal on Applied Mathematics* 76.6 (2016), pp. 2196–2217. DOI: 10.1137/15M1036658 (cit. on pp. ix, 41).

[18] Kevin M. Moroney, K. O'Connell, P. Meikle-Janney, et al. "Analysing extraction uniformity from porous coffee beds using mathematical modelling and computational fluid dynamics approaches". In: *PLoS ONE* 14.7 (2019). DOI: 10.1371/journal.pone.0219906 (cit. on pp. ix, 41, 129).

[19] Michael I Cameron, Dechen Morisco, Daniel Hofstetter, et al. "Systematically improving espresso: insights from mathematical modeling and experiment". In: *Matter* (2020). DOI: https://doi.org/10.1016/j.matt.2019.12.019 (cit. on pp. ix, 41, 45, 95, 100, 110).

[20] Nadaniela Egidi, Josephin Giacomini, Pierluigi Maponi, et al. "A reduced model for the coffee percolation and assessment of the extraction efficiency". Preprint (cit. on p. ix).

[21] Josephin Giacomini, Pierluigi Maponi, and Alessia Perticarini. "CMMSE: a reduced percolation model for espresso coffee". In: *Journal of Mathematical Chemistry* (2022), pp. 1–19 (cit. on pp. ix, 41, 45, 77, 94).

[22] K.M. Moroney, W.T. Lee, S.B.G. O'Brien, et al. "Modelling of coffee extraction during brewing using multiscale methods: An experimentally validated model". In: *Chemical Engineering Science* 137 (2015), pp. 216–234 (cit. on pp. x, 41, 95, 110).

[23] Josephin Giacomini, Gulzhan Khamitova, Pierluigi Maponi, et al. "Water flow and transport in porous media for in-silico espresso coffee". In: *International Journal of Multiphase Flow* (2020), p. 103252. DOI: https://doi.org/10.

1016/j.ijmultiphaseflow.2020.103252 (cit. on pp. x, 28, 36, 100, 129, 157).

[24] Simone Angeloni, Josephin Giacomini, Pierluigi Maponi, et al. "Computer Percolation Models for Espresso Coffee: State of the Art, Results and Future Perspectives". In: *Applied Sciences* 13.4 (2023), p. 2688 (cit. on pp. x, 36, 115, 119, 157).

[25] Arnold Sommerfeld. *Partial differential equations in physics*. Academic press, 1949 (cit. on p. 1).

[26] Leon Lapidus and George F Pinder. *Numerical solution of partial differential equations in science and engineering*. John Wiley & Sons, 1999 (cit. on p. 1).

[27] Marius Lysaker, Arvid Lundervold, and Xue-Cheng Tai. "Noise removal using fourth-order partial differential equation with applications to medical magnetic resonance images in space and time". In: *IEEE Transactions on image processing* 12.12 (2003), pp. 1579–1590 (cit. on p. 1).

[28] Raouf Boucekkine, Carmen Camacho, and Giorgio Fabbri. "On the optimal control of some parabolic partial differential equations arising in economics". In: (2013) (cit. on p. 1).

[29] Anthony W Leung. *Systems of nonlinear partial differential equations: applications to biology and engineering*. Vol. 49. Springer Science & Business Media, 2013 (cit. on p. 1).

[30] Nicola Fusco, Paolo Marcellini, and Carlo Sbordone. *Analisi matematica due*. Liguori, 1996 (cit. on p. 2).

[31] Haiyu Liu and Shujuan Lü. "A high-order numerical scheme for solving nonlinear time fractional reaction-diffusion equations with initial singularity". In: *Applied Numerical Mathematics* 169 (2021), pp. 32–43 (cit. on p. 4).

[32] Jean Clairambault. "Reaction-Diffusion-Advection Equation". In: *Encyclopedia of Systems Biology; Springer: New York, NY, USA* (2013), p. 1817 (cit. on p. 4).

[33] Hans-Jörg G Diersch. *FEFLOW: finite element modeling of flow, mass and heat transport in porous and fractured media*. Springer Science & Business Media, 2013 (cit. on pp. 4, 11, 23, 25, 30, 35, 36, 51, 117, 129).

[34] Alan D McNaught, Andrew Wilkinson, et al. *Compendium of chemical terminology*. Vol. 1669. Blackwell Science Oxford, 1997 (cit. on p. 4).

[35] Adrian Bejan. *Convection heat transfer*. John wiley & sons, 2013 (cit. on p. 4).

[36] R Byron Bird et al. "We stewart, and en lightfoot". In: *Transport phenomena* 11 (1960), p. 5 (cit. on p. 4).

[37] Sauro Succi. *The lattice Boltzmann equation: for fluid dynamics and beyond*. Oxford university press, 2001 (cit. on p. 12).

[38] Andrew Ilachinski. *Cellular automata: a discrete universe*. World Scientific Publishing Company, 2001 (cit. on p. 12).

[39] Zhangxin Chen, Stephen L Lyons, and Guan Qin. "Derivation of the Forchheimer law via homogenization". In: *Transport in porous media* 44 (2001), pp. 325–335 (cit. on p. 12).

[40] Reint De Boer. *Theory of porous media: highlights in historical development and current state*. Springer Science & Business Media, 2012 (cit. on p. 12).

[41] Majid Hassanizadeh and William G Gray. "General conservation equations for multi-phase systems: 1. Averaging procedure". In: *Advances in water resources* 2 (1979), pp. 131–144 (cit. on pp. 14, 19, 20).

[42] L Gary Leal. *Advanced transport phenomena: fluid mechanics and convective transport processes*. Vol. 7. Cambridge University Press, 2007 (cit. on p. 17).

[43] George F Pinder and William G Gray. *Essentials of multiphase flow and transport in porous media*. John Wiley & Sons, 2008 (cit. on p. 19).

[44] S Majid Hassanizadeh and Anton Leijnse. "A non-linear theory of high-concentration-gradient dispersion in porous media". In: *Advances in Water Resources* 18.4 (1995), pp. 203–215 (cit. on p. 22).

[45] RJ Schotting, H Moser, and SM Hassanizadeh. "High-concentration-gradient dispersion in porous media: experiments, analysis and approximations". In: *Advances in Water Resources* 22.7 (1999), pp. 665–680 (cit. on p. 22).

[46] Henry Darcy. *Les fontaines publiques de la ville de Dijon: exposition et application des principes à suivre et des formules à employer dans les questions de distribution d'eau*. Vol. 1. Victor dalmont, 1856 (cit. on p. 30).

[47] Jacob Bear. *Dynamics of fluids in porous media*. Courier Corporation, 2013 (cit. on p. 30).

[48] Nikolaus Rott. "Note on the history of the Reynolds number". In: *Annual review of fluid mechanics* 22.1 (1990), pp. 1–12 (cit. on p. 31).

[49] George F Pinder and Michael A Celia. *Subsurface hydrology*. John Wiley & Sons, 2006 (cit. on p. 32).

[50] Karl Terzaghi, Ralph B Peck, and Gholamreza Mesri. *Soil mechanics in engineering practice*. John wiley & sons, 1996 (cit. on p. 32).

[51] George F Pinder and Michael A Celia. *Subsurface hydrology*. John Wiley & Sons, 2006 (cit. on p. 36).

[52] Donald A Nield, Adrian Bejan, et al. *Convection in porous media*. Vol. 3. Springer, 2006 (cit. on p. 36).

[53] Anton Oberbeck. "Über die Wärmeleitung der Flüssigkeiten bei Berücksichtigung der Strömungen infolge von Temperaturdifferenzen". In: *Annalen der Physik* 243.6 (1879), pp. 271–292 (cit. on p. 37).

[54] Joseph Boussinesq. *Théorie analytique de la chaleur mise en harmonic avec la thermodynamique et avec la théorie mécanique de la lumière: Refroidissement et échauffement par rayonnement, conductibilité des tiges, lames et masses cristallines, courants de convection, théorie mécanique de la lumière. 1903. xxxii, 625,[1] p.* Vol. 2. Gauthier-Villars, 1903 (cit. on p. 37).

[55] Nadaniela Egidi, Josephin Giacomini, Pierluigi Maponi, et al. "An advection–diffusion–reaction model for coffee percolation". In: *Computational and Applied Mathematics* 41.6 (2022), p. 229 (cit. on pp. 41, 45, 77, 94, 100, 110).

[56] Majid Naderi. "Surface Area: Brunauer–Emmett–Teller (BET)". In: *Progress in filtration and separation*. Elsevier, 2015, pp. 585–608 (cit. on p. 43).

[57] Kevin M. Moroney, William T. Lee, Stephen BG OÕBrien, et al. "Coffee extraction kinetics in a well mixed system". In: *Journal of Mathematics in Industry* 7.1 (2016). DOI: 10.1186/s13362-016-0024-6 (cit. on p. 45).

[58] Peter D Lax. "Numerical solution of partial differential equations". In: *The American Mathematical Monthly* 72.sup2 (1965), pp. 74–84 (cit. on p. 51).

[59] RD Richtmyer. "K. w. morton". In: *Difference Methods for Initial-Value Problems, 2nd edn, Wiley Interscience, New York* (1967) (cit. on p. 51).

[60] James Hyman, Mikhail Shashkov, and Stanly Steinberg. "The effect of inner products for discrete vector fields on the accuracy of mimetic finite difference methods". In: *Computers & Mathematics with Applications* 42.12 (2001), pp. 1527–1547 (cit. on p. 51).

[61] Mikhail Shashkov and Stanly Steinberg. "Solving diffusion equations with rough coefficients in rough grids". In: *Journal of Computational Physics* 129.2 (1996), pp. 383–405 (cit. on p. 51).

[62] EJ Caramana, DE Burton, Mikhail J Shashkov, et al. "The construction of compatible hydrodynamics algorithms utilizing conservation of total energy". In: *Journal of Computational Physics* 146.1 (1998), pp. 227–262 (cit. on p. 51).

[63] Len G Margolin, Mikhail Shashkov, and Piotr K Smolarkiewicz. "A discrete operator calculus for finite difference approximations". In: *Computer methods in applied mechanics and engineering* 187.3-4 (2000), pp. 365–383 (cit. on p. 51).

[64] Siobhan O'Callaghan, Michael Walsh, and Tim McGloughlin. "Comparison of finite volume, finite element and theoretical predictions of blood flow through an idealised femoral artery". In: *2003 summer bioengineering conference*. 2003, pp. 417–418 (cit. on p. 51).

[65] Mattia Corti, Paola F Antonietti, Luca Dede', et al. "Numerical modeling of the brain poromechanics by high-order discontinuous Galerkin methods". In: *Mathematical Models and Methods in Applied Sciences* (2023), pp. 1–33 (cit. on p. 51).

[66] Rolland L Hardy. "Theory and applications of the multiquadric-biharmonic method 20 years of discovery 1968–1988". In: *Computers & Mathematics with Applications* 19.8-9 (1990), pp. 163–208 (cit. on p. 51).

[67] Jan Flusser. "An adaptive method for image registration". In: *Pattern Recognition* 25.1 (1992), pp. 45–54 (cit. on p. 51).

[68] Jonathan C Carr, W Richard Fright, and Richard K Beatson. "Surface interpolation with radial basis functions for medical imaging". In: *IEEE transactions on medical imaging* 16.1 (1997), pp. 96–107 (cit. on p. 51).

[69] Damiana Lazzaro and Laura B Montefusco. "Radial basis functions for the multivariate interpolation of large scattered data sets". In: *Journal of Computational and Applied Mathematics* 140.1-2 (2002), pp. 521–536 (cit. on p. 51).

[70] Tomaso Poggio and Federico Girosi. "Networks for approximation and learning". In: *Proceedings of the IEEE* 78.9 (1990), pp. 1481–1497 (cit. on p. 51).

[71] Carsten Franke and Robert Schaback. "Solving partial differential equations by collocation using radial basis functions". In: *Applied Mathematics and Computation* 93.1 (1998), pp. 73–82 (cit. on p. 51).

[72] John David Anderson and John Wendt. *Computational fluid dynamics*. Vol. 206. Springer, 1995 (cit. on pp. 53, 56, 60).

[73] H. B. Keller. *Numerical methods for two-points boundary value problems*. Dover Publications, 2018 (cit. on pp. 54, 56).

[74] Alfio Quarteroni and Alberto Valli. *Numerical approximation of partial differential equations*. Vol. 23. Springer Science & Business Media, 2008 (cit. on p. 58).

[75] Gregory E Fasshauer. *Meshfree approximation methods with MATLAB*. Vol. 6. World Scientific, 2007 (cit. on pp. 67, 70, 72, 74).

[76] Holger Wendland. *Scattered data approximation*. Vol. 17. Cambridge university press, 2004 (cit. on pp. 67, 69, 74).

[77] *FeFlow - DHI*. `https://www.mikepoweredbydhi.com/products/feflow`. Accessed: 2023 (cit. on pp. 75, 135, 161).

[78] John Crank and Phyllis Nicolson. "A practical method for numerical evaluation of solutions of partial differential equations of the heat-conduction type". In: *Mathematical proceedings of the Cambridge philosophical society*. Vol. 43. 1. Cambridge University Press. 1947, pp. 50–67 (cit. on p. 77).

[79] *Mythos 1 grinder - Victoria Arduino*. URL: `https://www.victoriaarduino.com/mythos-1/` (visited on 2021) (cit. on p. 85).

[80] *PUQ PRESS M2 tamper*. URL: `https://www.puqpress.com/products/puq-m-line/puqpress-m2-for-mythos/` (visited on 2021) (cit. on pp. 85, 92).

[81] *Victoria Arduino VA388 Black Eagle*. URL: `https://www.victoriaarduino.com/black-eagle/` (visited on 2021) (cit. on pp. 85, 92).

[82] *Mastersizer - Malvern Panalytical*. URL: `https://www.malvernpanalytical.com/en/products/product-range/mastersizer-range` (visited on 2021) (cit. on pp. 87, 92).

[83] *Mythos 2 grinder - Victoria Arduino*. `https://www.victoriaarduino.com/mythos-2/`. (Visited on 2021) (cit. on p. 92).

[84] Nadaniela Egidi, Josephin Giacomini, Elisabeth Larsson, et al. "An improved numerical scheme for coffee Extraction Yield evaluation". In: *submitted to Journal of Food Engineering* (2023) (cit. on p. 103).

[85] Ivo Babuška. "The finite element method with Lagrangian multipliers". In: *Numerische Mathematik* 20.179-192 (1973) (cit. on p. 117).

[86] C. Cuvelier, A. Segal, and A.A. Van Steenhoven. *Finite Element Methods and Navier Stokes equations*. D. Reidel Publishing Company, 1977 (cit. on p. 117).

[87] *Mythos 1*. `https://www.victoriaarduino.com/mythos-1/`. Accessed: 2023 (cit. on p. 118).

[88] *Puq Press*. `https://www.puqpress.com/products/puq-m-line/puqpress-m2-for-mythos/`. Accessed: 2023 (cit. on p. 118).

[89] *VA388 Black Eagle*. `https://www.victoriaarduino.com/wp-content/uploads/VA388.pdf`. Accessed: 2023 (cit. on p. 118).

[90] Giovanni Caprioli, Manuela Cortese, Filippo Maggi, et al. "Quantification of caffeine, trigonelline and nicotinic acid in espresso coffee: the influence of espresso machines and coffee cultivars". In: *International journal of food sciences and nutrition* 65.4 (2014), pp. 465–469 (cit. on p. 120).

[91] Carla Isabel Rodrigues, Liliana Marta, Rodrigo Maia, et al. "Application of solid-phase extraction to brewed coffee caffeine and organic acid determination by UV/HPLC". In: *Journal of Food Composition and Analysis* 20.5 (2007), pp. 440–448 (cit. on p. 120).

[92] Wenny B. Sunarharum, David J. Williams, and Heather E. Smyth. "Complexity of coffee flavor: A compositional and sensory perspective". In: *Food research international* 62 (2014), pp. 315–325 (cit. on p. 120).

[93] Susana Andueza, M Paz De Peña, and Concepción Cid. "Chemical and sensorial characteristics of espresso coffee as affected by grinding and torrefacto roast". In: *Journal of Agricultural and Food Chemistry* 51.24 (2003), pp. 7034–7039 (cit. on p. 120).

[94] Josephin Giacomini, Maria Chiara Invernizzi, Pierluigi Maponi, et al. "Testing a model of flow and heat transfer for u-shaped geothermal exchangers". In: *Advances in Modelling and Analysis A* 55.3 (2018), pp. 151–157 (cit. on p. 129).

[95] Jacob Bear and Arnold Verruijt. *Modeling Groundwater Flow and Pollution.* Vol. 2. Springer Science & Business Media, 1987 (cit. on p. 129).